

# Biocompatibility and Toxicity of Nanobiomaterials

Guest Editors: Xiaoming Li, Sang Cheon Lee, Shuming Zhang,  
and Tsukasa Akasaka



---



# **Biocompatibility and Toxicity of Nanobiomaterials**

## **Biocompatibility and Toxicity of Nanobiomaterials**

Guest Editors: Xiaoming Li, Sang Cheon Lee, Shuming Zhang,  
and Tsukasa Akasaka



Copyright © 2012 Hindawi Publishing Corporation. All rights reserved.

This is a special issue published in "Journal of Nanomaterials." All articles are open access articles distributed under the Creative Commons Attribution License, which permits unrestricted use, distribution, and reproduction in any medium, provided the original work is properly cited.

## Editorial Board

Katerina Aifantis, Greece	Do Kyung Kim, Korea	Nairong Tao, China
Nageh K. Allam, USA	Kin Tak Lau, Australia	Titipun Thongtem, Thailand
Margarida Amaral, Portugal	Burtrand Lee, USA	Somchai Thongtem, Thailand
Xuedong Bai, China	Benxia Li, China	Alexander Tolmachev, Ukraine
L. Balan, France	Jun Li, Singapore	Valeri P. Tolstoy, Russia
Enrico Bergamaschi, Italy	Shijun Liao, China	Tsung-Yen Tsai, Taiwan
Theodorian Borca-Tasciuc, USA	Gong Ru Lin, Taiwan	Takuya Tsuzuki, Australia
C. Jeffrey Brinker, USA	J.-Y. Liu, USA	Raquel Verdejo, Spain
Christian Brosseau, France	Jun Liu, USA	Mat U. Wahit, Malaysia
Xuebo Cao, China	Xing-Jie Liang, China	Shiren Wang, USA
Shafiu Chowdhury, USA	Tianxi Liu, China	Yong Wang, USA
Kwang-Leong Choy, UK	Songwei Lu, USA	Ruibing Wang, Canada
Cui ChunXiang, China	Daniel Lu, China	Cheng Wang, China
Miguel A. Correa-Duarte, Spain	Jue Lu, USA	Zhenbo Wang, China
Shadi A. Dayeh, USA	Ed Ma, USA	Jinquan Wei, China
Claude Estournes, France	Gaurav Mago, USA	Ching Ping Wong, USA
Alan Fuchs, USA	Santanu K. Maiti, Israel	Xingcai Wu, China
Lian Gao, China	Sanjay R. Mathur, Germany	Guodong Xia, Hong Kong
Russell E. Gorga, USA	A. McCormick, USA	Zhi Li Xiao, USA
Hongchen Chen Gu, China	Vikas Mittal, UAE	Ping Xiao, UK
Mustafa O. Guler, Turkey	Weihai Ni, Germany	Shuangxi Xing, China
John Zhanhu Guo, USA	Sherine Obare, USA	Yangchuan Xing, USA
Smrati Gupta, Germany	Abdelwahab Omri, Canada	N. Xu, China
Michael Harris, USA	Edward Andrew Payzant, USA	Doron Yadlovker, Israel
Zhongkui Hong, USA	Kui-Qing Peng, China	Ying-Kui Yang, China
Michael Z. Hu, USA	Anukorn Phuruangrat, Thailand	Khaled Youssef, USA
David Hui, USA	Ugur Serincan, Turkey	William W. Yu, USA
Y.-K. Jeong, Republic of Korea	Huaiyu Shao, Japan	Kui Yu, Canada
Sheng-Rui Jian, Taiwan	Donglu Shi, USA	Haibo Zeng, China
Wanqin Jin, China	Suprakas Sinha Ray, South Africa	Tianyou Zhai, Japan
Rakesh K. Joshi, India	Vladimir Sivakov, Germany	Renyun Zhang, Sweden
Zhenhui Kang, China	Marinella Striccoli, Italy	Yanbao Zhao, China
Fathallah Karimzadeh, Iran	Bohua Sun, South Africa	Lianxi Zheng, Singapore
Alireza Khataee, Iran	Saikat Talapatra, USA	Chunyi Zhi, Japan

## Contents

**Biocompatibility and Toxicity of Nanobiomaterials**, Xiaoming Li, Sang Cheon Lee, Shuming Zhang, and Tsukasa Akasaka  
Volume 2012, Article ID 591278, 2 page

**Properties of Surfactin C-15 Nanopeptide and Its Cytotoxic Effect on Human Cervix Cancer (HeLa) Cell Line**, Zahra Nozhat, Asadollah Asadi, and Saber Zahri  
Volume 2012, Article ID 526580, 5 page

**In Vitro Cytotoxicity Assay on Gold Nanoparticles with Different Stabilizing Agents**, S. Vijayakumar and S. Ganesan  
Volume 2012, Article ID 734398, 9 page

**Biocompatibility and Toxicity of Magnetic Nanoparticles in Regenerative Medicine**, H. Markides, M. Rotherham, and A. J. El Haj  
Volume 2012, Article ID 614094, 11 page

**Silver Nanoparticles in Alveolar Bone Surgery Devices**, Stefano Sivolella, Edoardo Stellini, Giulia Brunello, Chiara Gardin, Letizia Ferroni, Eriberto Bressan, and Barbara Zavan  
Volume 2012, Article ID 975842, 12 page

**In Vitro Biocompatibility of Endodontic Sealers Incorporating Antibacterial Nanoparticles**, Itzhak Abramovitz, Nurit Beyth, Guy Weinberg, Alon Borenstein, David Polak, Dana Kesler-Shvero, and Yael Hourie-Haddad  
Volume 2012, Article ID 858073, 9 page

**Cytotoxicity of Silver Nanoparticles in Human Embryonic Stem Cell-Derived Fibroblasts and an L-929 Cell Line**, Hui Peng, Xuehui Zhang, Yan Wei, Wentao Liu, Shenglin Li, Guangyan Yu, Xin Fu, Tong Cao, and Xuliang Deng  
Volume 2012, Article ID 160145, 9 page

**Toxicity of Aqueous Fullerene nC<sub>60</sub> to Activated Sludge: Nitrification Inhibition and Microtox Test**, Yongkui Yang, Norihide Nakada, Ryoji Nakajima, Chao Wang, and Hiroaki Tanaka  
Volume 2012, Article ID 512956, 6 page

**The Human Stratum Corneum Prevents Small Gold Nanoparticle Penetration and Their Potential Toxic Metabolic Consequences**, David C. Liu, Anthony P. Raphael, Daniel Sundh, Jeffrey E. Grice, H. Peter Soyer, Michael S. Roberts, and Tarl W. Prow  
Volume 2012, Article ID 721706, 8 page

**Control of *In Vivo* Transport and Toxicity of Nanoparticles by Tea Melanin**, Yu-Shiun Chen, Yao-Ching Hung, Meng-Yeng Hong, Andrei Aleksandrovich Onischuk, Jin Chern Chiou, Irina V. Sorokina, Tatiana Tolstikova, and G. Steve Huang  
Volume 2012, Article ID 746960, 11 page

**Biocompatibility and Toxicity of Nanoparticles and Nanotubes**, Xiaoming Li, Lu Wang, Yubo Fan, Qingling Feng, and Fu-zhai Cui  
Volume 2012, Article ID 548389, 19 page

---

**Biocompatibility of Nanoporous TiO<sub>2</sub> Coating on NiTi Alloy Prepared via Dealloying Method,**

Jin Huang, Junqiang Wang, Xiangdong Su, Weichang Hao, Tianmin Wang, Yiyi Xia, Guozu Da, and Yubo Fan

Volume 2012, Article ID 731592, 7 page

**Noninvasive Evaluation of Injectable Chitosan/Nano-Hydroxyapatite/Collagen Scaffold via Ultrasound,**

Yan Chen, Songjian Li, Xiaoming Li, Yichen Zhang, Zhi Huang, Qingling Feng, Zhilai Zhou, Bomiao Lin, and Bo Yu

Volume 2012, Article ID 939821, 7 page

**Biocompatible Single-Crystal Selenium Nanobelt Based Nanodevice as a Temperature-Tunable**

**Photosensor,** Yongshan Niu, Aimiao Qin, Wei Song, Menghang Wang, Xuenan Gu, Yangfei Zhang, Min Yu, Xiaoguang Zhao, Ming Dai, Ling Yan, Zhou Li, and Yubo Fan

Volume 2012, Article ID 384671, 6 page

**In Vitro Biocompatibility and Osteoblast Differentiation of an Injectable**

**Chitosan/Nano-Hydroxyapatite/Collagen Scaffold,** Yan Chen, Zhi Huang, Xiaoming Li, Songjian Li, Zhilai Zhou, Yichen Zhang, Qing ling Feng, and Bo Yu

Volume 2012, Article ID 401084, 6 page

**Nanotechnology-Based Therapies for Skin Wound Regeneration,** Ilaria Tocco, Barbara Zavan,

Franco Bassetto, and Vincenzo Vindigni

Volume 2012, Article ID 714134, 11 page

**Evaluation on Cartilage Morphology after Intra-Articular Injection of Titanium Dioxide Nanoparticles**

**in Rats,** Jiangxue Wang, Yu Gao, Ying Hou, Feng Zhao, Fang Pu, Xiaoyu Liu, Zhihong Wu, and Yubo Fan

Volume 2012, Article ID 452767, 11 page

## Editorial

# Biocompatibility and Toxicity of Nanobiomaterials

Xiaoming Li,<sup>1</sup> Sang Cheon Lee,<sup>2</sup> Shuming Zhang,<sup>3</sup> and Tsukasa Akasaka<sup>4</sup>

<sup>1</sup>Key Laboratory for Biomechanics and Mechanobiology of Ministry of Education, School of Biological Science and Medical Engineering, Beihang University, Beijing 100191, China

<sup>2</sup>Department of Maxillofacial Biomedical Engineering, School of Dentistry, Kyung Hee University, Seoul 130-701, Republic of Korea

<sup>3</sup>Department of Materials Science and Engineering, Johns Hopkins University, Baltimore, MD 21218, USA

<sup>4</sup>Department of Biomedical Materials and Engineering, Hokkaido University, Sapporo 060-8586, Japan

Correspondence should be addressed to Xiaoming Li, x.m.li@hotmail.com

Received 28 November 2012; Accepted 28 November 2012

Copyright © 2012 Xiaoming Li et al. This is an open access article distributed under the Creative Commons Attribution License, which permits unrestricted use, distribution, and reproduction in any medium, provided the original work is properly cited.

The nanodimensionality of nature has logically given rise to the interest in using nanomaterials in biomedical field [1–3]. Over the past decades, nanobiomaterials have played significant roles in the fields of biomedical engineering and pharmaceuticals. The wide variety of nanobiomaterials has encouraged their use in applications including drug delivery systems, imaging systems for diagnosis, tissue engineering, and dental/bone implant. For successful clinical applications, the investigations into biocompatibility and toxicity of nanobiomaterials are research interests of great significances. The same unique physical and chemical properties that may be beneficial in nanobiomaterials may be associated with potentially deleterious effects on human health. For example, nanobiomaterials designed for drug delivery deliberately overcome biological barriers or they may cross them unintentionally as a result of environmental exposure. Once they have been taken up, they can potentially be deposited in any region of the body. Due to their small size or specific functionalization, nanobiomaterials may cross important biological barriers and cause toxicity to very sensitive systems such as the brain or the developing fetus. Nanobiomaterials can be transported through the blood and accumulate in secondary target tissues and organs such as liver, spleen, kidney, placenta, the cardiovascular system, and central nervous system (CNS), where they may cause adverse effects [4–6]. But on the other hand, some nanobiomaterials have been found to be able to concentrate more proteins including specific proteins and these proteins might not only improve cell attachment and proliferation but also differentiate the inducible cells, which promote the tissue repair. Therefore, these nanobiomaterials might have the ability to modulate

downstream stem cellular response, without exogenous growth factors, coatings, or complex ligand incorporation, and have the potential to greatly facilitate the development of tissue engineering and cellular therapies [7–9].

Biocompatibility and toxicity of nanobiomaterials are tested at three levels. First, tests are performed *in vitro* in cell or tissue cultures. If these tests are shown promising, further testing is performed *in vivo* in animal models before clinical studies are performed on humans. Existing regulatory frameworks in principle cover all important aspects; however, different behavior of nanobiomaterials from the corresponding bulk material suggests the need for specific nanopolicies or adaptation of existing frames. Unfortunately, there is still lack of validated analytical and biological methods as well as certified reference standards for exposure and hazard assessment for establishing safe doses of nanobiomaterials. Well-characterized and defined nanobiomaterials to be used as certified reference standards need to be developed as quality controls additional to standardized test protocols. Furthermore, the underlying mechanisms, for example, oxidative stress, immunotoxicity, and genotoxicity, need to be investigated and possible adverse effects should be considered.

To date, many trials have been performed to estimate *in vitro* and *in vivo* biocompatibility and toxicity of nanobiomaterials. Based on such preclinical evaluation of biocompatibility and toxicity, current research trends are focused on whether the nanobiomaterials induce toxic effects in human body. For example, some nanomaterials may be taken up by phagocytic cells of the RES (reticuloendothelial system), to induce the production of reactive oxygen species

and cause oxidative stress or preinflammatory cytotoxic activity in the lungs, liver, heart, brain, and so forth.

In this special issue, a dozen of articles are devoted to interaction between nanobiomaterials and cell/tissue, effect of size, shape, and surface of nanobiomaterials on their biocompatibility and toxicity, immunogenicity of nanobiomaterials, design of novel biocompatible and biodegradable nanobiomaterials, instrumentation and technology to analyze toxicity of nanobiomaterials, and challenges to overcome the toxicity of nanobiomaterials. The readers can find in this special issue not only accurate data and updated reviews on the above-mentioned aspects but also the possibility to understand accurately how nanobiomaterials interact with organs, tissues, and cells, and what is their bioavailability and biopersistence, and self-assembly mechanism of natural tissues in order to better biomimetically prepare tissue repair nanobiomaterials, to find out how the biocompatibility and toxicity of nanobiomaterials depend on their properties such as dimensions, size, shape, chemical composition, surface chemistry, and coatings, and to realize the necessity to chemically functionalize nanobiomaterials or introduce various molecules, growth factors, antigens, and specific DNA sequences, which can subsequently have positive effect on the desired cellular functions or therapeutic efficacy and to develop standard toxicological tests for nanobiomaterials so that one set of experiments can be compared with another.

Xiaoming Li  
Sang Cheon Lee  
Shuming Zhang  
Tsukasa Akasaka

## References

- [1] X. Li, Q. Feng, X. Liu, W. Dong, and F. Cui, "Collagen-based implants reinforced by chitin fibres in a goat shank bone defect model," *Biomaterials*, vol. 27, no. 9, pp. 1917–1923, 2006.
- [2] X. Li, H. Gao, M. Uo et al., "Effect of carbon nanotubes on cellular functions *in vitro*," *Journal of Biomedical Materials Research A*, vol. 91, no. 1, pp. 132–139, 2009.
- [3] X. Li, H. Gao, M. Uo et al., "Maturation of osteoblast-like Saos2 induced by carbon nanotubes," *Biomedical Materials*, vol. 4, no. 1, Article ID 015005, 2009.
- [4] X. Li, X. Liu, J. Huang, Y. Fan, and F.-Z. Cui, "Biomedical investigation of CNT based coatings," *Surface and Coatings Technology*, vol. 206, no. 4, pp. 759–766, 2011.
- [5] X. Li, Y. Fan, and F. Watari, "Current investigations into carbon nanotubes for biomedical application," *Biomedical Materials*, vol. 5, no. 2, Article ID 022001, 12 pages, 2010.
- [6] M. Dusinska, Z. Magdolenova, and L. Fjellsbo, "Toxicological aspects for nanomaterial in humans," *Methods in Molecular Biology*, vol. 948, pp. 1–12, 2013.
- [7] X. Li, C. A. van Blitterswijk, Q. Feng, F. Cui, and F. Watari, "The effect of calcium phosphate microstructure on bone-related cells *in vitro*," *Biomaterials*, vol. 29, no. 23, pp. 3306–3316, 2008.
- [8] X. Li, H. Liu, X. Niu et al., "The use of carbon nanotubes to induce osteogenic differentiation of human adipose-derived MSCs *in vitro* and ectopic bone formation *in vivo*," *Biomaterials*, vol. 33, no. 19, pp. 4818–4827, 2012.
- [9] X. Li, H. Liu, X. Niu et al., "Osteogenic differentiation of human adipose-derived stem cells induced by osteoinductive calcium

phosphate ceramics," *Journal of Biomedical Materials Research B*, vol. 97, no. 1, pp. 10–19, 2011.

## Research Article

# Properties of Surfactin C-15 Nanopeptide and Its Cytotoxic Effect on Human Cervix Cancer (HeLa) Cell Line

Zahra Nozhat, Asadollah Asadi, and Saber Zahri

Departement of Biology, Faculty of Science, University of Mohaghegh Ardabili, Ardabil 11367-56199, Iran

Correspondence should be addressed to Asadollah Asadi, asad.asady@gmail.com

Received 16 February 2012; Revised 24 October 2012; Accepted 9 November 2012

Academic Editor: Xiaoming Li

Copyright © 2012 Zahra Nozhat et al. This is an open access article distributed under the Creative Commons Attribution License, which permits unrestricted use, distribution, and reproduction in any medium, provided the original work is properly cited.

Surfactin is one of the most powerful biosurfactants that has been known so far. It is an acidic cyclic nonribosomal lipoheptapeptide that is produced by *Bacillus subtilis*. In this presentation we investigated different properties of surfactin C-15. The nanomicelle forming ability of surfactin C-15 in different aqueous environments with various ionic strengths was studied by scanning electron microscope. Surfactin second structure was investigated by Far-UV CD spectrum. Its hemolytic activity and cytotoxicity were measured by hemolysis and MTT assays, respectively. Surfactin formed spherical nanomicelles in distilled water ( $\text{pH} = 7.4$ ) and amorphous nanomicelles in PBS buffer ( $\text{pH} = 7.4$ ). The hemolysis assay results indicated that  $\text{HC}_{50}$  of surfactin was  $47 \mu\text{M}$ . Surfactin C-15 arrested growth of human cervix cancer HeLa cell line in a time- and dosage-dependent method, so that its  $\text{IC}_{50}$  at 16, 24, and 48 h were 86.9, 73.1, and  $50.2 \mu\text{M}$ , respectively.

## 1. Introduction

Surfactin-like lipopeptides produced by the genus *Bacillus* are one of the most important classes of these natural compounds. They have low critical micelle concentration (CMC), stable emulsification properties, and excellent foamability [1]. Surfactin is an efficient biosurfactant produced by some *Bacillus subtilis* strains. It is a cyclic lipoheptapeptide containing seven amino acids and a  $\beta$ -hydroxyl fatty acid. In aqueous solution the peptide ring of surfactin shows a “horse-saddle” topology because of the two negatively charged amino acid residues L-Glu and L-Asp [2]. Due to its amphiphilic structure it shows unique surface-, interface-, and membrane-active properties [3]. It also has hemolytic, anticoagulant, antimicrobial and antitumoral activities [1, 4–6] inhibition of cAMP phosphodiesterase [7], and anti-HIV properties [7, 8]. These activities are related with their interactions with biomacromolecules such as enzymes and lipopolysaccharide. The surfactant properties and biological activities of surfactin analogues appear very interesting in the perspective of their utilization both in cosmetic and in pharmaceutical fields. Surfactins are a large variety of isoforms which differ by variation of the length and branching of their fatty acid components as well as by amino acid replacements in their peptide ring [1]. How this molecule can be effective

in various biological events is still largely unknown; however, it is speculated that the structural and lipophilic properties of surfactin may affect the stability of biological membranes [9]. With attention to the increasing application of diverse biocompatible nanoparticles in medicine and considering that active fields of research are currently also dedicated to investigate the applications of biosurfactants in pharmaceutical and biomedical sciences and knowing that the surfactin is one of the most powerful biosurfactants [10–15], in this presentation, after investigation of different properties of surfactin C-15 such as its nanomicellization ability, secondary structure, and hemolytic activity, we studied its cytotoxic effect on HeLa cell line.

## 2. Materials and Methods

2.1. Materials. Surfactin and 3-(4,5-Dimethylthiazol-2-yl)-2,5-diphenyl Tetrazolium Bromide (MTT) were obtained from Sigma. RPMI-1640, fetal bovine serum (FBS), and Trypsin-EDTA 5x were purchased from Gibco, and HeLa cell line was obtained from Pasteur Institute of Iran.

2.2. Surfactin Second Structure Study. The Far-UV CD spectrum of surfactin was recorded in PBS ( $\text{pH} = 7.4$ ). It

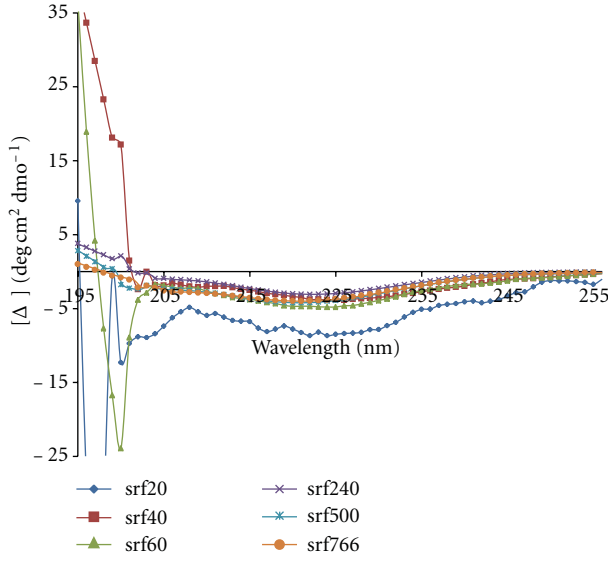


FIGURE 1: CD spectrum of surfactin in PBS.

was measured by AVIV 215 spectropolarimeter in different concentration (20, 40, 60, 240, 500, and 766  $\mu\text{M}$ ) at 25°C. The wavelength ranged between 195 and 260 nm.

**2.3. Physical Characterization of Surfactin Nanomicelles.** For the preparation of nanomicelles by surfactin, 1 mg surfactin was sonicated in 1 mL distilled water ( $\text{pH} = 7.4$ ) and 1 mL PBS (phosphate buffer saline,  $\text{pH} = 7.4$ ) for 15 min at 30°C. The size and shape of nanomicelles were studied by scanning electron microscope (SEM, LEO1430VP).

**2.4. Red Blood Cell Preparation.** Human red blood cells (RBCs) were separated by centrifugation at 2000  $\times g$ . RBCs were then washed once in PBS-EDTA and three times in an isotonic buffer (10 mM Tris, 150 mM NaCl adjusted to pH 8.5 with HCl). RBCs were then suspended in this buffer at a cell density of  $5 \times 10^8$  cells/mL [16].

**2.5. Hemolysis Assay.** 850  $\mu\text{L}$  of isotonic buffer was added to 50  $\mu\text{L}$  of a PBS solution containing the copolymer. 100  $\mu\text{L}$  of RBC suspension was added, and the reaction was performed at 25°C during 30 min. Unaltered RBCs were then removed by a 10000  $\times g$  centrifugation, and the absorbance of the supernatant at 540 nm was compared with two control samples in order to determine the percentage of hemolysis. The first one (100%) was totally hemolysed with distilled water [16], and the second one (0%) contained 900  $\mu\text{L}$  PBS plus 100  $\mu\text{L}$  of RBC suspension. Each test has been carried out at least twice.

**2.6. Cell Culture.** Human cervix cancer HeLa cell line was cultured in RPMI-1640 medium containing 10% fetal bovine serum, 100 U/mL penicillin, 100 U/mL streptomycin, and 1% glutamine in a humidified cell incubator with an atmosphere of 5% CO<sub>2</sub> at 37°C [17].

**2.7. MTT Assay.** Cell viability was estimated by MTT assay. Briefly,  $3 \times 10^6$  cells/well was plated in 24-well culture

plates. After overnight incubation, the cells were treated with different concentrations of surfactin (0, 20, 40, 60, and 80  $\mu\text{M}$ ) for 16, 24, and 48 hours. The cells were treated with 50  $\mu\text{L}$  of 5 mg/mL MTT and the resulting formazan crystals were dissolved in DMSO (500  $\mu\text{L}$ ). The optical density (OD) of each well was measured at 570 nm. Each test was performed in triplicate experiments. The effect of surfactin and surfactin-loaded nanoparticles on cell viability was assessed as percentage cell viability compared to vehicle-treated control cells, which were arbitrarily assigned 100% viability [18, 19].

**2.8. Statistical Analysis.** All of the experiments were done in triplicates, and the averages of the data were compared with independent *t*-test. A *P* value of <0.05 was considered as a statistical significance.

### 3. Results

**3.1. Surfactin Second Structure Study.** Surfactin C-15 in PBS showed a CD spectrum dominated by a broad negative band centered at 225 nm and a maximum peak at 195 nm (Figure 1). Surfactin second structure percents were measured (Table 1).

**3.2. Physical Characterization of Surfactin Nanomicelles.** Micellization ability of surfactin C-15 was studied by scanning electron microscope. The results exhibited that the nanomicelles in distilled water were spherical in shape and their size was about 100–200 nm (Figure 2(a)), while the nanomicelles shape in PBS was amorphous and their size was 100–400 nm (Figure 2(b)).

**3.3. Hemolysis Assay.** Surfactin C-15 was tested in different concentration for its hemolytic activity. The results were exhibited in Figure 3. It gives rise to a concentration-dependent hemolysis [10]. HC<sub>50</sub> which is defined as the

TABLE 1: Surfactin second structure percents.

Material	$\alpha$ -helix	Antiparallel	Parallel	$\beta$ -turn	Rndm.coil	Total sum
Srf 20 $\mu$ M	13.2	22.4	11.9	16.8	35.7	100
Srf 40 $\mu$ M	10.8	22.7	12.7	16.1	37.7	100
Srf 60 $\mu$ M	8.3	23.2	13.8	15.2	39.5	100
Srf 240 $\mu$ M	11.1	22.4	12.6	16.1	37.8	100
Srf 500 $\mu$ M	11.4	21.7	12.5	16.2	38.2	100
Srf 766 $\mu$ M	12.3	21.9	12.3	16.4	37.1	100

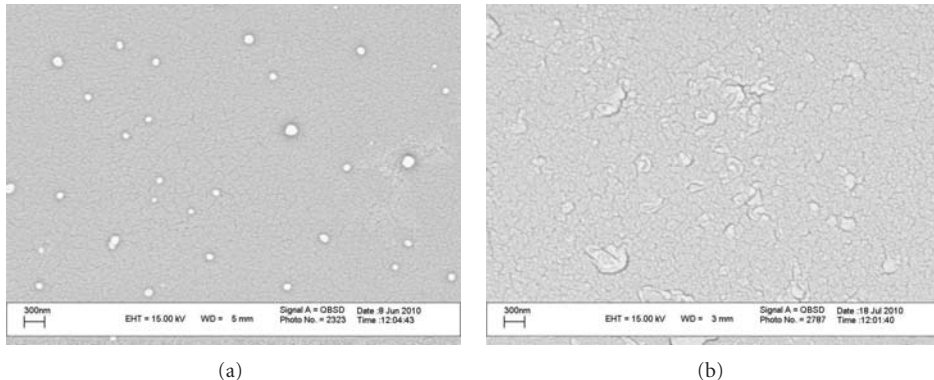
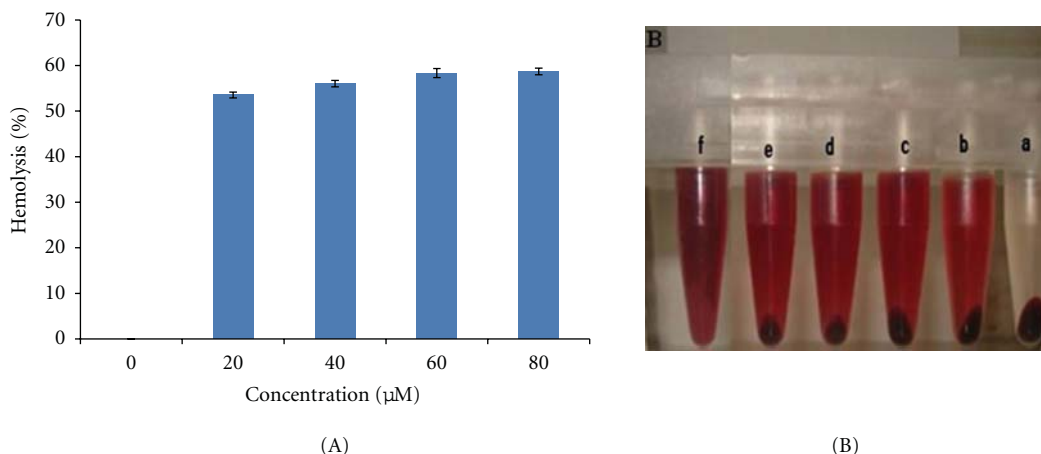


FIGURE 2: Scanning electron microscope scan of surfactin nanomicelles in distilled water (a) and PBS (pH = 7.4) (b).

FIGURE 3: Surfactin hemolysis assay. (A) HC<sub>50</sub> of surfactin C-15 was estimated 47  $\mu$ M; (B) the macroscopic figure of surfactin C-15 hemolysis assay in (a) negative control, (b) 20  $\mu$ M, (c) 40  $\mu$ M, (d) 60  $\mu$ M, (e) 80  $\mu$ M, and (f) positive control.

concentration of surfactin that bursts 50% of RBC [10] was 47  $\mu$ M.

**3.4. MTT Assay.** To study the cytotoxic effects of surfactin C-15, HeLa cell line was treated with different concentration of surfactin C-15 for 16, 24, and 48 h, and then cell viability was determined by MTT assay. Surfactin C-15 arrested HeLa cell line growth in a dose- and time-dependent method (Figure 4), with IC<sub>50</sub> at 16, 24, and 48 h of 86.9, 73.1, and 50.2  $\mu$ M, respectively.

#### 4. Discussion and Conclusion

In this study, scanning electron microscope determined that surfactin C-15 exhibits different manners in different

ionic aqueous solutions. Surfactin nanomicelles in PBS show the presence of large and amorphous aggregates. This is a similar result to that observed by Zou et al. [20]. The nanomicelles in distilled water are spherical in shape and smaller in size compared with the nanomicelles in PBA, and this caused different ionic strengths in distilled water and PBS. The study carried out by Li et al. showed that when the acyl chain length of the surfactin decreases, the hemolytic activity under hypotonic conditions decreases [10], and in this study the HC<sub>50</sub> of surfactin C-14 was recorded 300  $\mu$ M. According to our study, HC<sub>50</sub> of surfactin C-15 is 47  $\mu$ M that is consistent with Li et al. studies. Surfactins have been considered to be potential antitumoral agents. Recently, it is reported that the cytotoxic effects of surfactins on tumor cells are by inducing the apoptosis, which is related with

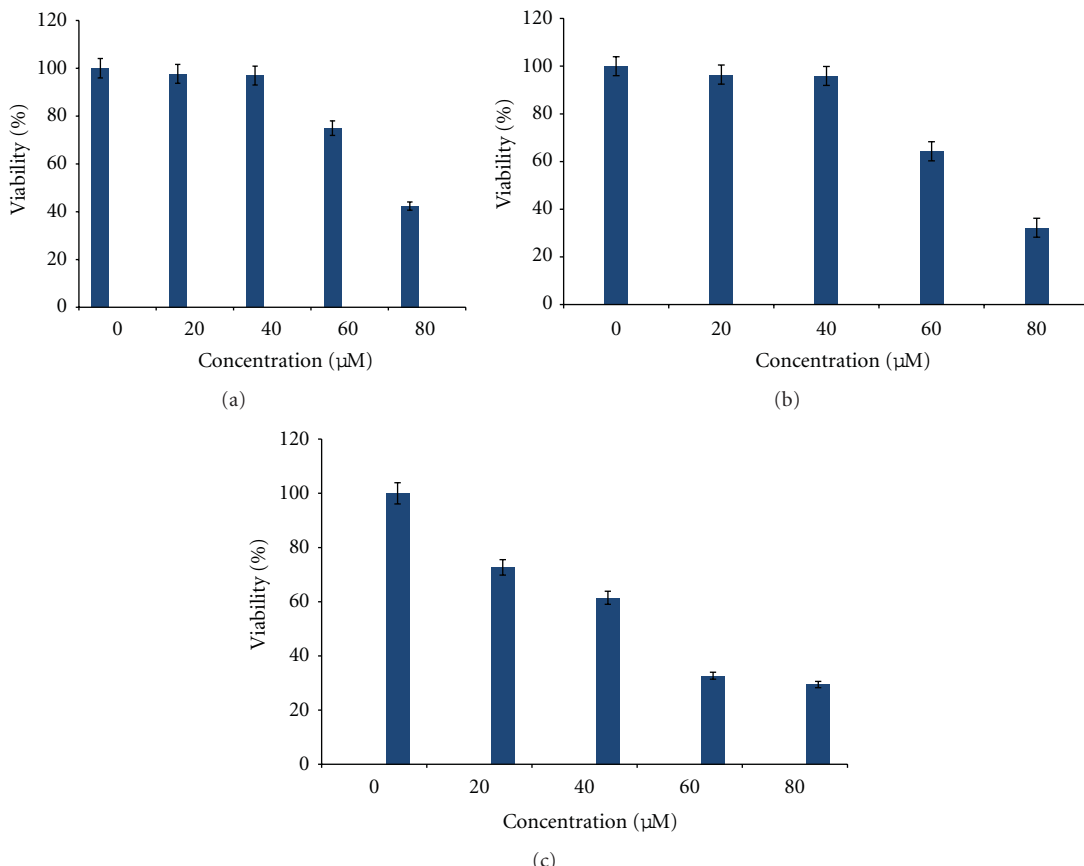


FIGURE 4: Cell viability assay for surfactin C-15 on HeLa cell line. The cell line was treated by different concentration of surfactin for (a) 16 h, (b) 24 h, and (c) 48 h with  $IC_{50}$  of 86.9, 73.1, and 50.2  $\mu$ M, respectively.

the enzyme activities. In addition, several biological activities of some lipopeptides are also related with their effects on the enzyme activities. For instance, the selective inhibitory effect of surfactin on cytosolic phospholipase A2 contributes to its anti-inflammatory activities. Another study indicates that the inhibitory effect of surfactin on the alkaline phosphatase had been attributed to a chelating action of the free carboxyl groups of the Asp and Glu residues in the peptide moiety of surfactin [1]. Although the obtained results show the cytotoxic effect of surfactin C-15 on HeLa cell line in a dose- and time-dependent method, more studies are necessary to confirm its anticancer effects. Also more studies are needed to determine and clarify the mechanism of surfactin action and anti-proliferative effects on cancerous cell lines targeted delivery.

## References

- [1] X. Y. Liu, S. Z. Yang, and B. Z. Mu, "Production and characterization of a C15-surfactin-O-methyl ester by a lipopeptide producing strain *Bacillus subtilis* HSO121," *Process Biochemistry*, vol. 44, no. 10, pp. 1144–1151, 2009.
- [2] J. Liu, A. Zou, and B. Mu, "Surfactin effect on the physico-chemical property of PC liposome," *Colloids and Surfaces A*, vol. 361, no. 1–3, pp. 90–95, 2010.
- [3] H. Kell, J. F. Holzwarth, C. Boettcher, R. K. Heenan, and J. Vater, "Physicochemical studies of the interaction of the lipo-heptapeptide surfactin with lipid bilayers of l- $\alpha$ -dimyristoyl phosphatidylcholine," *Biophysical Chemistry*, vol. 128, no. 2-3, pp. 114–124, 2007.
- [4] L. Rodrigues, I. M. Banat, J. Teixeira, and R. Oliveira, "Biosurfactants: potential applications in medicine," *Journal of Antimicrobial Chemotherapy*, vol. 57, no. 4, pp. 609–618, 2006.
- [5] P. Singh and S. S. Cameotra, "Potential applications of microbial surfactants in biomedical sciences," *Trends in Biotechnology*, vol. 22, no. 3, pp. 142–146, 2004.
- [6] S. S. Cameotra and R. S. Makkar, "Recent applications of biosurfactants as biological and immunological molecules," *Current Opinion in Microbiology*, vol. 7, no. 3, pp. 262–266, 2004.
- [7] M. Bortolato, F. Besson, and B. Roux, "Inhibition of alkaline phosphatase by surfactin, a natural chelating lipopeptide from *Bacillus subtilis*," *Biotechnology Letters*, vol. 19, no. 5, pp. 433–435, 1997.
- [8] R. Maget-Dana and M. Ptak, "Interactions of surfactin with membrane models," *Biophysical Journal*, vol. 68, no. 5, pp. 1937–1943, 1995.
- [9] S. Y. Kim, J. Y. Kim, S. H. Kim et al., "Surfactin from *Bacillus subtilis* displays anti-proliferative effect via apoptosis induction, cell cycle arrest and survival signaling suppression," *FEBS Letters*, vol. 581, no. 5, pp. 865–871, 2007.

- [10] X. Li, L. Wang, Y. Fan, Q. Feng, and F. Cui, "Biocompatibility and toxicity of nanoparticles and nanotubes," *Journal of Nanomaterials*, vol. 2012, Article ID 548389, 19 pages, 2012.
- [11] J. D. Desai and I. M. Banat, "Microbial production of surfactants and their commercial potential," *Microbiology and Molecular Biology Reviews*, vol. 61, pp. 47–64, 1997.
- [12] X. Li, C. A. van Blitterswijk, Q. Feng, F. Cui, and F. Watari, "The effect of calcium phosphate microstructure on bone-related cells in vitro," *Biomaterials*, vol. 29, no. 23, pp. 3306–3316, 2008.
- [13] X. Li, H. Liu, X. Niu et al., "The use of carbon nanotubes to induce osteogenic differentiation of human adipose-derived MSCs in vitro and ectopic bone formation in vivo," *Biomaterials* 33, pp. 4818–4827, 2012.
- [14] S. K. Smart, A. I. Cassady, G. Q. Lu, and D. J. Martin, "The biocompatibility of carbon nanotubes," *Carbon*, vol. 44, no. 6, pp. 1034–1047, 2006.
- [15] H. Abbasi, K. A. Noghabi, M. M. Hamedini et al., "Physicochemical characterization of a monorhamnolipid secreted by *Pseudomonas aeruginosa* MA01 in aqueous media. An experimental and molecular dynamics study," *Colloids and Surfaces B*, vol. 101, pp. 256–265, 2013.
- [16] S. Dufour, M. Deleu, K. Nott, B. Wathélet, P. Thonart, and M. Paquot, "Hemolytic activity of new linear surfactin analogs in relation to their physico-chemical properties," *Biochimica et Biophysica Acta*, vol. 1726, no. 1, pp. 87–95, 2005.
- [17] X. Cao, A. H. Wang, R. Z. Jiao et al., "Surfactin induces apoptosis and G2/M arrest in human breast cancer MCF-7 cells through cell cycle factor regulation," *Cell Biochemistry and Biophysics*, vol. 55, no. 3, pp. 163–171, 2009.
- [18] C. D. Helganson and C. L. Miller, *Basic Cell Culture Protocols*, vol. 290, Human Press, 2003.
- [19] A. Doyle and J. B. Griffiths, *Cell and Tissue Culture. Laboratory Procedures in Biotechnology*, John Wiley & Sons, 1998.
- [20] A. Zou, J. Liu, V. M. Garamus, Y. Yang, R. Willumeit, and B. Mu, "Micellization activity of the natural lipopeptide [Glu<sub>i</sub>, Asp<sub>5</sub>] surfactin-C15 in aqueous solution," *Journal of Physical Chemistry B*, vol. 114, no. 8, pp. 2712–2718, 2010.

## Research Article

# In Vitro Cytotoxicity Assay on Gold Nanoparticles with Different Stabilizing Agents

S. Vijayakumar<sup>1</sup> and S. Ganesan<sup>2</sup>

<sup>1</sup>Department of Physics, Sri Ramakrishna Institute of Technology, Pachapalayam, Peruruchettipalayam, Coimbatore 641010, India

<sup>2</sup>Department of Physics, Government College of Technology, Thadagam Road, Coimbatore 641013, India

Correspondence should be addressed to S. Vijayakumar, vijaysk.research@gmail.com

Received 9 April 2012; Revised 16 July 2012; Accepted 20 July 2012

Academic Editor: Xiaoming Li

Copyright © 2012 S. Vijayakumar and S. Ganesan. This is an open access article distributed under the Creative Commons Attribution License, which permits unrestricted use, distribution, and reproduction in any medium, provided the original work is properly cited.

Noble gold nanoparticles (AuNps) are generally nontoxic due to their inert nature. The gold nanoparticles are easily tagged with various proteins and biomolecules rich in aminoacid leading to important biomedical applications including targeted drug delivery, cellular imaging, and biosensing. In this study, three cytotoxicity detection assays 3-(4,5-dimethylthiazol-2-yl)-2,5-diphenyl tetrazolium bromide (MTT), neutral red cell, and lactate dehydrogenase (LDH) on gold nanoparticles stabilized with citrate, starch, and gum arabic are used. The assays used are based on different mode of detection like LDH release, MTT metabolism, and neutral red uptake. We found that the AuNps stabilized with citrate are very sensitive to the change of concentration and time assay compared to starch and gum arabic stabilized gold nanoparticles.

## 1. Introduction

Gold nanoparticles possess different physiochemical characteristics compared to the bulk gold [1, 2]. The six free electrons present in the conduction band of gold nanoparticles make them a potential candidate to bind with thiols and amines [3], also gold nanoparticles easily tagged with various proteins and biomolecules rich in aminoacids leading to important biomedical applications including targeted drug delivery [4, 5], cellular imaging [6], and biosensing [7]. The use of nanoparticles for biomedical applications such as drug and gene delivery, biosensors, cancer treatment, and diagnostic tools has been extensively studied throughout the past decade [8–17].

The toxicity has been expected to be in the following strategy [18]. The toxic CdSe can release poisonous cadmium ions inside the living organism and by competing with zinc for binding sites on metallothionein [19]. The nanoparticles have been shown to adhere to cell membranes [20] and also be ingested by cells [21]. The breaching of the cell membrane and the intracellular storage may have a negative effect on the cells regardless of the toxicity of the particles and their subsequent functionality.

Microstructure is essential for inductive bone formation in calcium phosphate materials after soft-tissue implantation. The increasing surface areas, microstructured calcium phosphate materials might concentrate more proteins that differentiate inducible cells from osteogenic cells that form inductive bone [22]. The multiwalled carbon nanotubes (MWNTs) might stimulate inducible cells in soft tissues to form inductive bone by concentrating more proteins, including bone-inducing proteins [23]. Distinctly shaped nanoparticles such as carbon nanotubes can rip cells like needle [24]. This suggests that nanomaterials of the same composition would have different biologic responses for different morphologies. The advantages of the *in vitro* approach includes simplicity, consistency of the experimental setup, and the reproducibility of the experimental results [25].

Cytotoxicity also depends on the type of cells used. The 33 nm citrate-capped gold nanoparticles were found to be nontoxic to baby hamster kidney and human hepatocellular liver carcinoma cells but toxic to a human carcinoma lung cell lines. AuNps may have advantages over other metallic nanoparticles in terms of biocompatibility and noncytotoxicity [26].

In this study, gold nanoparticles stabilized with citrate, starch, and gum arabic are used for cytotoxicity studies. The assays used are based on different modes of detection like LDH release, MTT metabolism, and Neutral Red uptake. We found some noticeable differences in the values for the cytotoxic effect depending on the assay and nanoparticle capping agent used. In particular, the citrate stabilized gold nanoparticles are having little toxicity compared to the starch and gum arabic stabilized nanoparticles, since we have used the same size of particles in all the cases.

## 2. Materials and Methods

All chemicals were obtained from Sigma-Aldrich and used as received. Double-distilled water was used in all experiments. The PC-3 and MCF-7 cell lines were obtained from the American Type Culture Collection (ATCC) through Department of Microbiology, PSG Institute of Medical Sciences and Research, Tamilnadu, India. The cell line (CHO22) was obtained from R&D-Bio, Coimbatore, India.

### 2.1. Preparation of Gold Nanoparticles

**2.1.1. Preparation of Citrate-Capped Gold Nanoparticles (Citrate-AuNps).** Conventional techniques for aqueous synthesis of gold nanoparticles involve reduction of Au(III)Cl<sub>3</sub> with trisodium citrate, a process pioneered by Turkevich and later refined by Frens [27–30]. In this method the citrate salt initially acts as a reducing agent by forming a layer of citrate ions over the gold nanoparticles surface, inducing enough electrostatic repulsion between individual particles to keep them well dispersed in the medium. This method provides uniform and fairly spherical nanoparticles.

This reduction process proceeds at a very slow rate and imparts a wine red color to the solution. 250 mL of 0.25 mM HAuCl<sub>4</sub> was heated to boiling. Then, 4 mL of aqueous solution of 1% solution of trisodium citrate was added to the HAuCl<sub>4</sub> solution under vigorous stirring and the boiling was continued for 15 min until it turns to a deep red colour. The citrate ions serve as both reducing agent for AuNp formation and a stabilizer, preventing agglomeration of gold nanoparticles.

**2.1.2. Preparation of Starch-Capped Gold Nanoparticles (Starch-AuNps).** Starch (0.0225 g) was dissolved in 6 mL of doubly ionized water by heating the solution to 90–100°C with continuous stirring. To this hot starch solution, 0.1 mL of 0.1 M HAuCl<sub>4</sub> solution (0.0393 g in 1 mL deionized water) was added, followed by the addition of 0.02 mL of 0.1 M trialanine phosphine (THPAL) solution (0.0337 g in 1 mL DI water) with continuous stirring. When the color of the solution changed to pinkish purple, stirring was continued for one minute without heating.

**2.1.3. Preparation of Gum Arabic-Capped Gold Nanoparticles (Gum Arabic-AuNps).** Gum Arabic (0.012 g) was dissolved in 6 mL of doubly ionized water by heating the solution to 90–100°C with continuous stirring. To this hot gum arabic solution, 0.1 mL of 0.1 M NaAuCl<sub>4</sub> solution (0.0338 g

TABLE 1: Average size, plasmon wavelength, and plasmon width of gold nanoparticles stabilized with starch, gum Arabic, and citrate.

Sample name	Average size (nm)	Plasmon wavelength $\lambda_{\text{max}}$ (nm)	Plasmon width $\Delta\lambda$ (nm)
C-AuNp	21 ± 1.4	523	90
S-AuNp	21 ± 1.5	525	90
GA-AuNp	20 ± 2.3	528	85

in 1 mL DI water) was added, followed by the addition of 0.02 mL of 0.1 M THPAL solution (0.0338 g in 1 mL DI water) with continuous stirring (Table 1). When the color of the solution changed to reddish purple, stirring was continued for one minute without heating. Table 2 shows the reaction condition for preparing citrate, starch, and gum arabic stabilized gold nanoparticles.

**2.2. Characterization.** Gold nanoparticles stabilized with citrate, starch, and gum arabic were characterized by UV-Vis absorption spectroscopy using UV-1700 series spectrometer (PSG Institute of Advanced Studies, Coimbatore, India) to study the peak absorption band. About 1 mL solution of nanoparticles in water was used. The peak absorption band obtained for citrate, starch, and gum arabic stabilized gold nanoparticles is 523 nm, 525 nm, and 528 nm, respectively, (Table 1). TEM images of citrate-, starch- and gum arabic-capped gold nanoparticles were collected on a Philips CM200 (Sophistical Analytical Instrument Facility, Indian Institute of Technology, Bombay, India). The operating voltage range was 20–200 kV with a resolution of 2.4 Å. Zeta potential measurements were performed using a Malvern Instruments Zeta sizer 1000 Hs operating with a variable power (5–50 mW) He-Ne laser at 633 nm (Indian Institute of Science, Bangalore, India). Measurements were taken at 25°C. Before and in between the measurements, the cells were washed with ultrahigh pure water. The AuNp thus, formed were characterized using UV-Vis spectroscopy, Zeta potential, and transmission electron microscopy shown in Figures 1, 2, and 3.

### 2.3. Cytotoxicity Assay

**2.3.1. MTT Assay.** Cytotoxicity evaluation of citrate-AuNps, starch-AuNps, and gum arabic-AuNps was performed using MTT assay as described by Mossman [31]. Approximately  $1 \times 10^5 \text{ mL}^{-1}$  cells (MCF-7 and PC-3) in their exponential growth phase were seeded in a flat-bottomed 96-well polystyrene coated plate and were incubated for 24 hrs at 37°C in a 5% CO<sub>2</sub> incubator. Series of dilution (20, 50, 80, 110, and 140 µg/mL) of gold nanoparticles in the medium was added to the plate in hexaplets. After 24 hours of incubation, 10 µL of MTT reagent was added to each well and was further incubated for 4 hours. Formazan crystals formed after 4 hours in each well were dissolved in 150 µL of detergent and the plates were read immediately in a microplate reader (BIO-RAD microplate reader-550) at 570 nm. Wells with complete medium, nanoparticles and MTT reagent, without cells were used as blanks. Untreated

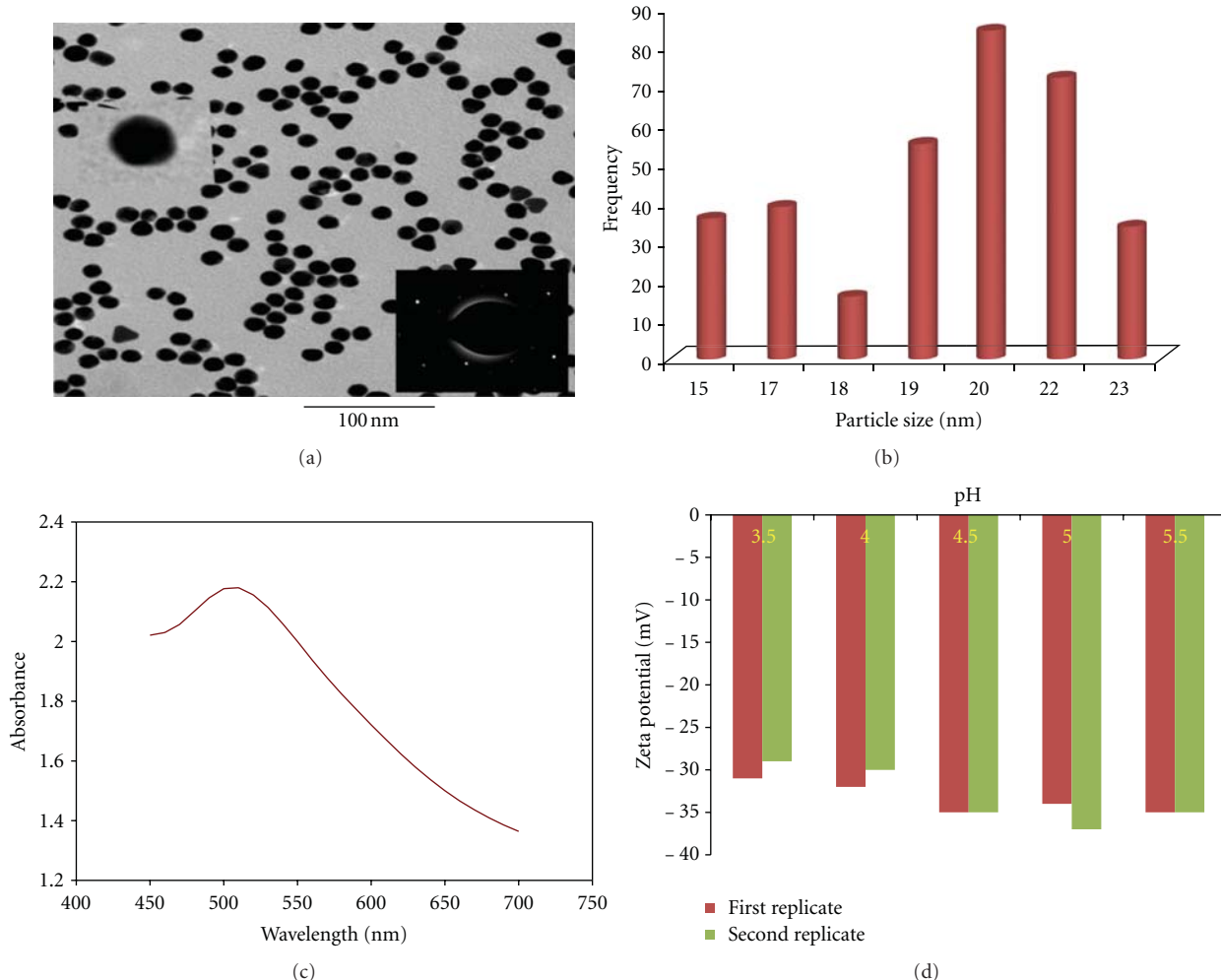


FIGURE 1: (a) TEM image of citrate stabilized gold nanoparticles. Insight SEAD pattern and an enlarged single nanoparticle. (b) Particle size histogram and is 21 nm averaged from 350 nanoparticles. (c) Plasmon resonance absorption and is 523 nm with plasmon width ( $\Delta\lambda$ ) of 90 nm. (d) Zeta potential of gold nanoparticles at different pH values.

TABLE 2: Reaction conditions for producing citrate (C-AuNp), starch (S-AuNp) and gum arabic (GA-AuNp)-capped gold nanoparticles.

Compound name	Stabilizer (C-AuNp)/(S-AuNp)/(GA-AuNp)	Gold precursor	Reducing agent	Time	Reaction solution color
C-AuNp	4 mL of 38.8 mM in 250 mL of DI	0.25 mM HAuCl <sub>4</sub>	4 mL of 1% trisodium citrate	1 min	Wine-red color Sodium citrate
S-AuNp	0.0225 g of starch in 6 mL of DI	0.1 mL of 0.1 M, NaAuCl <sub>4</sub>	0.02 mL of 0.1 M, THPAL	1 min	Pinkish purple
GA-AuNp	0.0225 g of gum arabic in 6 mL of DI	0.1 mL of 0.1 M, NaAuCl <sub>4</sub>	0.02 mL of 0.1 M, THPAL	1 min	Reddish purple

PC-3 and MCF-7 cells as well as the cell treated with (20, 50, 80, 110, and 140  $\mu$ g/mL) concentration of AuNPs for 24 hrs were subjected to the MTT assay for cell viability determination.

**2.3.2. Neutral Red Cytotoxicity Assay.** CHO22 cells were seeded at a population of  $1.5 \times 10^4$  cells per well in a 96-well plate. The cells were incubated for 24 hours and reached 80–90% confluence. The spent media were removed and the cells were washed with PBS (0.01 M phosphate

buffer, 0.0027 M KCl and 0.137 M NaCl) and 1  $\mu$ L fresh media was added. The media were then replaced with test nanoparticles of (20, 50, 80, 110, and 140  $\mu$ g/mL) concentrations mixed with fresh media. The plates were then incubated for 24 hrs at 37° in a humidified incubator with a 5% CO<sub>2</sub> environment. Following the incubation periods, the cells were washed twice with PBS (0.01 M phosphate buffer 0.0027 M KCl and 0.137 M NaCl) and 100  $\mu$ L serum-free media containing neutral red (100  $\mu$ g/mL) was added to each well and incubated for 2-3 hours.

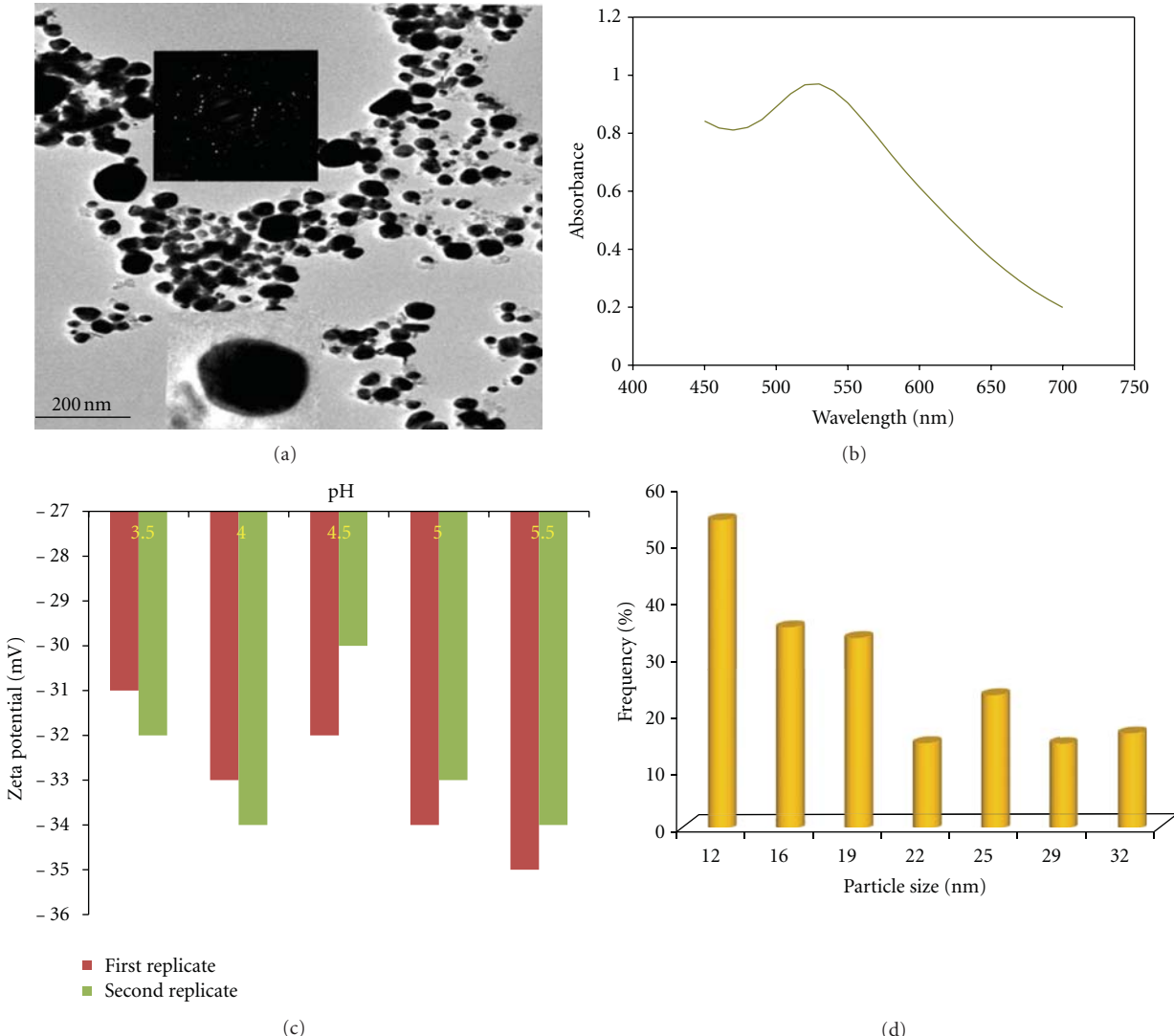


FIGURE 2: (a) TEM image of Starch stabilized gold nanoparticles. Insight SEAD pattern and an enlarged single nanoparticle. (b) Particle size histogram and is 21 nm averaged from 225 nanoparticles. (c) Plasmon resonance absorption and is 525 nm with plasmon width ( $\Delta\lambda$ ) of 90 nm. (d) Zeta potential of gold nanoparticles at different pH values.

After the incubation, the cells were washed twice with PBS (0.01 M phosphate buffer 0.0027 M KCl and 0.137 M NaCl) thereafter 50  $\mu$ L of dye release agent (a solution of 1% acetic acid: 50% ethanol) was added to each well and the plates were incubated for further 10 minutes. The plate was placed on a shaker (Vortex Genie) for 30 minutes after which the optical density at 540 nm was determined on a multiwall spectrophotometer.

**2.3.3. LDH Assay.** Cytotoxicity was assessed using an LDH cytotoxicity detection kit (Roche applied sciences). This assay measures the release of cytoplasm enzyme lactate dehydrogenase (LDH) by damaged cells. Cells cultured in 96 plates were treated with increasing concentrations of gold nanoparticles (20, 50, 80, 110, and 140  $\mu$ g/mL). After 48 hours of treatment, culture supernatant was collected and incubated with reaction mixture. The LDH catalyzed

conversion results in the reduction of the tetrazolium salt to formosan, which can be read at 490 nm absorbance. These data are measured in LDH activity as a percentage of the control. Any significant increase in LDH levels would indicate cellular disruption or death due to the treatment.

**2.3.4. Statistical Analysis.** For statistical analysis, all data are expressed as mean  $\pm$  standard deviation (SD). The graphs and curves are done with SigmaPlot 12.0, Adobe Photoshop 7.0, and Microsoft Office Excel 2007.

### 3. Results

In MTT assay only cells that are viable after 24 hours exposed to the sample were capable of metabolizing a dye (3-(4,5-dimethylthiazol-2-yl)-2,5-diphenyl tetrazolium bromide) efficiently and the purple colored precipitate which

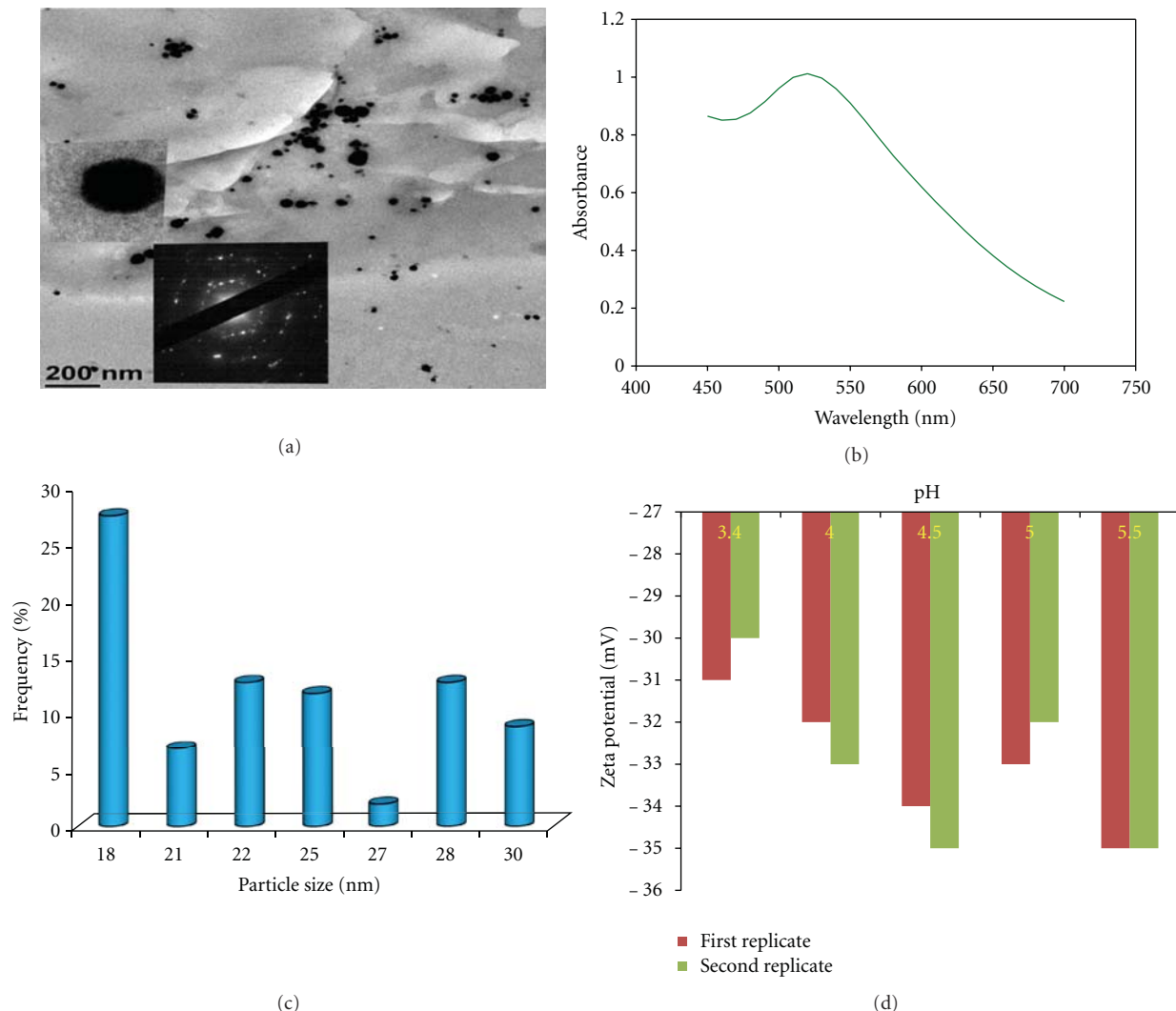


FIGURE 3: (a) TEM image of gum arabic stabilized gold nanoparticles. Insight SEAD pattern and an enlarged single nanoparticle. (b) Particle size histogram and is 20 nm averaged from 100 nanoparticles. (c) Plasmon resonance absorption and is 528 nm with plasmon width ( $\Delta\lambda$ ) of 85 nm. (d) Zeta potential of gold nanoparticles at different pH values.

is dissolved in a detergent was analyzed spectrophotometrically. After 24 hours of posttreatment, PC-3 and MCF-7 cells showed excellent viability even up to the concentration of 140  $\mu$ g of citrate-, starch-, and gum arabic-capped gold nanoparticles. These results clearly demonstrate that the photochemicals within these herbs provide nontoxic coating on AuNPs and corroborate the results of the internalization studies discussed above. The lack of any noticeable toxicity of starch and gum arabic stabilized gold nanoparticles provide new opportunities for the safe application in molecular imaging and therapy. But the data shows that there is a marginal cytotoxic effect of citrate stabilized gold nanoparticles with the cell lines used.

The mammalian Chinese hamster ovary (CHO22) cell line was used in the elucidation of cytotoxicity effects of the selected gold nanoparticles by neutral red assay. This cell line has been termed as the mammalian equivalent of the model bacterium *E. coli* [32]. For the elucidation of the cytotoxicity of the gold nanoparticles, the CHO22 cells were treated with

the nanomaterials for 24 hours. The gold nanoparticles were investigated at five concentrations. The spectrophotometric measurements were done for the neutral red dye uptake and release. The viability assay data for the comparison is presented in the Figures 4(a), 4(b), and 4(c).

#### 4. Discussion

Comparison of the stabilizing agents revealed that citrate produced more pronounced response and sensitivity to the dose changes and time assay. The higher dosage shows less viability of citrate stabilized nanoparticles than starch and gum arabic stabilized gold nanoparticles. Cell viability was also determined by an LDH release assay which was employed to measure the cytotoxicity of the gold nanoparticles at different concentrations. Damaged cells release cytoplasmic LDH, which catalyzes a conversion of tetrazolium salt to formazan.

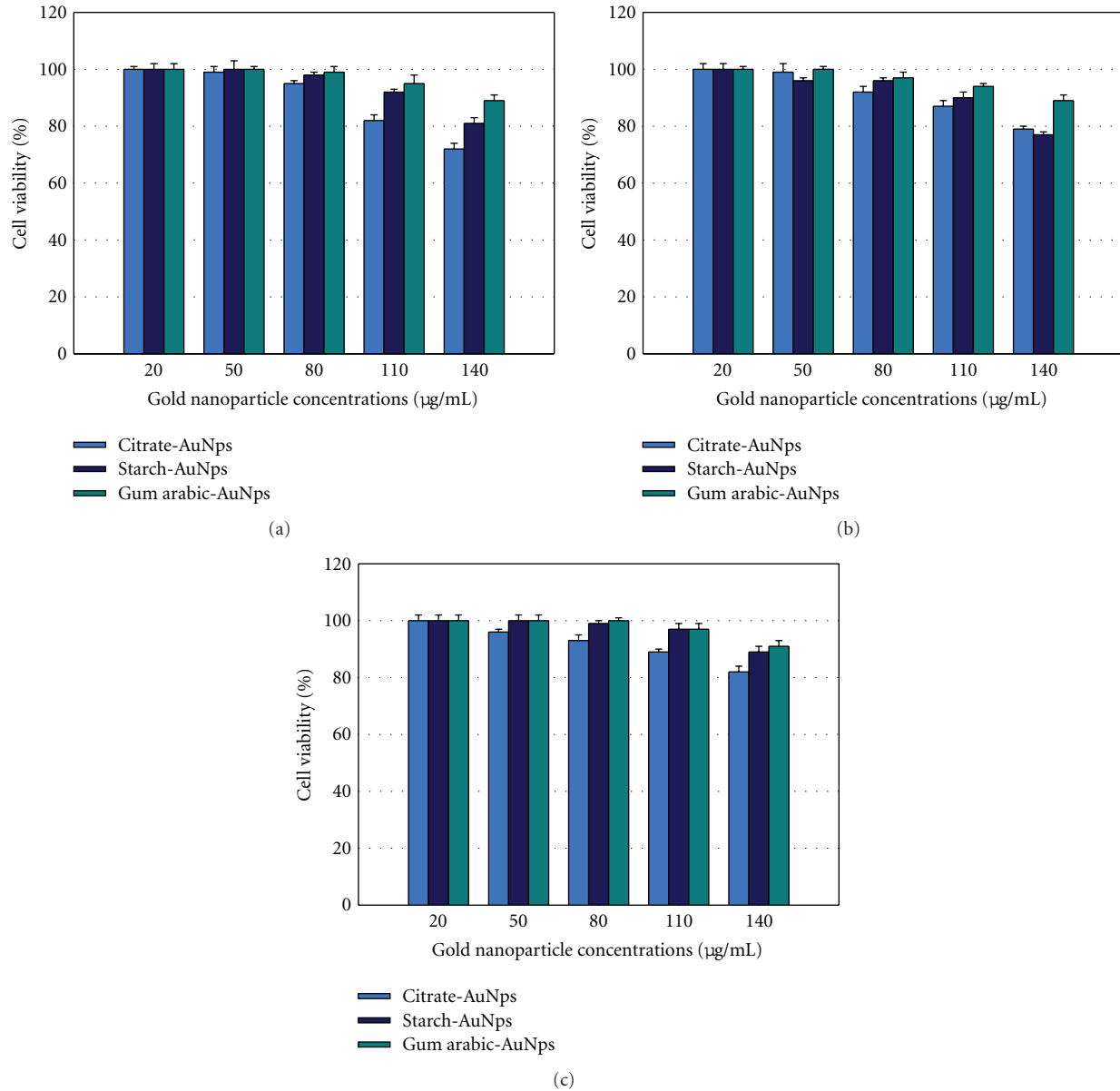


FIGURE 4: Cytotoxic assays by (a) MTT assay, (b) neutral red cell assay, and (c) LDH assay on gold nanoparticles stabilized with citrate, starch and gum arabic.

The absorbance of the produced formazan at 490 nm is proportional to the number of damaged or dying cells. The cytotoxicity of various cells in percent of LDH activity of the control, after exposure to increasing concentrations of nanoparticles stabilized with three different stabilizing agents for 24 hours, was analyzed. At each concentration, there was no significant cytotoxicity effect produced. The cell viability results indicate that gold nanoparticles are nontoxic to the array of cells tested. The incorporation of surface functionalities via citrate, starch, and gum arabic renders these nanoparticles highly biocompatible. Noble metal particles, such as gold are generally nontoxic due to their inert nature, this has also been seen with their  $\text{LD}_{50}$  in toxicity assays, high enough up to 1 mg/mL [33]. The

cell survival at different concentrations of gold nanoparticles stabilized with different capping agents showed a small variation with the increase in the concentration of the nanoparticles.

The gold nanoparticles of 20 nm are coated with citrate (citrate-AuNps), starch (starch-AuNps), and gum arabic (gum arabic-AuNps) are taken with a series of increasing concentrations (20, 50, 80, 110, and 140  $\mu\text{g}/\text{mL}$ ) along with cell cultures and studied under different cytotoxicity assays like MTT, neutral red cell, and LDH. In all the assays, the nanoparticles show excellent cell viability. The citrate stabilized gold nanoparticles rapidly show their cytotoxicity effect compared to starch and gum arabic. The gum arabic is highly viable than starch and citrate. In our observations,

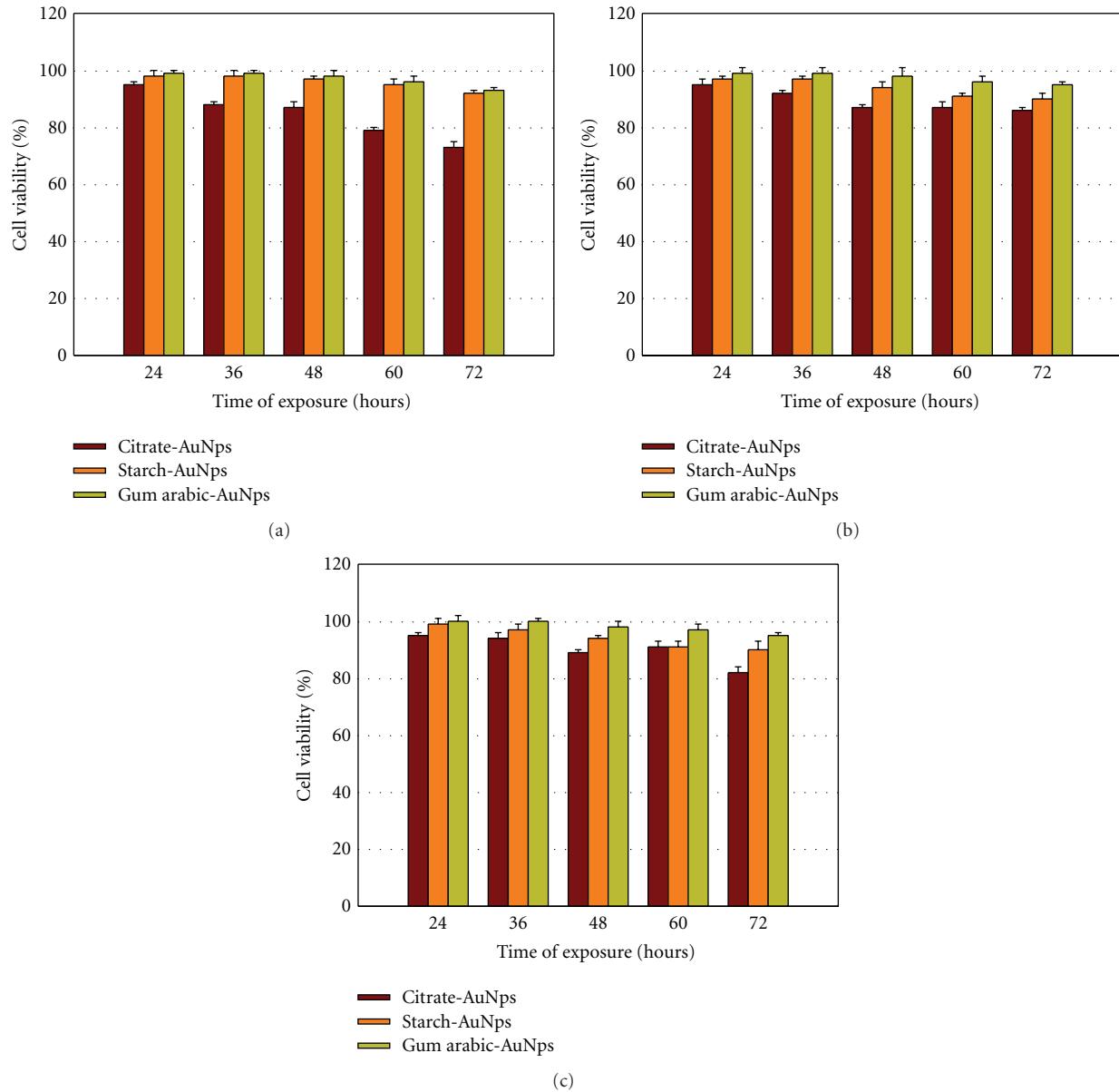


FIGURE 5: Cell viability studies at different time of exposure of citrate, starch, and gum arabic stabilized gold nanoparticles at a concentration of  $110 \mu\text{g/mL}$  by (a) MTT assay, (b) neutral red cell assay, and (c) LDH assay.

all the gold nanoparticles are viable to cells and because of the acidic nature of citrate show little less cell viability compared to other stabilizing agents with gold nanoparticles. The viability test based on the time of exposure of gold nanoparticles was also studied with different stabilizing agents at different cell assays, Figures 5(a), 5(b), and 5(c). In this study the starch-AuNPs and gum arabic-AuNPs show high viability to cell assays compared to citrate-AuNPs, Figures 6(a), 6(b), and 6(c). IC<sub>50</sub> is calculated as  $110 \mu\text{g/mL}$  of gold nanoparticles and this concentration is considered for the time of exposure assay.

Cell-based cytotoxic assay with different concentrations of gold nanoparticles shows very small variation among citrate, starch, and gum arabic. The gold nanoparticles used

here were having the same size  $20 \pm 1 \text{ nm}$ , they differs only in stabilizing agents. The citrate stabilized gold nanoparticles show less viability than starch and gum arabic, Figures 4(a), 4(b), and 4(c). This is mainly due to the fact that citrate is acidic in nature. More over the particle sizes are same in all three cases of citrate, starch and gum arabic. Hence in this study the size dependent cytotoxicity is ruled out and it is confirmed that the stabilizing agents are responsible for cytotoxicity.

These results are consistent with previous investigations performed with dermal fibroblasts [34] which demonstrated that the gold/citrate nanoparticles impaired the proliferation of dermal fibroblasts and induced an abnormal formation of actin filaments, causing therefore a reduced cellular

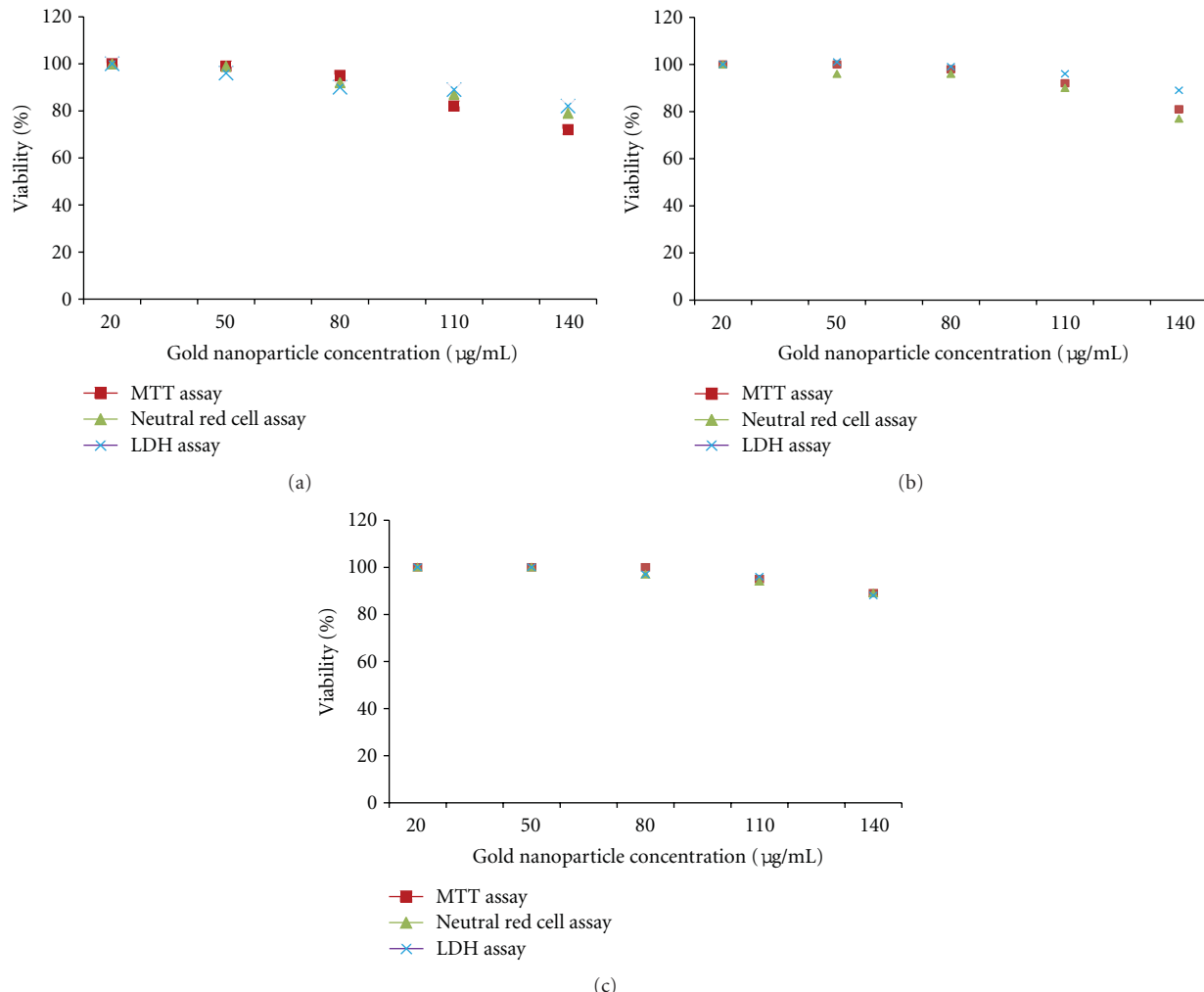


FIGURE 6: Different cell viability assays at different concentrations of gold nanoparticles for (a) citrate-capped (b) starch-capped, and (c) gum arabic capped.

motility and influencing the cell morphology. On contrary, [35] reported that citrated and biotinylated 18 nm gold nanoparticles did not induce toxicity in leukemic cells (cell line K562), whereas smaller particles were much more toxic.

## 5. Conclusion

In conclusion, we found that the gold nanoparticles stabilized with citrate, starch, and gum arabic are viable to different cells through different assays and with different concentrations of gold nanoparticles. The viability of the treated cells depending on the stabilizing agent and the types of cytotoxicity assay used. The cell viability test shows distinguishable cytotoxic effect for citrate stabilized gold nanoparticles at higher concentration and this is may be because the surface coating is acidic in nature compared to starch and gum arabic.

## References

- [1] A. P. Alivisatos, "Semiconductor clusters, nanocrystals, and quantum dots," *Science*, vol. 271, no. 5251, pp. 933–937, 1996.

- [2] D. L. Feldheim, A. F. Colby, and D. Marcel : , "Metal nanoparticles: synthesis, characterization and applications," *The Journal of Physical Chemistry*, vol. 300, pp. 11202–11208, 2002.
- [3] D. V. Leff, L. Brandt, and J. R. Heath, "Synthesis and characterization of hydrophobic, organically-soluble gold nanocrystals functionalized with primary amines," *Langmuir*, vol. 12, no. 20, pp. 4723–4730, 1996.
- [4] C. M. Niemeyer, "Nanoparticles, proteins, and nucleic acids: biotechnology meets materials science," *Angewandte Chemie—International Edition*, vol. 40, no. 22, pp. 4129–4158, 2001.
- [5] J. C. Sanford, F. D. Smith, and J. A. Russell, "Optimizing the biolistic process for different biological applications," *Methods in Enzymology*, vol. 217, pp. 483–509, 1993.
- [6] A. Bielinska, J. D. Eichman, I. Lee, J. R. Baker, and L. Balogh, "Imaging Au0-PAMAM gold-dendrimer nanocomposites in cells," *Journal of Nanoparticle Research*, vol. 4, no. 5, pp. 395–403, 2002.
- [7] L. Olofsson, T. Rindzevicius, I. Pfeiffer, M. Käll, and F. Höök, "Surface based Gold nanoparticle sensor for specific and quantitative DNAHybridization detection," *Langmuir*, vol. 19, no. 24, pp. 10414–10419, 2003.

- [8] P. Zrazhevskiy, M. Sena, and X. Gao, "Designing multifunctional quantum dots for bioimaging, detection, and drug delivery," *Chemical Society Reviews*, vol. 39, no. 11, pp. 4326–4354, 2010.
- [9] J. H. Lee, Y. M. Huh, Y. W. Jun et al., "Artificially engineered magnetic nanoparticles for ultra-sensitive molecular imaging," *Nature Medicine*, vol. 13, no. 1, pp. 95–99, 2007.
- [10] C. R. Thomas, D. P. Ferris, J. H. Lee et al., "Noninvasive remote-controlled release of drug molecules *in vitro* using magnetic actuation of mechanized nanoparticles," *Journal of the American Chemical Society*, vol. 132, no. 31, pp. 10623–10625, 2010.
- [11] T. Neuberger, B. Schöpf, H. Hofmann, M. Hofmann, and B. Von Rechenberg, "Superparamagnetic nanoparticles for biomedical applications: possibilities and limitations of a new drug delivery system," *Journal of Magnetism and Magnetic Materials*, vol. 293, no. 1, pp. 483–496, 2005.
- [12] X. Qian, X. H. Peng, D. O. Ansari et al., "*In vivo* tumor targeting and spectroscopic detection with surface-enhanced Raman nanoparticle tags," *Nature Biotechnology*, vol. 26, no. 1, pp. 83–90, 2008.
- [13] X. Bai, S. J. Son, S. Zhang et al., "Synthesis of superparamagnetic nanotubes as MRI contrast agents and for cell labeling," *Nanomedicine*, vol. 3, no. 2, pp. 163–174, 2008.
- [14] S. J. Son, X. Bai, and S. B. Lee, "Inorganic hollow nanoparticles and nanotubes in nanomedicine. Part 1. Drug/gene delivery applications," *Drug Discovery Today*, vol. 12, no. 15–16, pp. 650–656, 2007.
- [15] S. J. Son, J. Reichel, B. He, M. Schuchman, and S. B. Lee, "Magnetic nanotubes for magnetic-field-assisted bioseparation, biointeraction, and drug delivery," *Journal of the American Chemical Society*, vol. 127, no. 20, pp. 7316–7317, 2005.
- [16] D. T. Mitchell, S. B. Lee, L. Trofin et al., "Smart nanotubes for bioseparations and biocatalysis," *Journal of the American Chemical Society*, vol. 124, no. 40, pp. 11864–11865, 2002.
- [17] B. He, S. K. Kim, S. J. Son, and S. B. Lee, "Shape-coded silica nanotubes for multiplexed bioassay: rapid and reliable magnetic decoding protocols," *Nanomedicine*, vol. 5, no. 1, pp. 77–88, 2010.
- [18] C. Kirchner, T. Liedl, S. Kudera et al., "Cytotoxicity of colloidal CdSe and CdSe/ZnS nanoparticles," *Nano Letters*, vol. 5, no. 2, pp. 331–338, 2005.
- [19] R. A. Goyer, "Nutrition and metal toxicity," *American Journal of Clinical Nutrition*, vol. 61, no. 3, supplement, pp. 646S–650S, 1995.
- [20] L. Ghitescu and A. Fixman, "Surface charge distribution on the endothelial cell of liver sinusoids," *Journal of Cell Biology*, vol. 99, no. 2, pp. 639–647, 1984.
- [21] W. J. Parak, R. Boudreau, M. Le Gros et al., "Cell motility and metastatic potential studies based on quantum dot imaging of phagokinetic tracks," *Advanced Materials*, vol. 14, no. 12, pp. 882–885, 2002.
- [22] X. Li, C. A. van Blitterswijk, Q. Feng, F. Cui, and F. Watari, "The effect of calcium phosphate microstructure on bone-related cells *in vitro*," *Biomaterials*, vol. 29, no. 23, pp. 3306–3316, 2008.
- [23] X. Li, H. Liu, X. Niu et al., "The use of carbon nanotubes to induce osteogenic differentiation of human adipose-derived MSCs *in vitro* and ectopic bone formation *in vivo*," *Biomaterials*, vol. 33, no. 19, pp. 4818–4827, 2012.
- [24] D. B. Warheit, B. R. Laurence, K. L. Reed, D. H. Roach, G. A. M. Reynolds, and T. R. Webb, "Comparative pulmonary toxicity assessment of single-wall carbon nanotubes in rats," *Toxicological Sciences*, vol. 77, no. 1, pp. 117–125, 2004.
- [25] R. Judson, A. Richard, D. J. Dix et al., "The toxicity data landscape for environmental chemicals," *Environmental Health Perspectives*, vol. 117, no. 5, pp. 685–695, 2009.
- [26] R. Shukla, V. Bansal, M. Chaudhary, A. Basu, R. R. Bhonde, and M. Sastry, "Biocompatibility of gold nanoparticles and their endocytotic fate inside the cellular compartment: a microscopic overview," *Langmuir*, vol. 21, no. 23, pp. 10644–10654, 2005.
- [27] J. Turkevich, P. C. Stevenson, and J. Hillier, "A study of the nucleation and growth processes in the synthesis of colloidal gold," *Discussions of the Faraday Society*, vol. 11, pp. 55–75, 1951.
- [28] J. Kimling, M. Maier, B. Okenve, V. Kotaidis, H. Ballot, and A. Plech, "Turkevich method for gold nanoparticle synthesis revisited," *Journal of Physical Chemistry B*, vol. 110, no. 32, pp. 15700–15707, 2006.
- [29] G. Frens, "Particle size and sol stability in metal colloids," *Kolloid-Zeitschrift & Zeitschrift für Polymere*, vol. 250, no. 7, pp. 736–741, 1972.
- [30] K. Aika, L. T. Ban, I. Okura et al., "Journal of the Research Institute of Catalysis," *Hokkaido University*, vol. 24, no. 1, pp. 54–64, 1976.
- [31] T. Mosmann, "Rapid colorimetric assay for cellular growth and survival: application to proliferation and cytotoxicity assays," *Journal of Immunological Methods*, vol. 65, no. 1–2, pp. 55–63, 1983.
- [32] F. T. Kao and T. T. Puck, "Genetics of somatic mammalian cells, VII. Induction and isolation of nutritional mutants in Chinese hamster cells," *Proceedings of the National Academy of Sciences of the United States of America*, vol. 60, no. 4, pp. 1275–1281, 1968.
- [33] Z. P. Xu, Q. H. Zeng, G. Q. Lu, and A. B. Yu, "Inorganic nanoparticles as carriers for efficient cellular delivery," *Chemical Engineering Science*, vol. 61, no. 3, pp. 1027–1040, 2006.
- [34] N. Pernodet, X. Fang, Y. Sun et al., "Adverse effects of citrate/gold nanoparticles on human dermal fibroblasts," *Small*, vol. 2, no. 6, pp. 766–773, 2006.
- [35] E. E. Connor, J. Mwamuka, A. Gole, C. J. Murphy, and M. D. Wyatt, "Gold nanoparticles are taken up by human cells but do not cause acute cytotoxicity," *Small*, vol. 1, no. 3, pp. 325–327, 2005.

## Review Article

# Biocompatibility and Toxicity of Magnetic Nanoparticles in Regenerative Medicine

**H. Markides, M. Rotherham, and A. J. El Haj**

*Institute of Science and Technology in Medicine, Keele University Medical School, Thornburrow Drive, Hartshill, Stoke-on-Trent, Staffordshire ST4 7QB, UK*

Correspondence should be addressed to H. Markides, h.markides@istm.keeple.ac.uk

Received 4 May 2012; Revised 28 June 2012; Accepted 16 July 2012

Academic Editor: Xiaoming Li

Copyright © 2012 H. Markides et al. This is an open access article distributed under the Creative Commons Attribution License, which permits unrestricted use, distribution, and reproduction in any medium, provided the original work is properly cited.

Regenerative medicine is a pioneering field aimed at restoring and regenerating the function of damaged cells, organs and tissues in order to establish normal function. It demands the cross communication of disciplines to develop effective therapeutic stem cell based therapies. Nanotechnology has been instrumental in the development and translation of basic research to the clinically relevant therapies. In particular, magnetic nanoparticles (MNPs) have been applied to tag, track and activate stem cells offering an effective means of monitoring *in vitro* and *in vivo* behaviour. MNPs are comprised of an iron oxide core with a biocompatible biological polymer. Safety is an issue of constant concern and emphasises on the importance of investigating the issue of toxicity. Any indication of toxicity can ultimately limit the therapeutic efficiency of the therapy. Toxicity is highly dependent on the physical, chemical and structural properties of the MNP itself as well as dose and intended use. Few *in vitro* studies have reported adverse effects of MNP on cells at *in vitro* in therapeutic doses. However, long term *in vivo* studies have not been studied as extensively. This review aims to summarise current research in this topic highlighting commonly used toxicity assays to investigate this.

## 1. Introduction

Nanotechnology is an emerging field with growing interest for its numerous applications ranging from information technologies to medicinal applications [1]. Subsequent social and economic implications of this field have resulted in its increased popularity and demand with a competitive drive [2]. It is heavily dependent upon the cross-collaboration of various scientific disciplines to manipulate and alter the dimensions of materials at an atomic scale resulting in the formation of nanomaterials [1]. Nanomaterials are defined as materials with one, two, or three external dimensions ranging from 1 to 100 nm—the nanoscale [2, 3].

Recently, nanoscale materials have been the centre of research, particularly in the fields of regenerative medicine and tissue engineering. Examples include nanoparticles, nanofibers, and nanotubes, all of which can be specifically tailored to their role and function within tissue engineering [4]. Nanoscale materials in these forms have been used in conjunction with stem cells to produce stem cell-based therapies with emphasis on replacing and restoring the function of cells, tissues, or organs in order to establish normal function

[5]. Examples include the transplantation of mesenchymal stem cells for the treatment of Huntington's disease [6]. This paper will focus specifically on the implications of applying nanoparticles in regenerative medicine and tissue engineering.

A nanoparticle can be defined as a material with three external dimensions of equal nanoscale dimensions [2]. The major benefit of using nanoparticles is that, due to their size, they can be accurately manoeuvred and targeted to a specific biological entity or marker [7] and interact on a cellular (10–100 nm), subcellular (20–250 nm), protein (3–50 nm), or genetic scale (10–100 nm) [8, 9]. Their unique, electronic, optical, and magnet properties coupled with their specific dimensions have furthered their attractiveness in this field [10–12]. Furthermore, nanoparticles can be customised for a specific biological purpose such as cell isolation, drug delivery, diagnostics (magnetic resonance imaging MRI), cellular imaging, and hyperthermia [8, 11, 13–15]. Examples of nanoparticles include quantum dots and magnetic nanoparticles (MNPs) [12, 16]. Magnetic nanoparticles will be the main focus of this paper.

**1.1. Magnetic Nanoparticles (MNPs).** Magnetic nanoparticles have a particle size within the nanoscale with magnetic properties. Various metals can be used to convey the magnetic properties of MNPs; nickel, cobalt, and iron have demonstrated to be such examples. Organic and inorganic polymers including RGD peptides, fibronectin, and dextran can be used to coat the magnetic core resulting in improved biocompatibility by protecting biological entities from adverse toxic reactions [14, 17]. The customisation of surface coatings to desired specifications can be achieved via surface charge alterations, protein-binding capacity, and surface topography [18]; this increases functionalization of the particles encouraging enhanced interaction with biological entities, with minimal toxic effects [8, 11]. Additional factors that can further influence the behaviour of MNPs are the size [19] and magnetisation (paramagnetic, ferromagnetic, ferromagnetic, and superparamagnetic) of the particles themselves [20].

Before nanoparticles can be considered for the use in regenerative medicine, they must fulfil the following specifications.

#### Specifications:

- (i) biocompatible that is nontoxic to the cells [21–23],
- (ii) biodegradable [22, 24],
- (iii) maintain physical properties after surface modification [11],
- (iv) must not affect stem cell characteristics [21],
- (v) effective at therapeutic doses [21, 22],
- (vi) ideally have regulatory approval [20],
- (vii) minimal or no transfer of by-products to surrounding tissue/cells [22, 25],
- (viii) chemically stable in physiological conditions [24].

MNPs for the use in biomedical applications are desired to exhibit superparamagnetic properties (SPIONs) [26]. SPIONs are typically small particles composed of either a magnetite ( $\text{Fe}_3\text{O}_4$ ) or maghemite ( $\gamma\text{-Fe}_2\text{O}_3$ ) core [20, 27] coated with a biocompatible organic/inorganic polymer [17, 28] or precipitated throughout a porous biocompatible polymer [10, 20]. Both maghemite and magnetite are traditionally ferromagnetic in nature. However, as they decrease in size to 30 nm or smaller, they lose their permanent magnetism and become superparamagnetic [2]. Iron (Fe) oxide-based MNPs are suitable for biological application for the following reasons: the superparamagnetic nature implies that the particles will not be attracted to each other, and so the risk of agglomeration in a medical setting is minimised [23]. Fe is a naturally occurring metal in the human body (ferritin), and hence iron-containing nanoparticles are biocompatible as the body is adapted to metabolising the particles into its elements; these can be utilised by the body in subsequent metabolic processes [19, 29–32].

The precedent for using SPIONs in regenerative medicine comes from the application of SPION-based magnetic resonance imaging (MRI) contrast agents [33] which are accepted T2 weighted contrast agents [26]. MR imaging is a

safe and effective noninvasive means of imaging anatomical tissue [34]. It is thought that these contrast agents can be used for a variety of purposes in the clinical translation of stem cell-based therapies for the tagging, tracking, and activation of stem cells and other cell types [26, 29, 35]. Feridex (USA), also referred to as Endorem (EU) is example of FDA-approved, iron-based MRI contrast agent which has recently been taken off the market [20, 36]. These particles have an iron oxide core and are between 50 and 180 nm in diameter with an overall negative charge along with biodegradable and biocompatible properties [20, 32]. The dextran coating prevents the coagulation of particles; however a limitation to using dextran is its inability to enable the efficient uptake of these particles by cells. In these cases, transfection agents may be required.

The high resolution and impressive tissue penetration depth attributed to SPION-based MRI contrast agents has not only driven diagnostics to higher levels but also encouraged the multidisciplinary applications of these agents in fields such as regenerative medicine. These agents are, however, limited by their poor sensitivity thus preventing microscopic examination of tissue over time which is a crucial requirement in the development of stem cell-based therapies [12]. Other imaging modalities such as positive emission topography (PET scan), X-ray, ultrasound, and computed tomography (CT) [34] (available in a clinical setting) offer greater sensitivity in some cases but are lacking in other aspects such as the use of radioisotopes which could result in detrimental side effects in the case of PET scans [34]. This has therefore encouraged the integration of imaging modalities [12, 34, 37] and, as a consequence, the development of multifunctional nanoparticles to be used in conjunction with various imaging techniques. In the context of regenerative medicine, this could further our understanding of biological processes related to stem cell-based therapies [12, 26]. Unlike individual nanoparticles, multifunctional nanoparticles exploit the benefits of the imaging modalities of choice while minimising the disadvantages. In many instances this is translated in enhanced cellular tracking with high spatial resolution and high anatomical contrast without the issues of ionizing radiation for extended periods of time [12, 26, 37].

**1.2. Multifunctional Nanoparticles.** The development of multifunctional nanoparticles requires the reengineering and modification of particle surfaces to meet a greater variety of applications. It is highly desirable to incorporate fluorescent properties, near infrared absorption, and photon scattering, all of which enable *in vivo* imaging to a greater extent. This however is no easy task. It is a highly challenging task to incorporate the properties that make a particle a good MRI contrast agent and those that allow good NIR response, for example [12]. It involves novel and intricate approaches to achieve all the desired characteristics. In a study by Jin et al., the surface of nanoparticles was coated with gold (a noble metal) [12] in an effort to expand on the multifunctional aspect of MNP and incorporate near infrared absorption and photon scattering properties. This group successfully created smooth particles with the core spatially separated from the

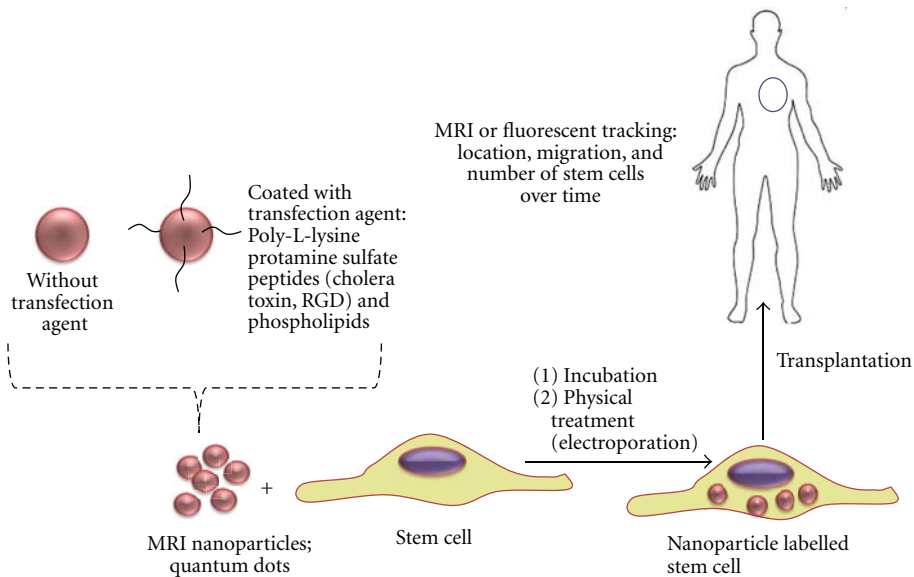


FIGURE 1: Schematic diagram highlighting the use of SPIONs in regenerative medicine. Cells require the internalisation of SPIONs. Labelled cells are then implanted within the body and visualised by MRI [52].

shell thus resulting in uniform gold-coated MNP while still maintaining dimensions, electronic, magnetic, and thermal properties and still being responsive to NIR spectra [12]. Mahmoudi et al. took this one step further and created gold-coated magnetic nanoparticles with jagged edges to allow for ramen spectroscopy to be employed and in this way imaging at the molecular level [26]. In another study, Mahmoudi and Shokrgozar sought to add to the multifunctionality of these particles by adding and trapping a fluorescent polymeric dye between the core and the gold coating [37]. This simple addition adds an extra imaging modality for either *in vivo* or *in vitro* imaging.

**1.3. Application of SPIONs in Regenerative Medicine.** SPIONs are particularly useful and have a multifunctional aspect within regenerative medicine where their functions include tagging, tracking, and activation of stem cells both *in vitro* and *in vivo*; this multifunctionality makes them highly desirable tools in this field.

**1.3.1. Tagging.** Incorporating SPIONs into cells allows for the remote manipulation of cells using an external magnetic field gradient. This encourages the precise positioning or targeting of cells to desired sites for tissue regeneration or repair [45, 46], allowing them to function as a powerful, noninvasive tool in stem cell therapy [47, 48].

**1.3.2. Tracking.** A universal issue central to all cell-based therapies is the *in vivo* migration of stem cells within tissues and on substrates, which is often guided by the presence of chemical mediators and material topography [49]. The migration of these cells to and from the target location requires precise monitoring to determine the effectiveness of the therapy. The use of nanoparticles can provide answers to questions such as optimal delivery route; extent of

engraftment; migratory patterns after transplantation; ideal dosage schemes. Having the answer to these questions will help in the optimisation of the overall therapy and thus increase its therapeutic potential [50]. It is thought that MNP can be employed in conjunction with the use of magnetic resonance imaging (MRI) to track implanted cells *in vivo* (Figure 1). In essence, stem cells are encouraged to internalise iron-based MNP; in this way magnetic properties are transferred to the cells. The intracellular iron essentially disturbs the local magnetic field thus allowing cells to be visualised as a lack of signal with MRI [51].

**1.3.3. Activation.** Mechanical stimulation can be used to facilitate cell proliferation, differentiation, and migration of stem cells [53]; physical forces include fluid flow, axial compression, tension, and magnetism [54]. Biological responses are achieved through the process of mechanotransduction, whereby cells convert physiological mechanical stimuli into biochemical signals to activate the biological response [55]. Using MNP functionalised with antibodies or peptides, it is possible to attach SPIONs to specific mechanosensitive cell surface receptors and ion channels. This has been shown to result in membrane polarisation, receptor activation, and subsequent downstream second messenger signals in hMSC [56]. Using this technology it has been shown that it is possible to promote an osteochondral phenotype of hMSC and human osteoblasts in response to magnetic activation using an external oscillating magnetic field [57, 58].

**1.3.4. MNP-Mediated Transfection.** The transfection of therapeutic genes could play a pivotal role in regenerative medicine. This technology allows the replacement of defective genes or addition of extra copies of therapeutic genes that are known to play a crucial part in the regeneration of tissue. One example is the treatment of ischemia by

transfected human umbilical vein endothelial cells with vascular endothelial growth factor to promote upregulation of survival factors and subsequent improved cell viability [59]. There are many mechanisms of inserting exogenous genetic material into cells. Transfection with viruses can be an effective technique but there are safety and efficacy concerns with this strategy. Nonviral transfection methods, for example, electroporation, transfection reagents, are considered safer. However these mechanisms often suffer from poor transfection efficiency or impact on cell viability to unacceptable levels depending on cell type. Therefore, a stable, high transfection system with minimised toxicity that can successfully deliver genes of interest without compromising gene function is required [60]. MNPs are currently being considered as alternate gene delivery vehicles; coated with nucleic acid MNPs have shown the capacity to further increase transfection efficiencies using magnetic fields to attract the MNP towards the cell membrane; the particles are then taken up by the cells by various uptake mechanisms such as endocytosis. Upon uptake the DNA dissociates from the nanoparticle and can then be expressed. One study has successfully transfected the MG63 cell line without any major effects on cell viability [61].

To summarise, all three applications require the labelling of stem cells with SPIONs. This can be achieved through either the internalisation of SPIONs or the binding of SPIONs to cell surface markers, for example, integrins, or to specific antibodies [50, 62, 63].

## 2. Safety and Biocompatibility of Magnetic Nanoparticles

Toxicity issues are a major concern and are important factors in the context of regenerative medicine and tissue engineering. As mentioned previously, the use of MNPs in regenerative medicine requires the labelling of cells (the therapeutic agents) with MNPs which may then be implanted within the body. Employing particles which are toxic in nature over a long period of time can significantly diminish the therapeutic efficiency of the cell-based therapy [38]. It is valid at this point to state that toxicology is defined as the study of adverse effects of chemical, physical, and biological agents in people, animals, and the environment [64]. Toxic cellular effects are translated into impaired mitochondrial activity, membrane leakage, and morphological changes. This can have adverse effects on cell viability, proliferation, and metabolic activity and impair the therapeutic efficiency of the therapy [65]. In cases where the MNPs are incorporated into the therapy and transplanted within the body, the risk of MNPs migrating through the organism, entering, and accumulating within organs is a constant concern. This could trigger an immunological or an inflammatory response by the body [2, 17, 64]. These are all highly undesirable consequences. Labelling stem cells for this application therefore demands the preservation of physiological cellular properties and the retention of MNPs over prolonged periods [66]. This formulates the following question: would any of the properties related to MNPs indicated for regenerative

medicinal use provoke an adverse effect on either the cells (*in vitro* applications) or the body (*in vivo* applications)?

The toxicity of MNPs on biological entities is highly dependent on a range and combination of factors related to the properties of the MNP itself; structural properties, dosage, and the intended use are among dominating factors [38, 64]. The chemical composition of the particles themselves can be naturally toxic. Interestingly, some materials which are known to be inert in large quantities are in fact toxic at nanoscale, such as gold [64]. It has been found that certain metals such as cobalt, nickel, cadmium, zinc, and silver are toxic to biological entities and therefore not suitable for biomedical applications while others such as titanium and iron oxide-based particles are considered significantly less damaging to cells [17, 30, 33]. In the case of cadmium selenide (CdSe), cadmium ions demonstrated to cause cell death in primary hepatocytes [38]. Additionally the location of MNPs in relation to the cells is an extremely important consideration [38]. For instance, MNPs could invoke a cytotoxic response when internalised by potentially interfering with the biological function of the cells but not when attached to the cell membrane [11, 38]. In other cases however, SPIONs attached to the surface of cells may interfere with cell surface interaction [11]. Furthermore, the physical properties such as the particle size, shape, and surface coating can also evoke a toxic response by aggregating and coagulating according to size and shape [38, 64]. When addressing the possible *in vivo* application of MNP, it is equally important to consider the fate of the MNPs after they have been released by the cells. Further issues arise when considering the degradation of the MNPs and the outcome of accumulated MNPs or MNP by-products in various tissues and organs [2]. Degradation products are thought to possibly react with various components of the body or cells. Therefore, the effects of the breakdown products on the surrounding tissue should be fully investigated [2, 29]. Therefore assumptions on this matter cannot be made, and appropriate investigations should always be performed.

At the cellular level, oxidative stress is thought to be the main cause of toxicity by MNPs [40]. Oxidative stress arises when there is an imbalance between damaging oxidants also referred to as reactive oxygen species (ROS) such as hydrogen peroxide, hydroxyl radicals, and the protective antioxidants of which vitamin C and glutathione are examples. ROS are primarily formed by the incomplete reduction of oxygen [67]. The accumulation of oxidants eventually leads to destruction of cellular proteins, enzymes, lipids, and nucleic acids, and as a consequence the normal cellular processes become impaired leading to the development of diseases and cell apoptosis and necrosis [17, 23, 40, 67]. ROS can be generated from the surface of MNP, the leaching of metal ions from the core, or release of oxidants by enzymatic degradation of the MNP [2]. ROS production can be measured using dichlorofluorescein diacetate fluorescent probe after SPION administration [65]. It has been reported that dissociated iron oxide MNP can promote the formation of ROS and hydroxyl radicals, and as a result may lead to cellular toxicity along with impaired cell metabolism and increases in

apoptosis [11]. On the other hand, ROS can be used in cancer therapies to destroy damaging cancer, for example [67].

### 3. Studies

Years of research have demonstrated the ability of SPIONs to be taken up by a wide variety of cells by simple incubation. Cell types include fibroblasts, lung cells, liver cells, stem cells, kidney cells, macrophages, nerve cells, endothelial cells, and various cancer cell lines [2]. There is also an impressive portfolio of MNPs that have been used with a variety of cell types. The degree of toxicity has been known to vary with cell type, MNPs, and a combination of these two factors. It is therefore essential to carry out toxicity studies to evaluate the toxicity of specific MNP on the particular cell type of interest [29]. For instance, it has been reported that uncoated SPIONs caused significant cell death in dermal fibroblasts while lung cells appeared not to be affected [2]. This highlights the importance of cell type and MNP relationship. The general consensus is that labelling cells with SPIONs is safe validated by the viability, proliferation, and differentiation capacity of cells being unaffected thus justifying its use in regenerative medicine [20, 29]. Other studies have shown that internalised silica-coated magnetic nanoparticles are biocompatible with stem cells [38]. Silica is a particular beneficial coating for nanoparticles since it can easily be functionalised, and it is resistant to degradation within a cellular environment whilst still being biocompatible [38, 40].

Toxicity is investigated through a series of *in vitro* and *in vivo* experiments, following the general schema below (Figure 2). *In vitro* toxicity tests offer a quick and simple means of gathering preliminary toxicity data which is also cost effective with minimal ethical issues [17]. When carrying out *in vitro* investigations, it is essential to identify and apply reproducible *in vivo* environments in terms of expanding conditions and sample preparation *in vitro* [2]. Data revealing marginal or no toxicity via *in vitro* tests can then be moved onto *in vivo* studies [68]. In these situations, small animal experiments are carried out and monitored over time to investigate the long-term effects of MNPs in a biological setting. Toxicity validation tests include histology on injection sites and major metabolic sites (liver, pancreas, kidney, brain) to look for signs of MNP spreading and accumulation. Sections are stained for iron by prussian blue stain and caspase 3 as an indicator for apoptosis within these areas [69]. It is not unlikely to have contradicting *in vitro* and *in vivo* results. This may be attributed to *in vivo* bodily functions/processes such as homeostasis, working to expel foreign reagents which are not present *in vitro*, for example, kidneys acting to filter blood [17]. Should *in vivo* studies reveal encouraging results, both the therapeutic efficiency and the safety of the MNP can be fully evaluated, and the MNP treatment will have to be approved for clinical use by regulatory bodies such as the Food and Drug Agency (FDA). This requires human clinical trials. An important question is whether the particles are regulated in combination with the therapy or independently. This question highlights the fact that the regulatory framework relating to these particles is limited, thus making it difficult to evaluate the safety of the

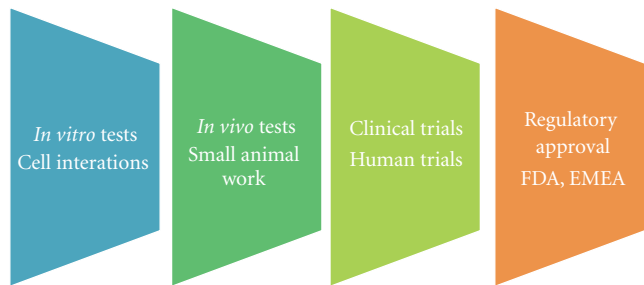


FIGURE 2: Schematic highlighting the route of translating stem cell-based therapies (incorporating the use of MNP) from bench to bed side.

nanomaterials in conjunction with regenerative medicine. For this reason, extensive safety assessment of these particles must be carried out to satisfy not only the regulators but also the patient. Even though SPION-based MRI contrast agents have been used and approved, the use of these for stem cell-based therapies still requires FDA approval as their intended use is different from their use as contrast agents [36]. An essential requirement of contrast agents is to be excreted relatively quickly and not remain in the body in the long term. However, for some applications, especially within the remit of regenerative medicine, long-term treatment of MNPs and presence in the body may be necessary. Using FDA-approved contrast agents will however make this task easier [66].

Table 1 highlights commonly used *in vitro* tests for MNP-mediated toxicity and cell viability. It can be concluded that MTT (3-(4,5-Dimethylthiazol-2-yl)-2,5-diphenyltetrazolium bromide), PI (Propidium Iodide), for example, live/dead assay [70] and trypan blue [71] stains are most commonly used. Other popular tests not mentioned in this table include BrdU (5-bromo-2'-deoxyuridine) assay and the LDH (Lactate dehydrogenase) assay for metabolic activity [10]. Toxicity assays are aimed at investigating vital cellular activity such as cell death and cell viability. Cell death or apoptosis is most commonly assessed using the tetrazolium compound MTT [72, 73], LDH [74], and PI [75] assay while cell proliferation is assessed using BrdU [76] and MTT [73]. Figure 3 describes each test in greater detail. Other notable cytotoxicity assays include cell-life cycle assay, TUNEL assay (i.e., for apoptosis detection) [77], and various redox assays [78]. Immunohistochemistry can also be performed to look for markers of apoptosis or necrosis [79]. Furthermore, many toxic effects caused by MNP may stop mitochondrial activity which is measured by assays such as MTT. Added to this, there are inherent issues associated with MNP-cell interaction, dosage, and time course, all of which may impact on results [79]. It should be noted that *in vitro* tests that produce specific and quantitative toxicity read-outs are particularly convenient for the initial evaluation of toxicity and biocompatibility of new MNP [79]. An important consideration when interpreting the results of these types of *in vitro* assays is that they often provide little information on the mechanism of toxicity or the cause of cell death. In addition it can be noticed that SPIONs do not affect cell viability, proliferation, or differentiation capacity of stem

TABLE 1: Summary of *in vitro* studies performed in recent years highlighting commonly used assays aimed at investigating toxicity of SPIONs on stem cells and the results.

Particle used	Biological polymer	Particle size	Cells type	Particle concentration	Toxicity assay	Result	Reference
Feridex (FDA approved)	Dextran	80–150 nm	rMSC & mMSC	25 µg/mL	Live/dead (7 days after labelling) differentiation assays	No loss of cell viability observed after 7 days with or without either TA	[32]
Ferric oxide (noncommercial)	Poly-L-lysine	15 nm	HUC	20 µg/mL	MTT (5 days continued culture) cellular apoptosis—annexin V/PI double stain assay	No reduction in viability after 1 hour. No reduction in cell proliferation	[19]
Noncommercial	Silica	110 nm	hMSCs	200 µg/mL	MTT (1 hr and 24 hrs) Trypan Blue	No reduction in viability after 12 hours	[38]
Feridex	Dextran	80–150 nm	hMSC	100 µg/mL	FACS (fluorescence-activated cell sorting) to evaluate cell death—to determine if iron oxide incorporation affects surface markers expression Trypan Blue	No reduction in viability after 12 hours	[39]
Iron fluorescent particle	Polystyrene	900 nm	pMSC		MTT Morphological observations	Cells maintained viability and retained label for up to 3 months. Differentiation capacity not altered	[22]
Manganese oxide nanoparticles	Mesoporous silica	65 nm	mMSCs		MTS	75% cell viability Limited cell differentiation in the osteogenic lineage	[40]
Commercially available Feridex		1630 nm	rMSCs	2.8 µg/mL	Trypan Blue	Did not affect cell viability	[41]
	Dextran	150 nm	ESCs	50 µg/mL	Trypan Blue	Did not affect cell viability	[42]
	HEDP		rMSC	25, 50, 100 µg/mL	MTS	Cell viability not affected at lower concentrations but viability decreased to 70% at 100 µg/mL	[43]
Feridex	uncoated	80–150	hMSC	50–250 µg/mL	Comet assay	Did not affect viability	[44]

rMSC: rat mesenchymal stem cells; mMSC: mouse mesenchymal stem cell; hMSC: human mesenchymal stem cells; pMSC: porcine mesenchymal stem cells; HUC: human umbilical cells; HEDP: hydroxyethylidene bisphosphonic acid.

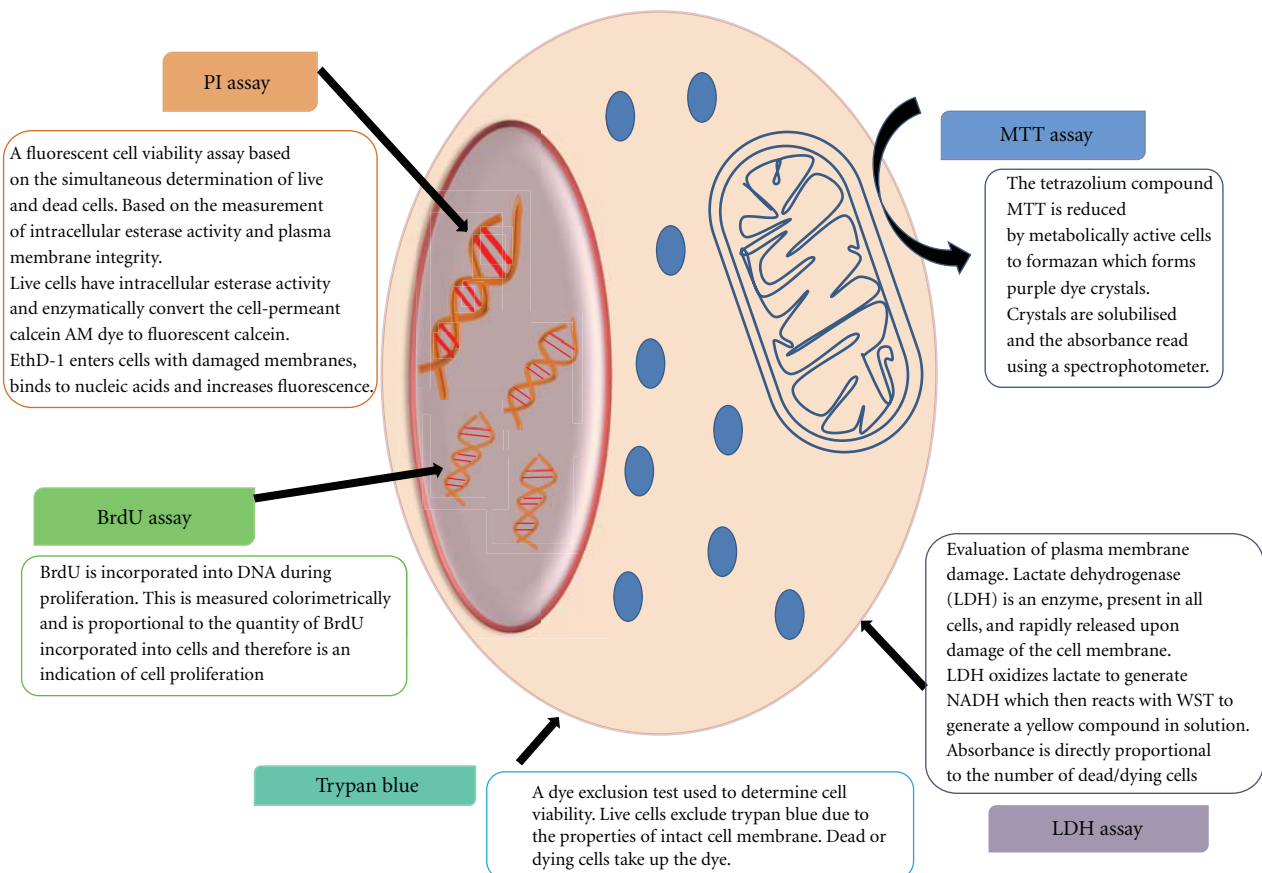


FIGURE 3: Overview of *in vitro* toxicity assays. Cell image adapted from [2]. PI [75], MTT [72, 73], LDH [59], Trypan Blue [71] and BrdU [76].

cells. In fact it can be said that number of studies reporting adverse or toxic effects of MNP are few [17].

Despite cost, time, and ethical considerations, *in vivo* tests in relevant animal models are crucial for the study of biological effects that cannot be modelled *in vitro*. This includes the pharmacokinetics of MNP in the body, that is, absorption, distribution, metabolism, and elimination. These studies allow information about the systemic toxicities to be elucidated including immunological, neurological, reproductive, cardiovascular, reproductive, and developmental as well as any carcinogenic effects [79].

As far as *in vivo* assays are concerned, one of the important functions to assess is the blood contact properties of the MNP, that is, blood compatibility. In terms of *in vivo* application of MNP, should the MNP be incompatible with bio fluids such as blood, this could lead to haemolysis, coagulation, and blood clots due to adsorption and/or activation of biomolecules, for example, plasma protein, complement factors, and so forth. As such it is critical to assess these properties before clinical use. One such test is the haemolysis assay which uses erythrocytes to assess the MNP toxicity. The coagulation tendencies can be assessed using common clinical assays including prothrombin time (PT), activated clotting time (ACT), and activated partial thromboplastin time (APTT) [79]. Another parameter to assess is the inflammatory response. This can be evaluated

by looking at levels of chemokines and proinflammatory cytokines, for example, IL-8 in the blood as these can indicate potential oxidative stress toxic effects caused by MNP [34]. Gene expression analysis for transcription factors associated with oxidative stress can also be examined and may reveal useful information about the mechanism of toxicity. This raises the possibility of correlating MNP characteristics with toxic effects observed in certain cell lines and tissues [79].

Once the MNPs have entered body, MNPs come into direct contact with biological macromolecules such as proteins, lipids, and enzymes found within the biological fluid. These biomolecules interact with the surface of the MNP to form a complex layer of molecules over the MNP. This biological layer is termed “corona” [80, 81]. The physical and chemical properties of MNP (size, surface coating, and functionalization) dictate the binding of molecules to the particles resulting in either a hard or weak corona which is significantly different to that of the surface of the MNP [80, 81]. This affects the initial interaction of the cell with the MNP as the cell’s first point of contact is with the corona and not the surface of the particle [80]. In turn, this dictates subsequent cellular and tissue responses [81]. This protein corona could be responsible for various toxic outcomes [80]. The formation of the corona is a dynamic process, and competitive process involving the attachment and detachment of various proteins as the particle moves from one biological

environment to another [81]. Movement of particles from one biological environment to another causes proteins from original fluid to be replaced by proteins from new fluid—leaving evidence of the previously attached proteins [80, 81]. Approximately 10–50 proteins with the highest affinity for the surface are bound at one time [81]. The parameters affecting MNP-protein interaction include physiochemical properties (such as surface chemistries, particle size, shape, charge, surface area, surface defects, smoothness/roughness, and functional groups) of MNP and the composition of biological fluid (proteins types and ratios) [81].

The interaction of proteins with the surface of MNPs of different types and coatings is also an important consideration when assessing *in vitro* toxicity. When MNPs are added to culture media, media proteins and other nutrients may adsorb onto MNPs and thus are unavailable for cellular activities. This naturally has implications on cell growth and viability. It is paramount therefore to test different culture media as MNP-protein interaction is dependent on the *in vitro* environment and MNP composition, so different media recipes could influence the outcome of cytotoxicity assays [78, 82].

A related concept is the effect of “cell vision” presented by Laurent et al. [82]. This refers to the contact point between MNP and the cell membrane, which is characterised by its surface molecules, that is, proteins, sugars, and phospholipid composition. The binding of MNP to these structures which may be different for different cell types defines how individual cell lines “see” MNPs. As a result the binding of exogenous objects like MNP to these structures may cause different responses and influence uptake and metabolism depending on the cell type. This concept is exemplified by Laurent et al. who showed that the same concentration of SPIONS can cause significant toxicity on neuronal and glial cells whilst displaying little toxicity on other cell types like heart and kidney cells [82, 83]. The issues of cell vision and MNP-media interactions raise questions about the reliability of toxicity assays when studying the toxic effects of MNP. This issue is highlighted by the seemingly contradictory results of some MNP toxicity assays [34]. To address this issue Mahmoudi et al. have modified the MTT protocol by exposing SPIONS to culture media thereby allowing MNP to interact with culture media proteins before adding them to cell cultures. This led to improvements in the reliability of *in vitro* MNP toxicity results. Their results showed that uncoated and coated SPIONs were less toxic as previously thought and induced toxicity in various cell lines at greater doses than permitted for humans [78]. Furthermore another problem is posed by the sedimentation of MNPs, as this phenomenon effectively leads to an apparent increase in MNP concentration at the cell surface and so should be taken into account when performing toxicity assays [82].

#### 4. Conclusion and Future Perspectives

It has been mentioned that *in vitro* and *in vivo* toxicity results often contradict each other. This can be attributed to the issue of protein adsorption onto the surface of MNP. It has also been suggested that various biomaterials intended

for biological/tissue engineering purposes may benefit from exposure to biological fluids prior to implantation. This would allow for a layer of preadsorbed proteins to adhere on the surface of the material which may offer several advantages in terms of cellular mediated responses [84]. Following this theory, *in vivo* toxicity studies could be mimicked to a closer extent *in vitro* with the MNP in question when exposed to the desired biological fluid.

The multifunctional applications of MNP have been established. However utilizing micro- or nanoporous structures with nanometer superparamagnetic particles embedded within this structure could offer an alternative means of activating and inducing differentiation of stem cells for tissue engineering *in vivo*. Various biocompatible and bioactive materials have been used to fabricate these porous structures and have had impressive results in terms of cellular compatibility and differentiation in terms of osteogenesis and chondrogenesis [84, 85]. Examples of such porous nanoparticles include nickel titanium nanoparticles coated with titanium oxide [85] and calcium phosphate ceramics [84]. Preexposing nanoparticles to solutions of specific proteins could also warrant increased cell attachment, proliferations, and the differentiation of stem cells down various lineages such as osteogenic or chondrogenic pathways [84, 85]. Thus combining the use of biocompatible materials known to promote or induce differentiation with magnetic properties could be of great benefit in tissue engineering and regenerative medicine.

This paper has addressed the relevance of MNP in regenerative medicine, highlighting their diverse and significant applications within this field. MNPs offer a noninvasive, practical means of monitoring, controlling, and targeting stem cells to optimise the therapy with clinical adoption in mind. However, safety concerns could ultimately prevent the adoption of MNP in regenerative medicine. This would demand the development of alternative ways of monitoring and controlling stem cells *in vivo*. It is essential to confirm the safety of the procedure prior to *in vivo* transplantation despite clinical efficacy of the technique. In reality, there is an enormous portfolio of particles available both commercially and in research. This makes it very difficult to give a definitive answer to the following question: are MNPs toxic? The toxic effects of MNPs should be evaluated for each specific purpose. A large number of *in vitro* toxicity investigations have shown no adverse side effect of labelling stem cells with SPIONs. However, long-term *in vivo* studies have not been studied as extensively and hence are an area of much needed research.

#### Acknowledgments

The authors would like to thank D. Kumar for his contributions to this work. Support was received from the EPSRC Doctoral Training Centre (EP/F/500491/1) and LOLA BB/G/010579/1.

#### References

- [1] M. Chakraborty, S. Jain, and V. Rani, “Nanotechnology: emerging tool for diagnostics and therapeutics,” *Applied*

- Biochemistry and Biotechnology*, vol. 165, no. 5-6, pp. 51178–51687, 2011.
- [2] H. H. Morteza Mahmoudi, R.-R Barbara, and P.-F Alke, *Assessing the In Vitro and In Vivo Toxicity of Superparamagnetic Iron Oxide Nanoparticles*, American Chemical Society, 2011.
  - [3] J. Wang, Y. Gao, and Y. Hou, “Evaluation on cartilage morphology after intra-articular injection of titanium dioxide nanoparticles in rats,” *Journal of Nanomaterials*, vol. 2012, Article ID 452767, 11 pages, 2012.
  - [4] K. Riehemann, S. W. Schneider, T. A. Luger, B. Godin, M. Ferrari, and H. Fuchs, “Nanomedicine—challenge and perspectives,” *Angewandte Chemie*, vol. 48, no. 5, pp. 872–897, 2009.
  - [5] C. Mason and P. Dunnill, “A brief definition of regenerative medicine,” *Regenerative Medicine*, vol. 3, no. 1, pp. 1–5, 2008.
  - [6] O. Sadan, N. Shemesh, R. Barzilay et al., “stem cells induced to secrete neurotrophic factors attenuate quinolinic acid toxicity: a potential therapy for Huntington’s disease,” *Experimental Neurology*, vol. 234, no. 2, pp. 417–427, 2012.
  - [7] K. M. Krishnan, “Biomedical nanomagnetics: a spin through possibilities in imaging, diagnostics, and therapy,” *IEEE Transactions on Magnetics*, vol. 46, no. 7, pp. 2523–2558, 2010.
  - [8] Q. A. Pankhurst, J. Connolly, S. K. Jones, and J. Dobson, “Applications of magnetic nanoparticles in biomedicine,” *Journal of Physics D*, vol. 36, no. 13, pp. R167–R181, 2003.
  - [9] R. Banerjee, Y. Katsenovich, L. Lagos, M. Mcintosh, X. Zhang, and C. Z. Li, “Nanomedicine: magnetic nanoparticles and their biomedical applications,” *Current Medicinal Chemistry*, vol. 17, no. 27, pp. 3120–3141, 2010.
  - [10] M. Mahmoudi, S. Sant, B. Wang, S. Laurent, and T. Sen, “Superparamagnetic iron oxide nanoparticles (SPIONs): development, surface modification and applications in chemotherapy,” *Advanced Drug Delivery Reviews*, vol. 63, no. 1-2, pp. 24–46, 2011.
  - [11] A. Solanki, J. D. Kim, and K.-B. Lee, “Nanotechnology for regenerative medicine: nanomaterials for stem cell imaging,” *Nanomedicine*, vol. 3, no. 4, pp. 567–578, 2008.
  - [12] Y. Jin, C. Jia, S.-W. Huang, M. O’Donnell, and X. Gao, “Multifunctional nanoparticles as coupled contrast agents,” *Nature Communications*, vol. 1, no. 41, 2010.
  - [13] N. S. Barakat, “Magnetically modulated nanosystems: a unique drug-delivery platform,” *Nanomedicine*, vol. 4, no. 7, pp. 799–812, 2009.
  - [14] M. M. Lin, D. K. Kim, A. J. El Haj, and J. Dobson, “Development of superparamagnetic iron oxide nanoparticles (SPIONs) for translation to clinical applications,” *IEEE Transactions on Nanobioscience*, vol. 7, no. 4, pp. 298–305, 2008.
  - [15] A. Ito and M. Kamihira, “Tissue engineering using magnetite nanoparticles,” *Progress in Molecular Biology and Translational Science*, vol. 104, pp. 355–395, 2011.
  - [16] L. Ferreira, “Nanoparticles as tools to study and control stem cells,” *Journal of Cellular Biochemistry*, vol. 108, no. 4, pp. 746–752, 2009.
  - [17] M. Mahmoudi, A. Simchi, M. Imani et al., “A new approach for the in vitro identification of the cytotoxicity of superparamagnetic iron oxide nanoparticles,” *Colloids and Surfaces B*, vol. 75, no. 1, pp. 300–309, 2010.
  - [18] S. Hughes, A. J. El Haj, and J. Dobson, “Magnetic micro- and nanoparticle mediated activation of mechanosensitive ion channels,” *Medical Engineering and Physics*, vol. 27, no. 9, pp. 754–762, 2005.
  - [19] S. Ju, G. Teng, Y. Zhang, M. Ma, F. Chen, and Y. Ni, “In vitro labeling and MRI of mesenchymal stem cells from human umbilical cord blood,” *Magnetic Resonance Imaging*, vol. 24, no. 5, pp. 611–617, 2006.
  - [20] S. M. Cromer Berman, P. Walczak, and J. W. Bulte, “Tracking stem cells using magnetic nanoparticles,” *Wiley Interdisciplinary Reviews*, vol. 3, no. 4, pp. 343–355, 2011.
  - [21] K.-S. Park, J. Tae, B. Choi et al., “Characterization, in vitro cytotoxicity assessment, and in vivo visualization of multimodal, RITC-labeled, silica-coated magnetic nanoparticles for labeling human cord blood-derived mesenchymal stem cells,” *Nanomedicine*, vol. 6, no. 2, pp. 263–276, 2010.
  - [22] J. M. Hill, A. J. Dick, V. K. Raman et al., “Serial cardiac magnetic resonance imaging of injected mesenchymal stem cells,” *Circulation*, vol. 108, no. 8, pp. 1009–1014, 2003.
  - [23] M. Getzlaff, *Fundamentals of Magnetism*, Springer, New York, NY, USA, 2008.
  - [24] M. Getzelt, *Fundamentals of Magnetism*, Springer, 2008.
  - [25] J. V. Frangioni and R. J. Hajjar, “In vivo tracking of stem cells for clinical trials in cardiovascular disease,” *Circulation*, vol. 110, no. 21, pp. 3378–3383, 2004.
  - [26] M. Mahmoudi, H. Amiri, M. A. Shokrgozar et al., “Raman active jagged-shaped gold-coated magnetic particles as a novel multimodal nanoprobe,” *Chemical Communications*, vol. 47, no. 37, pp. 10404–10406, 2011.
  - [27] A. K. Gupta and M. Gupta, “Synthesis and surface engineering of iron oxide nanoparticles for biomedical applications,” *Biomaterials*, vol. 26, no. 18, pp. 3995–4021, 2005.
  - [28] H. Pardoe, W. Chua-anusorn, T. G. S. Pierre, and J. Dobson, “Structural and magnetic properties of nanoscale iron oxide particles synthesized in the presence of dextran or polyvinyl alcohol,” *Journal of Magnetism and Magnetic Materials*, vol. 225, no. 1-2, pp. 41–46, 2001.
  - [29] J. W. M. Bulte, “In vivo MRI cell tracking: clinical studies,” *American Journal of Roentgenology*, vol. 193, no. 2, pp. 314–325, 2009.
  - [30] C. C. Berry, “Possible exploitation of magnetic nanoparticle-cell interaction for biomedical applications,” *Journal of Materials Chemistry*, vol. 15, no. 5, pp. 543–547, 2005.
  - [31] H. S. Kim, S. Y. Oh, H. J. Joo, K.-R. Son, I.-C. Song, and W. K. Moon, “The effects of clinically used MRI contrast agents on the biological properties of human mesenchymal stem cells,” *NMR in Biomedicine*, vol. 23, no. 5, pp. 514–522, 2010.
  - [32] Jasmin, A. L. M. Torres, H. M. P. Nunes et al., “Optimized labeling of bone marrow mesenchymal cells with superparamagnetic iron oxide nanoparticles and in vivo visualization by magnetic resonance imaging,” *Journal of Nanobiotechnology*, vol. 9, article 4, 2011.
  - [33] M. Hofmann-Amtenbrink, H. Hofmann, and X. Montet, “Superparamagnetic nanoparticles—a tool for early diagnostics,” *Swiss Medical Weekly*, vol. 140, pp. 7–13, 2010.
  - [34] M. Mahmoudi, H. Hosseinkhani, M. Hosseinkhani et al., “Magnetic resonance imaging tracking of stem cells in vivo using iron oxide nanoparticles as a tool for the advancement of clinical regenerative medicine,” *Chemical Reviews*, vol. 111, no. 2, pp. 253–280, 2011.
  - [35] G. M. van Buul, E. Farrell, N. Kops et al., “Ferumoxides-protamine sulfate is more effective than ferucarbotran for cell labeling: implications for clinically applicable cell tracking using MRI,” *Contrast Media and Molecular Imaging*, vol. 4, no. 5, pp. 230–236, 2009.
  - [36] R. Zhou, P. D. Acton, and V. A. Ferrari, “Imaging stem cells implanted in infarcted myocardium,” *Journal of the American College of Cardiology*, vol. 48, no. 10, pp. 2094–2106, 2006.

- [37] M. A. Mahmoudi and M. A. Shokrgozar, "Multifunctional stable fluorescent magnetic nanoparticles," *Chemical Communications*, vol. 48, no. 33, pp. 3957–3959, 2012.
- [38] D. M. Huang, T. H. Chung, Y. Hung et al., "Internalization of mesoporous silica nanoparticles induces transient but not sufficient osteogenic signals in human mesenchymal stem cells," *Toxicology and Applied Pharmacology*, vol. 231, no. 2, pp. 208–215, 2008.
- [39] T. H. Kim, J. K. Kim, W. Shim, S. Y. Kim, T. J. Park, and J. Y. Jung, "Tracking of transplanted mesenchymal stem cells labeled with fluorescent magnetic nanoparticle in liver cirrhosis rat model with 3-T MRI," *Magnetic Resonance Imaging*, vol. 28, no. 7, pp. 1004–1013, 2010.
- [40] T. Kim, E. Momin, J. Choi et al., "Mesoporous silica-coated hollow manganese oxide nanoparticles as positive T 1 contrast agents for labeling and MRI tracking of adipose-derived mesenchymal stem cells," *Journal of the American Chemical Society*, vol. 133, no. 9, pp. 2955–2961, 2011.
- [41] K. J. Saldanha, R. P. Doan, K. M. Ainslie, T. A. Desai, and S. Majumdar, "Micrometer-sized iron oxide particle labeling of mesenchymal stem cells for magnetic resonance imaging-based monitoring of cartilage tissue engineering," *Magnetic Resonance Imaging*, vol. 29, no. 1, pp. 40–49, 2011.
- [42] R. T. Castaneda, S. Boddington, T. D. Henning et al., "Labeling human embryonic stem-cell-derived cardiomyocytes for tracking with MR imaging," *Pediatric Radiology*, vol. 41, no. 11, pp. 1384–1392, 2011.
- [43] G. J. R. Delcroix, M. Jacquot, L. Lemaire et al., "Mesenchymal and neural stem cells labeled with HEDP-coated SPIO nanoparticles: in vitro characterization and migration potential in rat brain," *Brain Research*, vol. 1255, pp. 18–31, 2009.
- [44] A. Omidkhoda, H. Mozdaran, A. Movasaghpoor, and A. A. P. Fatholah, "Study of apoptosis in labeled mesenchymal stem cells with superparamagnetic iron oxide using neutral comet assay," *Toxicology in Vitro*, vol. 21, no. 6, pp. 1191–1196, 2007.
- [45] P. G. Kyrtatos, P. Lehtolainen, M. Junemann-Ramirez et al., "Magnetic tagging increases delivery of circulating progenitors in vascular injury," *Cardiovascular Interventions*, vol. 2, no. 8, pp. 794–802, 2009.
- [46] V. H. B. Ho, A. Barcza, R. Chen, K. H. Müller, N. J. Darton, and N. K. H. Slater, "The precise control of cell labelling with streptavidin paramagnetic particles," *Biomaterials*, vol. 30, no. 33, pp. 6548–6555, 2009.
- [47] J. A. Kim, H.-J. Lee, H. J. Kang, and T. H. Park, "The targeting of endothelial progenitor cells to a specific location within a microfluidic channel using magnetic nanoparticles," *Biomedical Microdevices*, vol. 11, no. 1, pp. 287–296, 2009.
- [48] J.-K. Hsiao, M.-F. Tai, H.-H. Chu et al., "Magnetic nanoparticle labeling of mesenchymal stem cells without transfection agent: cellular behavior and capability of detection with clinical 1.5 T magnetic resonance at the single cell level," *Magnetic Resonance in Medicine*, vol. 58, no. 4, pp. 717–724, 2007.
- [49] M. Hoehn, E. Küstermann, J. Blunk et al., "Monitoring of implanted stem cell migration in vivo: a highly resolved in vivo magnetic resonance imaging investigation of experimental stroke in rat," *Proceedings of the National Academy of Sciences of the United States of America*, vol. 99, no. 25, pp. 16267–16272, 2002.
- [50] S. M. C. Berman, P. Walczak, and J. W. M. Bulte, "Tracking stem cells using magnetic nanoparticles," *Wiley Interdiscip Rev-Nanomed Nanobiotechnol*, vol. 3, no. 4, pp. 343–355, 2011.
- [51] S. Ramaswamy, J. B. Greco, M. C. Uluer et al., "Magnetic resonance imaging of chondrocytes labeled with superparamagnetic iron oxide nanoparticles in tissue-engineered cartilage," *Tissue Engineering A*, vol. 15, no. 12, pp. 3899–3910, 2009.
- [52] I. Wimpenny, H. Markides, and A. El Haj, "Orthopaedic applications of nanoparticle-based stem cell therapies," *Stem Cell Research & Therapy*, vol. 3, no. 2, p. 13, 2012.
- [53] N. J. Sniadecki, "Minireview: a tiny touch: activation of cell signaling pathways with magnetic nanoparticles," *Endocrinology*, vol. 151, no. 2, pp. 451–457, 2010.
- [54] S. H. Cartmell, J. Dobson, S. B. Verschueren, and A. J. El Haj, "Development of magnetic particle techniques for long-term culture of bone cells with intermittent mechanical activation," *IEEE Transactions on Nanobioscience*, vol. 1, no. 2, pp. 92–97, 2002.
- [55] D. E. Ingber, "Cellular mechanotransduction: putting all the pieces together again," *FASEB Journal*, vol. 20, no. 7, pp. 811–827, 2006.
- [56] G. R. Kirkham, K. J. Elliot, A. Keramane et al., "Hyperpolarization of human mesenchymal stem cells in response to magnetic force," *IEEE Transactions on Nanobioscience*, vol. 9, no. 1, pp. 71–74, 2010.
- [57] J. M. Kanczler, H. S. Sura, J. Magnay et al., "Controlled differentiation of human bone marrow stromal cells using magnetic nanoparticle technology," *Tissue Engineering A*, vol. 16, no. 10, pp. 3241–3250, 2010.
- [58] S. H. Cartmell, J. Dobson, S. B. Verschueren, and A. J. El Haj, "Development of magnetic particle techniques for long-term culture of bone cells with intermittent mechanical activation," *IEEE Transactions on Nanobioscience*, vol. 1, no. 2, pp. 92–97, 2002.
- [59] S.-W Cho, F. Yang, S. M. Son et al., "Therapeutic angiogenesis using genetically engineered human endothelial cells," *Journal of Controlled Release*, vol. 160, no. 3, pp. 515–524, 2012.
- [60] M. C. Duran, S. Willenbrock, A. Barchanski et al., "Comparison of nanoparticle-mediated transfection methods for DNA expression plasmids: efficiency and cytotoxicity," *Journal of Nanobiotechnology*, vol. 9, article 47, 2011.
- [61] A. Fouriki, M. A. Clements, N. Farrow, and J. Dobson, "Efficient transfection of MG-63osteoblasts using magnetic nanoparticles and oscillating magnetic fields," *Journal of Tissue Engineering and Regenerative Medicine*. In press.
- [62] C.-W. Lu, Y. Hung, J.-K. Hsiao et al., "Bifunctional magnetic silica nanoparticles for highly efficient human stem cell labeling," *Nano Letters*, vol. 7, no. 1, pp. 149–154, 2007.
- [63] C. K. Sung, K. A. Hong, S. Lin et al., "Dual-modal nanoprobes for imaging of mesenchymal stem cell transplant by MRI and fluorescence imaging," *Korean Journal of Radiology*, vol. 10, no. 6, pp. 613–622, 2009.
- [64] "The dose makes the poison," *Nature Nanotechnology*, vol. 6, no. 6, p. 329, 2011.
- [65] C.-Y. Yang, J.-K. Hsiao, M.-F. Tai et al., "Direct labeling of hMSC with SPIO: the long-term influence on toxicity, chondrogenic differentiation capacity, and intracellular distribution," *Molecular Imaging and Biology*, vol. 13, no. 3, pp. 443–451, 2011.
- [66] V. Dousset, T. Tourdias, B. Brochet, C. Boizieu, and K. G. Petry, "How to trace stem cells for MRI evaluation?" *Journal of the Neurological Sciences*, vol. 265, no. 1-2, pp. 122–126, 2008.
- [67] M. K. Khaing Oo, Y. Yang, Y. Hu, M. Gomez, H. Du, and H. Wang, "Gold nanoparticle-enhanced and size-dependent generation of reactive oxygen species from protoporphyrin IX," *ACS Nano*, vol. 6, no. 3, pp. 1939–1947, 2012.

- [68] R. Weissleder, D. D. Stark, B. L. Engelstad et al., "Superparamagnetic iron oxide: pharmacokinetics and toxicity," *American Journal of Roentgenology*, vol. 152, no. 1, pp. 167–173, 1989.
- [69] E. K. Schlachter, H. R. Widmer, A. Bregy et al., "Metabolic pathway and distribution of superparamagnetic iron oxide nanoparticles: in vivo study," *International Journal of Nanomedicine*, vol. 6, pp. 1793–1800, 2011.
- [70] M. F. Kircher, S. S. Gambhir, and J. Grimm, "Noninvasive cell-tracking methods," *Nature Reviews Clinical Oncology*, vol. 8, no. 11, pp. 677–688, 2011.
- [71] W. Strober, *Trypan Blue Exclusion Test of Cell Viability. Current Protocols in Immunology*, John Wiley & Sons, 2001.
- [72] B. C. Saravanan, C. Sreekumar, G. C. Bansal, D. Ray, J. R. Rao, and A. K. Mishra, "A rapid MTT colorimetric assay to assess the proliferative index of two Indian strains of *Theileria annulata*," *Veterinary Parasitology*, vol. 113, no. 3-4, pp. 211–216, 2003.
- [73] "TACS MTT Cell Proliferation Assays," 2009, [http://www.trevigen.com/docs/protocol\\_4890-XX-K.pdf](http://www.trevigen.com/docs/protocol_4890-XX-K.pdf).
- [74] "LDH-Cytotoxicity Assay Kit II (500 assays)," 2012, <http://www.abcam.com/LDH-Cytotoxicity-Assay-Kit-II-500-assays-ab65393.pdf>.
- [75] "LIVE/DEAD Viability/Cytotoxicity Kit \*for mammalian cells\*," 2005, <http://tools.invitrogen.com/content/sfs/manuals/mp03224.pdf>.
- [76] "BrdU Cell Proliferation Assay Kit," 2011, <http://www.cellsignal.com/pdf/6813.pdf>.
- [77] S. Laurent, S. Dutz, U. O. Häfeli, and M. Mahmoudi, "Magnetic fluid hyperthermia: focus on superparamagnetic iron oxide nanoparticles," *Advances in Colloid and Interface Science*, vol. 166, no. 1-2, pp. 8–23, 2011.
- [78] M. Mahmoudi, M. A. Sahraian, M. A. Shokrgozar, and S. Laurent, "Superparamagnetic iron oxide nanoparticles: promises for diagnosis and treatment of multiple sclerosis," *ACS Chemical Neuroscience*, vol. 2, no. 3, pp. 118–140, 2011.
- [79] S. Sharifi, S. Behzadi, S. Laurent, M. Laird Forrest, P. Stroeve, and M. Mahmoudi, "Toxicity of nanomaterials," *Chemical Society Reviews*, vol. 41, no. 6, pp. 2323–2343, 2012.
- [80] M. Lundqvist, J. Stigler, and T. Cedervall, "The evolution of the protein corona around nanoparticles: a test study," *ACS Nano*, vol. 5, no. 9, pp. 7503–7509, 2011.
- [81] M. Mahmoudi, I. Lynch, M. R. Ejtehadi, M. P. Monopoli, F. B. Bombelli, and S. Laurent, "Protein–nanoparticle interactions: opportunities and challenges," *Chemical Reviews*, vol. 111, no. 9, pp. 5610–5637, 2011.
- [82] S. Laurent, C. Burtea, C. Thirifays, H. UO, and M. Mahmoudi, "Crucial ignored parameters on nanotoxicology: the importance of toxicity assay modifications and "cell vision"," *Plos One*, vol. 7, no. 1, Article ID e29997, 2012.
- [83] M. Mahmoudi, S. Laurent, M. A. Shokrgozar, and M. Hosseinkhani, "Toxicity evaluations of superparamagnetic iron oxide nanoparticles: cell "vision" versus physicochemical properties of nanoparticles," *ACS Nano*, vol. 5, no. 9, pp. 7263–7276, 2011.
- [84] X. Li, C. A. van Blitterswijk, Q. Feng, F. Cui, and F. Watari, "The effect of calcium phosphate microstructure on bone-related cells in vitro," *Biomaterials*, vol. 29, no. 23, pp. 3306–3316, 2008.
- [85] J. Huang, J. Wang, X. Su et al., "Biocompatibility of nanoporous TiO<sub>2</sub> coating on NiTi alloy prepared via dealloying method," *Journal of Nanomaterials*, vol. 2012, Article ID 731592, 7 pages, 2012.

## Review Article

# Silver Nanoparticles in Alveolar Bone Surgery Devices

**Stefano Sivolella,<sup>1,2</sup> Edoardo Stellini,<sup>3</sup> Giulia Brunello,<sup>1</sup> Chiara Gardin,<sup>4</sup> Letizia Ferroni,<sup>4</sup> Eriberto Bressan,<sup>2,5</sup> and Barbara Zavan<sup>4</sup>**

<sup>1</sup>Department of Oral Surgery, University of Padova Institute of Clinical Dentistry, Via Venezia, 90, 35129 Padova, Italy

<sup>2</sup>Department of Experimental and Diagnostic Medicine, Section of General Pathology,

Interdisciplinary Center for the Study of Inflammation (ICSI) and LTAA Center, University of Ferrara, 44121 Ferrara, Italy

<sup>3</sup>Department of Prosthodontics, University of Padova Institute of Clinical Dentistry, Via Venezia, 90, 35129 Padova, Italy

<sup>4</sup>Department of Biomedical Sciences, University of Padova, Via G. Colombo 3, 35100 Padova, Italy

<sup>5</sup>Department of Periodontology, University of Padova Institute of Clinical Dentistry, Via Venezia, 90, 35129 Padova, Italy

Correspondence should be addressed to Barbara Zavan, barbara.zavan@unipd.it

Received 15 March 2012; Accepted 11 June 2012

Academic Editor: Sang Cheon Lee

Copyright © 2012 Stefano Sivolella et al. This is an open access article distributed under the Creative Commons Attribution License, which permits unrestricted use, distribution, and reproduction in any medium, provided the original work is properly cited.

Silver (Ag) ions have well-known antimicrobial properties and have been applied as nanostrategies in many medical and surgical fields, including dentistry. The use of silver nanoparticles (Ag NPs) may be an option for reducing bacterial adhesion to dental implant surfaces and preventing biofilm formation, containing the risk of peri-implant infections. Modifying the structure or surface of bone grafts and membranes with Ag NPs may also prevent the risk of contamination and infection that are common when alveolar bone augmentation techniques are used. On the other hand, Ag NPs have revealed some toxic effects on cells *in vitro* and *in vivo* in animal studies. In this setting, the aim of the present paper is to summarize the principle behind Ag NP-based devices and their clinical applications in alveolar bone and dental implant surgery.

## 1. Introduction

In recent years, silver nanoparticles (Ag NPs) have been studied and suggested for a variety of medical, surgical, and biological applications. Due to their antimicrobial activity, Ag NPs are widely used to reduce burns, chronic ulcers, and wound infections by means of AgNP-impregnated wound dressings [1]. Antimicrobial coatings are especially important in connection with indwelling catheters carrying a high risk of bacterial line infections, such as vascular and urinary catheters [2, 3]. Ag NPs are also added to surgical instruments, prosthetic devices, and bone replacement materials [4–6].

The oral cavity is populated by a variety of microorganisms. The microbial communities in the oral cavity are polymicrobial and exist primarily as biofilms. These biofilms can be responsible for several local diseases, including periodontal and peri-implant diseases, which can lead to the

loss of teeth or implants, respectively, [7]. In fact, “peri-implantitis” remains one of the most serious complications after implant placement [8]. The potential of Ag NPs to reduce bacterial adhesion to dental implant surfaces and to prevent biofilm formation has been investigated by many authors [7, 9–12] with a view to reducing the risk of peri-implant infections.

Another interesting application of Ag NPs in dentistry is for the structural and surface modification of bone grafts and membranes with a view to preventing the risk of contamination and associated infection that are common when bone augmentation techniques such as guided bone regeneration (GBR) and guided tissue regeneration (GTR) are used [5, 13–17].

Despite the widespread use of Ag NPs, there is still a shortage of information on their biological effects on human cells and environments. Some authors have investigated the potential toxicity of Ag NPs in different cell

systems, including bacteria and mammalian cells [18–26]. Such studies have attributed the cytotoxicity of Ag NPs to several possible mechanisms, including the dissolving or release of Ag ions from the nanoparticles, the disruption of cell membrane integrity, oxidative stress, protein or DNA binding and damage, the generation of reactive oxygen species, and apoptotic cell death [27].

The toxic mechanism seems likely to depend on the nanoparticles' properties too, for example, surface area, size and shape, capping agent, surface charge, particle purity, structural distortion, and the bioavailability of the individual particles [24].

In the light of the above considerations, the aim of the present paper was to describe the antibacterial properties, bone biocompatibility and toxicity of Ag NPs incorporated in devices used for alveolar bone regeneration and in dental implants.

## 2. Alveolar Bone Surgery, Controlling Bacterial Infection and Ag NPs

**2.1. Periodontitis and Peri-Implantitis.** The most common infectious diseases in alveolar bone are periodontitis and peri-implantitis. Periodontitis is an inflammatory disease caused by infection of the supporting tissue around the teeth. Bacteria are essential to its onset, but not enough to cause the disease, which requires a susceptibility of the host to develop [28].

The prevalence of severe, generalized periodontitis ranges from 5% to 20% of any population, while mild-to-moderate periodontitis affects the majority of adults [28].

Peri-implant mucositis is an inflammatory lesion confined to the mucosa, while peri-implantitis also affects the supporting bone [29]. Peri-implantitis is seen in up to 43% of individuals with implants, and peri-implant mucositis in up to 50% [30].

Bone loss occurring after initial remodeling is assumed to be due mainly to bacterial infection. The bacterial biofilm forming on implant surfaces is no different from the one that forms on tooth surfaces, but it may be influenced by surface roughness [8]. The initial colonizers that adhere to tooth and implant surfaces include *Streptococcus oralis*, *Streptococcus sanguis*, and *Streptococcus mitis*. There is also a predominant component of Gram-negative species, such as *Eikenella corrodens*, *Veillonella atypica*, and *Prevotella loeschii*. Coaggregation bridges are common between these early colonizers and *Fusobacterium nucleatum*, which then coaggregates with many late colonizers, which are mostly Gram-negative and anaerobic, and include *Aggregatibacter actinomycetemcomitans*, *Porphyromonas gingivalis*, *Treponema denticola*, *Prevotella intermedia*, and *Tannerella forsythia* [31–33].

Treatments for periodontal and peri-implant diseases usually include local and systemic measures to combat the infection, and surgical treatment in certain cases to reduce the inflammation and the depth of the periodontal/peri-implant pockets, and restore healthy conditions for the soft and hard tissues surrounding the tooth/implant. In some

cases, regenerative techniques and materials are used in an effort to regenerate the periodontal or peri-implant soft and hard tissues. The success of such surgical bone regeneration procedures may be negatively affected by infections caused by oral microbia. Chiapasco and Zaniboni [17] conducted a systematic review on the clinical outcome of guided bone regeneration (GBR) procedures for correcting peri-implant dehiscences and fenestrations associated with implant placement. Peri-implant defects were treated with resorbable or nonresorbable membranes, with or without graft materials. In the postoperative period, 20% of the nonresorbable membranes and 5% of the resorbable ones became exposed and infected. In the studies considered, the membrane had to be removed in almost all cases of its exposure and infection, lowering the success rate of the GBR procedure.

**2.2. Ag NPs Antimicrobial Strategy.** Strategies for reducing bacterial adhesion to dental implants seem to be one of the main fields of interest in dental implantology. Ag NPs are among the products of nanotechnology already used in dental practice for their antimicrobial properties and incorporating them in implant coatings may inhibit biofilm formation on the implant surfaces and prevent dental implant failure [7, 9–12]. The use of Ag NPs has also been suggested to reduce the risk of infections after oral regenerative surgery. The presence of silver ions in scaffolds or membranes may prove a desirable measure for minimizing the risk of infections [5, 13–16].

Nanoparticles are routinely defined as particles in sizes ranging between around 1 and 100 nm, and with properties that are not found in bulkier samples of the same material. Nanoparticles have a greater surface-to-volume ratio (per unit of mass) than larger-scale particles of the same material, and are therefore more reactive. Particles smaller than 50 nm are subject to the laws of quantum physics [34].

Many new methods of synthesis have emerged and are being assessed for the purpose of Ag NP production for medical applications. A number of reports are available in the literature on the synthesis of Ag NPs: from the chemical reduction of silver ions by sodium citrate or sodium borohydride [35]; by reduction into reverse micelles [36]; using biological [37], electrochemical [38], or photochemical methods [39]; radiation [40], laser ablation [41], solvent reduction in the presence of surfactants [42], and sonochemical [43] methods.

There has recently been a renewed interest in the synthesis of organic-inorganic and inorganic-inorganic nanocomposite materials [44].

Nanotechnology is a rapidly-growing field, with nanoparticles being produced and used in a broad range of commercial products all over the world. Several products containing Ag NPs are already on the market. Over the years, the antibacterial activity exhibited by silver compounds and Ag NPs has resulted in their widespread use in bedding, washing machines, water purification, toothpaste, shampoo, nursing bottles, fabrics, deodorants, filters, kitchen utensils, toys, and humidifiers [45].

In particular, Ag NPs have lately emerged in a variety of biomedical applications exploiting their antibacterial

activity. They have proved to be important in improving wound healing, and, now that several pathogenic bacteria have become resistant to various antibiotics, they could be a safer alternative to conventional antimicrobial agents in topical antimicrobial formulations [1, 46].

Due to their antibacterial properties, Ag NPs are also useful for reducing bacterial adhesion and preventing biofilm formation on medical devices, such as catheters or dental implants, where a bacteria-killing activity is highly desirable [47–51].

$\text{Ag}^+$  ions and  $\text{Ag}^+$  salts have been used for decades as antimicrobial agents in various fields because of their growth-inhibiting effect on microorganisms, but they are of only limited use for a number of reasons—including the interfering effects of salts and the antimicrobial mechanism related to a continuous release of a sufficient concentration of  $\text{Ag}^+$  ion from the metal form—but such drawbacks can be overcome by using Ag NPs. It is essential, however, to be able to prepare the  $\text{Ag}^+$  with cost-effective methods and to understand the mechanism behind their antimicrobial effect [22].

**2.3. Ag NPs Mechanism of Action.** What gives silver its inhibitory effects on microorganisms is still not entirely clear, and further studies are needed to ascertain all of its properties.

Silver ions deactivate sulfhydryl enzymes when combined with amino, imidazole, carboxyl, and phosphate groups. They also affect DNA replication and stop mitosis in prokaryotes [52].

Some authors believe that silver's antimicrobial activity depends on its ions, which bind strongly to electron donor groups in biological molecules containing sulfur, oxygen, or nitrogen. This may result in defects in the bacterial cell wall, with a consequent loss of the cell's contents. A complex formed by silver ions and proteins may disturb the bacterial cells' metabolism and their power functions (such as permeability and respiration), leading to bacterial cell death. Silver ions can also interact with the DNA of bacteria, preventing cell reproduction [53, 54].

Silver interacts with sulfhydryl groups of proteins and DNA, altering hydrogen bonding, respiratory processes, DNA unwinding, cell wall synthesis, and cell division. It also induces denaturation and oxidization of the cell wall, leading to the rupture of the internal cell organelles, and thus resulting in bacterial cell death. Ag NPs also modulate the phosphotyrosine profile of putative bacterial peptides, which could affect bacterial signal transduction and inhibit the organisms' growth [55].

Ag NPs are known to have an antimicrobial activity against Gram-negative bacteria, creating “pits” in the wall of the bacteria. Amro et al. suggested that metal depletion may cause the formation of irregularly shaped pits in the outer membrane and change the membrane's permeability, which is due to the progressive release of lipopolysaccharide molecules and membrane proteins [56].

The specific bactericidal and antiadhesive efficacy of a hydroxyapatite/titania nanocomposite coating on titanium

plates on Gram-negative bacteria known to be periodontal and peri-implantitis pathogens, such as *Streptococcus mutans*, *Porphyromonas gingivalis*, and *Fusohacterium nucleatum* was tested by Mo et al. in 2007 [57]; they found that the bactericidal rate on Gram-negative bacteria reached almost 90% after 3 hours of anaerobic culturing. According to these authors, adding a suitable amount of  $\text{Ag}^+$  anatase  $\text{TiO}_2$  prompted a photocatalytic activity without UV light. The existence of  $\text{Ag}^+$  acted beneficially both on the photocatalytic oxidation of  $\text{TiO}_2$  and as a bactericide. The experimental group also showed am anti-adhesion ability to *S. mutans* and *P. gingivalis*. After 3 hours of incubation, there were hardly any bacterial cells on the nAg-HA/ $\text{TiO}_2$ -coated plates, unlike the situation in the control group.

Liao et al. [58] found that a Ti-AgNP surface had remarkable antibacterial and antiadhesive activities *in vitro* in relation to *Porphyromonas gingivalis* and *Actinobacillus actinomycetemcomitan*, which are two of the main culprits responsible for periodontal and peri-implant diseases. Flores et al. [59] also reported that a modified AgNP-Ti/ $\text{TiO}_2$  surface exhibited a good resistance to colonization by *Pseudomonas aeruginosa* *in vitro*.

Other studies investigated the effect of Ag NPs, mainly against *Escherichia coli* and *Staphylococcus aureus*. The Ag NPs' antimicrobial activity against *E. coli* was investigated by Sondi and Salopek-Sondi as a model of Gram-negative bacteria [23]. Their study confirmed that the *E. coli* cells were damaged, showing the formation of “pits” in the cell wall of the bacteria, while the Ag NPs were found to accumulate in the bacterial membrane. A membrane with these morphological features becomes significantly more permeable, resulting in cell death. The antibacterial activity and mechanism of action of Ag NPs on *Escherichia coli* were also investigated by Li et al. [60], who analyzed the growth, the permeability, and the morphology of the bacterial cells after treatment with Ag NPs. The experimental results indicated an inhibited growth of *E. coli* cells *in vitro*. Meanwhile, the Ag NPs prompted reducing sugar and protein leakage, and induced respiratory chain dehydrogenase inactivation, suggesting that they were able to disrupt the bacterial membranes' permeability. These results would indicate that Ag NPs may damage the structure of the bacterial cell membrane and inhibit the activity of some membrane enzymes, eventually causing the death of the *E. coli* bacteria.

Kim et al. [22] tested Ag NPs in three representative microorganisms, that is, yeast, *E. coli*, and *Staphylococcus aureus*. They found that yeast and *E. coli* growth was effectively inhibited. The Ag NPs' antimicrobial activity against yeast and *E. coli* was consistent with the findings reported by Sondi and Salopek-Sondi [23]. The inhibitory effect of Ag NPs was milder on *S. aureus* than on the other microorganisms, however, giving the impression that the antimicrobial effects of Ag NPs may be associated with the particular characteristics of certain bacterial species. Differences between bacterial species may influence their susceptibility to antibacterial agents.

Gram-positive and Gram-negative bacteria have differences in their membrane structures, the most distinctive

of which is the thickness of the peptidoglycan layer. The cell walls of Gram-positive species contain 3–20 times more peptidoglycan than those of Gram-negative bacteria. Since peptidoglycans are negatively charged, they probably bind some portion of the silver ions in the broth; this would make Gram-positive bacteria generally less susceptible to antibacterial agents containing silver ions than Gram-negative species [61].

Danilczuk et al. found that Ag<sup>+</sup> generated free radicals by means of an ESR (electron spin resonance) study on Ag NPs [62]. Kim et al. also observed an Ag<sup>+</sup>-specific ESR spectrum. The Ag NP peak they obtained in an ESR assay corresponded to the one obtained by Danilczuk et al. To clarify the relationship between free radical and antimicrobial activity, Kim et al. used the antioxidant N-acetylcysteine (NAC) to test whether the antioxidant could influence AgNP-induced antimicrobial activity. The results of ESR tests and antioxidant studies suggest that free radicals may derive from the surface of Ag NPs and be responsible for their antimicrobial activity in the experimental conditions considered [22].

Some researchers have reported that the positive charge on the Ag<sup>+</sup> ion is crucial for its antimicrobial activity through the electrostatic attraction between the microorganisms' negatively charged cell membrane and the positively charged nanoparticles [6].

The shape of Ag NPs may influence with their antimicrobial effect. Pal et al. [63] found that triangular Ag NPs had a greater biocidal action against *E. coli* than rod-shaped or spherical nanoparticles. The differences can be explained by the proportion of active facets on the nanoparticles of different shapes. An oriented particulate monolayer X-ray diffraction pattern indicated that triangular nanoparticles have more high-atom-density facets than other shapes, favoring the silver's reactivity. Pal et al. also speculated that the action of Ag NPs is broadly similar to that of silver ions. Sulfur-containing proteins in the membrane or in the cells, as well as phosphorus-containing elements such as DNA, are likely to be the preferential binding sites for Ag NPs.

Another factor that may influence the effectiveness of these particles' antimicrobial activity is their size. In the report from Baker et al. [64], the Ag NPs exhibited antibacterial effects at low concentrations these antibacterial properties correlated with the total surface area of the nanoparticles, that is, smaller particles with a larger surface-to-volume ratio provided a more efficient medium for antibacterial activity. The nanoparticles were found to be completely cytotoxic for *E. coli* at surface concentrations as low as 8 microg of Ag<sup>+</sup>/cm<sup>2</sup>.

In agreement with Baker et al., Panáček et al. [53] reported that the antibacterial activity of Ag NPs depended on the size of the silver particles: smaller particles with a larger surface area available for interaction had a greater bactericidal effect than larger particles.

Many studies investigated the antifungal activity of silver nanoparticles against the main fungi frequently found in the oral cavity, but further studies are needed in this area as regards the formulations and means of delivery [65–67].

TABLE 1: Synthesis of the various mechanisms of action of Ag<sup>+</sup> ions and Ag NPs.

Author, year	Action
Sondi and Salopek-Sondi, 2004 [23];	
Amro et al., 2000 [56];	Cell wall Pit formation
Li et al., 2010 [60];	
Kawahara et al., 2000 [61].	
Li et al., 2010 [60];	Protein binding
Pal et al., 2007 [63].	
Pal et al., 2007 [63].	DNA binding
Danilczuk et al., 2006 [62].	Free radicals formation

Ag NPs have also shown an antiviral potential, proving active against several types of virus, including *human immunodeficiency virus*, *hepatitis B virus*, *herpes simplex virus*, *respiratory syncytial virus*, and *monkeypox virus* [68].

A summary of the antimicrobial activities of Ag NPs is given in Table 1.

### 3. Ag NPs and Devices

The capacity of silver nanoparticles to control the formation of biofilms in the oral cavity, as a result of their antibacterial activity, has led to their use in prosthetic device coatings, as topical agents, and in dental materials. Several devices have recently been proposed for use in the fields of dental implantology, periodontology, and alveolar bone regeneration. The prevention of dental implant contamination by bacteria and the need for biocompatible scaffolds or membranes for use in bone grafts with antibacterial properties (achieved by including silver particles in the scaffold, while maintaining its structure and characteristics) seem to be interesting applications of Ag NPs. Below is a review of some of the devices in which Ag NPs have been used, for example, membranes for guided tissue regeneration (GTR) and guided bone regeneration (GBR) applications, scaffolds for bone regeneration, and dental implant coatings.

**3.1. Membranes.** Barrier membranes are devices used in GTR/GBR procedures to prevent the rapid ingrowth of fibroblasts and/or epithelial cells in a bony defect where slower-growing bone tissue is desired. Barrier membranes thus keep out the unwanted soft tissues and provide a secluded space into which osteogenic cells can migrate and form new bone.

Over the years, numerous resorbable and nonresorbable membranes have been used for GTR and GBR applications [69, 70], but they have been unable to reduce the risk of graft infection, especially when the membranes are exposed to the oral cavity. Antimicrobial membranes have been developed to overcome this problem.

Li et al. [14] analyzed a silver ion-substituted nanohydroxyapatite, titania nanoparticles, and polyamide 66 (Ag-nHA/TiO<sub>2</sub>/PA66) membrane, prepared with the intent of producing an antimicrobial membrane with a gradient porous structure for GBR with good mechanical properties,

biocompatibility, and antimicrobial activity. Cytocompatibility and bone formation were assessed by both *in vitro* and animal experiments. *In vitro* assays were carried out with osteoblastlike cells (MG63), and cell viability, alkaline phosphatase activity (ALP), and morphology of cells cultured on the membrane were ascertained, demonstrating good cell affinity and an increased cell attachment, migration, and proliferation. *In vivo* experiments resulted in the complete closure of 5-mm bone defects created in the skull of Sprague-Dawley rats 8 weeks after implantation. The same capabilities were seen for the nHA/PA66 membrane, whereas the cranial defects were still not fully covered by newly formed bone 8 weeks after implantation of the PA66 or empty membranes.

Ye et al. [16] studied the effects of the Ag-nHA-nTiO<sub>2</sub>/PA66 membrane on MG63 osteoblastlike cells *in vitro*; nHA/PA66 and expanded polytetrafluoroethylene (e-PTFE) membranes were used for control purposes in their assays. The authors found that the Ag-nHA-nTiO<sub>2</sub>/PA66 membrane had no negative effects on the growth of osteoblastlike cells, while it favored cell adhesion, thus indicating an excellent tissue compatibility.

Consistently with the previous article, the same group of researchers found that the osteogenic activity of Ag-nHA-nTiO<sub>2</sub>/PA66 membranes was comparable with that of conventional e-PTFE membranes in a rat model, proving to be a safe strategy for reducing inflammatory response and enhancing bone regeneration, and thus suggesting interesting prospects for further research and the development in antibacterial GBR membranes [71].

The above findings are summarized in Table 2.

**3.2. Scaffolds for Bone Regeneration.** Bone augmentation procedures have entailed the use of different methods, including GBR and GTR techniques. Especially in nonspace-making defects, the use of grafts (autografts, allografts, xenografts, or alloplasts) prevents membrane collapse, and the graft provides a scaffold on which bone cells can adhere, migrate, grow, and divide, forming new bone. A suitably macroporous structure is important to ensure rapid vascularization, bone ingrowth and—especially in the case of implant placement—bone remodeling, with newly formed bone occupying the site previously taken up by the scaffold [73].

To enhance the regeneration of new bone and reduce the healing time, bone tissue engineering relies on 3-dimensional scaffolds delivering biofactors to assist bone regeneration. In addition to facilitating new bone deposition, some authors are interested in producing osteoconductive scaffolds with bactericidal properties with a view to controlling infection after alveolar bone surgery.

Wu et al. [13] demonstrated that the Ag-nHA/TiO<sub>2</sub>/PA66 antimicrobial scaffold they developed had a highly porous structure that would be effective for the sustained Ag<sup>+</sup> release at the bone-implant interface. According to the authors, these scaffolds would provide good mechanical support and protection for cell adhesion, migration and proliferation, and hold promise in clinical application in bone augmentation techniques.

Saravanan et al. [5] analyzed the *in vitro* antimicrobial activity of another biocomposite bone tissue engineering

scaffold containing chitosan/nanohydroxyapatite/nanosilver (CS/nHAp/nAg). The results suggested that CS/nHAp/nAg biocomposite scaffolds have the potential for controlling implant-associated bacterial infection during bone reconstruction surgery thanks to the strong antibacterial activity seen on testing the prepared scaffolds with Gram-positive (*S. aureus*) and Gram-negative (*E. coli*) bacterial strains. The CS/nHAp/nAg scaffolds were also found non-toxic for rat osteoprogenitor cells and human osteosarcoma cell lines.

Finally, Schneider et al. [15] assessed the *in vivo* performance in sheep of synthetic, cotton woollike nanocomposites consisting of a biodegradable poly(lactide-co-glycolide) fibrous matrix containing silver-doped calcium phosphate nanoparticles (PLGA/Ag-CaP). The area of new bone formation measured histomorphometrically 8 weeks after implantation was very similar for the PLGA/CaP (control) and the PLGA/Ag-CaP. In fact, the highly porous PLGA/Ag-CaP scaffolds enabled an efficient cell ingrowth, which facilitated new bone formation everywhere inside the former defect, and also led to the resorption of the biodegradable polymer fibers. No signs of any inflammatory reaction were detected.

These data are summarized in Table 3.

**3.3. Dental Implant Surfaces.** Peri-implantitis remains one of the most serious complications in dental implant surgery and sometimes necessitates implant removal. In fact, the success and long-term survival of dental implants depend not only on bone-implant osteointegration, but also on the prevention of bacterial infection after placement. Incorporating Ag NPs in implant coatings may inhibit biofilm formation on the surfaces and prevent dental implant failure.

Secinti et al. [74] investigated whether Ag NP coatings could inhibit biofilm formation even in slime-forming bacteria; 20 New Zealand rabbits were randomly divided into two equal groups and had bacteria applied to surgical sites on the iliac crests: screws coated with silver using the sol-gel method were inserted in the rabbits in Group I, uncoated Ti screws in the rabbits in Group II. The rabbits were sacrificed after 28 days, and the screws and adjacent bone were examined under transmission (TEM) and scanning electron microscopy (SEM). The antibacterial effect of Ag NPs was also confirmed microbiologically. All silver-coated screws, but only 10% of the uncoated titanium screws, were sterile. Biofilm formation was inhibited on all the silver-coated screws, whereas all the uncoated screws developed a biofilm on their surfaces. These findings suggest that AgNP-coated screws are as safe as uncoated titanium screws and that the coating helps to prevent both biofilm formation and infection.

A recent report from Flores et al. [59] describes a method for modifying Ti/TiO<sub>2</sub> surfaces with citrate-capped Ag NPs. The nanoparticles spontaneously adsorb on the Ti/TiO<sub>2</sub>, forming nanometer-sized aggregates consisting of individual Ag NPs that evenly cover the surface. The modified AgNP-Ti/TiO<sub>2</sub> surface exhibits a good resistance to colonization by *Pseudomonas aeruginosa*, a model of biofilm formation.

Ionita et al. [11] demonstrated the synergistic antibacterial effect of a HA-silver coating with Ag NPs by comparing the behavior of such a coating with uncoated samples, and

TABLE 2: Studies about membranes containing Ag NPs proposed in alveolar bone regenerative surgery.

Author, year	Type of study	Device	Description of Ag NPs included	Main results
Podsiadlo et al., 2005 [72]	<i>In vitro</i>	Layer-by-layer assembly of nacre-like nanostructured composites with antimicrobial properties.	Ag NPs	(i) Excellent structural stability with no detectable levels of silver lost over a 1 month period (ii) Almost complete growth inhibition of <i>E. coli</i> over an 18 h period. (iii) Biocompatibility with the human osteoblast cell line
Li et al., 2012 [14]	<i>In vitro. In vivo</i> (animal)	Antimicrobial composite membrane with an asymmetric porous structure	Ag-nHA/TiO <sub>2</sub> /PA66	(i) <i>In vitro</i> : good cell (osteoblast-like cells) affinity and increase of cell attachment, migration, and proliferation. (ii) <i>In vivo</i> : complete closure of 5-mm bone defects created in the skull of Sprague-Dawley rats after 8 weeks of implantation.
Ye et al., 2011 [16]	<i>In vitro</i>	Ag-nHA-nTiO <sub>2</sub> /PA66 membrane	Ag-nHA-nTiO <sub>2</sub> /PA66	(i) No negative effects on growth of osteoblast-like cells. (ii) Loose porous structure of the membrane helped the adhesion and proliferation of osteoblast-like cells.
Zhang et al., 2010 [71]	<i>In vivo</i> (animal)	Ag-nHA-nTiO <sub>2</sub> /PA66 membrane	Ag-nHA-nTiO <sub>2</sub> /PA66	(i) Osteogenic activity comparable with e-PTFE.

TABLE 3: Studies about scaffolds containing Ag NPs proposed in alveolar bone regenerative surgery.

Author, year	Type of study	Device	Description of Ag NPs included	Main results
Wu et al., 2010 [13]	<i>In vitro</i>	Antimicrobial composite scaffolds	Ag-nHA/TiO <sub>2</sub> /PA66	(i) Ag <sup>+</sup> release: time and concentration dependent. (ii) Ag <sup>+</sup> release properties influenced by the immersion medium.
Saravanan et al., 2011 [5]	<i>In vitro</i>	Bio-composite scaffold for bone tissue engineering	Chitosan/nano-hydroxyapatite/nano-silver	(i) Antibacterial activity against both Gram-positive and Gram-negative bacteria. (ii) Non-toxic to rat osteoprogenitor cells and human osteosarcoma cell line.
Schneider et al., 2011 [15]	<i>In vivo</i> , animal	Cotton wool-like flexible artificial bone substitutes	PLGA/Ag-CaP	(i) Bone formation was not negatively influenced by the 0.4% silver. (ii) Area fraction of new bone in formation after 8 weeks implantation in hole defects of long bone in sheep was very similar for PLGA/CaP and PLGA/Ag-CaP.

with samples covered with Ag NPs or hydroxyapatite (HA), or incorporating an antibiotic (Tobrex). The bacteriological experiments performed *in vitro* demonstrated the efficacy of the silver-coated TiAlZr implants against *E. coli* bacterial growth. The hydrophilic nature of the coatings investigated increased in the same direction percentage inhibition. The

antibacterial effect of the biomimetic coating with Ag NPs was high and similar to that of a biomimetic coating with Ag NPs and antibiotic.

Zhao et al. [9] reviewed the current status of antibacterial coatings on titanium implants, acknowledging that *in vivo* data on these antibacterial coatings were still scarce and that

surfaces with both an excellent tissue-integrating ability and good antibacterial properties should be explored.

In a recent study by the same authors [10], titania nanotubes ( $\text{TiO}_2$ -NTs) incorporated with Ag NPs were fabricated on Ti implants for the purpose of preventing implant-associated infections. The amount of  $\text{Ag}^+$  introduced in the NTs was varied by adjusting the processing parameters. The authors noted *in vitro* that the NT-Ag killed all the planktonic bacteria in the suspension over the first few days, retaining this ability with no obvious decline for 30 days, which would normally be long enough to prevent postoperative infection in the early and intermediate stages and possibly even late infection around the implant. Although the NT-Ag samples showed some cytotoxicity, this could be contained by controlling the  $\text{Ag}^+$  release rate, and the properties could be further tailored to achieve both long-term antibacterial ability and biointegration.

As mentioned earlier, Mo et al. [57] evaluated the bactericidal and antiadhesive efficacy of rough-surfaced titanium plates coated with silver-hydroxyapatite/titania nanocomposites (nAg-HA/ $\text{TiO}_2$ ) in combating oral bacteria, and particularly Gram-negative bacteria, which are known periodontal pathogens and involved in the etiology of peri-implantitis (*Porphyromonas gingivalis*, *Fusobacterium nucleatum*, and *Streptococcus mutans*). The viability of each type of bacteria on the antibacterial film was suppressed to about 10% after anaerobic incubation for 3 hours. Adherence of the bacteria to the nAg-HA/ $\text{TiO}_2$ -coated surfaces was considerably lower than for the uncoated surfaces.

Liao et al. [12] investigated AgNP-modified titanium (Ti-AgNP) surfaces using a silanization method and demonstrated that titanium (Ti) plates with Ag NPs deposited on them acquired an antibacterial activity. After 24 hours of incubation, 94% of *Staphylococcus aureus* and more than 95% of *Escherichia coli* were killed on the Ti-AgNP surface. SEM examination of the antiadhesive properties also showed that there were fewer bacteria attached to the Ti-AgNP surface than to an untreated Ti control surface.

Since dental implants, being used in the oral cavity, should also have an antibacterial activity in relation to oral bacteria, Liao et al. [58] also tested the antibacterial and antiadhesive action of a silver nanoparticle-modified titanium (Ti-AgNP) surface in relation to two of the most common periodontal pathogens, that is, *Porphyromonas gingivalis* and *Actinobacillus actinomycetemcomitans*. Their findings indicate that the Ti-AgNP surface had remarkable anti-bacterial and antiadhesive effects on *P. gingivalis* and *A. actinomycetemcomitans*, suggesting that Ti-AgNP is a promising implantable biomaterial in terms of its antibacterial properties. The Ti surfaces modified with Ag NPs also showed no signs of cytotoxicity on cultured human gingival fibroblasts (hGFs), suggesting their potential application also in transgingival abutments, which are an important doorway for bacteria.

Implants are in contact not only with bone but also with gingival tissues, and are partially exposed to the oral cavity. With a view to the rapid achievement of a firm soft tissue seal around dental implants that can resist bacterial invasion, Ma et al. [75] created a surface with a lower

cytotoxicity while preserving its antibacterial properties by modifying the Ti surface, immobilizing the AgNP/FGF-2 (fibroblast growth factor 2) compound's bioactive factors on a titania nanotube surface. The immobilized AgNP/FGF-2 samples displayed an excellent cytocompatibility, negligible cytotoxicity, and enhanced hFGF functions such as cell attachment, proliferation, and ECM-related gene expression. The absence of any significant cytotoxicity may be due to the negligible amounts of  $\text{Ag}^+$  ions released by the Ag NP solution, and, as Williams et al. demonstrated [76], small concentrations of  $\text{Ag}^+$  released into the extracts are not cytotoxic. The Ag NPs also exhibited some bioactivity. These results lead to the same conclusions as the previous paper and encourage the use of this material in dental implant abutments.

The data presented above are summarized in Table 4.

#### 4. Ag NP Toxicity

The impact of Ag NPs on cell viability has been investigated to establish the feasibility of their use in clinical applications. Several studies have been performed *in vitro* (on osteoblasts and other cell lines), and *in vivo* (in animal models) for this purpose.

**4.1. In Vitro Studies.** Mahmood et al. [77] reported on the *in vitro* effects of different types of nanomaterial (single-walled carbon nanotubes—SWCNTs, hydroxyapatite nanoparticles—HAP, titanium dioxide nanoparticles— $\text{TiO}_2$ , and silver nanoparticles—Ag NPs) on cell calcification and mineralization by bone cells. The greatest of cell mineralization enhancement coincided with the use of Ag NPs, followed by HAP,  $\text{TiO}_2$  and SWCNTs. Ag NPs were found to alter microRNA expression; the numerous transcriptional factors associated with bone formation (Runx2, Dlx3, and Msx2) were affected by correspondent miRNAs only in the bone cells exposed to Ag NPs. Exposure to Ag NPs also resulted in the miRNA regulation of several gene-target BMPs not found in the controls. The authors also said that preliminary cytotoxicity studies performed with the nanoparticle concentrations used in the experiments gave no indication of any onset of cytotoxic effects.

Studying layer-by-layer (LBL) assemblies of nacrelike nanostructured composites containing Ag NPs, Podsiadlo et al. [72] also reported finding no detectable levels *in vitro* of silver being lost over a 1-month period, associated with a bactericidal effect (*E. coli* growth was almost completely inhibited over an 18 h period), and the concentration of silver did not prevent the growth of mammalian tissue cultures. The LBL composite showed biocompatibility with human osteoblast cell lines.

On the other hand, Zhao et al. [10] found *in vitro* that titania nanotubes ( $\text{TiO}_2$ -NTs) incorporating Ag NPs showed some cytotoxicity in primary rat osteoblasts, which could be reduced by controlling the rate of  $\text{Ag}^+$  release.

Albers et al. [78] investigated the cytotoxicity of Ag NPs (50 nm) *in vitro* on osteoblasts (OBs) and osteoclasts (OCs) at antibacterial concentrations: they demonstrated that Ag

TABLE 4: Studies about dental implants surfaces containing Ag NPs.

Author, year	Type of study	Device	Description of Ag NPs included	Main results
Zhao et al., 2011 [10]	<i>In vitro</i>	Coatings for titanium implants	Titania nanotubes ( $TiO_2$ -NTs) incorporated with Ag NPs.	(i) The NT-Ag structure shows some cytotoxicity, that can be reduced by controlling the $Ag^+$ release rate. (ii) Long-term antibacterial ability. Satisfactory osteoconductivity (osteoblast from rat calvarial bone).
Secinti et al., 2011 [74]	<i>In vivo, animal</i>	Coatings on titanium implants	Ag NPs	(i) Biofilm formation inhibition. (ii) Nontoxic, and no harmful side effects detected on the kidney, liver, brain, or cornea.
Ionita et al., 2011 [11]	<i>In vitro</i>	Coatings on titanium implants	Ag NPs-HA/TiAlZr	(i) Inhibition of growth of <i>E. coli</i> bacteria. (ii) Antibacterial effect of biomimetic coating with Ag NPs is high and close to value of biomimetic coating with silver and antibiotic (Tobrex).
Liao et al., 2010 [12]	<i>In vitro</i>	Coatings on titanium implants	Ag NPs	(i) Ti-Ag NPs specimens significantly inhibited the growth of both <i>Staphylococcus aureus</i> and <i>Escherichia coli</i> than Ti-polished specimen.
Liao et al., 2010 [58]	<i>In vitro</i>	Antibacterial titanium plate	Ag NPs	(i) Ti-Ag NPs surface: remarkable antibacterial and antiadhesive activities to <i>Porphyromonas gingivalis</i> and <i>Actinobacillus actinomycetemcomitans</i> . (ii) No detectable cytotoxicity on cultured human gingival fibroblasts (hFGFs).
Ma et al., 2011 [75]	<i>In vitro</i>	Modified titanium implant surface	$TiO_2$ nanotubular surface with immobilized compound Ag/FGF-2 (fibroblast growth factor-2)	(i) The $TiO_2$ nanotubular surface with immobilized compound Ag/FGF-2 has excellent cytocompatibility compared to pure Ti.
Flores et al., 2010 [59]	<i>In vitro</i>	Coatings on titanium implants	Ag NPs spontaneously adsorb on Ti/ $TiO_2$	(i) Good resistance to colonization by <i>Pseudomonas aeruginosa</i> .
Mo et al., 2007 [57]	<i>In vitro</i>	Coatings on titanium plates	Ag-HA/ $TiO_2$	(i) Antibacterial activity against: <i>Porphyromonas gingivalis</i> , <i>Prevotella intermedia</i> , <i>Fusohacterium nucleatum</i> , and <i>Streptococcus mutans</i> .

NPs had cytotoxic effects on both cell lines, as indicated by dose-dependent decreases in the number of viable cells and differentiations. The inhibitory activity of microparticles of silver ( $3\text{ }\mu\text{m}$ ) was significantly weaker, a finding consistent with the results of previous studies [79–81]. According to these authors, the size-dependent cytotoxicity is due to the size- and surface-area-dependent release of silver ions from the particles. OBs were found more susceptible to the AgNP-mediated inhibition of cell viability and differentiation than OCs; both OBs and OCs were more susceptible to silver treatment than *S. epidermidis*. The MICs of  $\text{Ag}^+$  deriving from  $\text{AgNO}_3$  or Ag NPs used to inhibit bacterial growth were 2–4 times higher than the minimal  $\text{Ag}^+$  concentration needed to reduce the viability and proliferation of OBs and OCs. Finally, Albers et al. confirmed the antimicrobial properties of Ag NPs on *S. epidermidis*, but they were critical regarding the biological safety of silver-releasing implantable materials.

Suresh et al. [27] also found that Ag NPs caused cell-dependent cytotoxicity: their data emphasized the role of surface coatings or surface charges and particle aggregation in dictating the cytotoxicity of Ag NPs, but also showed that the cell type influenced their cytotoxic effect. Lung epithelial cells were more resistant than macrophages to the differently surface-coated Ag NPs being tested.

The results obtained by Greulich et al. [82] confirmed a cell-specific uptake of Ag NPs by peripheral blood mononuclear cells (PBMC) and accordingly different cellular responses after the exposure of monocytes and lymphocytes (T cells).

Ag NPs revealed no detectable cytotoxicity on cultured human gingival fibroblasts (hGFGs) *in vitro* [58, 75].

**4.2. In Vivo Studies.** Other studies have raised concerns regarding the safety of silver applications in animal models.

Hyun et al. [83] investigated the effects of repeated exposure to Ag NPs on the histological structure and mucins of the nasal respiratory mucosa: rats were exposed to different concentrations of silver nanoparticles in an inhalation chamber for 6 hours a day, 5 times a week for 28 days, after which the animals were sacrificed. The study indicated that the silver nanoparticles influenced the neutral mucins in the respiratory mucosa, but not to a toxicologically significant degree.

Kim et al. [84] found some significant dose-dependent changes in the alkaline phosphatase and cholesterol levels in male and female rats, which seemed to indicate that exposure to more than 300 mg of Ag NPs might result in mild liver damage. Ag NPs were found to induce no genetic toxicity in male or female rat bone marrow *in vivo*.

In their *in vivo* study, Secinti et al. [74] investigated the antibacterial effect of silver-coated titanium implants in rabbits, examining their liver, kidney, brain and cornea under transmission (TEM), and scanning electron microscopy (SEM). They detected no harmful side effects in these rabbit organs after the placement of Ag NPs coated screws.

## 5. Conclusions

Ag NPs have been studied as an alternative strategy for reducing bacterial adhesion and preventing biofilm formation thanks to their antimicrobial properties. Ag NPs have been included in devices used in alveolar bone surgery with promising results.

Membranes and scaffolds for bone regeneration containing Ag NPs have the potential to reduce the incidence of postoperative bacterial contamination. One of the most interesting applications of Ag NPs in dentistry is for preventing or delaying peri-implantitis. Ag NP coatings could be applied to the whole dental implant surface or to selected areas, such as the most coronal area of the implant or the inner threaded surface. Another strategy to reduce biofilm formation on dental implants and the related prosthetic components in the oral cavity might be to apply Ag NPs to prosthetic devices such as the healing screws, abutments, and fixing screws.

Published data highlight the importance of surface coatings, surface charge, speed of release, concentration of  $\text{Ag}^+$ , and particle aggregation in dictating the cytotoxicity of Ag NPs, which also seems to depend on the type of cell affected.

Reproducibility issues arising from the type of Ag NP application, the tests conducted and the subjects involved (cell lines or animals) have made any comparison of the results reported in different studies arduous or controversial. For the time being, most of the studies analyzed here were conducted *in vitro*, and there is a clear need for further clinical trials. *In vitro*, and animal studies are needed on the devices described, focusing particularly on the oral microbiota responsible for periodontal and peri-implant diseases.

## Conflict of Interests

The authors confirm that there is no conflicts of interests.

## References

- [1] K. Madhumathi, P. T. Sudheesh Kumar, S. Abhilash et al., "Development of novel chitin/nanosilver composite scaffolds for wound dressing applications," *Journal of Materials Science*, vol. 21, no. 2, pp. 807–813, 2010.
- [2] K. N. J. Stevens, O. Crespo-Biel, E. E. M. van den Bosch et al., "The relationship between the antimicrobial effect of catheter coatings containing silver nanoparticles and the coagulation of contacting blood," *Biomaterials*, vol. 30, no. 22, pp. 3682–3690, 2009.
- [3] M. A. Syed, S. Babar, A. S. Bhatti, and H. Bokhari, "Antibacterial effects of silver nanoparticles on the bacterial strains isolated from catheterized urinary tract infection cases," *Journal of Biomedical Nanotechnology*, vol. 5, no. 2, pp. 209–214, 2009.
- [4] M. S. Cohen, J. M. Stern, A. J. Vanni et al., "In vitro analysis of a nanocrystalline silver-coated surgical mesh," *Surgical Infections*, vol. 8, no. 3, pp. 397–404, 2007.
- [5] S. Saravanan, S. Nethala, S. Pattnaik, A. Tripathi, A. Moorthi, and N. Selvamurugan, "Preparation, characterization and

- antimicrobial activity of a bio-composite scaffold containing chitosan/nano-hydroxyapatite/nano-silver for bone tissue engineering,” *International Journal of Biological Macromolecules*, vol. 49, no. 2, pp. 188–193, 2011.
- [6] D. R. Monteiro, L. F. Gorup, A. S. Takamiya, A. C. Ruvollo-Filho, E. R. de Camargo, and D. B. Barbosa, “The growing importance of materials that prevent microbial adhesion: antimicrobial effect of medical devices containing silver,” *International Journal of Antimicrobial Agents*, vol. 34, no. 2, pp. 103–110, 2009.
- [7] R. P. Allaker, “The use of nanoparticles to control oral biofilm formation,” *Journal of Dental Research*, vol. 89, no. 11, pp. 1175–1186, 2010.
- [8] N. P. Lang and T. Berglundh, “Periimplant diseases: where are we now?—consensus of the Seventh European Workshop on Periodontology,” *Journal of Clinical Periodontology*, vol. 38, no. 11, pp. 178–181, 2011.
- [9] L. Zhao, P. K. Chu, Y. Zhang, and Z. Wu, “Antibacterial coatings on titanium implants,” *Journal of Biomedical Materials Research*, vol. 91, no. 1, pp. 470–480, 2009.
- [10] L. Zhao, H. Wang, K. Huo et al., “Antibacterial nanostructured titania coating incorporated with silver nanoparticles,” *Biomaterials*, vol. 32, no. 24, pp. 5706–5716, 2011.
- [11] D. Ionita, M. Grecu, C. Ungureanu, and I. Demetrescu, “Antimicrobial activity of the surface coatings on TiAlZr implant biomaterial,” *Journal of Bioscience and Bioengineering*, vol. 112, no. 6, pp. 630–634, 2011.
- [12] J. Liao, Z. Zhu, A. Mo, L. Li, and J. Zhang, “Deposition of silver nanoparticles on titanium surface for antibacterial effect,” *International Journal of Nanomedicine*, vol. 5, no. 1, pp. 261–267, 2010.
- [13] X. Wu, J. Li, L. Wang, D. Huang, Y. Zuo, and Y. Li, “The release properties of silver ions from Ag-nHAs/TiO<sub>2</sub>/PA66 antimicrobial composite scaffolds,” *Biomedical Materials*, vol. 5, no. 4, Article ID 044105, 2010.
- [14] J. Li, Y. Zuo, Y. Man et al., “Fabrication and biocompatibility of an antimicrobial composite membrane with an asymmetric porous structure,” *Journal of Biomaterials Science*, vol. 23, no. 1–4, pp. 81–96, 2012.
- [15] O. D. Schneider, D. Mohn, R. Fuhrer et al., “Biocompatibility and bone formation of flexible, cotton wool-like PLGA/calcium phosphate nanocomposites in sheep,” *The Open Orthopaedics Journal*, vol. 5, pp. 63–71, 2011.
- [16] J. Ye, Q. Yao, A. Mo et al., “Effects of an antibacterial membrane on osteoblast-like cells in vitro,” *International journal of nanomedicine*, vol. 6, pp. 1853–1861, 2011.
- [17] M. Chiapasco and M. Zaniboni, “Clinical outcomes of GBR procedures to correct peri-implant dehiscences and fenestrations: a systematic review,” *Clinical Oral Implants Research*, vol. 20, pp. 113–123, 2009.
- [18] P. V. AshaRani, G. L. K. Mun, M. P. Hande, and S. Valiyaveettill, “Cytotoxicity and genotoxicity of silver nanoparticles in human cells,” *ACS Nano*, vol. 3, no. 2, pp. 279–290, 2009.
- [19] H. J. Johnston, G. Hutchison, F. M. Christensen, S. Peters, S. Hankin, and V. Stone, “A review of the in vivo and in vitro toxicity of silver and gold particulates: particle attributes and biological mechanisms responsible for the observed toxicity,” *Critical Reviews in Toxicology*, vol. 40, no. 4, pp. 328–346, 2010.
- [20] Y. Li, D. H. Chen, J. Yan et al., “Genotoxicity of silver nanoparticles evaluated using the Ames test and in vitro micronucleus assay,” *Mutation Research/Genetic Toxicology and Environmental Mutagenesis*, vol. 745, no. 1–2, pp. 4–10, 2012.
- [21] C. Greulich, J. Diendorf, T. Simon, G. Eggeler, M. Epple, and M. Köller, “Uptake and intracellular distribution of silver nanoparticles in human mesenchymal stem cells,” *Acta Biomaterialia*, vol. 7, no. 1, pp. 347–354, 2011.
- [22] J. S. Kim, E. Kuk, K. N. Yu et al., “Antimicrobial effects of silver nanoparticles,” *Nanomedicine*, vol. 3, no. 1, pp. 95–101, 2007.
- [23] I. Sondi and B. Salopek-Sondi, “Silver nanoparticles as antimicrobial agent: a case study on *E. coli* as a model for Gram-negative bacteria,” *Journal of Colloid and Interface Science*, vol. 275, no. 1, pp. 177–182, 2004.
- [24] A. K. Suresh, D. A. Pelletier, W. Wang et al., “Silver nanocrystallites: biofabrication using *shewanella oneidensis*, and an evaluation of their comparative toxicity on gram-negative and gram-positive bacteria,” *Environmental Science & Technology*, vol. 44, no. 13, pp. 5210–5215, 2010.
- [25] M. Ahamed, M. Karns, M. Goodson et al., “DNA damage response to different surface chemistry of silver nanoparticles in mammalian cells,” *Toxicology and Applied Pharmacology*, vol. 233, no. 3, pp. 404–410, 2008.
- [26] M. Ahamed, M. S. AlSalhi, and M. K. J. Siddiqui, “Silver nanoparticle applications and human health,” *Clinica Chimica Acta*, vol. 411, no. 23–24, pp. 1841–1848, 2010.
- [27] A. K. Suresh, D. A. Pelletier, W. Wang, J. L. Morrell-Falvey, B. Gu, and M. J. Doktycz, “Cytotoxicity induced by engineered silver nanocrystallites is dependent on surface coatings and cell types,” *Langmuir*, vol. 28, no. 5, pp. 2727–2735, 2012.
- [28] B. Burt, “Position paper: epidemiology of periodontal diseases,” *Journal of Periodontology*, vol. 76, no. 8, pp. 1406–1419, 2005.
- [29] J. Lindhe and J. Meyle, “Peri-implant diseases: consensus Report of the Sixth European Workshop on Periodontology,” *Journal of Clinical Periodontology*, vol. 35, supplement 8, pp. 282–285, 2008.
- [30] N. U. Zitzmann and T. Berglundh, “Definition and prevalence of peri-implant diseases,” *Journal of Clinical Periodontology*, vol. 35, no. 8, pp. 286–291, 2008.
- [31] S. S. Socransky and A. D. Haffajee, “Periodontal microbial ecology,” *Periodontology 2000*, vol. 38, pp. 135–187, 2005.
- [32] S. S. Socransky, C. Smith, and A. D. Haffajee, “Subgingival microbial profiles in refractory periodontal disease,” *Journal of Clinical Periodontology*, vol. 29, no. 3, pp. 260–268, 2002.
- [33] P. E. Kolenbrander, R. J. Palmer, A. H. Rickard, N. S. Jakubovics, N. I. Chalmers, and P. I. Diaz, “Bacterial interactions and successions during plaque development,” *Periodontology 2000*, vol. 42, no. 1, pp. 47–79, 2006.
- [34] M. Auffan, J. Rose, J. Y. Bottino, G. V. Lowry, J. P. Jolivet, and M. R. Wiesner, “Towards a definition of inorganic nanoparticles from an environmental, health and safety perspective,” *Nature Nanotechnology*, vol. 4, no. 10, pp. 634–641, 2009.
- [35] P. V. Kamat, M. Flumiani, and G. V. Hartland, “Picosecond dynamics of silver nanoclusters. Photoejection of electrons and fragmentation,” *The Journal of Physical Chemistry B*, vol. 102, no. 17, pp. 3123–3128, 1998.
- [36] A. Taleb, C. Petit, and M. P. Pilani, “Synthesis of highly monodisperse silver nanoparticles from AOT reverse micelles: a way to 2D and 3D self-organization,” *Chemistry of Materials*, vol. 9, no. 4, pp. 950–959, 1997.
- [37] R. R. Naik, S. J. Stringer, G. Agarwal, S. E. Jones, and M. O. Stone, “Biomimetic synthesis and patterning of silver nanoparticles,” *Nature Materials*, vol. 1, no. 3, pp. 169–172, 2002.
- [38] L. Rodríguez-Sánchez, M. C. Blanco, and M. A. López-Quintela, “Electrochemical synthesis of silver nanoparticles,”

- The Journal of Physical Chemistry B*, vol. 104, no. 41, pp. 9683–9688, 2000.
- [39] H. H. Huang, X. P. Ni, G. L. Loy et al., “Photochemical formation of silver nanoparticles in poly(N-vinylpyrrolidone),” *Langmuir*, vol. 12, no. 4, pp. 909–912, 1996.
- [40] N. M. Dimitrijevic, D. M. Bartels, C. D. Jonah, K. Takahashi, and T. Rajh, “Radiolytically induced formation and optical absorption spectra of colloidal silver nanoparticles in supercritical ethane,” *Journal of Physical Chemistry B*, vol. 105, no. 5, pp. 954–959, 2001.
- [41] F. Mafuné, J. Y. Kohno, Y. Takeda, and T. Kondow, “Structure and stability of silver nanoparticles in aqueous solution produced by laser ablation,” *Journal of Physical Chemistry B*, vol. 104, no. 35, pp. 8336–8337, 2000.
- [42] G. Rodríguez-Gattorno, D. Díaz, L. Rendón, and G. O. Hernández-Segura, “Metallic nanoparticles from spontaneous reduction of silver(I) in DMSO. Interaction between nitric oxide and silver nanoparticles,” *Journal of Physical Chemistry B*, vol. 106, no. 10, pp. 2482–2487, 2002.
- [43] V. G. Pol, D. N. Srivastava, O. Palchik et al., “Sonochemical deposition of silver nanoparticles on silica spheres,” *Langmuir*, vol. 18, no. 8, pp. 3352–3357, 2002.
- [44] S. K. Arumugam, T. P. Sastry, B. Sreedhar, and A. B. Mandal, “One step synthesis of silver nanorods by autoreduction of aqueous silver ions with hydroxyapatite: an inorganic-inorganic hybrid nanocomposite,” *Journal of Biomedical Materials Research*, vol. 80, no. 2, pp. 391–398, 2007.
- [45] A. D. Maynard, *Nanotechnology: a research strategy for addressing risk*, PEN 03. Washington DC: Woodrow Wilson International Center for Scholars, Project on Emerging Nanotechnologies, 2006.
- [46] J. Jain, S. Arora, J. M. Rajwade, P. Omray, S. Khandelwal, and K. M. Paknikar, “Silver nanoparticles in therapeutics: development of an antimicrobial gel formulation for topical use,” *Molecular Pharmaceutics*, vol. 6, no. 5, pp. 1388–1401, 2009.
- [47] H. Cao and X. Liu, “Silver nanoparticles-modified films versus biomedical device-associated infections,” *Wiley Interdisciplinary Reviews*, vol. 2, no. 6, pp. 670–684, 2010.
- [48] K. Chaloupka, Y. Malam, and A. M. Seifalian, “Nanosilver as a new generation of nanoproduct in biomedical applications,” *Trends in Biotechnology*, vol. 28, no. 11, pp. 580–588, 2010.
- [49] F. Furno, K. S. Morley, B. Wong et al., “Silver nanoparticles and polymeric medical devices: a new approach to prevention of infection?” *Journal of Antimicrobial Chemotherapy*, vol. 54, no. 6, pp. 1019–1024, 2004.
- [50] S. Abuskhuna, J. Briody, M. McCann et al., “Synthesis, structure and anti-fungal activity of dimeric Ag(I) complexes containing bis-imidazole ligands,” *Polyhedron*, vol. 23, no. 7, pp. 1249–1255, 2004.
- [51] T. Hamouda, A. Myc, B. Donovan, A. Y. Shih, J. D. Reuter, and J. R. Baker, “A novel surfactant nanoemulsion with a unique non-irritant topical antimicrobial activity against bacteria, enveloped viruses and fungi,” *Microbiological Research*, vol. 156, no. 1, pp. 1–7, 2001.
- [52] E. Berman, *Toxic Metals and Their Analysis*, Heyden, London, UK, 1980.
- [53] A. Panáček, L. Kvítek, R. Prucek et al., “Silver colloid nanoparticles: synthesis, characterization, and their antibacterial activity,” *Journal of Physical Chemistry B*, vol. 110, no. 33, pp. 16248–16253, 2006.
- [54] C. Damm, H. Münstedt, and A. Rösch, “The antimicrobial efficacy of polyamide 6/silver-nano- and microcomposites,” *Materials Chemistry and Physics*, vol. 108, no. 1, pp. 61–66, 2008.
- [55] R. García-Contreras, L. Argueta-Figueroa, C. Mejía-Rubalcava et al., “Perspectives for the use of silver nanoparticles in dental practice,” *International Dental Journal*, vol. 61, no. 6, pp. 297–301, 2011.
- [56] N. A. Amro, L. P. Kotra, K. Wadu-Mesthrige, A. Bulychev, S. Mobashery, and G. Y. Liu, “High-resolution atomic force microscopy studies of the *Escherichia coli* outer membrane: structural basis for permeability,” *Langmuir*, vol. 16, no. 6, pp. 2789–2796, 2000.
- [57] A. C. Mo, W. Xu, S. Q. Xian, Y. B. Li, and S. Bai, “Antibacterial activity of silver-hydroxyapatite/titania nanocomposite coating on titanium against oral bacteria,” *Key Engineering Materials*, vol. 330–332, pp. 455–458, 2007.
- [58] J. Liao, M. Anchun, Z. Zhu, and Y. Quan, “Antibacterial titanium plate deposited by silver nanoparticles exhibits cell compatibility,” *International Journal of Nanomedicine*, vol. 5, no. 1, pp. 337–342, 2010.
- [59] C. Y. Flores, C. Diaz, A. Rubert et al., “Spontaneous adsorption of silver nanoparticles on Ti/TiO<sub>2</sub> surfaces. Antibacterial effect on *Pseudomonas aeruginosa*,” *Journal of Colloid and Interface Science*, vol. 350, no. 2, pp. 402–408, 2010.
- [60] W. R. Li, X. B. Xie, Q. S. Shi, H. Y. Zeng, Y. S. Ou-Yang, and Y. B. Chen, “Antibacterial activity and mechanism of silver nanoparticles on *Escherichia coli*,” *Applied Microbiology and Biotechnology*, vol. 85, no. 4, pp. 1115–1122, 2010.
- [61] K. Kawahara, K. Tsuruda, M. Morishita, and M. Uchida, “Antibacterial effect of silver-zeolite on oral bacteria under anaerobic conditions,” *Dental Materials*, vol. 16, no. 6, pp. 452–455, 2000.
- [62] M. Danilczuk, A. Lund, J. Sadlo, H. Yamada, and J. Michalik, “Conduction electron spin resonance of small silver particles,” *Spectrochimica Acta*, vol. 63, no. 1, pp. 189–191, 2006.
- [63] S. Pal, Y. K. Tak, and J. M. Song, “Does the antibacterial activity of silver nanoparticles depend on the shape of the nanoparticle? A study of the gram-negative bacterium *Escherichia coli*,” *Applied and Environmental Microbiology*, vol. 73, no. 6, pp. 1712–1720, 2007.
- [64] C. Baker, A. Pradhan, L. Pakstis, D. J. Pochan, and S. I. Shah, “Synthesis and antibacterial properties of silver nanoparticles,” *Journal of Nanoscience and Nanotechnology*, vol. 5, no. 2, pp. 244–249, 2005.
- [65] A. Panáček, M. Kolář, R. Večeřová et al., “Antifungal activity of silver nanoparticles against *Candida* spp,” *Biomaterials*, vol. 30, no. 31, pp. 6333–6340, 2009.
- [66] D. R. Monteiro, L. F. Gorup, S. Silva et al., “Silver colloidal nanoparticles: antifungal effect against adhered cells and biofilms of *Candida albicans* and *Candida glabrata*,” *Biofouling*, vol. 27, no. 7, pp. 711–719, 2011.
- [67] D. R. Monteiro, S. Silva, M. Negri et al., “Silver nanoparticles: influence of stabilizing agent and diameter on antifungal activity against *Candida albicans* and *Candida glabrata* biofilms,” *Letters in Applied Microbiology*, vol. 54, no. 5, pp. 383–391, 2012.
- [68] S. Galdiero, A. Falanga, M. Vitiello, M. Cantisani, V. Marra, and M. Galdiero, “Silver nanoparticles as potential antiviral agents,” *Molecules*, vol. 16, no. 10, pp. 8894–8918, 2011.
- [69] A. S. AlGhamdi and S. G. Ciancio, “Guided tissue regeneration membranes for periodontal regeneration—a literature

- review," *Journal of the International Academy of Periodontology*, vol. 11, no. 3, pp. 226–231, 2009.
- [70] N. U. Zitzmann, R. Naef, and P. Schärer, "Resorbable versus nonresorbable membranes in combination with Bio-Oss for guided bone regeneration," *International Journal of Oral and Maxillofacial Implants*, vol. 12, no. 6, pp. 844–852, 1997.
- [71] J. Zhang, Q. Xu, C. Huang, A. Mo, J. Li, and Y. Zuo, "Biological properties of an anti-bacterial membrane for guided bone regeneration: an experimental study in rats," *Clinical Oral Implants Research*, vol. 21, no. 3, pp. 321–327, 2010.
- [72] P. Podsiadlo, S. Paternel, J. M. Rouillard et al., "Layer-by-layer assembly of nacre-like nanostructured composites with antimicrobial properties," *Langmuir*, vol. 21, no. 25, pp. 11915–11921, 2005.
- [73] S. S. Jensen and H. Terheyden, "Bone augmentation procedures in localized defects in the alveolar ridge: clinical results with different bone grafts and bone-substitute materials," *The International journal of oral and maxillofacial implants*, vol. 24, pp. 218–236, 2009.
- [74] K. D. Secinti, H. Özalp, A. Attar, and M. F. Sargon, "Nanoparticle silver ion coatings inhibit biofilm formation on titanium implants," *Journal of Clinical Neuroscience*, vol. 18, no. 3, pp. 391–395, 2011.
- [75] Q. Ma, S. Mei, K. Ji, Y. Zhang, and P. K. Chu, "Immobilization of Ag nanoparticles/FGF-2 on a modified titanium implant surface and improved human gingival fibroblasts behavior," *Journal of Biomedical Materials Research*, vol. 98, no. 2, pp. 274–286, 2011.
- [76] R. L. Williams, P. J. Doherty, D. G. Vince, G. J. Grashoff, and D. F. Williams, "The biocompatibility of silver," *Critical Reviews in Biocompatibility*, vol. 5, no. 3, pp. 221–243, 1989.
- [77] M. Mahmood, Z. Li, D. Casciano et al., "Nanostructural materials increase mineralization in bone cells and affect gene expression through miRNA regulation," *Journal of Cellular and Molecular Medicine*, vol. 15, no. 11, pp. 2297–2306, 2011.
- [78] C. E. Albers, W. Hofstetter, K. A. Siebenrock, R. Landmann, and F. M. Klenke, "In vitro cytotoxicity of silver nanoparticles on osteoblasts and osteoclasts at antibacterial concentrations," *Nanotoxicology*. In press.
- [79] W. Liu, Y. Wu, C. Wang et al., "Impact of silver nanoparticles on human cells: effect of particle size," *Nanotoxicology*, vol. 4, no. 3, pp. 319–330, 2010.
- [80] S. M. Hussain, K. L. Hess, J. M. Gearhart, K. T. Geiss, and J. J. Schlager, "In vitro toxicity of nanoparticles in BRL 3A rat liver cells," *Toxicology in Vitro*, vol. 19, no. 7, pp. 975–983, 2005.
- [81] C. Carlson, S. M. Hussein, A. M. Schrand et al., "Unique cellular interaction of silver nanoparticles: Size-dependent generation of reactive oxygen species," *The Journal of Physical Chemistry B*, vol. 112, no. 43, pp. 13608–13619, 2008.
- [82] C. Greulich, J. Diendorf, J. Geßmann et al., "Cell type-specific responses of peripheral blood mononuclear cells to silver nanoparticles," *Acta Biomaterialia*, vol. 7, no. 9, pp. 3505–3514, 2011.
- [83] J. S. Hyun, B. S. Lee, H. Y. Ryu, J. H. Sung, K. H. Chung, and I. J. Yu, "Effects of repeated silver nanoparticles exposure on the histological structure and mucins of nasal respiratory mucosa in rats," *Toxicology Letters*, vol. 182, no. 1–3, pp. 24–28, 2008.
- [84] Y. S. Kim, J. S. Kim, H. S. Cho et al., "Twenty-eight-day oral toxicity, genotoxicity, and gender-related tissue distribution of silver nanoparticles in Sprague-Dawley rats," *Inhalation Toxicology*, vol. 20, no. 6, pp. 575–583, 2008.

## Research Article

# In Vitro Biocompatibility of Endodontic Sealers Incorporating Antibacterial Nanoparticles

Itzhak Abramovitz,<sup>1</sup> Nurit Beyth,<sup>2</sup> Guy Weinberg,<sup>2</sup> Alon Borenstein,<sup>2</sup> David Polak,<sup>3</sup> Dana Kesler-Shvero,<sup>2</sup> and Yael Houri-Haddad<sup>2</sup>

<sup>1</sup>Department of Endodontics, Hebrew University-Hadassah School of Dental Medicine, 91120 Jerusalem, Israel

<sup>2</sup>Department of Prosthodontics, Hebrew University-Hadassah School of Dental Medicine, 91120 Jerusalem, Israel

<sup>3</sup>Department of Periodontics, Hebrew University-Hadassah School of Dental Medicine, 91120 Jerusalem, Israel

Correspondence should be addressed to Nurit Beyth, nuritb@ekmd.huji.ac.il

Received 2 April 2012; Revised 12 June 2012; Accepted 14 June 2012

Academic Editor: Xiaoming Li

Copyright © 2012 Itzhak Abramovitz et al. This is an open access article distributed under the Creative Commons Attribution License, which permits unrestricted use, distribution, and reproduction in any medium, provided the original work is properly cited.

The main cause of endodontic disease is bacteria. Disinfection is presently achieved by cleaning the root canal system prior to obturation. Following setting, root canal filling is devoid of any antibacterial effect. Endodontic sealers with antimicrobial properties yet biocompatible may enhance root canal therapy. For this purpose, quaternized polyethylenimine nanoparticles which are antibacterial polymers, biocompatible, nonvolatile, and stable may be used. The aim of the present study was to examine the impact of added QPEI on the cytotoxicity of AH Plus, Epiphany, and GuttaFlow endodontic sealers. The effect of these sealers on the proliferation of RAW 264.7 macrophage and L-929 fibroblast cell lines and on the production of TNF $\alpha$  from macrophages was examined. Cell vitality was evaluated using a colorimetric XTT assay. The presence of cytokines was determined by two-site ELISA. Results show that QPEI at 1% concentration does not impair the basic properties of the examined sealers in both macrophages and fibroblast cell lines. Incorporation of 1% QPEI into the sealers did not impair their biocompatibility. QPEI is a potential clinical candidate to improve antibacterial activity of sealers without increasing cytotoxicity.

## 1. Introduction

Endodontic disease of human teeth, a common reality, is caused primarily by bacteria [1, 2]. State-of-the-art disinfection is achieved through biomechanical preparation that includes mechanical instrumentation and antiseptic irrigation. Shaping the root canal space allows for a three-dimensional obturation and seal of the root canal system. The endodontic sealer coats the walls of the canals and fills the space between the root canal filling material and the root, thus filling the root canal and sealing its ports of entry and exit. The set root canal filling material is mostly inert. However, it is expected to physically prevent oral bacterial contamination as well as regrowth of residual bacterial contamination thus protecting the tooth supporting tissues [3, 4]. Regrettably, even when effective instrumentation, irrigation, and an adequate obturation of the root canal are

performed the irregularity in shape (lateral ducts, and anastomosis) allows for bacterial persistence. In most cases, failure of endodontic treatment is associated to the persistence of bacteria in the root canal system [5] or their consecutive coronal leakage. Consequently, bacterial eradication from the root canal system and prevention of coronal leakage are of utter importance. Therefore, root canal sealers with good sealing ability and longer antimicrobial activity are desirable. Moreover, antibacterial endodontic sealers should be lethal against contaminating bacteria without harming tooth-supporting tissues [6].

Research has shown a positive correlation between antibacterial properties of sealers and their cytotoxic effect [7]. Cytotoxicity becomes even more relevant since extrusion of sealer during root canal obturation is a common clinical finding [8]. The cytotoxic effect depends on the leachability of the material [9]. Root canal filling materials

TABLE 1

Material	Composition		Manufacturer
	Paste A	Paste B	
AH Plus	(i) Diglycidil-bisphenol-A-ether.	(i) Amina 1-adamantane.	AH Plus Dentsply/Maillefer, Konstanz, Germany.
	(ii) Calcium.	(ii) N,N dibenzyl-5-oxanonandiamine-1,9.	
	(iii) Tungsten.	(iii) TCD-diamine.	
	(iv) Zirconium oxide.	(iv) Calcium tungsten.	
	(v) Aerosol.	(v) Zirconium oxide.	
	(vi) Iron.	(vi) Silicone oxide.	
	(vii) Oxide.		
Epiphany	BisGMA, ethoxylated BisGMA, UDMA, hydrophilic difunctional methacrylates.	Calcium hydroxide, barium sulphate, barium glass, bismuth oxychloride, silica.	Epiphany SE Pentron Clinical Technologies, Wallingford, CT, USA.
	(i) Polydimethylsiloxane particles.  (ii) Silicone.  (iii) Paraffin oil.  (iv) Platinum catalyst.  (v) Zirconium dioxide.  (vi) Nano-silver.  (vii) Gutta-percha powder.		GuttaFlow Coltene-whaledent Langenau, Germany.

and medicaments may leach through dentin [10] or when extruded beyond the root apex and cause a cytotoxic damage [11]. Nonresorbable sealers may cause a cytotoxic effect for several days due to polymerization derivatives release such as formaldehyde [12]. Regardless, these sealers are widely used in the clinical daily practice and are accepted owing to their chemical stability.

Based on the above, the antimicrobial activity of endodontic sealers may be an important tool for infection control. To reach this goal, antibacterial quaternary ammonium polyethylenimine (QPEI) nanoparticles were incorporated into conventional endodontic sealers. Previously, we showed that when these nanoparticles were immobilized into resin-based materials, they caused a strong, long-lasting antibacterial effect upon contact without leaching of the nanoparticles and without compromise of the mechanical properties [13]. Furthermore, dental restorative composites incorporating up to 2% wt/wt QPEI nanoparticles caused no inflammatory *in vivo* response [14].

It seems that incorporation of QPEI nanoparticles into endodontic sealers may be beneficial in achieving antibacterial activity [13]. Nonetheless, biocompatibility of modified endodontic sealers with antibacterial nanoparticles needs to be established by comparing these new materials to nonmodified sealers. In the present study, the cytotoxic effect was tested using fibroblasts and macrophages cells. These cells have been shown to play a critical role in the biological response to materials [15]. Due to the fact that macrophages direct much of the chronic inflammatory response, the ability of a material to alter a cell's viability or secretion function may have significant consequences on the overall biological response to a given material [16].

The aim of the present study was to compare the cytotoxic effect of 3 commercially available sealers prior and following incorporation of 1%, or 2% QPEI on macrophages and fibroblast cell lines and on the secretion of TNF $\alpha$  from the macrophages.

## 2. Materials and Methods

**2.1. QPEI Nanoparticle Preparation.** The synthesis of quaternary ammonium PEI nanoparticle was previously described by Beyth et al. [13]. Briefly, PEI (10 g, 0.23 mol monomer units) dissolved in 100 mL ethanol was reacted with dibromopentane at a 1:0.04 mol ratio (monomer units of PEI/dibromopentane) under reflux for 24 hrs. N-alkylation was conducted as follows: octyl halide was added at a 1:1 mol ratio (monomer units PEI/octyl halide). Alkylation was carried out under reflux for 24 hrs, followed by neutralization with sodium hydroxide (1.25 equimolar, 0.065 mol) for an additional 24 hrs under the same conditions. N-methylation was conducted as follows: 43 mL (0.68 mol) of methyl iodide were added and methylation was continued at 42°C for 48 hrs followed by neutralization with sodium bicarbonate (0.23 mol, 19 g) for an additional 24 hrs. The supernatant obtained was decanted and precipitated in 300 mL of double distilled water (DDW), washed with hexane and DDW, and then freeze-dried. The purification step was repeated using additional amounts of hexane and DDW. The average yield was 70% (mol/mol).

**2.2. Preparation of the Test Samples.** The tested materials AHplus, Epiphany, and GuttaFlow (Table 1) were prepared according to the manufacture instructions and applied on

TABLE 2: Summary of atomic percentage values of elements determined by XPS analysis and DLS measurements.

Tested material	Atomic concentration %/Mass concentration %				DLS Analysis
	I 3d	O 1s	C 1s	Si 2p	
AH Plus	—	21.79/21.85	59.08/44.48	19.13/33.67	—
AH Plus + 2% QPEI	0.08/0.64	21.17/21.46	61.09/46.48	17.66/31.42	—

AHPlus with and without added QPEI nanoparticles.

<sup>a</sup>QPEI nanoparticle presence in the modified sealers was estimated using X-ray photoelectron spectroscopy; using Kratos Axis Ultra spectrometer (Kratos Analytical Ltd., Manchester, UK), using Al K $\alpha$  monochromatic radiation X-ray source (1,486.7 eV). AH plus discs incorporating 0% or 2% wt/wt were prepared and left to dry in the incubator for 1 week.

<sup>b</sup>Supernatant of AHPlus with and without QPEI nanoparticles was determined using dynamic light scattering analyzer (Zetasizer Nano-S, Malvernd); samples ( $n = 8$ ) were incubated for 1 week; supernatant was collected and tested—no particles.

specially designed plastic inserts. The nanoparticle powder was added at 0, 1, or 2% wt/wt to each of the endodontic sealers and homogeneously mixed according to the manufacturer's instructions. These plastic inserts were sterilized under gas condition for 24 hrs and placed in a 96-well tissue culture plate directly to the cells. In some of the experiments, the inserts were immersed in media for another 24 hrs, for residual materials washing, before challenging the cells.

**2.3. Material Characterization.** The FT-IR spectra of the QPEI nanoparticles were recorded on a Perkin-Elmer, 2000 FTIR. FT-IR: 3,440 cm<sup>-1</sup> (N-H), 2,956, 2,926, and 2,853 cm<sup>-1</sup> (C-H), 1,617 cm<sup>-1</sup> (N-H, small band), 1,465 cm<sup>-1</sup> (C-H), 967 cm<sup>-1</sup> quaternary nitrogen. 1H-NMR (DMSO): 0.845 ppm (t, 3H, CH<sub>3</sub>, octane hydrogens), 1.24 ppm (m, 10H, -CH<sub>2</sub>-, octyl hydrogens) 1.65 ppm (m, 2H, CH, octyl hydrogens), 3.2–3.6 ppm (m, CH<sub>3</sub> of quaternary amine, 4H, -CH<sub>2</sub>-, PEI hydrogens and 2H, -CH<sub>2</sub>-, octyl hydrogens. QPEI nanoparticle presence in the modified sealers was estimated using X-ray photoelectron spectroscopy (XPS). X-Ray photoelectron spectra (XPS) were recorded using Kratos Axis Ultra spectrometer (Kratos Analytical Ltd., Manchester, UK), using Al K $\alpha$  monochromatic radiation X-ray source (1,486.7 eV). The emission current was set for 15 mA, and the anode high voltage to 15 kV. All XPS spectra were collected with 90° take off angle (normal to analyzer), vacuum condition in the chamber was  $1.9 \cdot 10^{-9}$  Torr. The survey XPS spectra were acquired with pass energy 160 eV and 1 eV step size, and the high-resolution spectra were collected for C 1s, O 1s, Si 2p, Zr 3d and I 3d levels, with pass energy 20 eV and 0.1 eV step size. Additionally, the leaching of QPEI nanoparticles from the modified sealers was recorded using DLS measurements. Samples' size distributions were evaluated by a dynamic light scattering analyzer (Zetasizer Nano-S, Malvern. Surface characterization of the nonmodified versus the modified sealers is summarized in Table 2. Nanoparticle electronic microscopy and full characterization of the QPEI nanoparticles was previously described by Yudovin-Farber et al. [17].

**2.4. Cell Cultures (Macrophages and Fibroblast Cells).** The raw 264.7 macrophage cell line and fibroblast (CCL-1 L-929 american type culture collection) cell lines were cultured separately in Petri dishes in Dulbecco's minimum

essential Medium (DMEM) supplemented with 10% fetal calf serum (FCS), 1% penicillin/streptomycin, and 1% glutamine. Before the assay, the cells were seeded at a density of 60,000 cells in 200  $\mu$ L media per well in 96-well tissue culture plates (NUNC). Twenty-four hours after plating, the cells were activated by 10  $\mu$ L of heat-killed *Porphyromonas gingivalis* 33277 ATCC and exposed to the materials layered on the special inserts that was placed in the wells. Following 24 hrs of incubation at 37°C in a humidified atmosphere of 5% CO<sub>2</sub>, the plates were analyzed for cell viability and the secreted levels of TNF $\alpha$  of macrophages. Based on our preliminary data on the kinetics of TNF $\alpha$  secretion, the cytokine level was tested by ELISA following 24 hours of *P. gingivalis* challenge.

**2.5. Cell Viability.** The viability of the cells was evaluated using a colorimetric XTT assay as described by Scudiero et al. [18]. At the end of incubation the suspended cells were exposed to the tested materials, the cells were centrifuged and all cells were subjected to XTT assay. Results present the total effect of the materials on the cells in all groups compared to control. The assay is based on the ability of metabolically active cells to reduce the tetrazolium salt XTT to orange-colored compounds of formazan. Following 24 hrs of incubation, 50 mL of XTT labeling mixture were added to each well and the microplate was incubated for a further 4 hrs. A Vmax microplate reader (Molecular Devices, Palo Alto, CA) with a 450 nm optical filter and a 650 nm reference wavelength was used to measure the absorbance of each well.

**2.6. Cytokine Analysis.** The presence of cytokines was determined by two-site ELISA [19]. The TNF $\alpha$  assay was based on commercially available antibody pairs (Pharmingen, San Diego, CA). The 96-well ELISA plates were coated with 1 mg/mL anti-mouse cytokine monoclonal antibodies, and blocked with 3% bovine serum albumin (BSA). After addition of the samples, a secondary biotinylated antibody was used as the detecting antibody, followed by a streptavidin-horseradish peroxidase conjugate (Jackson Immunoresearch Laboratories, West Grove, PA). The substrate used was o-phenylenediamine (Zymed, San Francisco, CA). The reaction was terminated by the addition of 4 N sulfuric acid, and the optical density was read with the aid of a Vmax microplate reader (Molecular Devices) at 490–650 nm.

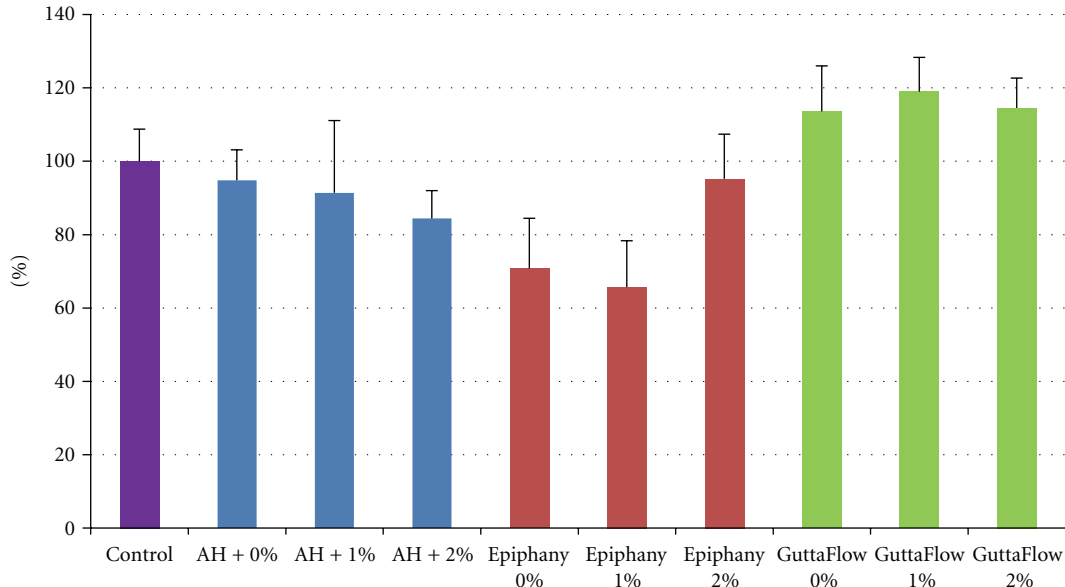


FIGURE 1: The effect of AH+, Epiphany, and GuttaFlow endodontic sealers on the mitochondrial activity of the L-929 fibroblast cell line. Mitochondrial activity was normalized to the control without sealers stimulation. Stimulated fibroblasts (with heat-killed *P. gingivalis*) with and without the various endodontic sealers were cultured for 24 hrs. Cell viability was tested using the XTT test. The results are expressed as the mean + SD. Statistically significant differences between the control (media) and the different groups are indicated by asterisks ( $P < 0.05$ ) and  $n = 8$  wells.

**2.7. Heat-killed Bacterium *P. gingivalis*.** *P. gingivalis*, strain ATCC 33277, was grown on blood agar plates in an anaerobic chamber with 85% N<sub>2</sub>, 5% H<sub>2</sub>, 10% CO<sub>2</sub>. After incubation at 37°C for 2-3 days the bacteria were inoculated into peptone yeast extract and incubated for 3-4 days, under the same conditions. To obtain heat-killed bacteria, the bacteria were washed 3 times with PBS and then exposed to 80°C for 10 min [20]. The bacterial concentration was standardized to an optical density of OD<sub>650</sub> = 0.1, corresponding to 10<sup>10</sup> CFU/mL [21]. The heat-killed bacteria were stored at 4°C until used when they were resuspended in solution by brief sonication.

**2.8. Statistical Analysis.** Data analysis was performed using SigmaStat statistical software (Jandel Scientific, San Rafael, CA). One way repeated measure of analysis of variance (RM ANOVA) was used to test the significance of the differences between the treated groups. If significance was established, the intergroup differences were tested for significance using Student's *t*-test with the Bonferroni correction for multiple testing. The significance of the differences between two treatment groups was evaluated using the *t*-test. The level of significance was set at  $P < 0.05$ . All the results are presented as the mean  $\pm$  standard error.

### 3. Results

**3.1. The Cytotoxic Effect on Fibroblasts.** The cytotoxicity of endodontic sealers incorporating 0, 1, or 2% wt/wt was evaluated using the XTT test. Fibroblasts were exposed to the tested materials for 24 hrs, and their viability was

normalized according to the control (cells without any material) mitochondrial activity and evaluated. Results show that the fibroblast's viability varied when exposed to the different sealers: in the presence of AHplus viability of the cells was not affected when compared to the control, Epiphany caused significant decrease ~20% in the cell viability and GuttaFlow increased cell viability. The addition of antibacterial nanoparticles had an insignificant effect on cell viability when compared to the nonmodified endodontic sealer material: cell viability was similar in the presence of Epiphany and GuttaFlow with or without added QPEI nanoparticles, AHPlus incorporating 2% QPEI nanoparticles caused some decrease in cell viability only no significant decrease was seen in the 1% group (Figure 1).

Immersion of the test materials after their setting in media for 24 hrs, did not affect the viability of the fibroblasts. The same pattern of cytotoxicity of the different sealers independent of nanoparticles incorporation can be seen in Figure 2. AHplus sealer incorporating 2% QPEI was the only group to show a slight decrease in fibroblast viability compared to the nonmodified sealer.

**3.2. The Cytotoxic Effect on Macrophages.** Macrophages were exposed to the tested materials for 24 hrs, and their viability was normalized according to the control (cells without any material) mitochondrial activity. Two of the three different sealers, AH Plus and Epiphany, caused a decrease in macrophage viability, while GuttaFlow had no effect when compared to control. The incorporation of the nanoparticles into the sealers had no effect when added at 1% wt/wt, whereas when 2% wt/wt of nanoparticles were incorporated

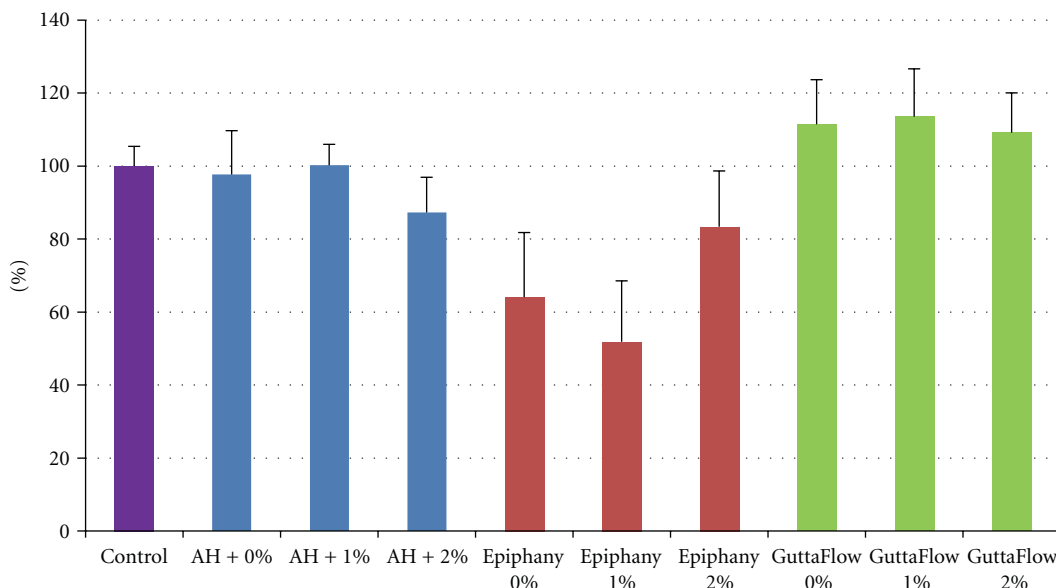


FIGURE 2: The effect of AH+, Epiphany and GuttaFlow endodontic sealers on the mitochondrial activity of the L-929 fibroblast cell line after 24 hrs immersion in media. Mitochondrial activity was normalized to the control without sealers stimulation. Stimulated fibroblasts (with heat-killed *P. gingivalis*) with and without the various endodontic sealers were immersed in media for 24 hrs, and then transferred to cell cultured fibroblasts for another 24 hrs. Cell viability was tested using the XTT test. The results are expressed as the mean + SD. Statistically significant differences between the control (media) and the different groups are indicated by asterisks ( $P < 0.05$ ) and  $n = 8$  wells.

reduced viability of the cells was seen in all three sealers when modified (Figure 3).

Immersion of the test materials after their setting on the inserts in media for 24 hrs, reduced the cytotoxicity of all three materials. The viability of the macrophages was similar to the control (Figure 4). Incorporation of the nanoparticles into the sealers had no effect when added at 1% wt/wt, whereas when 2% wt/wt of nanoparticles were incorporated reduced viability of the cells was seen with all the tested materials similarly as in the nonwashed materials (Figure 4).

**3.3. TNF $\alpha$  Secretion by Macrophages.** Macrophages were exposed to the materials for 24 hrs combined with heat-killed *P. gingivalis* challenge to stimulate the cells. The secretion of TNF $\alpha$  by macrophages was measured and normalized according to the control (cells with bacterial challenge alone). Challenged macrophages showed reduced secretion of TNF $\alpha$  in the presence of AHPlus and Epiphany. Similar TNF $\alpha$  secretion was seen when nanoparticles were incorporated into AH Plus with no effect on macrophage activity. However, incorporation of nanoparticles into Epiphany reduced the levels of TNF $\alpha$  to nondetectable (Figure 5). The effect of GuttaFlow on macrophage activity seemed neglectable. Both the nonmodified sealer and the sealer incorporating 1% or 2% nanoparticles did not affect TNF $\alpha$ , secretion and the levels were similar to the control with no statistical significance.

#### 4. Discussion

Results show that the incorporation of 1% wt/wt of QPEI-nanoparticles into endodontic sealers has no cytotoxic effect

for all three tested materials. The viability of both cell lines: fibroblasts and the macrophages remain stable when compared to the nonmodified sealers. The incorporation of 2% nanoparticles seems slightly toxic depending on: the tested material, the culture conditions, and the cell type. This diverse effect of the materials with different cell lines is a very important outcome for future designing cytotoxic studies.

Endodontic sealers are routinely used to fill gaps within the solid components of the root canal filling and allow its adaptation to the dentin walls [4]. Since root canal filling is the ultimate barrier between the oral cavity and inner body (e.g., periodontal ligament and bone) an antibacterial effect is desirable. However, previous attempts to render sealers with antibacterial properties resulted in severe cytotoxic effect [22]. This effect was evident when sealer leaching through dentin various ports of exit from the root canal system to the tooth surrounding tissues occurred [10, 11, 14]. Such events were reported to be responsible for cases of pain, nerve paresthesia, anesthesia and delayed healing due to their cytotoxic effect. More troubling is the possible cytotoxic effect to remote organs once these materials are dissolved [23].

Several materials constituting endodontic sealers were recognized as cytotoxic. For example, eugenol that was proved to leach out of zinc-eugenol bases sealers was found cytotoxic to nerve cells as well as to human periodontal ligament (PDL) fibroblasts [24–26]. Another example is paraformaldehyde that was vastly used in the past and is a byproduct of contemporary epoxy resin based sealers [27]. Paraformaldehyde was reported to be cytotoxic and mutagenic [28]. Another component that is released during setting is polyketone. It can be found in the polyketone-based cement Diaket which was reported to be cytotoxic to

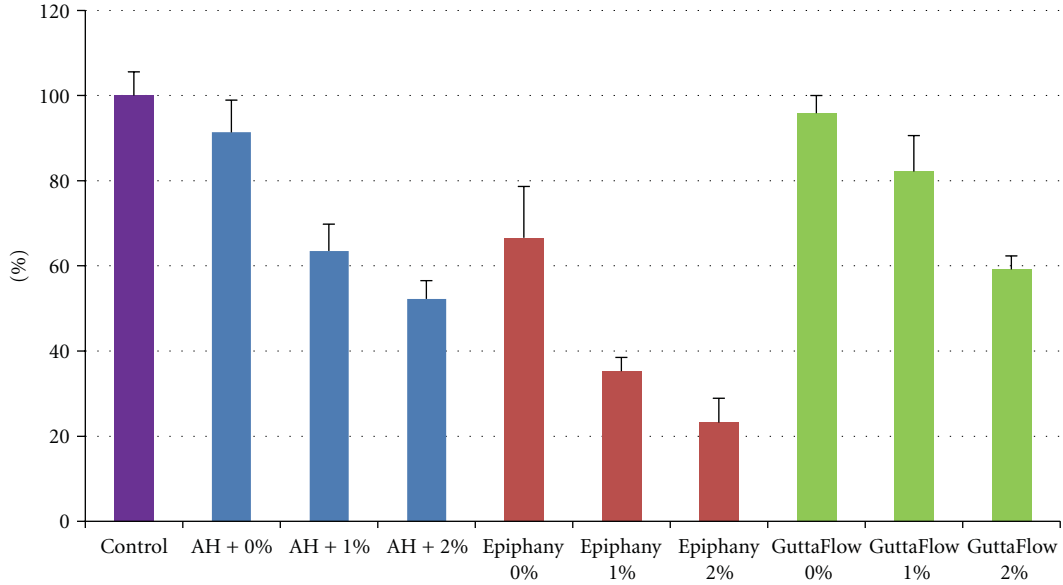


FIGURE 3: The effect of AH+, Epiphany and GuttaFlow endodontic sealers on the mitochondrial activity of the RAW macrophage cell line. Mitochondrial activity was normalized to the control without sealers stimulation. Stimulated macrophages (with heat killed *P. gingivalis*) with and without the various endodontic sealers were cultured for 24 hrs. Cell viability was tested using the XTT test. The results are expressed as the mean + SD. Statistically significant differences between the control (media) and the different groups are indicated by asterisks ( $P < 0.05$ )  $n = 8$  wells.

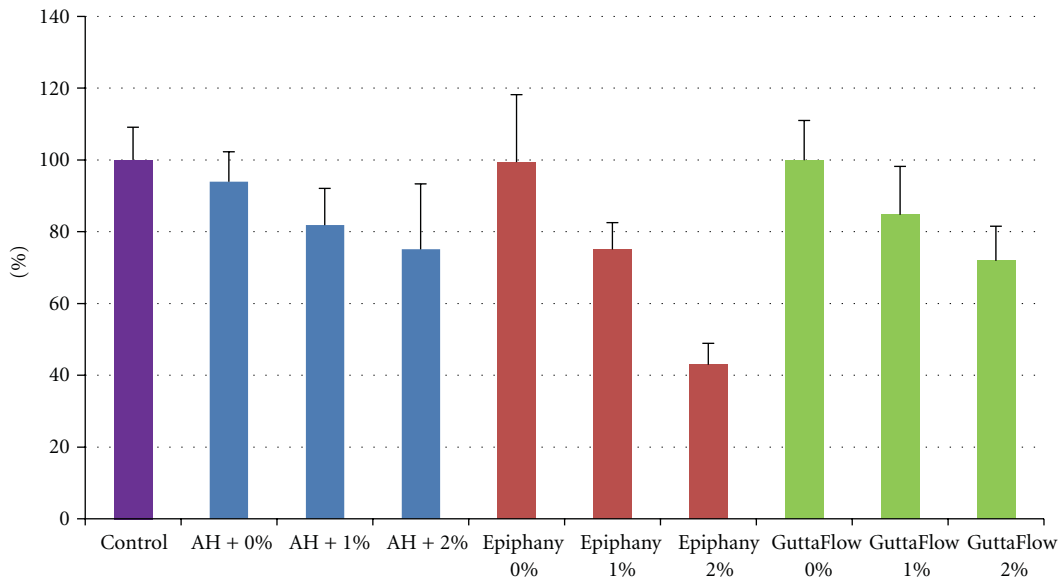


FIGURE 4: The effect of AH+, Epiphany, and GuttaFlow endodontic sealers on the mitochondrial activity of the RAW macrophage cell line after 24 hrs immersion in media. Mitochondrial activity was normalized to the control without sealers stimulation. Stimulated macrophages (with heat-killed *P. gingivalis*) with and without the various endodontic sealers were immersed in media for 24 hrs and then transferred to cell cultured macrophages for another 24 hrs. Cell viability was tested using the XTT test. The results are expressed as the mean + SD. Statistically significant differences between the control (media) and the different groups are indicated by asterisks ( $P < 0.05$ ) and  $n = 8$  wells.

HeLa cells and L-645 fibroblast cells [29]. Another group of materials that was reported to release cytotoxic components such as triethylene glycol dimethacrylate monomer, urethane dimethacrylate (UDMA), HEMA initiators, and silica are resin-reinforced materials [19].

In the present study, it was observed that the cytotoxic effect differed between materials. AHPlus caused a moderate cytotoxic effect that could be attributed to bisphenol A diglycidyl ether release. This resin-based component is known to be potentially cytotoxic and mutagenic [30]. In addition,

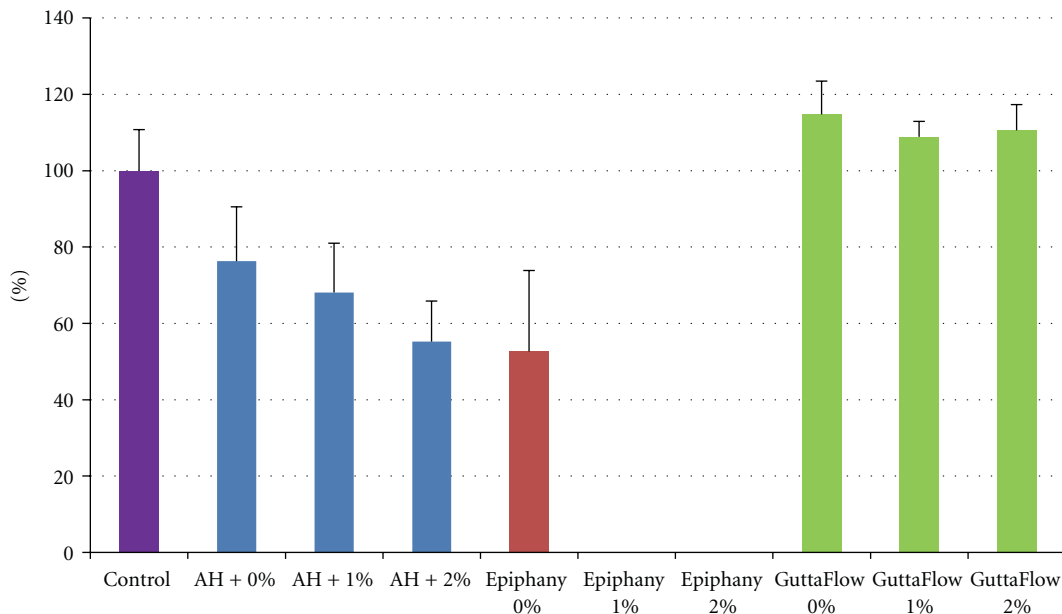


FIGURE 5: The effect of AH+, Epiphany, and GuttaFlow endodontic sealers on TNF $\alpha$  secretion in the RAW macrophage cell line. Mitochondrial activity was normalized to the control without sealers stimulation. Stimulated macrophages (with heat-killed *P. gingivalis*) with and without the various endodontic sealers were cultured for 24 hrs in the presence of heat-killed *P. gingivalis*. The secreted TNF $\alpha$  levels in the media were analyzed by ELISA. The results are expressed as the mean  $\pm$  SD. Statistically significant differences between the control (media) and the different groups are indicated by asterisks ( $P < 0.05$ ) and  $n = 8$  wells.

the cytotoxic effect can be attributed to the release of small amounts of formaldehyde or amine and epoxy resin components from the sealer [31]. The resin component urethane dimethacrylate (UDMA) that can be found in Endo-Rez sealer was reported to cause intracellular glutathione depletion even at low concentrations within a short period of time resulting in a cytotoxic effect [32]. Resin-based endodontic sealers such as Epiphany or Metaseal consist of polymerized resin components reinforced by inorganic fillers. The resin matrix comprise a mixture of bisphenol A-glycidyl methacrylate (Bis-GMA), ethoxylated Bis-GMA, UDMA, and hydrophilic difunctional methacrylates [33], all of which when leaching out may produce a toxic effect. Metaseal contains HEMA which is reported to inhibit intracellular tyrosine phosphorylation in L929 cells [34]. It also induces cell-growth inhibition and cycle perturbation as well as glutathione depletion and reactive oxygen species production [35]. Glutathione depletion was reported to be responsible for the cytotoxic effect of eugenol [36]. Formaldehyde releasing sealers such as AH26 and N2, were shown to downregulate alkaline phosphatase causing inhibition of new bone formation [37].

*In vitro* cytotoxicity evaluation of endodontic sealers provides a controlled setup that allows quick evaluation and comparison between different sealers. Previous studies showed that a silicon-based sealer (Roekoseal) and an epoxy resin-based sealer (AHPlus) are non-toxic when freshly prepared or following a setting period of one to seven days, showing 40–60% cells viability as compared to Teflon controls. Under the same conditions Epiphany was found to

be highly cytotoxic showing 0% viability [38]. Similarly, 12-week-aged AHPlus retained its ability to suppress cytokine secretion of monocytic cells without induction of secretion of TNF $\alpha$ , IL $\beta$ , or IL6. One year analysis of elutes of AH Plus and Roekoseal showed minimal cytotoxic effect on 3t3 fibroblasts as well as on periodontal ligament fibroblasts [9]. A study by Al-Hiyasat et al. showed that different cytotoxic effect of AHPlus and Epiphany depends on magnitude of dilution of the samples [19]. Contradictory to traditional root canal sealers that polymerize inside the root canal and may release antibacterial and cytotoxic derivates as byproducts, QPEI are prepolymerized and do not release any by products. QPEI was reported to possess an excellent antibacterial activity [39]. When these polymers are synthesized as insoluble antibacterial nano-sized particles and are incorporated into resin base materials, potent and long-lasting antibacterial surface properties can be attained *in vitro* and *in vivo* [13, 40]. Usage of nanomaterials altering surface properties has been shown suitable for various biomedical applications [41, 42]. QPEI is a stable antibacterial compound that does not leach out from the material into the surrounding environment rendering perpetual antibacterial surface properties. The present study results coincide with our previous results showing that the incorporation of QPEI nanoparticles does not affect the base material's biocompatibility.

Incorporation of QPEI nanoparticles into noncytotoxic endodontic sealers such as silicon-based sealers may provide added value of antibacterial properties without compromising the materials' biocompatibility. Furthermore, this

antibacterial effect is expected to last longer as QPEI nanoparticles are nonleachable components encapsulated in the material matrix while the antibacterial effect of traditional sealer is self-limited to the setting or degradation periods.

## Conflict of Interests

A patent entitled “Antimicrobial Nanoparticulate Additives Forming Non-Leachable Sustained Antimicrobial Polymeric Compositions” is pending approval.

## Author's Contribution

I. Aramovitz and N. Beyth contributed equally to this work.

## Acknowledgments

The authors would like to acknowledge the Dentsply Israeli branch and Dentorient Fuss Ltd. for kindly supplying the endodontic sealer materials.

## References

- [1] S. Kakehashi, H. R. Stanley, and R. J. Fitzgerald, “The effects of surgical exposures of dental pulps in germ-free and conventional laboratory rats,” *Oral Surgery, Oral Medicine, Oral Pathology*, vol. 20, no. 3, pp. 340–349, 1965.
- [2] D. J. Caplan, “Epidemiologic issues in the studies of association between apical periodontitis and systemic health,” *Endodontic Topics*, vol. 8, pp. 15–35, 2004.
- [3] L. B. Peters, P. R. Wesselink, and W. R. Moorer, “The fate and the role of bacteria left in root dentinal tubules,” *International Endodontic Journal*, vol. 28, no. 2, pp. 95–99, 1995.
- [4] J. L. Gutmann and D. E. Witherspoon, “Obturation of the cleaned and shaped root canal system,” in *Pathways of the Pulp*, S. Choen and R. C. Burns, Eds., Mosby, St. Louis, Mo, USA, 2002.
- [5] U. Sjögren, D. Figdor, S. Persson, and G. Sundqvist, “Influence of infection at the time of root filling on the outcome of endodontic treatment of teeth with apical periodontitis,” *International Endodontic Journal*, vol. 30, no. 5, pp. 297–306, 1997.
- [6] I. M. Saleh, I. E. Ruyter, M. Haapasalo, and D. Ørstavik, “Bacterial penetration along different root canal filling materials in the presence or absence of smear layer,” *International Endodontic Journal*, vol. 41, no. 1, pp. 32–40, 2008.
- [7] I. Willershausen, A. Callaway, B. Briseño, and B. Willershausen, “*In vitro* analysis of the cytotoxicity and the antimicrobial effect of four endodontic sealers,” *Head & Face Medicine*, vol. 7, p. 15, 2011.
- [8] L. Peng, L. Ye, H. Tan, and X. Zhou, “Outcome of root canal obturation by warm gutta-percha versus cold lateral condensation: a meta-analysis,” *Journal of Endodontics*, vol. 33, no. 2, pp. 106–109, 2007.
- [9] T. Schwarze, G. Leyhausen, and W. Geurtzen, “Long-term cyocompatibility of various endodontic sealers using a new root canal model,” *Journal of Endodontics*, vol. 28, no. 11, pp. 749–753, 2002.
- [10] L. G. Breault, G. S. Schuster, M. A. Billman et al., “The effects of intracanal medicaments, fillers, and sealers on the attachment of human gingival fibroblasts to an exposed dentin surface free of a smear layer,” *Journal of Periodontology*, vol. 66, no. 7, pp. 545–551, 1995.
- [11] A. Tamse, I. Kaffe, M. M. Littner, and A. Kozlovsky, “Paresthesia following overextension of AH-26: report of two cases and review of the literature,” *Journal of Endodontics*, vol. 8, no. 2, pp. 88–90, 1982.
- [12] H. Lovschall, M. Eiskjaer, and D. Arenholt-Bindslev, “Formaldehyde cytotoxicity in three human cell types assessed in three different assays,” *Toxicology in Vitro*, vol. 16, no. 1, pp. 63–69, 2002.
- [13] N. Beyth, Y. Houri-Haddad, L. Baraness-Hadar, I. Yudovin-Farber, A. J. Domb, and E. I. Weiss, “Surface antimicrobial activity and biocompatibility of incorporated polyethyleneimine nanoparticles,” *Biomaterials*, vol. 29, no. 31, pp. 4157–4163, 2008.
- [14] I. Yudovin-Farber, N. Beyth, A. Nyska, E. I. Weiss, J. Golenser, and A. J. Domb, “Surface characterization and biocompatibility of restorative resin containing nanoparticles,” *Biomacromolecules*, vol. 9, no. 11, pp. 3044–3050, 2008.
- [15] J. M. Anderson and K. M. Miller, “Biomaterial biocompatibility and the macrophage,” *Biomaterials*, vol. 5, no. 1, pp. 5–10, 1984.
- [16] K. M. Miller and J. M. Anderson, “*In vitro* stimulation of fibroblast activity by factors generated from human monocytes activated by biomedical polymers,” *Journal of Biomedical Materials Research*, vol. 23, no. 8, pp. 911–930, 1989.
- [17] I. Yudovin-Farber, N. Beyth, E. I. Weiss, and A. J. Domb, “Antibacterial effect of composite resins containing quaternary ammonium polyethyleneimine nanoparticles,” *Journal of Nanoparticle Research*, vol. 12, no. 2, pp. 591–603, 2010.
- [18] D. A. Scudiero, R. H. Shoemaker, K. D. Paull et al., “Evaluation of a soluble tetrazolium/formazan assay for cell growth and drug sensitivity in culture using human and other tumor cell lines,” *Cancer Research*, vol. 48, no. 17, pp. 4827–4833, 1988.
- [19] A. S. Al-Hiyasat, M. Tayyar, and H. Darmani, “Cytotoxicity evaluation of various resin based root canal sealers,” *International Endodontic Journal*, vol. 43, no. 2, pp. 148–153, 2010.
- [20] L. Kesavalu, J. L. Ebersole, R. L. Machen, and S. C. Holt, “Porphyromonas gingivalis-virulence in mice: induction of immunity to bacterial components,” *Infection and Immunity*, vol. 60, no. 4, pp. 1455–1464, 1992.
- [21] I. Frolov, Y. Houri-Hadad, A. Soskolne, and L. Shapira, “*In vivo* exposure to Porphyromonas gingivalis up-regulates nitric oxide but suppresses tumour necrosis factor- $\alpha$  production by cultured macrophages,” *Immunology*, vol. 93, no. 3, pp. 323–328, 1998.
- [22] American Association of Endodontics—position paper, *Concerning Paraformaldehyde-Containing Endodontic Filling Materials and Sealers*, A.A.E. Endodontics, Chicago, Ill, USA, 1988.
- [23] W. Geurtzen, “Biocompatibility of root canal filling materials,” *Australian Endodontic Journal*, vol. 27, no. 1, pp. 12–21, 2001.
- [24] A. D. Wilson, D. J. Clinton, and R. P. Miller, “Zinc oxide-eugenol cements. IV. Microstructure and hydrolysis,” *Journal of Dental Research*, vol. 52, no. 2, pp. 253–260, 1973.
- [25] P. Brodin, “Neurotoxic and analgesic effects of root canal cements and pulp-protecting dental materials,” *Endodontics & dental traumatology*, vol. 4, no. 1, pp. 1–11, 1988.
- [26] A. Samara, Y. Sarri, D. Stravopodis, G. N. Tzanetakis, E. G. Kontakiotis, and E. Anastasiadou, “A comparative study of the effects of three root-end filling materials on proliferation and adherence of human periodontal ligament fibroblasts,” *Journal of Endodontics*, vol. 37, no. 6, pp. 865–870, 2011.
- [27] M. R. Leonardo, L. A. B. D. Silva, M. T. Filho, and R. S. D. Silva, “Release of formaldehyde by 4 endodontic sealers,” *Oral*

- Surgery, Oral Medicine, Oral Pathology, Oral Radiology, and Endodontics*, vol. 88, no. 2, pp. 221–225, 1999.
- [28] H. Ersev, G. Schmalz, G. Bayirli, and H. Schweikl, “Cytotoxic and mutagenic potencies of various root canal filling materials in eukaryotic and prokaryotic cells *in vitro*,” *Journal of Endodontics*, vol. 25, no. 5, pp. 359–363, 1999.
  - [29] J. D. Kettering and M. Torabinejad, “Cytotoxicity of root canal sealers: a study using HeLa cells and fibroblasts,” *International Endodontic Journal*, vol. 17, no. 2, pp. 60–66, 1984.
  - [30] J. Heil, G. Reifferscheid, P. Waldmann, G. Leyhausen, and W. Geurtzen, “Genotoxicity of dental materials,” *Mutation Research*, vol. 368, no. 3-4, pp. 181–194, 1996.
  - [31] B. I. Cohen, M. K. Pagnillo, B. L. Musikant, and A. S. Deutsch, “Formaldehyde evaluation from endodontic materials,” *Oral health*, vol. 88, no. 12, pp. 37–39, 1998.
  - [32] J. Volk, J. Engelmann, G. Leyhausen, and W. Geurtzen, “Effects of three resin monomers on the cellular glutathione concentration of cultured human gingival fibroblasts,” *Dental Materials*, vol. 22, no. 6, pp. 499–505, 2006.
  - [33] M. A. Versiani, J. R. Carvalho, M. I. A. F. Padilha, S. Lacey, E. A. Pascon, and M. D. Sousa-Neto, “A comparative study of physicochemical properties of AH Plus and Epiphany root canal sealants,” *International Endodontic Journal*, vol. 39, no. 6, pp. 464–471, 2006.
  - [34] M. Kaga, M. Noda, J. L. Ferracane, W. Nakamura, H. Oguchi, and H. Sano, “The *in vitro* cytotoxicity of eluates from dentin bonding resins and their effect on tyrosine phosphorylation of L929 cells,” *Dental Materials*, vol. 17, no. 4, pp. 333–339, 2001.
  - [35] H. H. Chang, M. K. Guo, F. H. Kasten et al., “Stimulation of glutathione depletion, ROS production and cell cycle arrest of dental pulp cells and gingival epithelial cells by HEMA,” *Biomaterials*, vol. 26, no. 7, pp. 745–753, 2005.
  - [36] Y. C. Ho, F. M. Huang, and Y. C. Chang, “Mechanisms of cytotoxicity of eugenol in human osteoblastic cells *in vitro*,” *International Endodontic Journal*, vol. 39, no. 5, pp. 389–393, 2006.
  - [37] F. M. Huang, S. F. Yang, and Y. C. Chang, “Effects of root canal sealers on alkaline phosphatase in human osteoblastic cells,” *Journal of Endodontics*, vol. 36, no. 7, pp. 1230–1233, 2010.
  - [38] M. G. Brackett, A. Marshall, P. E. Lockwood et al., “Cytotoxicity of endodontic materials over 6-weeks *ex vivo*,” *International Endodontic Journal*, vol. 41, no. 12, pp. 1072–1078, 2008.
  - [39] B. Gao, X. Zhang, and Y. Zhu, “Studies on the preparation and antibacterial properties of quaternized polyethyleneimine,” *Journal of Biomaterials Science, Polymer Edition*, vol. 18, no. 5, pp. 531–544, 2007.
  - [40] N. Beyth, I. Yudovin-Farber, R. Bahir, A. J. Domb, and E. I. Weiss, “Antibacterial activity of dental composites containing quaternary ammonium polyethyleneimine nanoparticles against *Streptococcus mutans*,” *Biomaterials*, vol. 27, no. 21, pp. 3995–4002, 2006.
  - [41] X. Li, C. A. van Blitterswijk, Q. Feng, F. Cui, and F. Watari, “The effect of calcium phosphate microstructure on bone-related cells *in vitro*,” *Biomaterials*, vol. 29, no. 23, pp. 3306–3316, 2008.
  - [42] X. Li, H. Liu, X. Niu et al., “The use of carbon nanotubes to induce osteogenic differentiation of human adipose-derived MSCs *in vitro* and ectopic bone formation *in vivo*,” *Biomaterials*, vol. 33, no. 19, pp. 4818–4827, 2012.

## Research Article

# Cytotoxicity of Silver Nanoparticles in Human Embryonic Stem Cell-Derived Fibroblasts and an L-929 Cell Line

Hui Peng,<sup>1</sup> Xuehui Zhang,<sup>1</sup> Yan Wei,<sup>1</sup> Wentao Liu,<sup>1</sup> Shenglin Li,<sup>2,3</sup> Guangyan Yu,<sup>4</sup> Xin Fu,<sup>5</sup> Tong Cao,<sup>5</sup> and Xuliang Deng<sup>1</sup>

<sup>1</sup>Department of Geriatric Dentistry, Peking University School and Hospital of Stomatology, Beijing 100081, China

<sup>2</sup>Central Laboratory, Peking University School and Hospital of Stomatology, Beijing 100081, China

<sup>3</sup>Laboratory of Oral and Maxillofacial Surgery, Peking University School and Hospital of Stomatology, Beijing 100081, China

<sup>4</sup>Department of Oral and Maxillofacial Surgery, Peking University School and Hospital of Stomatology, Beijing 100081, China

<sup>5</sup>Faculty of Dentistry Research Laboratories, National University of Singapore, Singapore 119083

Correspondence should be addressed to Xuliang Deng, kqdengxuliang@bjmu.edu.cn

Received 4 April 2012; Accepted 20 May 2012

Academic Editor: Xiaoming Li

Copyright © 2012 Hui Peng et al. This is an open access article distributed under the Creative Commons Attribution License, which permits unrestricted use, distribution, and reproduction in any medium, provided the original work is properly cited.

Consensus about the toxicity of silver nanoparticles (Ag-NPs) has not been reached, even though extensive attention has been paid to this issue. This confusion may be due to physicochemical factors of Ag-NPs and the cell model used for biological safety evaluation. In the present study, human embryonic stem cell-derived fibroblasts (EBFs), which have been considered a closer representative of the *in vivo* response, were used as a novel cell model to assess the cytotoxicity of Ag-NPs (~20 nm and ~100 nm) in comparison with L-929 fibroblast cell line. Cell proliferation, cell cycle, apoptosis, p53 expression, and cellular uptake were examined. Results showed that Ag-NPs presented higher cytotoxicity to EBF than to L-929. EBF demonstrated a stronger capacity to ingest Ag-NPs, a higher G2/M arrest, and more upregulated p53 expression after exposed to Ag-NPs for 48 h when compared with L-929. It could be concluded that EBF exhibited a more sensitive response to Ag-NPs compared with L-929 cells, indicating that EBF may be a valid candidate for cytotoxicity screening assays of nanoparticles.

## 1. Introduction

The unique physicochemical properties of nanomaterials have allowed their rapid progress and acceptance into nanobiotechnology and life science. There are reports that silver nanoparticles (Ag-NPs) have been widely accepted in catheters [1], wound dressings [2], and the clothing and food industry [3] due to their efficacy as antimicrobial agents. Despite this progress, their potential adverse effects on human health and the environment have not yet been elaborately elucidated, and their biocompatibility remains controversial.

Ag-NPs may translocate to the circulatory system and distribute throughout the main organs of the body, especially the kidney, liver, and brain [4], and they can penetrate the blood-testis and blood-brain barriers [5]. This observation implies that Ag-NPs could become neurotoxic and genotoxic [4]. A previous study has reported that 15 nm Ag-NPs

could lead to drastically reduced mitochondrial function and cell viability of mouse spermatogonial stem cells at concentration of 5–10 µg/mL [6]. Hussain et al. [7] reported that 15 nm Ag-NPs exhibited significant cytotoxicity at 10–50 µg/mL in the BRL 3A cell line. Other studies have also reported adverse cellular reactions of Ag-NPs to other cell types, such as NIH3T3, vascular smooth muscle cells [8], and mouse embryonic stem cells [9]. But inconsistency, such as different toxic concentration, indeed exists among the results of numerous cytotoxicity studies, which may be ascribed to the varied cell models used in the evaluation of Ag-NPs cytotoxicity to a certain degree.

Recently, embryonic stem cells (ESCs) have gained great attention and showed multiple potential in tissue regeneration, drug screening, and biomaterial cytotoxicity test [10, 11]. With the development of methodologies for obtaining cells derived from human ESCs (hESCs), several advantages of the differentiated progenies from hESCs have been

reported. Unlike immortalized cell lines, which are usually of cancerous origin, containing chromosomal and genetic aberrations that produce immortality, and highly accustomed to *in vitro* culture conditions after countless passages, hESCs have been demonstrated to be genetically and karyotypically normal, which would make them more representative of how a normal cell should behave *in vivo*. Nowadays, several established hESC lines are readily available, from which an almost limitless supply of differentiated somatic progenies can be obtained. Furthermore, differentiated somatic progenies are expected to show little inter-batch variability, provided *in vitro* culture and differentiation protocols are well standardized [12]. Therefore, we proposed the hypothesis that differentiated somatic progenies derived from hESCs may be advantageous in the evaluation of Ag-NPs toxicity and may be used as a novel option in nanocytotoxicity studies.

This study was planned to study the cytotoxicity of Ag-NPs ( $\sim 20$  nm and  $\sim 100$  nm) to human embryonic stem cell-derived fibroblasts (EBFs) in comparison with L-929 cell line. Cell proliferation, cell cycle, apoptosis, p53 expression, and cellular uptake were examined. Whether EBF could be a valid candidate as a cell model for cytotoxicity screening of Ag-NPs or not was analyzed.

## 2. Materials and Methods

**2.1. Materials and Chemicals.** Ag-NPs with two different sizes, that is, Ag-NPs-1 ( $\sim 20$  nm) and Ag-NPs-2 ( $\sim 100$  nm), were provided by Hongwu Nanomaterial Co. Ltd. (Xuzhou, China). L-929 cells were obtained from the American Type Cell Culture Collection (ATCC, Rockville, MD, USA). Dulbecco's Modified Eagle's Medium (DMEM), RPMI 1640, fetal bovine serum (FBS), antibiotic agent (penicillin-streptomycin, PS), trypsin-EDTA, DMEM/F-12, knockout serum replacement, nonessential amino acid, and L-glutamine were purchased from Gibco (Grand Island, NY, USA). Basic fibroblast growth factor (bFGF) was obtained from Invitrogen (Carlsbad, CA, USA).  $\beta$ -mercaptoethanol was provided by Sigma-Aldrich (St. Louis, MO, USA). Annexin-V-FLUOS staining kit was purchased from Roche Molecular Biochemicals (Mannheim, Germany). Cell Counting Kit-8 (CCK-8) was purchased from Dojindo Laboratories (Tokyo, Japan). All other chemical solvents were of analytical grade with no further purification.

**2.2. Characterization of Ag-NPs.** Scanning electron microscopy (SEM), transmission electron microscope (TEM), and energy-dispersive X-ray spectroscopy (EDX) analysis were used to characterize the size, morphology, distribution, and chemical purity of the Ag-NPs.

**2.3. Cell Culture.** The NIH-registered hESC line, H9, was obtained from the National University of Singapore. H9 cells were cultured on a layer of mitomycin C-inactivated mouse embryonic fibroblasts (MEFs) in ESC medium (Table 1) at  $37^{\circ}\text{C}$  with 5%  $\text{CO}_2$  atmosphere and 95% humidity. H9 cells were digested with 1 mg/mL collagenase IV, scraped down from MEF feeder layers, and cultured as embryonic bodies (EBs) in suspension with EB medium (Table 1) for

5 days. Then, the EBs were transferred to a new flask coated with 0.1% gelatin and cultured with differentiation medium (Table 1). EBs differentiated spontaneously to fibroblast-like cells, named EBF cells. EBF and L-929 cells were, respectively, cultured in DMEM and RPMI 1640. Cells were maintained at  $37^{\circ}\text{C}$  in a 5%  $\text{CO}_2$  atmosphere and 95% humidity. The cells were subcultivated when they reached 80% confluence.

### 2.4. In Vitro Assay for Cytotoxic Activity of Ag-NPs

**2.4.1. Cell Viability Assay.** Cell viability was quantified using a CCK-8 assay as per manufacturer's protocol. In brief, cells were seeded in 96 well plates at a density of  $1 \times 10^4$  cells (200  $\mu\text{L}$ /well) followed by overnight incubation. The supernatant was then aspirated from the well, and fresh aliquots of growth medium (containing Ag-NPs in concentration of 0.5, 5, 50, and 500  $\mu\text{g}/\text{mL}$ ) after ultrasonic dispersion were added. After 24, 48, and 72 h, the supernatant was again aspirated, and cell monolayers were washed with PBS. Subsequently, water-soluble tetrazolium (WST) reagent (20  $\mu\text{L}$ ) was added in each well, incubated for 4 h, centrifuged, the supernatant obtained, and absorbance at two wavelengths (415 nm and 630 nm) was recorded using a microplate reader (Bio-Rad 680, Microplate Master, Hercules, CA, USA). The effect of nanoparticles on cells was expressed as the percentage of cell viability compared with the controls or relative proliferation rate (RPR), which is calculated as the following formula:  $\text{RPR} (\%) = (A - A_N) / A_N \times 100\%$ , where  $A$  represents the absorbance of each different concentration group;  $A_N$  is the absorbance of negative control group.

**2.4.2. Cell Cycle Analysis.** Cell cycle analysis was carried out by propidium iodide (PI) staining followed by flow cytometry measurement of the fluorescence. Approximately,  $1 \times 10^5$  cells were placed in cell culture flask. Following treatment with Ag-NPs (50  $\mu\text{g}/\text{mL}$ ) for 24, 48, and 72 h, the medium was removed and stored. Cells were washed in PBS, trypsinized, harvested in the stored medium, and centrifuged. The pellet was washed, fixed in ice-cold ethanol (70%), and stored at  $-20^{\circ}\text{C}$ . Before flow cytometry analysis, cells were washed in PBS and stained with PI in RNase (50  $\mu\text{g}/\text{mL}$  PI and 0.25 mg/mL RNase A) and incubated at  $37^{\circ}\text{C}$  for 1 h, followed by incubation at  $4^{\circ}\text{C}$  until analysis. Flow cytometry analysis was performed using BD FACS Calibur (BD Biosciences) at an excitation wavelength of 488 nm and emission wavelength of 610 nm. Data collected for  $1 \times 10^6$  cells was analyzed using CellQuest software 6.0 (BD Biosciences).

**2.4.3. Annexin-V Staining Apoptosis Analysis.** Annexin-V staining was performed to analyze apoptosis induced by Ag-NPs. Cells were treated with 50  $\mu\text{g}/\text{mL}$  Ag-NPs for 48 h. Cell preparation and experimental procedures were as for cell cycle analysis. The staining was performed as per manufacturer's instructions. Data analyses were performed using Cell Quest software 6.0.

TABLE 1: The component of cells culture medium.

Cells culture medium	Component
ESC medium	DMEM/F-12 supplemented with 20% knockout serum replacement, 4 ng/mL bFGF, 1 mmol/L L-glutamine, 1% non essential amino acid, and 0.1 mmol/L $\beta$ -mercaptoethanol
EB medium	DMEM/F-12 supplemented with 20% knockout serum replacement, 1 mmol/L L-glutamine, 1% non essential amino acid, and 0.1 mmol/L $\beta$ -mercaptoethanol
Differentiation medium	DMEM, 1 mmol/L L-glutamine and 10% FBS
EBF medium	DMEM containing 10 units/mL penicillin, 10 units/mL streptomycin and, 10% FBS
L-929 medium	RPMI 1640 containing 10 units/mL penicillin, 10 units/mL streptomycin, and 10% FBS

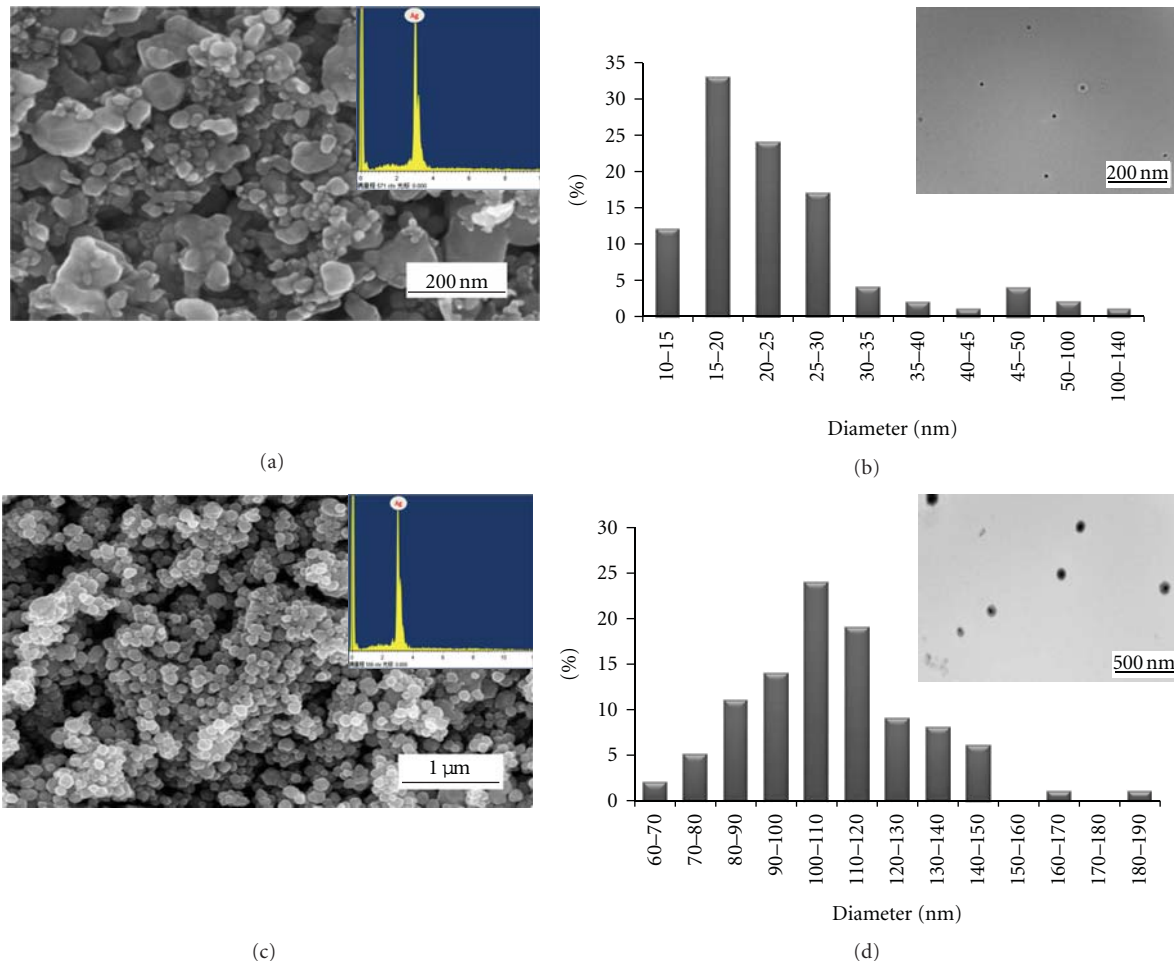


FIGURE 1: Characterization of Ag-NPs by SEM, EDX and TEM: (a) Ag-NPs-1 SEM with DEX image, (b) size distribution histogram and TEM image of Ag-NPs-1, (c) Ag-NPs-2 SEM with DEX images, (d) size distribution histogram and TEM image of Ag-NPs-2.

**2.5. Cellular Uptake and Quantitative Determination of the Uptake of Ag-NPs.** Ultrathin sections of cells were analyzed using TEM to reveal the uptake and distribution of NPs. Briefly, the cells ( $1.5 \times 10^6$ ) were treated with Ag-NPs (50  $\mu$ g/mL) for 48 h. At the end of the incubation period, culture flasks were washed many times with PBS to remove excess unbound NPs. Cells were trypsinized and fixed in 2.5% glutaraldehyde for 2 h. Fixed cells were washed with PBS. Postfixation staining was achieved using 1% osmium tetroxide for 1 h at room temperature. Cells were washed well, dehydrated in alcohol, and treated with propylene oxide

for 30 min, followed by treatment with propylene oxide, Spurr's low viscosity resin (1 : 1) for 18 h. Cells were further treated with pure resin for 24 h and embedded in BEEM capsules containing pure resin. Resin blocks were hardened at 70°C for 2 days. Ultrathin sections (70 nm) were cut using an ultramicrotome (Lecia EM UC6). The sections were stained with 1% lead citrate and 0.5% uranyl acetate and analyzed under transmission electron microscope examination (H-7650B, Hitachi, Japan).

Subconfluent cells were incubated at 37°C in the presence or absence of 50  $\mu$ g/mL Ag-NPs for 24 h under cell culture

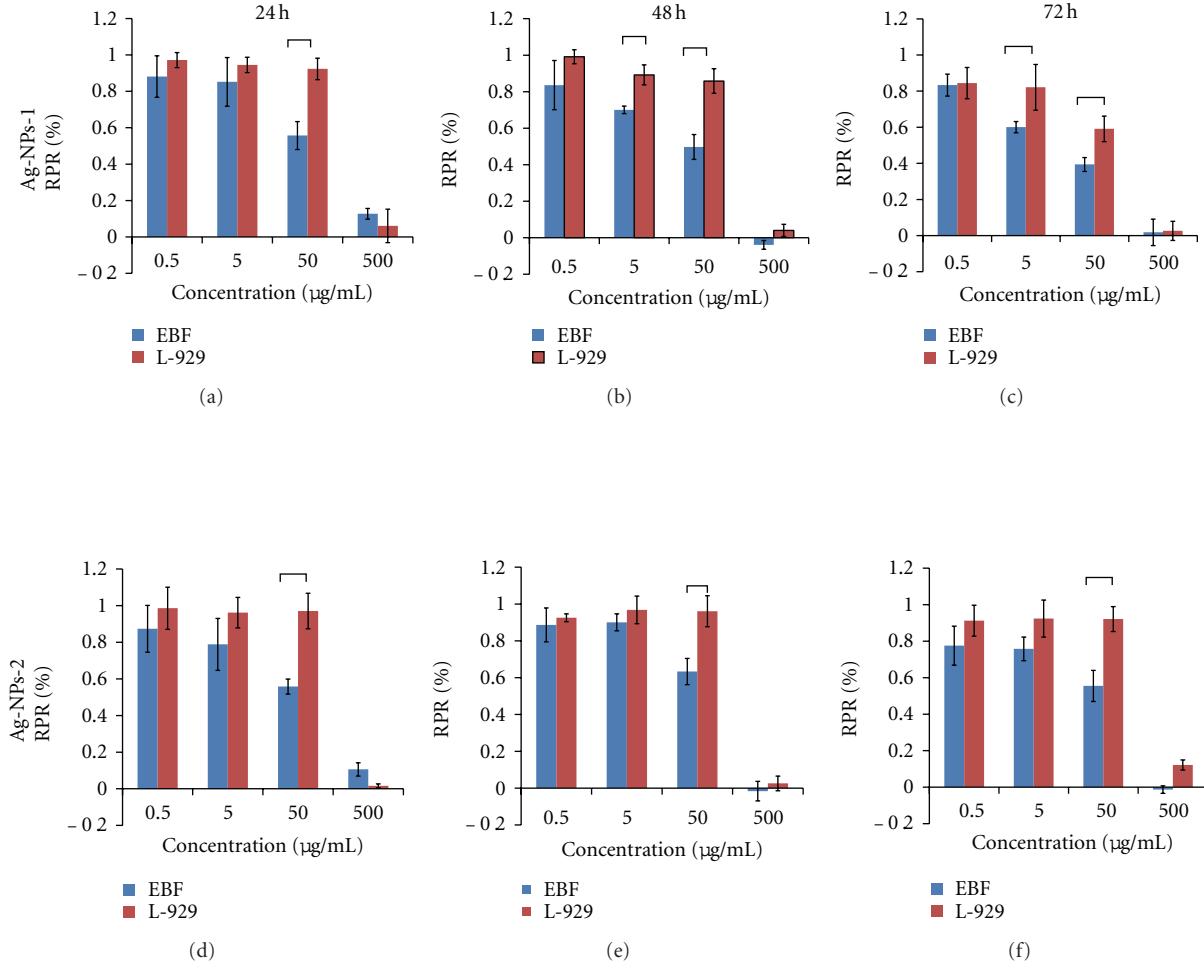


FIGURE 2: Cytotoxicity assay of EBF and L-929 cells after treatment with Ag-NPs (0.5–500 µg/mL) for 24, 48, and 72 h. (a) Ag-NPs-1 24 h, (b) Ag-NPs-1 48 h, (c) Ag-NPs-1 72 h, (d) Ag-NPs-2 24 h, (e) Ag-NPs-2 48 h, (f) Ag-NPs-2 72 h. \*Astatistically significant difference between EBF and L-929 cells ( $P < 0.05$ ).

conditions. Subsequently, the cells were washed with PBS, detached with trypsin and suspended in medium. The uptake of particles into cells was analyzed using flow cytometry. The side scatter data were analyzed using CELL Quest 6.0 software. Calibration reagents and solutions for flow cytometry were from Becton Dickinson. Ten thousand cells were acquired for each measurement.

**2.6. Real-Time Quantitative-Polymerase Chain Reaction (RTq-PCR).** To assess DNA damage associated with the Ag-NPs, the level of p53 expression in cells was detected using RTq-PCR. The cells were seeded with  $1 \times 10^5$  cells/dish and cultured with the 50 µg/mL Ag-NPs solution for 48 h. Total RNA was isolated with TRIZOL Reagent (Invitrogen) and was reverse transcribed using an iScript cDNA synthesis kit (Bio-Rad Laboratories). RTq-PCR was performed with a two-step RTq-PCR kit (Invitrogen) according to the manufacturer's instructions. The mRNA expression of p53, an important signaling molecule in checkpoint responses to DNA damage [13], was detected after treatment by a 7500 real-time PCR System (Applied Biosystems) with the SYBR

TABLE 2: Primers used for RTq-PCR.

Gene Name	Sequence
p53-human-R	CCGCAGTCAGATCCTAGCG
p53-human-F	AATCATCCAITGCTTGGGACG
p53-mouse-R	GTCACAGCACATGACGGAGG
p53-mouse-F	TCTTCCAGATGCTGGGATAC
GAPDH-human-R	AGGGGCCATCCACAGTCTTC
GAPDH-human-F	AGAAGGCTGGGCTATTG
GAPDH-mouse-R	GCTCCTGGAAGAGGGTGT
GAPDH-mouse-F	TCGTCCCGTAGACAAAATG

Premix Ex Taq Perfect Real Time kit (Takara Mirus Bio, Madison, WI). The sequences of the primer pairs are shown in Table 2.

**2.7. Statistical Analysis.** All experiments were performed in duplicate and repeated at least three times. The statistical significance of the data was expressed as mean  $\pm$  SD. Statistical

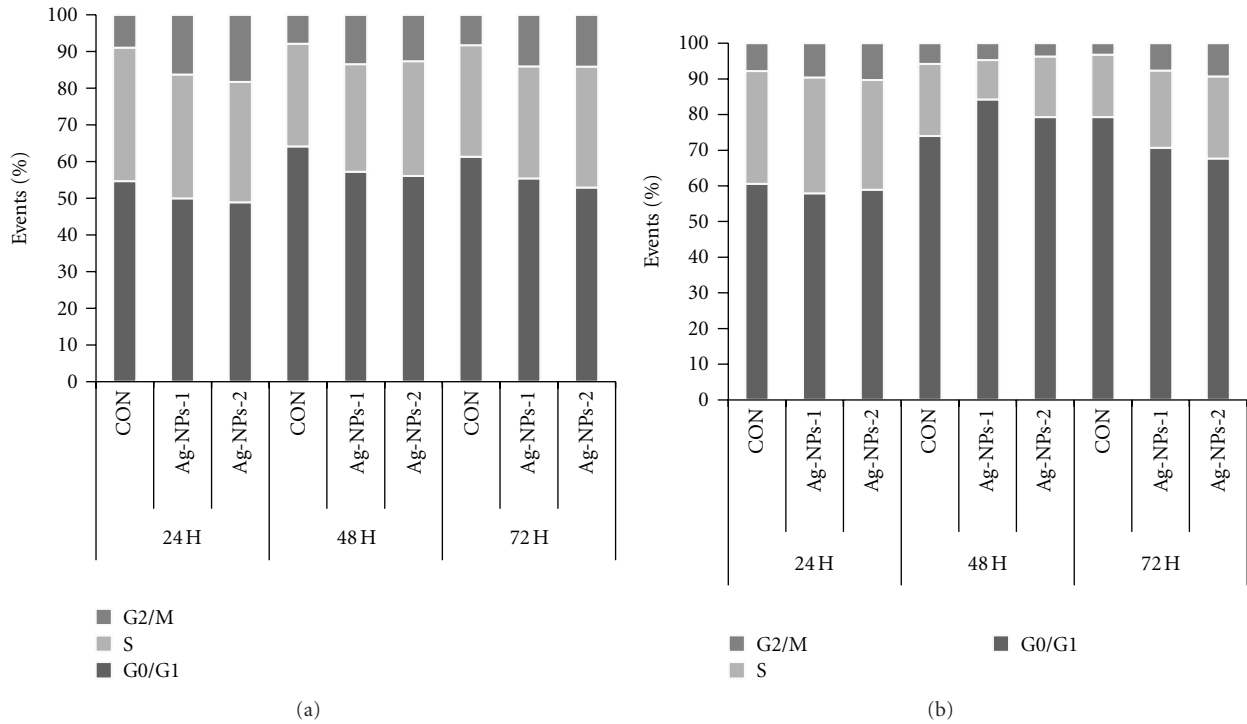


FIGURE 3: Cell cycle population of EBF (a) and L-929 cells (b) after treatment with Ag-NPs-1 and Ag-NPs-2.

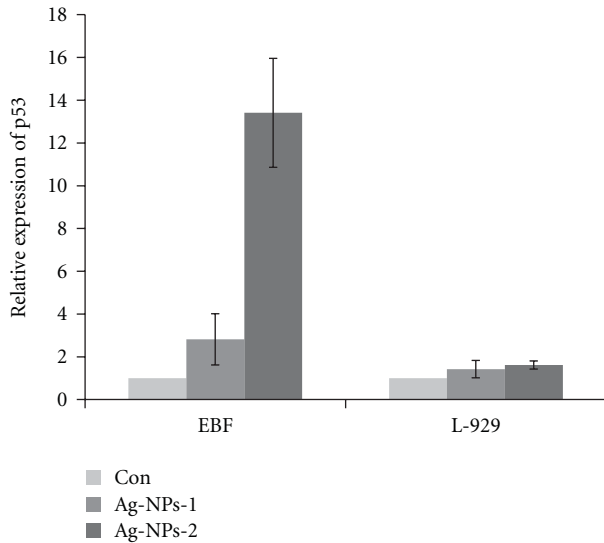


FIGURE 4: Expression of p53 in EBF and L-929 following Ag-NPs exposure for 48 h. \*Significant differences in comparison with control group ( $P < 0.05$ ). \*\*Highly significant differences in comparison with control group ( $P < 0.01$ ).

differences between groups were evaluated by Student *t*-test using the software SPSS 13.0 (SPSS Science). *P* values of less than 0.05 were considered to be statistically significant.

### 3. Results and Discussion

#### 3.1. Characterization of Ag-NPs.

Both kinds of Ag-NPs were observed to be spherical in shape (Figures 1(a) and 1(c))

under SEM, with average size of  $20 \text{ nm} \pm 12.6 \text{ nm}$  (Ag-NPs-1, Figure 1(b)) and  $100 \pm 21.3 \text{ nm}$  (Ag-NPs-2, Figure 1(d)), as measured by software Image J (National Institutes of Health, USA). EDX results demonstrated that the nanoparticles were 100% pure silver. TEM image showed the even distribution of Ag-NPs dispersed in water.

#### 3.2. Cytotoxicity of Ag-NPs

**3.2.1. Cell Viability of EBF and L-929 Cells.** Cell viability was quantified using a CCK-8 assay. Figure 2 displays the RPR of EBF and L-929 cells after 24, 48, and 72 h exposure to Ag-NPs-1 and Ag-NPs-2 at concentration of  $0.5\text{--}500 \mu\text{g/mL}$ . The RPR were decreased in a dose-dependent manner and the RPR of EBF treated with Ag-NPs of both size were lower than that of L-929 cells at the same concentration and time point.  $50 \mu\text{g/mL}$  was shown the threshold concentration that significantly inhibited EBF proliferation, and this concentration was used in all subsequent experiments including cell cycle analysis, apoptosis assay, cellular uptake, and p53 expression. When the NPs concentration reached  $500 \mu\text{g/mL}$ , nearly no viable cells existed. CCK-8 results also showed apparent size-dependent cytotoxic effects on cell proliferation. The RPR of EBF treated with Ag-NPs-1 was lower than that of Ag-NPs-2 at  $5\text{--}50 \mu\text{g/mL}$ , both at 48 and 72 h. However, the size-dependent cytotoxic effects on L-929 cells occurred only at  $50 \mu\text{g/mL}$  after 72 h exposure in this study. These results indicated that EBF may be more vulnerable to Ag-NPs treatment when compared with L-929 cell line.

The dose-dependent toxicity pattern of Ag-NPs was consistent with previous studies on mammalian germline stem cells [6] and may be due to the impact of endocytosis

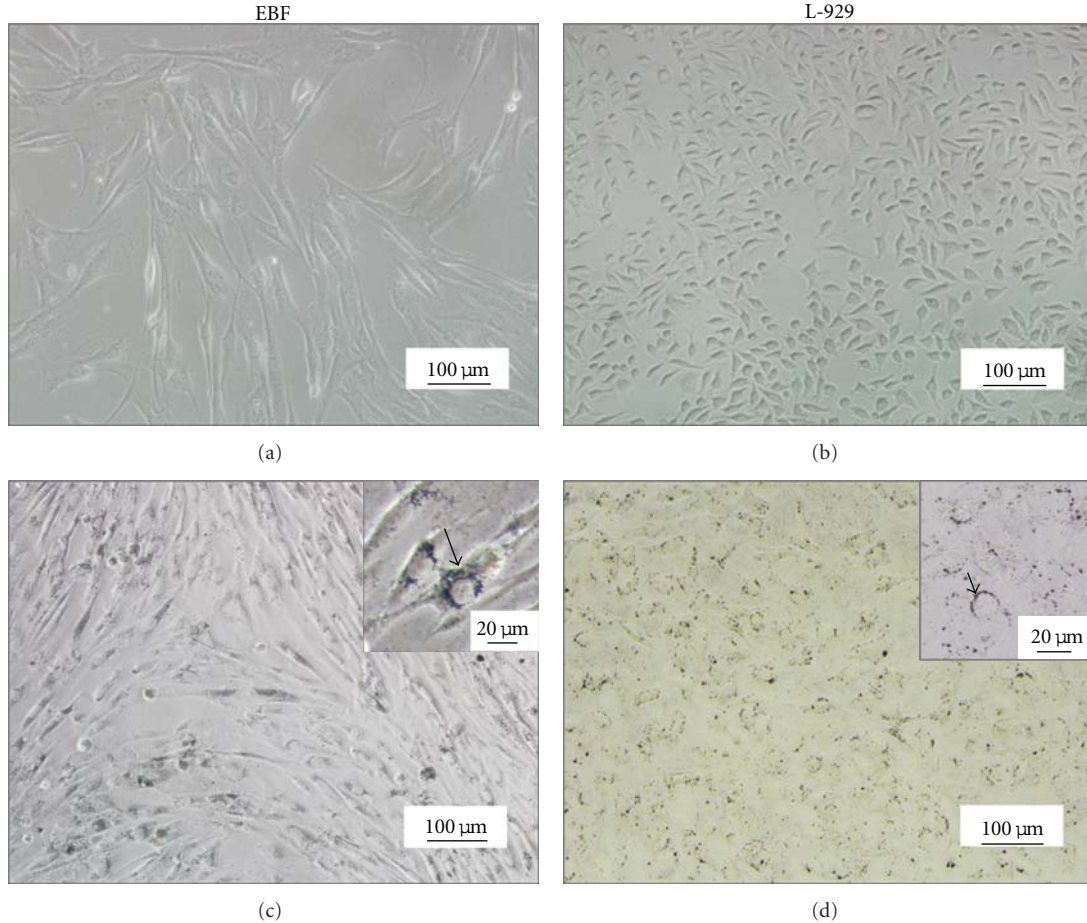


FIGURE 5: Phase-contrast micrographs (magnification 200x) of EBF and L-929 cells before (a) and (b) and after (c) and (d) treatment with Ag-NPs-1 at 50  $\mu\text{g}/\text{mL}$  for 48 h. The insets show the high magnification (magnification 400x).

and metabolism inhibiting normal cellular activity at larger concentrations of Ag-NPs. The results in our study that cell proliferation in EBF was more sensitive to Ag-NPs give evidence for a cell-type-dependent response in biomaterials cytotoxicity test. Similarly, Cao et al. [14] reported that mitomycin C decreased EBF viability more obviously than L-929 cells and considered that EBF were more sensitive than L-929 cells in cytotoxicity screening tests. Tedja et al. [15] noticed that the different level of biological response should be primarily attributed to the difference in the amount of cellular particle uptake between different cell types. Hence, the cell-type-specific response of cells to Ag-NPs here could be due to that EBF are genetically and karyotypically normal and exhibited a stronger capacity to ingest NPs (Figure 7). Previous studies have also indicated that Ag-NPs have a size-dependent cytotoxicity, with smaller particles being more toxic [16, 17]. According to Carlson et al. [18], Ag-15 nm and Ag-30 nm NPs showed more cytotoxicity than that of Ag-55 nm. Our study revealed similar findings that the RPR of EBF and L-929 cells treated with Ag-NPs-1 was lower than that with Ag-NPs-2. The reason may be that smaller Ag-NPs have a larger surface area available for interaction and lead to a stronger effect than larger particles [19].

**3.2.2. Cell Cycle Analysis.** The influence of NPs on the cell cycle was analyzed by subjecting the NP-treated cells to flow cytometry. In control group, major cell populations were observed in the G1 phase, whereas in Ag-NPs treated cells, a decrease in the G1 cell population was accompanied by an increase in the G2/M cell population (Figure 3). The G2/M population of Ag-NPs treated EBF cells were significantly increased to almost twice the control values at 24, 48, and 72 h (Figure 3(a)). G2/M arrest of L-929 cells was observed at 72 h (Figure 3(b)). DNA damage was proposed to be the main cause of cell cycle arrest [20]. AshaRani et al. [21] reported oxidative stress in Ag-NPs treated cells indicating the possibility of DNA damage and chromosomal aberrations which was considered the prime factors resulting in cell cycle arrest. The results in this study indicated that EBF cells may be more vulnerable to Ag-NPs than the L-929 cell line.

**3.2.3. Apoptosis and DNA Damage Induced by Ag-NPs.** Annexin-V staining indicated that the rate of EBF cells apoptosis was increased from  $0.77 \pm 0.08\%$  (control) to  $2.88 \pm 0.23\%$  (Ag-NPs-1) and  $1.49 \pm 0.33\%$  (Ag-NPs-2) at 50  $\mu\text{g}/\text{mL}$ , whereas that of L-929 cells treated with the

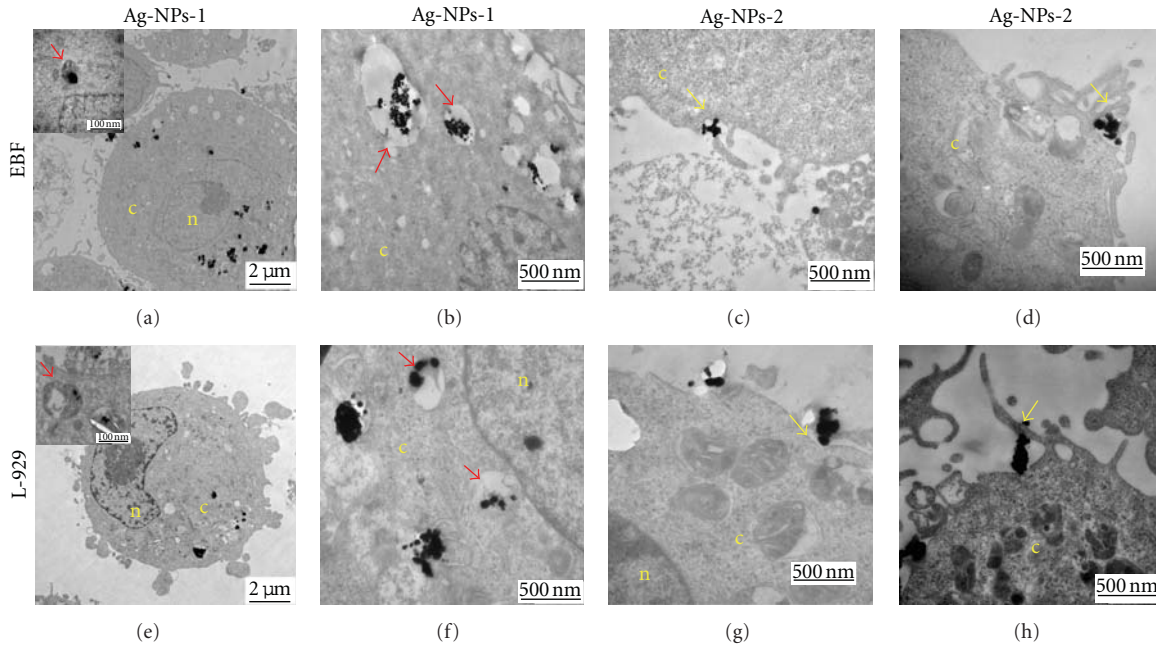


FIGURE 6: TEM images of ultrathin sections of EBF (a)-(d) and L-929 (e)-(h) cells treated with Ag-NPs after 48 h. Nanoparticles were showed inside the cytoplasm (c), but they were not in the nucleus (n) of both cell types. Cells showed large endosomes (a) and (e) and lysosomes (b) and (f) with nanoparticles inside (red arrow). Invagination (c) and (g) and protrusion (d) and (h) of the plasma membrane were observed when Ag-NPs attached the cells (yellow arrow).

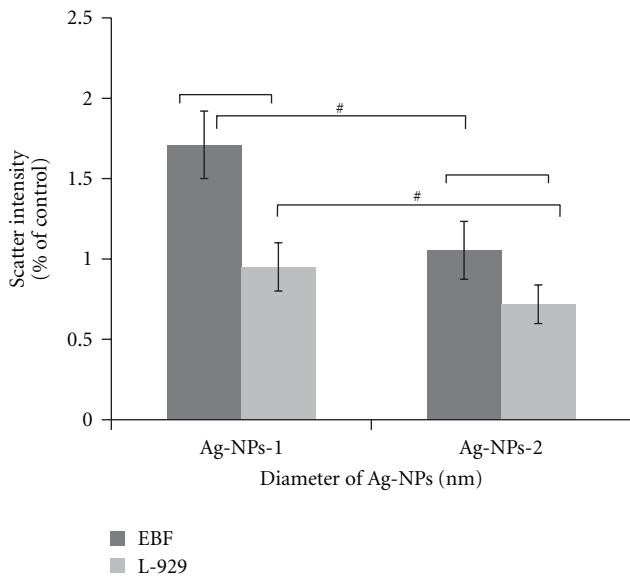


FIGURE 7: Intracellular occurrence of Ag-NPs agglomerates analyzed using flow cytometric light scatter. \*Significant differences between EBF and L-929 cells ( $P < 0.05$ ). #Significant differences between Ag-NPs-1 and Ag-NPs-2 groups.

same concentration of Ag-NPs had no significant change compared with the control (Table 3). This result showed that the impact of early apoptosis, at the concentration of Ag-NPs selected in our study, was not apparent, but the value

TABLE 3: The rate of apoptosis treated with Ag-NPs.

	Control	Ag-NPs-1	Ag-NPs-2
EBF	$0.77 \pm 0.08$	$2.88 \pm 0.23^*$	$1.49 \pm 0.33^*$
L-929	$0.63 \pm 0.13$	$0.74 \pm 0.09$	$0.67 \pm 0.29$

\*  $P < 0.05$  compared with control.

did show that Ag-NPs might cause EBF apoptosis. In the presence of DNA damage, p53 accumulates and triggers cell cycle arrest to provide time for the damage to be repaired [22]. Therefore, p53 expression could be assessed by RTq-PCR to monitor the DNA damage indirectly. Data in Figure 4 showed that expression of p53 in EBF cells treated with both sized Ag-NPs within 48 h increased significantly. Especially in Ag-NPs-2 treated EBF cells, their p53 expression even reached almost 14 times of the control group. While the changes observed in the L-929 cells were not statistically significant (Figure 4). Ahamed et al. [9] have also indicated that Ag-NPs up-regulated p53, Rad51 and phosphorylated-H2AX expression. This observation supported the hypothesis that Ag-NPs can cause DNA damage and resulted in G2/M cell cycle arrest, which may be correlated to long-term effects, such as mutagenesis or carcinogenesis [23].

**3.3. Cellular Uptake and Distribution of Ag-NPs.** Under phase-contrast microscopy, Ag-NPs were observed in the cytoplasm of both cell types and gathered in the perinucleus.

Single or clustered NPs were attached to the cell membrane and were internalized into cells (Figures 5(c) and 5(d)). TEM images also showed that the NPs were distributed throughout the cytoplasm, but they were not observed in the nucleus of both cell types (Figures 6(a) and 6(e)). According to the TEM images, there were no significant differences in cellular uptake between the two cell types. Large endosomes and lysosomes with Ag-NPs were also observed (Figures 6(a), 6(b), 6(e), and 6(f)). Invagination of plasma membranes (Figures 6(c) and 6(g)) denoted the endocytosis of nanomaterials. The protrusion of the plasma membrane (Figures 6(d) and 6(h)) for uptake of the nanospheres indicated the characteristics of endocytosis and macropinocytosis. These results suggested that Ag-NPs were entering the cells through pinocytosis rather than diffusion. Greulich et al. [24] have reported that the uptake of PVP-coated Ag-NPs was significantly inhibited by chlorpromazine and wortmannin, suggesting endocytosis and macropinocytosis were the primary uptake mechanisms.

The uptake of nanomaterials depended not only on the particle size and charge, but also on the cell type [25]. The quantitative uptake of Ag-NPs was determined by analysis of the intracellular side scatter signal using flow cytometry. As Figure 7 demonstrated, EBF had the stronger uptake capacity of Ag-NPs compared with L-929 cells. The results also showed that both cell types took up more Ag-NPs-1 particles than Ag-NPs-2, which might be due to the smaller diameter and resulted in size-dependent nanotoxicity. The differences in uptake capacity between cell lines can be explained by the differentiation state of the cells. There was report that endocytosis was normally downregulated after treatment of dendritic cells with maturation stimuli [26]. As differentiated progenies from hESCs, EBFs were less mature than L-929 immortalized cells. Hence, it could be reasonable to speculate that the difference between uptake capacity of EBFs and L-929 might be owing to the differing differentiation state. The cellular uptake mechanisms, depending on cell type and particle size, may also be contributed to, or triggered by, the ability of NPs to penetrate the plasma membrane [27]. The uptake of the NPs appears to be quite complicated, therefore, further work is required to elucidate the underlying cellular uptake mechanism elaborately.

#### 4. Conclusion

In this study, the results showed that cytotoxicity of Ag-NPs was dependent on dose, cell type, and particle size. Ag-NPs presented higher cytotoxicity to EBF than to L-929. EBF exhibited an higher G2/M arrest and more upgraded p53 expression after exposed to Ag-NPs for 48 h when compared with L-929. According to the cellular uptake analysis, the NPs were found in the cytoplasm and lysosomes, but they were not observed in the nucleus. EBF demonstrated a stronger capacity to ingest Ag-NPs. According to the results of this study, it could be postulated that EBF was more sensitive to Ag-NPs than L-929. Taking into account of its more representative of how a normal cell should behave *in vivo*, EBF could be considered a promising candidate for cell model of nanomaterials cytotoxicity screening.

#### Acknowledgments

The authors would like to thank the National University of Singapore for the stem cell resources and Center of Biomedical Analysis at Tsinghua University for the electron microscopy resources. This work was supported by the National Basic Research Program of China (2012CB933904), the National Natural Science Foundation of China (no. 81171000) and International S&T Cooperation Program of China (ISTCP, 2011DFA32190).

#### References

- [1] U. Samuel and J. P. Guggenbichler, "Prevention of catheter-related infections: the potential of a new nano-silver impregnated catheter," *International Journal of Antimicrobial Agents*, vol. 23, no. 1, supplement 1, pp. S75–S78, 2004.
- [2] J. Chen, C. M. Han, X. W. Lin, Z. J. Tang, and S. J. Su, "Effect of silver nanoparticle dressing on second degree burn wound," *Zhonghua Wai Ke Za Zhi*, vol. 44, no. 1, pp. 50–52, 2006.
- [3] N. Vigneshwaran, A. A. Kathe, P. V. Varadarajan, R. P. Nachane, and R. H. Balasubramanya, "Functional finishing of cotton fabrics using silver nanoparticles," *Journal of Nanoscience and Nanotechnology*, vol. 7, no. 6, pp. 1893–1897, 2007.
- [4] J. Tang, L. Xiong, S. Wang et al., "Distribution, translocation and accumulation of silver nanoparticles in rats," *Journal of Nanoscience and Nanotechnology*, vol. 9, no. 8, pp. 4924–4932, 2009.
- [5] H. S. Sharma, S. Hussain, J. Schlager, S. F. Ali, and A. Sharma, "Influence of nanoparticles on blood-brain barrier permeability and brain edema formation in rats," *Acta Neurochirurgica Supplement*, vol. 106, pp. 359–364, 2010.
- [6] L. Braydich-Stolle, S. Hussain, J. J. Schlager, and M. C. Hofmann, "In vitro cytotoxicity of nanoparticles in mammalian germline stem cells," *Toxicological Sciences*, vol. 88, no. 2, pp. 412–419, 2005.
- [7] S. M. Hussain, K. L. Hess, J. M. Gearhart, K. T. Geiss, and J. J. Schlager, "In vitro toxicity of nanoparticles in BRL 3A rat liver cells," *Toxicology in Vitro*, vol. 19, no. 7, pp. 975–983, 2005.
- [8] Y.-H. Hsin, C.-F. Chen, S. Huang, T.-S. Shih, P.-S. Lai, and P. J. Chueh, "The apoptotic effect of nanosilver is mediated by a ROS- and JNK-dependent mechanism involving the mitochondrial pathway in NIH3T3 cells," *Toxicology Letters*, vol. 179, no. 3, pp. 130–139, 2008.
- [9] M. Ahamed, M. Karns, M. Goodson et al., "DNA damage response to different surface chemistry of silver nanoparticles in mammalian cells," *Toxicology and Applied Pharmacology*, vol. 233, no. 3, pp. 404–410, 2008.
- [10] J. Rohwedel, K. Guan, C. Hegert, and A. M. Wobus, "Embryonic stem cells as an in vitro model for mutagenicity, cytotoxicity and embryotoxicity studies: present state and future prospects," *Toxicology in Vitro*, vol. 15, no. 6, pp. 741–753, 2001.
- [11] H. Spielmann, E. Genschow, G. Scholz et al., "Preliminary results of the ECVAM validation study on three in vitro embryotoxicity tests," *ATLA Alternatives to Laboratory Animals*, vol. 29, no. 3, pp. 301–303, 2001.
- [12] G. Sinha, "Cell biology. Human embryonic stem cells may be toxicology's new best friends," *Science*, vol. 308, no. 5728, p. 1538, 2005.
- [13] A. Sancar, L. A. Lindsey-Boltz, K. Ünsal-Kaçmaz, and S. Linn, "Molecular mechanisms of mammalian DNA repair and the

- DNA damage checkpoints," *Annual Review of Biochemistry*, vol. 73, pp. 39–85, 2004.
- [14] T. Cao, K. Lu, X. Fu, and B. C. Heng, "Differentiated fibroblastic progenies of human embryonic stem cells for toxicology screening," *Cloning and Stem Cells*, vol. 10, no. 1, pp. 1–10, 2008.
  - [15] R. Tedja, C. Marquis, M. Lim, and R. Amal, "Biological impacts of TiO<sub>2</sub> on human lung cell lines A549 and H1299: particle size distribution effects," *Journal of Nanoparticle Research*, vol. 13, no. 9, 2011.
  - [16] B. Carlson, K. Leschkies, E. S. Aydil, and X. Y. Zhu, "Valence band alignment at cadmium selenide quantum dot and zinc oxide (10(1)over-bar0) interfaces," *Journal of Physical Chemistry C*, vol. 112, no. 22, pp. 8419–8423, 2008.
  - [17] M. V. Park, A. M. Neigh, J. P. Vermeulen, L. J. de la Fonteyne, H. W. Verharen, J. J. Briede et al., "The effect of particle size on the cytotoxicity, inflammation, developmental toxicity and genotoxicity of silver nanoparticles," *Biomaterials*, vol. 32, no. 36, pp. 9810–9817, 2011.
  - [18] C. Carlson, S. M. Hussein, A. M. Schrand et al., "Unique cellular interaction of silver nanoparticles: size-dependent generation of reactive oxygen species," *Journal of Physical Chemistry B*, vol. 112, no. 43, pp. 13608–13619, 2008.
  - [19] R. C. Doty, T. R. Tshikhudo, M. Brust, and D. G. Fernig, "Extremely stable water-soluble Ag nanoparticles," *Chemistry of Materials*, vol. 17, no. 18, pp. 4630–4635, 2005.
  - [20] M. C. Stensberg, Q. Wei, E. S. McLamore, D. M. Porterfield, A. Wei, and M. S. Sepúlveda, "Toxicological studies on silver nanoparticles: challenges and opportunities in assessment, monitoring and imaging," *Nanomedicine*, vol. 6, no. 5, pp. 879–898, 2011.
  - [21] P. V. AshaRani, G. L. K. Mun, M. P. Hande, and S. Valiyaveettill, "Cytotoxicity and genotoxicity of silver nanoparticles in human cells," *ACS Nano*, vol. 3, no. 2, pp. 279–290, 2009.
  - [22] C. J. Sherr, "Principles of Tumor Suppression," *Cell*, vol. 116, no. 2, pp. 235–246, 2004.
  - [23] R. Paillot, F. Laval, J. C. Audonnet, C. Andreoni, and V. Juillard, "Functional and phenotypic characterization of distinct porcine dendritic cells derived from peripheral blood monocytes," *Immunology*, vol. 102, no. 4, pp. 396–404, 2001.
  - [24] C. Greulich, J. Diendorf, T. Simon, G. Eggeler, M. Epple, and M. Köller, "Uptake and intracellular distribution of silver nanoparticles in human mesenchymal stem cells," *Acta Biomaterialia*, vol. 7, no. 1, pp. 347–354, 2011.
  - [25] L. W. Zhang and N. A. Monteiro-Riviere, "Mechanisms of quantum dot nanoparticle cellular uptake," *Toxicological Sciences*, vol. 110, no. 1, pp. 138–155, 2009.
  - [26] F. Sallusto and A. Lanzavecchia, "Efficient presentation of soluble antigen by cultured human dendritic cells is maintained by granulocyte/macrophage colony-stimulating factor plus interleukin 4 and downregulated by tumor necrosis factor  $\alpha$ ," *Journal of Experimental Medicine*, vol. 179, no. 4, pp. 1109–1118, 1994.
  - [27] K. Kostarelos, L. Lacerda, G. Pastorin et al., "Cellular uptake of functionalized carbon nanotubes is independent of functional group and cell type," *Nature Nanotechnology*, vol. 2, no. 2, pp. 108–113, 2007.

## Research Article

# Toxicity of Aqueous Fullerene nC<sub>60</sub> to Activated Sludge: Nitrification Inhibition and Microtox Test

**Yongkui Yang,<sup>1</sup> Norihide Nakada,<sup>1</sup> Ryoji Nakajima,<sup>2</sup> Chao Wang,<sup>1</sup> and Hiroaki Tanaka<sup>1</sup>**

<sup>1</sup> Research Center for Environmental Quality Management, Kyoto University, 1-2 Yumihama, Otsu 520-0811, Japan

<sup>2</sup> Testing and Analysis Division, Shimadzu Techno Research Inc., 1 Nishinokyo-Shimoaicho, Nakagyo-ku, Kyoto 604-8436, Japan

Correspondence should be addressed to Yongkui Yang, ykyang@biwa.eqc.kyoto-u.ac.jp

Received 3 April 2012; Accepted 11 June 2012

Academic Editor: Xiaoming Li

Copyright © 2012 Yongkui Yang et al. This is an open access article distributed under the Creative Commons Attribution License, which permits unrestricted use, distribution, and reproduction in any medium, provided the original work is properly cited.

The increasing production and use of fullerene nanomaterials raised their exposure potential to the activated sludge during biological wastewater treatment process. In this study, the toxicity of aqueous nanoscaled C<sub>60</sub> (nC<sub>60</sub>) to activated sludge was investigated using nitrification inhibition and Microtox test. The test solutions of nC<sub>60</sub> were prepared using two methods: long stirring (Stir/nC<sub>60</sub>) and toluene exchange (Tol/nC<sub>60</sub>). The nC<sub>60</sub> aggregation in test medium was also evaluated for toxicity assessment. The results showed that the nC<sub>60</sub> aggregation behaved differently in two test mediums during the incubation periods. The nC<sub>60</sub> toxicity was greatly influenced by the preparation method. Stir/nC<sub>60</sub> presented no significant toxicity to both the nitrification sludge and bioluminescent bacteria at the maximum concentration studied. In contrast, the EC<sub>20</sub> of Tol/nC<sub>60</sub> was obtained to be 4.89 mg/L (3 h) for the nitrification inhibition and 3.44 mg/L (30 min) for Microtox test, respectively.

## 1. Introduction

Fullerenes, carbon-based nanomaterials, are demonstrating rapid increase in the commercial and scientific interest by their unique properties, such as, chemically and thermally stable, excellent electron acceptor and radical scavenger, and special optical properties [1, 2]. The production is expected up to 1500 t in 2007 compared to 400 kg in 2002 by the largest fullerene production company in the world [3]. In addition, until 2011 the class of fullerenes and other carbon-based nanomaterials is ranked as the second among all the nanomaterials used in consumer products available [4].

The C<sub>60</sub>, the main type of fullerenes, showed the toxicity on cell [5], bacterial [6, 7], and fish [8, 9]. Although the toxicity mechanism is still not clear, the most published is due to the oxidative stress via reactive oxygen species dependent [5] or independent [10]. The toxicities suggested the potential of adverse effect of C<sub>60</sub> on the activated sludge which is important for the removal of organic matters and nutrient compounds in wastewater. Recent studies pointed out the toxicity of metal nanoparticles (silver [11, 12], copper [13], zinc oxide, and titanium dioxide [14]), on the aerobic/anaerobic activated sludge. However, very limited

studies focused on fullerene C<sub>60</sub> toxicity on the activated sludge. Kang et al. [15] reported about 30% inactivation of microorganism in wastewater samples after 1 h exposure to nC<sub>60</sub>-coated filter. However, no significant change was identified to microbial community structure in the anaerobic sludge using the denaturing gradient gel electrophoresis analysis under 50 g/kg biomass [16].

The objective of this study is to assess the toxicity of aqueous nC<sub>60</sub> on the activated sludge. The effect of nC<sub>60</sub> on nitrification activities was investigated using the cultivated activated nitrifying sludge. The Microtox test was also conducted as a standardized screening test. To our best knowledge, this is the first study on the nC<sub>60</sub> toxicity on activated sludge by checking the nitrification inhibition. This work is expected to provide useful information to assess the effect of nC<sub>60</sub> on activated sludge and consequent treatment performance of biological wastewater treatment process.

## 2. Materials and Methods

**2.1. Preparation of Aqueous nC<sub>60</sub> Suspension.** Two types of aqueous nC<sub>60</sub> were prepared using the extended mixing of

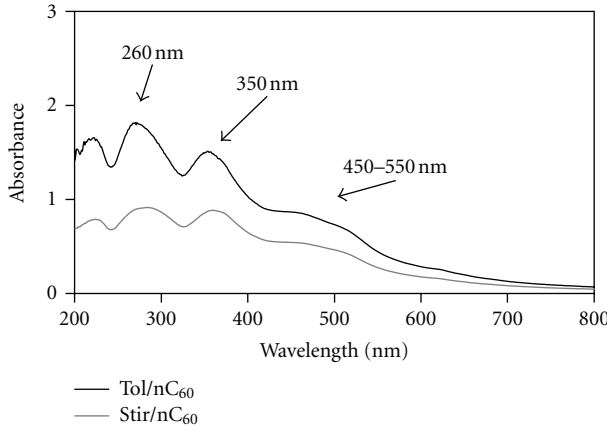


FIGURE 1: UV-visible absorption spectra of prepared nC<sub>60</sub> (pH 5.6).

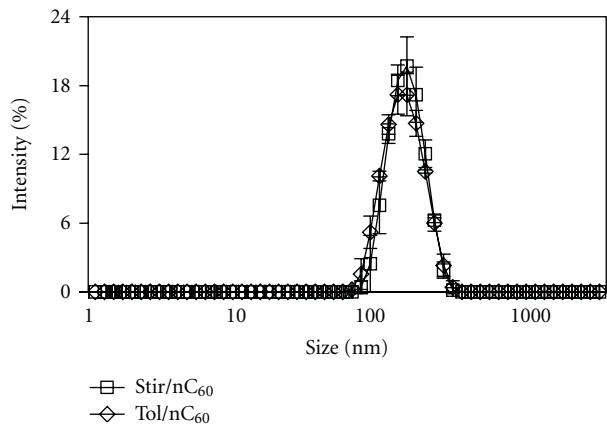


FIGURE 2: Size distribution of prepared nC<sub>60</sub>. Error bars represent the standard error (pH 5.6,  $n = 2$ ).

powder C<sub>60</sub> in water (Stir/nC<sub>60</sub>) and the toluene-involved solvent exchange method (Tol/nC<sub>60</sub>), both of which are widely used for the studies of the C<sub>60</sub> toxicity [7, 9, 15] and its fate [17, 18]. Briefly, the Stir/nC<sub>60</sub> was produced by adding 200 mg of powder C<sub>60</sub> (purity: 99.9%, SES research, USA) to 300 mL of ultrapure water (Millipore, USA) and then mixing with a magnetic stirrer at 500 rpm for three weeks. And the Tol/nC<sub>60</sub> was prepared by following the previously reported method with minor modifications [7]. Specifically, 1000 mg/L C<sub>60</sub> solution was obtained by dissolving the powder C<sub>60</sub> into HPLC grade toluene (stock C<sub>60</sub> toluene solution). And then 40 mL of the solution was added to 100 mL ultrapure water. The toluene was removed by sonication at 40°C using an ultrasonic cleaner (AS ONE, Japan) followed by the purge with gentle stream of nitrogen gas at 0.5 L/min for 1 h. The prepared Stir/nC<sub>60</sub> and Tol/nC<sub>60</sub> suspensions were, both of yellow colour, sequentially filtered through a glass filter (pore size: 1 μm, Pall Life Sciences, USA) and cellulose acetate filter (pore size: 0.45 μm, Advantec, Japan). In addition, a blank sample for Tol/nC<sub>60</sub> was also prepared by adding the same amount of toluene (without C<sub>60</sub>) in the pure water followed by the same procedures of

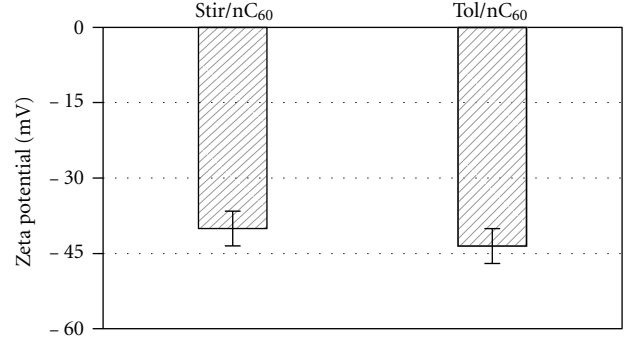


FIGURE 3: Zeta potential of prepared nC<sub>60</sub>. Error bars represent the standard error (pH 5.6,  $n = 2$ ).

sonication and filtrations. The resulting suspensions were stored in the dark at 4°C until use. The nC<sub>60</sub> concentration was determined by extracting nC<sub>60</sub> into the toluene phase and quantifying it at 332 nm by the UV/vis spectrometer, described elsewhere [7, 19, 20]. The calibration curve was obtained by the stock C<sub>60</sub> toluene solution at different concentrations ( $n = 5$ ).

**2.2. Cultivation of Nitrifying Activated Sludge.** The seed-activated sludge was collected from the nitrification tank of a biological wastewater treatment plant. The nitrifying activated sludge was obtained by cultivating the seed sludge at 30°C in a 3 L water-jacketed glass reactor. The reactor was operated at fill and draw mode at a hydraulic retention time of 12 h and sludge retention time of 20 d in the dark. Dissolved oxygen was kept at above 1.0 mg/L by introducing the filtered compressed air via diffusers, and the pH was maintained at 7.5 ± 0.1 with the automatic addition of 1 M Na<sub>2</sub>CO<sub>3</sub>. The feed solution only consisted of the inorganic medium with the 25 mM (NH<sub>4</sub>)<sub>2</sub>SO<sub>4</sub>. The other nutrient composition, data acquisition, and process control were described in the previous study [21]. After reaching the steady state by checking the NH<sub>4</sub><sup>+</sup> removal efficiency, the mixed liquor in the reactor was collected and washed three times using 40 mM KH<sub>2</sub>PO<sub>4</sub> buffer (pH 7.8) by centrifugation (2000 g × 5 min).

**2.3. Nitrification Inhibition Experiment.** The nitrification inhibition studies were conducted in accordance with the ISO 9509 test guideline [22]. Batch experiments were carried out by agitating 100 mL Erlenmeyer flasks containing 50 mL medium solution (2 mM (NH<sub>4</sub>)<sub>2</sub>SO<sub>4</sub> and 6 mM (NaHCO<sub>3</sub>)), determined nitrifying activated sludge and different amounts of nC<sub>60</sub> at controlled room temperature (25°C). The experimental conditions, the incubating time of 3 h and MLSS of 40 mg/L, were determined to ensure about 50% of initial NH<sub>4</sub><sup>+</sup> that was left at the end of incubating time to avoid rate limiting [22]. The dissolved oxygen was kept at above 4 mg/L by the shaking (150 rpm) on a rotary shaker. The nitrification inhibition (I) was calculated by the difference of oxidized N

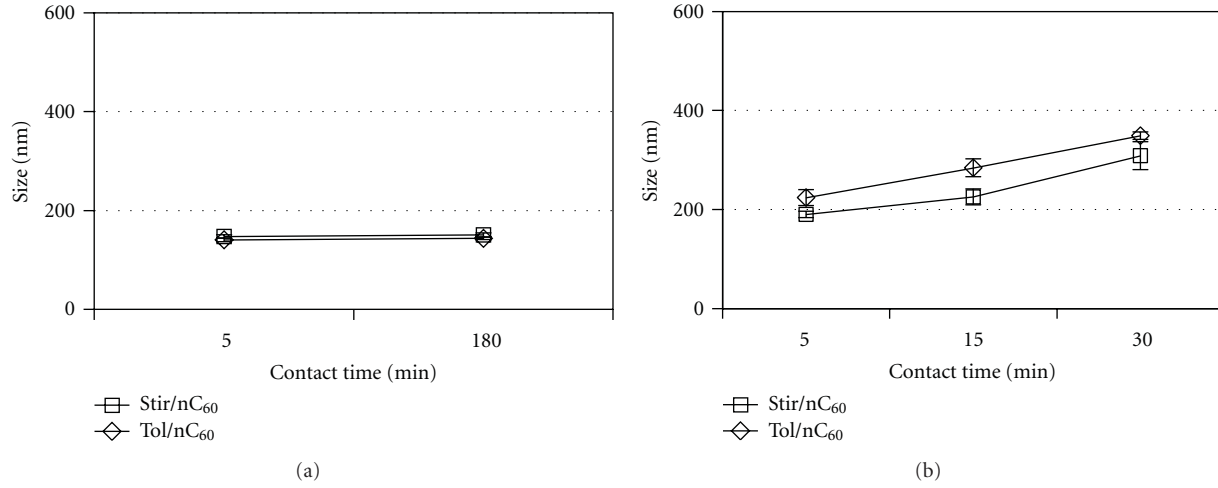


FIGURE 4: Change in nC<sub>60</sub> size in medium for nitrification inhibition (a) and Microtox test (b). Error bars represent the standard error ( $n = 2$ ).

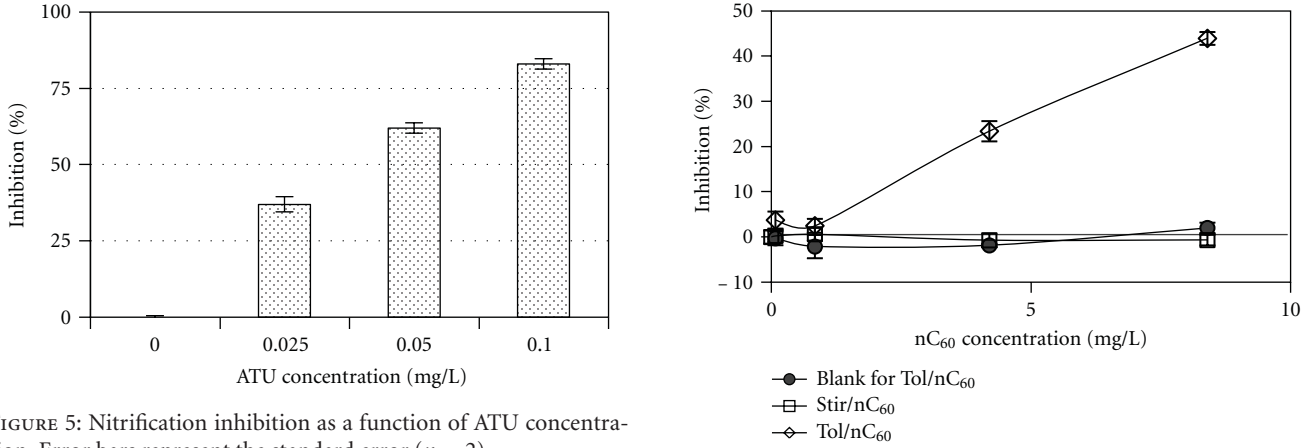


FIGURE 5: Nitrification inhibition as a function of ATU concentration. Error bars represent the standard error ( $n = 2$ ).

formation (NO<sub>3</sub><sup>-</sup> and NO<sub>2</sub><sup>-</sup>) between the control and the nC<sub>60</sub> exposure test after 3 h. The equation is given as,

$$I (\%) = \frac{(N_c - N_f)}{(N_c - N_i)} \times 100, \quad (1)$$

where N<sub>c</sub> (mg-N/L) is the concentration of oxidized N in the control flask after 3 h, N<sub>f</sub> (mg-N/L) is the concentration of oxidized N in the flask containing nC<sub>60</sub> after 3 h, N<sub>i</sub> (mg-N/L) is the concentration of oxidized N in the flask containing the reference inhibitor of N allylthiourea (ATU). The EC<sub>20</sub>, nC<sub>60</sub> concentration with a reduction of oxidized N formation by 20%, was calculated using the SPSS probit regression analysis (SPSS, USA).

**2.4. Microtox Test.** The *V. fischeri* bioassay is also used for assessing the toxicity of compounds on the activated sludge [23, 24] which is based on the decrease in bioluminescence from the bacterium due to the exposure to the toxicants. The experiment was carried out using a Model 500 luminometer (Azur Environmental, USA) in accordance with the Microtox

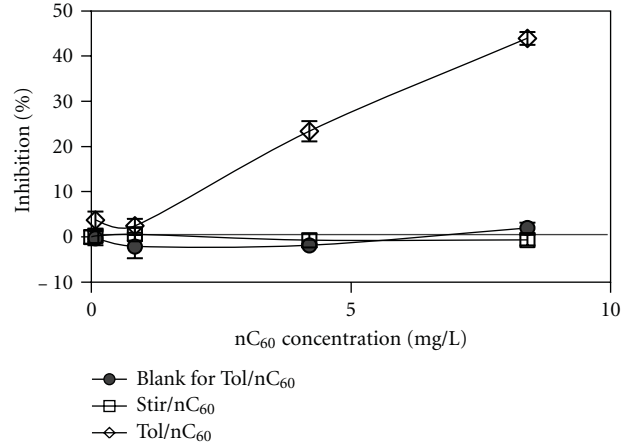


FIGURE 6: Nitrification inhibition of nC<sub>60</sub> as a function of preparation method and exposure concentration. Error bars represent the standard error ( $n = 2$ ).

acute toxicity procedure [25]. The reagent (freeze-dried *V. fischeri*) and the solutions (diluent, reconstitution, and osmotic adjusting solution) were purchased from Strategic Diagnostics Inc., USA. The EC<sub>20</sub>, nC<sub>60</sub> concentration with a reduction of bioluminescence by 20%, was calculated at each test with different exposure periods (5, 15, and 30 min) using the Microtox Omni Software (Strategic Diagnostics, USA). The phenol was used for the quality control of this test.

**2.5. nC<sub>60</sub> Aggregation in the Incubation Medium for the Toxicity Test.** The aggregation of nC<sub>60</sub> as a function of incubation time was determined using the same medium of the toxicity tests. For the nitrification inhibition test, the nC<sub>60</sub> size in medium (2 mM (NH<sub>4</sub>)<sub>2</sub>SO<sub>4</sub>, 6 mM NaHCO<sub>3</sub> and 2 mM KH<sub>2</sub>PO<sub>4</sub> buffer) was measured after 5 min (minimum time for one measurement) and 3 h. And for the Microtox

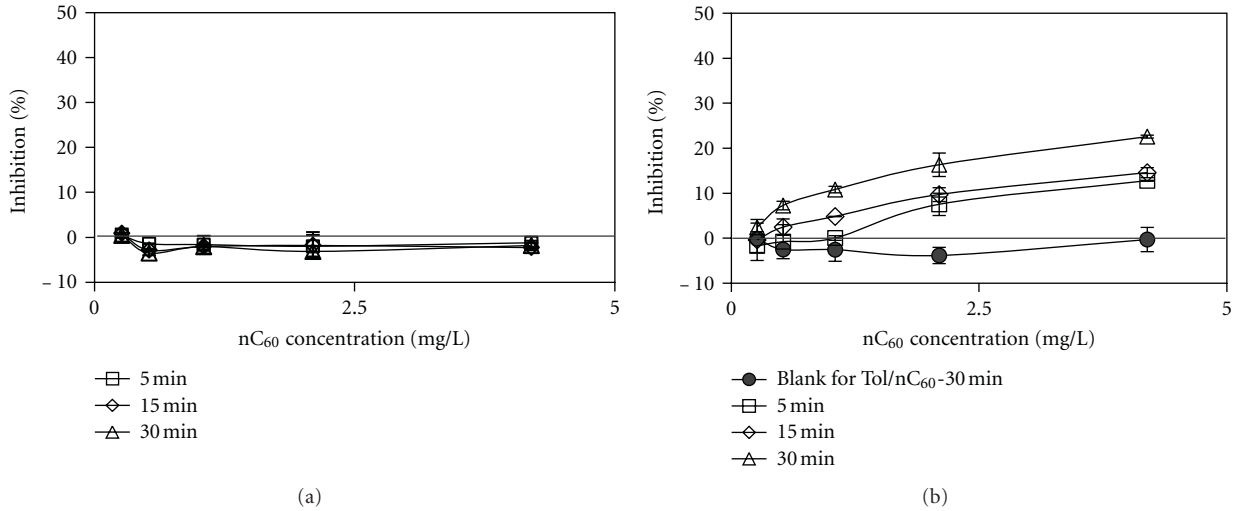


FIGURE 7: Bioluminescence inhibition of Stir/nC<sub>60</sub> (a) and Tol/nC<sub>60</sub> (b) as a function of exposure time and concentration. The Error bars represent the standard error ( $n = 2$ ).

test, the nC<sub>60</sub> size in 2% NaCl solution was measured after 5, 15, and 30 min.

**2.6. Analysis.** The NH<sub>4</sub><sup>+</sup>, NO<sub>3</sub><sup>-</sup>, and NO<sub>2</sub><sup>-</sup> concentrations were determined based on the standard methods [26]. The UV absorbance of the stock C<sub>60</sub> toluene solution and nC<sub>60</sub> suspension in water was measured using a UV-2500 spectrophotometer (Shimadzu Scientific Instruments, Japan). nC<sub>60</sub> size and its distribution were determined by the dynamic light scattering using a Zetasizer Nano ZS equipped with a 633 nm laser source and a detection angle of 173°C (Malvern Instruments, UK). The same instrument was used to measure the electrophoretic mobility which was subsequently calculated into Zeta potential using the Smoluchowski equation. All the tests in this study were conducted in duplicate.

### 3. Results and Discussion

**3.1. Characterization of Prepared nC<sub>60</sub>.** Figure 1 shows the UV-visible absorption spectra of Stir/nC<sub>60</sub> and Tol/nC<sub>60</sub>. Both nC<sub>60</sub> show the absorption peaks at 260 and 350 nm for the electronic structure of molecular C<sub>60</sub> cage [27] and a broad absorption band at 450–550 nm for the aggregated C<sub>60</sub>-C<sub>60</sub> interactions [6]. Similar findings have also been reported for nC<sub>60</sub> prepared via tetrahydrofuran (THF) [28]. However, the ratio of absorbance at 260, 350, and 450 nm varied with the nC<sub>60</sub> types suggesting the difference in the structure and composition of nC<sub>60</sub> aggregates [29].

Two types of nC<sub>60</sub> demonstrated very similar size distribution with an average size of 154 and 144 nm for Stir/nC<sub>60</sub> and Tol/nC<sub>60</sub>, respectively, as shown in Figure 2. Both nC<sub>60</sub> were negatively charged with no significant difference at pH 5.6 (Figure 3), which is in agreement with the reported results of nC<sub>60</sub> prepared using similar methodologies [29].

**3.2. Aggregation of nC<sub>60</sub> in Toxicity Test Medium.** The aggregate size is an essential information when assessing the toxicity of nanoparticles because of proved correlation [7, 30]. Figure 4(a) shows the nC<sub>60</sub> size with time in medium for nitrification inhibition test. After the incubation time of 3 h the aggregate remained stable with only several nm of increase in size for both nC<sub>60</sub>. It can be explained by the low ionic strength of this medium (~15.8 mM) which was much lower than the reported threshold destabilization concentration of ~120 mM for the nC<sub>60</sub> [31]. In contrast, the obvious increase in size was found in medium with high ionic strength (~342 mM) for the Microtox test (Figure 4(b)). Compared to the initial sizes in pure water, the size in medium increased by 31, 56, and 114% for Stir/nC<sub>60</sub> and 55, 97, and 142% for Tol/nC<sub>60</sub> after 5, 15, and 30 min. In addition, the aggregation rate of Stir/nC<sub>60</sub> was slower than that of Tol/nC<sub>60</sub> presumably due to the difference in the structure and chemistry of nC<sub>60</sub> aggregate. Brant et al. found the hydrophobicity of Stir/nC<sub>60</sub> was lower than the nC<sub>60</sub> prepared via the organic solvent, such as, toluene and THF [29].

**3.3. Effect of nC<sub>60</sub> on Nitrification Activity.** The sludge nitrification activity and test performance were confirmed using the ATU. The EC<sub>50</sub> was calculated to be 0.040 mg/L from the data (Figure 5) which was close to the published value of 0.025 mg/L [32]. Figure 6 shows the percent nitrification inhibition by two types of nC<sub>60</sub> at varying concentrations after 3 h, as well as the blank sample for Tol/nC<sub>60</sub>. For the Stir/nC<sub>60</sub>, no nitrification inhibition was observed up to 8.4 mg/L indicating its low toxicity on nitrifying activated sludge. Previous studies also presented similar results that no significant impact was identified on the microbial community structure in aerobic soil [33] and anaerobic sludge [16]. In the case of the Tol/nC<sub>60</sub>, no obvious effect was found in the blank sample (less than 2%).

But ~40% nitrification was inhibited at 8.40 mg/L, and the EC<sub>20</sub> was calculated to 4.89 mg/L for Tol/nC<sub>60</sub>. It clearly showed that the nC<sub>60</sub> toxicity depended on the preparation method. Zhu et al. [8] compared the toxicity of Stir/nC<sub>60</sub> and nC<sub>60</sub> produced via THF on *Daphnia magna* and founded EC<sub>50</sub> (48 h) for the latter was at least one order of magnitude (0.8 mg/L) less than that for Stir/nC<sub>60</sub> (>35 mg/L).

**3.4. Effect of nC<sub>60</sub> on Bioluminescent Bacteria.** Figure 7(a) shows the percent inhibition due to the exposure to Stir/nC<sub>60</sub> at different concentrations. No inhibition was observed at the concentration up to 4.2 mg/L for all the incubation time. In contrast, the Tol/nC<sub>60</sub> showed obvious inhibition at >1.05 mg/L, and the toxicity increased with the incubation time (Figure 7(b)). No inhibition was also observed for the blank sample up to 30 min. The EC<sub>20</sub> was calculated to 4.96, 4.98, and 3.44 mg/L for 5, 15, and 30 min, respectively. Both the facts above confirmed the low toxicity of Stir/nC<sub>60</sub> and the toxicity dependent on the preparation methods. The result is consistent with that obtained from the nitrification inhibition test.

## 4. Conclusions

The prepared Stir/nC<sub>60</sub> and Tol/nC<sub>60</sub> showed similar surface properties, such as, the size distribution, zeta potential, and UV-vis absorption spectra. However, two types of nC<sub>60</sub> presented different aggregation rates in test medium during the incubation periods. Both the nitrification inhibition and Microtox test showed that the nC<sub>60</sub> toxicity was greatly affected by the preparation method. Stir/nC<sub>60</sub> presented no significant toxicity to the nitrification sludge and bioluminescent bacteria at maximum concentration studied. In contrast, the EC<sub>20</sub> of Tol/nC<sub>60</sub> was obtained to be 4.89 mg/L (3 h) for the nitrification inhibition and 3.44 mg/L (30 min) for Microtox test, respectively.

## Conflict of Interests

The authors declare that there is no conflict of interests.

## Acknowledgments

This research was partly supported by Grant-in-Aid for Scientific Research (B), Japan Society for the Promotion of Science (JSPS) and CREST project, Japan Science and Technology (JST).

## References

- [1] S. J. Duclos, K. Brister, R. C. Haddon, A. R. Kortan, and F. A. Thiel, "Effects of pressure and stress on C<sub>60</sub> fullerite to 20 GPa," *Nature*, vol. 351, no. 6325, pp. 380–382, 1991.
- [2] B. S. Sherigara, W. Kutner, and F. D'Souza, "Electrocatalytic properties and sensor applications of fullerenes and carbon nanotubes," *Electroanalysis*, vol. 15, no. 9, pp. 753–772, 2003.
- [3] H. Murayama, S. Tomonoh, J. M. Alford, and M. E. Karpuk, "Fullerene production in tons and more: from science to industry," *Fullerenes Nanotubes and Carbon Nanostructures*, vol. 12, no. 1–2, pp. 1–9, 2004.
- [4] Woodrow Wilson, "The project on emerging technologies," 2012, <http://www.nanotechproject.org/consumerproducts>.
- [5] C. M. Sayes, J. D. Fortner, W. Guo et al., "The differential cytotoxicity of water-soluble fullerenes," *Nano Letters*, vol. 4, no. 10, pp. 1881–1887, 2004.
- [6] J. D. Fortner, D. Y. Lyon, C. M. Sayes et al., "C<sub>60</sub> in water: nanocrystal formation and microbial response," *Environmental Science and Technology*, vol. 39, no. 11, pp. 4307–4316, 2005.
- [7] D. Y. Lyon, L. K. Adams, J. C. Falkner, and P. J. J. Alvarez, "Antibacterial activity of fullerene water suspensions: effects of preparation method and particle size," *Environmental Science and Technology*, vol. 40, no. 14, pp. 4360–4366, 2006.
- [8] S. Zhu, E. Oberdörster, and M. L. Haasch, "Toxicity of an engineered nanoparticle (fullerene, C<sub>60</sub>) in two aquatic species, *Daphnia* and fathead minnow," *Marine Environmental Research*, vol. 62, supplement 1, pp. S5–S9, 2006.
- [9] K. T. Kim, M. H. Jang, J. Y. Kim, and S. D. Kim, "Effect of preparation methods on toxicity of fullerene water suspensions to Japanese medaka embryos," *Science of the Total Environment*, vol. 408, no. 22, pp. 5606–5612, 2010.
- [10] D. Y. Lyon, L. Brunet, G. W. Hinkal, M. R. Wiesner, and P. J. J. Alvarez, "Antibacterial activity of fullerene water suspensions (nC<sub>60</sub>) is not due to ROS-mediated damage," *Nano Letters*, vol. 8, no. 5, pp. 1539–1543, 2008.
- [11] Z. Liang, A. Das, and Z. Hu, "Bacterial response to a shock load of nanosilver in an activated sludge treatment system," *Water Research*, vol. 44, no. 18, pp. 5432–5438, 2010.
- [12] T. S. Radniecki, D. P. Stankus, A. Neigh, J. A. Nason, and L. Semprini, "Influence of liberated silver from silver nanoparticles on nitrification inhibition of *Nitrosomonas europaea*," *Chemosphere*, vol. 85, no. 1, pp. 43–49, 2011.
- [13] R. Ganesh, J. Smeraldi, T. Hosseini, L. Khatib, B. H. Olson, and D. Rosso, "Evaluation of nanocopper removal and toxicity in municipal wastewaters," *Environmental Science and Technology*, vol. 44, no. 20, pp. 7808–7813, 2010.
- [14] H. Mu, Y. Chen, and N. Xiao, "Effects of metal oxide nanoparticles (TiO<sub>2</sub>, Al<sub>2</sub>O<sub>3</sub>, SiO<sub>2</sub> and ZnO) on waste activated sludge anaerobic digestion," *Bioresource Technology*, vol. 102, no. 22, pp. 10305–10311, 2011.
- [15] S. Kang, M. S. Mauter, and M. Elimelech, "Microbial cytotoxicity of carbon-based nanomaterials: implications for river water and wastewater effluent," *Environmental Science and Technology*, vol. 43, no. 7, pp. 2648–2653, 2009.
- [16] L. Nyberg, R. F. Turco, and L. Nies, "Assessing the impact of nanomaterials on anaerobic microbial communities," *Environmental Science and Technology*, vol. 42, no. 6, pp. 1938–1943, 2008.
- [17] Z. Chen, P. Westerhoff, and P. Herkes, "Quantification of C<sub>60</sub> fullerene concentrations in water," *Environmental Toxicology and Chemistry*, vol. 27, no. 9, pp. 1852–1859, 2008.
- [18] H. Hyung and J. H. Kim, "Dispersion of C<sub>60</sub> in natural water and removal by conventional drinking water treatment processes," *Water Research*, vol. 43, no. 9, pp. 2463–2470, 2009.
- [19] S. Deguchi, R. G. Alargova, and K. Tsujii, "Stable dispersions of fullerenes, C<sub>60</sub> and C<sub>70</sub>, in water. Preparation and characterization," *Langmuir*, vol. 17, no. 19, pp. 6013–6017, 2001.
- [20] C. Wang, C. Shang, and P. Westerhoff, "Quantification of fullerene aggregate nC<sub>60</sub> in wastewater by high-performance liquid chromatography with UV-vis spectroscopic and mass spectrometric detection," *Chemosphere*, vol. 80, no. 3, pp. 334–339, 2010.

- [21] G. C. Ghosh, T. Okuda, N. Yamashita, and H. Tanaka, "Occurrence and elimination of antibiotics at four sewage treatment plants in Japan and their effects on bacterial ammonia oxidation," *Water Science and Technology*, vol. 59, no. 4, pp. 779–786, 2009.
- [22] ISO, 9509, "Water quality-toxicity test for assessing the inhibition of nitrification of activated sludge microorganisms," International Organization for Standardization, 2006.
- [23] D. J. B. Dalzell, S. Alte, E. Aspichueta et al., "A comparison of five rapid direct toxicity assessment methods to determine toxicity of pollutants to activated sludge," *Chemosphere*, vol. 47, no. 5, pp. 535–545, 2002.
- [24] S. Ren, "Assessing wastewater toxicity to activated sludge: recent research and developments," *Environment International*, vol. 30, no. 8, pp. 1151–1164, 2004.
- [25] Azur, *Microtox Acute Toxicity Basic Test Procedures*, Azur Environmental, Carlsbad, Calif, USA, 1995.
- [26] APHA, *Standard Methods for the Examination of Water and Wastewater*, American Public Health Association, Washington, DC, USA, 20th edition, 1999.
- [27] J. Lee, M. Cho, J. D. Fortner, J. B. Hughes, and J. H. Kim, "Transformation of aggregated C<sub>60</sub> in the aqueous phase by UV irradiation," *Environmental Science and Technology*, vol. 43, no. 13, pp. 4878–4883, 2009.
- [28] J. D. Fortner, D. I. Kim, A. M. Boyd et al., "Reaction of water-stable C<sub>60</sub> aggregates with ozone," *Environmental Science and Technology*, vol. 41, no. 21, pp. 7497–7502, 2007.
- [29] J. A. Brant, J. Labille, J. Y. Bottero, and M. R. Wiesner, "Characterizing the impact of preparation method on fullerene cluster structure and chemistry," *Langmuir*, vol. 22, no. 8, pp. 3878–3885, 2006.
- [30] M. Luna-delRisco, K. Orupöld, and H. C. Dubourguier, "Particle-size effect of CuO and ZnO on biogas and methane production during anaerobic digestion," *Journal of Hazardous Materials*, vol. 189, no. 1-2, pp. 603–608, 2011.
- [31] K. L. Chen and M. Elimelech, "Aggregation and deposition kinetics of fullerene (C<sub>60</sub>) nanoparticles," *Langmuir*, vol. 22, no. 26, pp. 10994–11001, 2006.
- [32] R. Cui, W. J. Chung, and D. Jahng, "A rapid and simple respirometric biosensor with immobilized cells of *Nitrosomonas europaea* for detecting inhibitors of ammonia oxidation," *Biosensors and Bioelectronics*, vol. 20, no. 9, pp. 1788–1795, 2005.
- [33] Z. Tong, M. Bischoff, L. Nies, B. Applegate, and R. F. Turco, "Impact of fullerene (C<sub>60</sub>) on a soil microbial community," *Environmental Science and Technology*, vol. 41, no. 8, pp. 2985–2991, 2007.

## Research Article

# The Human Stratum Corneum Prevents Small Gold Nanoparticle Penetration and Their Potential Toxic Metabolic Consequences

**David C. Liu,<sup>1,2</sup> Anthony P. Raphael,<sup>1</sup> Daniel Sundh,<sup>1,3</sup> Jeffrey E. Grice,<sup>2</sup> H. Peter Soyer,<sup>1</sup> Michael S. Roberts,<sup>2,4</sup> and Tarl W. Prow<sup>1,2</sup>**

<sup>1</sup> Dermatology Research Centre, School of Medicine, Princess Alexandra Hospital, The University of Queensland, Brisbane, QLD 4102, Australia

<sup>2</sup> Therapeutics Research Centre, School of Medicine, Princess Alexandra Hospital, The University of Queensland, Brisbane, QLD 4102, Australia

<sup>3</sup> Institute of Neuroscience and Physiology, The Sahlgrenska Academy, University of Gothenburg, 405 30 Gothenburg, Sweden

<sup>4</sup> School of Pharmacy and Medical Science, University of South Australia, Adelaide, SA 5001, Australia

Correspondence should be addressed to Tarl W. Prow, t.prow@uq.edu.au

Received 20 January 2012; Accepted 12 April 2012

Academic Editor: Xiaoming Li

Copyright © 2012 David C. Liu et al. This is an open access article distributed under the Creative Commons Attribution License, which permits unrestricted use, distribution, and reproduction in any medium, provided the original work is properly cited.

Nanoparticles are being used in multiple applications, ranging from biomedical and skin care products (e.g., sunscreen) through to industrial manufacturing processes (e.g., water purification). The increase in exposure has led to multiple reports on nanoparticle penetration and toxicity. However, the correlation between nanoparticle size and its penetration without physical/chemical enhancers through the skin is poorly understood—with studies instead focusing primarily on skin penetration under disrupted conditions. In this paper, we investigate the penetration and metabolic effects of 10 nm, 30 nm, and 60 nm gold nanoparticles within viable excised human skin after 24-hour exposure using multiphoton tomograph-fluorescence lifetime imaging microscopy. After 24 hour treatment with the 10, 30, and 60 nm gold nanoparticles, there was no significant penetration detected below the stratum corneum. Furthermore, there were no changes in metabolic output (total NAD(P)H) in the viable epidermis posttreatment correlating with lack of penetration of nanoparticles. These results are significant for estimating topical nanoparticle exposure in humans where other model systems may overestimate the exposure of nanoparticles to the viable epidermis. Our data shows that viable human skin resists permeation of small nanoparticles in a size range that has been reported to penetrate deeply in other skin models.

## 1. Introduction

The skin is the largest organ of the body and is the primary barrier to nanoparticle exposure from naturally occurring and engineered nanomaterials found in the environment and workplace [1–3]. Therefore, it is important to understand the penetration characteristics of nanoparticles within the skin. However, accurate assessment of nanoparticle penetration is challenging, with results dependant on the model used (e.g., rat, pig, or human skin), barrier integrity (i.e., skin preparation prior to and during studies), nanoparticle properties (e.g., size, shape, surface structures, and charge), and degradation kinetics.

A number of reports have shown that nanoparticles penetrate skin into the dermis under various physically disrupted conditions [4–8]. In addition, nanoparticles have also

been shown to penetrate skin in the presence of chemical enhancers [3]. We have previously shown *ex vivo* that skin treated with gold nanoparticles suspended in toluene results in nanoparticle penetration into the epidermis due to toluene acting as a chemical enhancer and disrupting the stratum corneum [8]. Even though there are multiple reviews on nanoparticle toxicity and penetration within the skin [9–13], the correlation between nanoparticle size and its penetration without physical/chemical enhancers is poorly understood—with studies instead focusing primarily on skin penetration under disrupted conditions.

A recent report by Filon et al. (2011) showed 12.9 nm gold nanoparticle penetration in thawed human skin [14]. The results showed that gold nanoparticle penetration occurred after 24 hours of treatment in both intact and damaged skin. Gold nanoparticles were detected in the

receiving solution of the Franz cells after 24 hours of skin exposure. This report supports a previous study conducted by Sonavane et al. (2008) where 15 nm gold nanoparticles penetrated through the excised rat skin into the dermis also after 24-hour treatment [15].

In the last 20 years, multiphoton tomography (MPT) has developed into a technique that enables the concurrent monitoring of both the organ morphology and solute transported into that organ, including the skin, with use increasing in clinical applications [16–18]. A benefit of MPT is that it can be used in conjunction with fluorescence lifetime imaging (FLIM). FLIM is a sensitive, time-resolved technique that enables the detection of the lifetimes and intensity of fluorescent molecules within the image plane [19]. MPT-FLIM is also used to monitor the autofluorescence of fluorophores within the skin including NAD/NADP (i.e., NAD[P]H), flavin adenine dinucleotide (FAD), and porphyrins. We have previously shown that FLIM can also be used to separate metal nanoparticle signals from skin autofluorescence [20]. However, the fluorescence lifetime decay curves of gold nanoparticles and NAD(P)H cannot directly be separated [8]. Instead, the photon intensity output based on the  $\alpha\%$  parameters can be used to differentiate the gold nanoparticle and NAD(P)H signal.

In this paper, our aim is to investigate the relationship between gold nanoparticle size and its penetration into viable human skin following topical exposure without physical/chemical enhancers. Gold nanoparticles (10 nm, 30 nm, and 60 nm) were applied to freshly excised human skin for 24 hours. Following application the penetration profile was analysed using microscopy of whole intact skin and histology sections. Changes in the metabolic state of viable skin following gold nanoparticle treatment were evaluated by analysing the change in NAD(P)H using MPT-FLIM. Our data showed that there was no significant penetration of the different sized nanoparticles into the viable tissue even after 24 hours of treatment. Instead, the nanoparticles were located on the skin surface, within the stratum corneum and within the skin furrows. There were also no significant metabolic perturbations associated with gold nanoparticle treatment due to their lack of penetration. Overall, the data show that excised viable human skin is important for an accurate and reliable understanding of nanoparticle penetration.

## 2. Materials and Methods

**2.1. Materials.** Three different sized gold nanoparticles (10 nm [21], 30 nm [22], and 60 nm [23]) suspended in 5 mL sodium citrate were prepared and purchased from National Institute of Standards and Technology (NIST) of USA. The concentration of gold nanoparticles was 5 mg/mL. The gold nanoparticles were characterized by NIST in relation to their size and chemical and electrochemical properties (10 nm [21], 30 nm [22], and 60 nm [23]). The particle size and morphology were determined by atomic force microscopy (AFM), scanning electron microscopy (SEM), transmission

electron microscopy (TEM), electrospray-differential mobility analysis (ES-DMA), dynamic light scattering (DLS), and small-angle X-ray scattering (SAXS). The mean size range varied slightly between the techniques, resulting in the average diameter  $\pm 95\% \text{ CI}$ :

10 nm particles:  $8.5 \pm 0.3 \text{ nm}$  (AFM),  $9.9 \pm 0.1 \text{ nm}$  (SEM),  $8.9 \pm 0.1 \text{ nm}$  (TEM),  $11.3 \pm 0.1 \text{ nm}$  (ES-DMA),  $13.5 \pm 0.1 \text{ nm}$  (DLS), and  $9.1 \pm 1.8 \text{ nm}$  (SAXS).

30 nm particles:  $24.9 \pm 1.1 \text{ nm}$  (AFM),  $26.9 \pm 0.1 \text{ nm}$  (SEM),  $27.6 \pm 2.1 \text{ nm}$  (TEM),  $28.4 \pm 1.1 \text{ nm}$  (ES-DMA),  $26.5 \sim 28.6 \pm 0.9 \sim 3.6 \text{ nm}$  (DLS), and  $24.9 \pm 1.2 \text{ nm}$  (SAXS).

60 nm particles:  $55.4 \pm 0.3 \text{ nm}$  (AFM),  $54.9 \pm 0.4 \text{ nm}$  (SEM),  $56.0 \pm 0.5 \text{ nm}$  (TEM),  $56.3 \pm 1.5 \text{ nm}$  (ES-DMA),  $55.3 \sim 56.6 \pm 1.4 \sim 8.3 \text{ nm}$  (DLS), and  $53.2 \pm 5.3 \text{ nm}$  (SAXS).

The shape of the gold nanoparticles was determined by SAXs with each measurement calculated from the mean primary component peak value by fitting the  $I(Q)$  data resulting in a Q-range:  $0.01 \text{ \AA}^{-1}$  to  $2.0 \text{ \AA}^{-1}$  (10 nm),  $0.0001 \text{ \AA}^{-1}$  to  $1 \text{ \AA}^{-1}$  (30 nm), and  $0.01 \text{ \AA}^{-1}$  to  $2.0 \text{ \AA}^{-1}$  (60 nm). Particle aggregation within the sodium citrate buffer was determined by SEM images and analysed with ImageJ v1.37. The data analysis of the Otsu threshold algorithm was produced from the binary image, distinguishing particles from the background. A total of 140 (10 nm), 1185 (30 nm), and 425 (60 nm) particles were analysed within an area of roughly  $35 \times 35$  pixels (10 nm),  $50 \times 50$  pixels (30 nm),  $100 \times 100$  pixels (60 nm) from 2 (10 nm), 3 (30 nm), and 3 (60 nm) randomly prepared ampoules.

All other chemicals and solvents were of reagent grade.

**2.2. Excised Human Skin Preparation.** Human skin was donated from abdominoplasty patients with the approval of the Princess Alexandra Hospital Research Ethics Committee (no. 1997/097). A total of three skin donors were used in this study. The donor skin was obtained on the day of removal from the patient, and the experiment was performed within 24 hours to preserve the viability of the skin. The subcutaneous fatty tissue was removed from the skin using a scalpel prior to the start of the experiments. The surface of skin was cleaned with deionised water, and the excised tissue was stored covered on saline moistened gauze in a  $4^\circ\text{C}$  cold room until use. Skin handling and experimental design was conducted to maintain metabolic functionality throughout the course of these studies [24].

**2.3. Skin Penetration Studies.** The excised skin was cut into 25 mm diameter skin discs and mounted in a Franz diffusion cell with a diffusion area of  $1.1 \text{ cm}^2$  and a receptor chamber volume of 3.2 mL. High vacuum grease (Ajax, FineChem) was used to seal the edges of the two chambers. Phosphate buffered saline, pH 7.4, was then pipetted into the receptor chamber and magnetically stirred at 500 rpm in a water bath at  $35^\circ\text{C}$ . Prior to trans-epidermal water loss (TEWL) analysis the combined skin/Franz cell was equilibrated for 30

minutes. TEWL was then measured using a Biox AquaFlux condenser chamber unit (model no. AF200) to evaluate the surface integrity of the skin surface prior to nanoparticle treatment [8]. After confirmation of intact viable skin, 500  $\mu\text{L}$  of 5 mg/mL gold nanoparticle suspensions was topically applied to the skin ( $n = 3$  per group). The two control groups were topical application of saline and sodium citrate solution, respectively. The Franz diffusion cells were maintained at 35°C throughout the 24-hour exposure period. After treatment, any excess gold nanoparticle suspension was drained and the skin removed. The treated skin was then dried at ambient conditions, and the TEWL was analysed again to determine any detrimental effect to the stratum corneum during treatment.

**2.4. MPT-FLIM of Viable Treated Skin.** Non-invasive microscopy analysis was conducted using MPT-FLIM with a DermaInspect (JenLab GmbH, Jena, Germany) equipped with time-correlated single-photon counting, SPC 830 FLIM detector (Becker & Hickl, Berlin, Germany). The excitation source consisted of an ultrashort (65-femtosecond pulse width) pulsed mode-locked tuneable laser at 80 MHz (Mai Tai, Spectra physics, Mountain View, USA), with a wavelength range of 710–920 nm. MPT-FLIM was used to simultaneously image the gold nanoparticles and endogenous NAD(P)H using an excitation wavelength of 740 nm [10]. The skin was optically sectioned from the stratum corneum to the stratum basale in 5  $\mu\text{m}$  increments using a 40x objective lens with an acquisition size image size of 210  $\times$  210  $\mu\text{m}^2$ . The image was scanned at 13.4 seconds per frame at 600 zoom of region of interest (ROI). The emission filter used was a 350–650 nm bandpass filter (BG39) with a long wavelength cut-off of <700 nm. A constant incident optical excitation power of 30 mW at the rear of the objective was used throughout the experiment. Three replicates of treated skin were analysed after 24 hours of treatment. FLIM data were analysed with a SPC 830 2.9 Image software (Becker and Hickl) to generate fluorescence lifetime decay and photon contribution curves from NAD(P)H autofluorescence in the skin and gold luminescence. The instrument response function of each FLIM image of treated skin was calibrated to a sucrose crystal standard (Ajax Finechem Pty Ltd.). Each FLIM image was calculated using the “Decay matrix” command, and a selected ROI was cropped and analysed pixel by pixel and line by line in the selected fit parameter shown in a lifetime distribution histogram. Gold nanoparticle multiphoton enhanced photoluminescence was quantified using relative amplitude of pixel intensity/pixel frequency signal  $\alpha_1\%$  from 95 to 100%, and metabolic changes were quantified using  $\alpha_1/\alpha_2$  ratio and total NAD(P)H lifetime intensity. The  $\alpha_1\%$  is defined as the quantity of emission photons that return to the detector during the short lifetime decay curve phase, and the  $\alpha_2\%$  is the long lifetime phase. The  $\alpha_1\%$  is not affected by the microenvironment of the skin. The total NAD(P)H lifetime intensity is the combined total of free and bound NAD(P)H signals and was quantified using exported grey-scale image of each FLIM image with photons per pixel. The grey-scale image was imported to

ImageJ 1.43u (National Institutes of Health, USA) at 8-bit image quality and a selected cell area of 200  $\times$  200  $\mu\text{m}^2$ . The selected cell area was measured, and the total NAD(P)H mean intensity was quantified.

**2.5. Cryosectioning of Treated Skin.** Treated skin was fixed in 2% paraformaldehyde in 0.1 M phosphate buffer, pH 7.4, for 2 hours at room temperature. After fixation, the treated skin was embedded in OCT (Sakura Tissue-Tek) in a mold block and frozen at 70°C for 30 minutes. The tissue samples were sectioned at 10  $\mu\text{m}$  at –25°C using a Leica CM1850 cryostat (Leica Microsystems, Heidelberger, Nussloch, Germany). The sections were mounted in Prolong Gold (Invitrogen, Mulgrave, Victoria, Australia) prior to MPT-FLIM imaging.

**2.6. Statistical Analysis.** The differences in the measured macroscopic parameters between treated and control groups were compared by applying the nonparametric Mann-Whitney U-test. Two-way ANOVA analysis was used to determine the significance between groups. All calculations were done using Graphpad Prism version 5.03 (GraphPad software, Inc., USA) analysis. The level of significance was accepted at  $P \leq 0.05$ .

### 3. Results

**3.1. Surface Barrier Integrity of Excised Viable Human Skin.** Prior to and after treatment, the integrity of the stratum corneum (surface barrier) was analysed using transepidermal water loss (TEWL). The mean  $\pm$  SE of the TEWL was 30.6  $\pm$  4.1, 28.2  $\pm$  1.2, 30.1  $\pm$  0.9, 28.9  $\pm$  1.4, and 27.9  $\pm$  1.1 for the saline, sodium citrate, 10 nm, 30 nm, and 60 nm gold nanoparticle groups respectively, before treatment. After 24-hour treatment, the TEWL had increased an average of 1.6, 1.8, 1.8, 1.5 and 1.7 times compared to the pre-treatment values for saline, sodium citrate, 10 nm, 30 nm and 60 nm gold-nanoparticle-treated groups, respectively. There were no significant differences between any two groups within a single time point. However, there was a significant increase in TEWL for all groups after treatment.

**3.2. Gold Nanoparticle Penetration into Skin.** To determine the effect on penetration of the different sized nanoparticles, 10, 30, and 60 nm gold nanoparticles were topically applied to the skin for 24 hours followed by MPT and MPT-FLIM analysis. Two aspects of nanoparticle penetration within human skin were studied using MPT. The first consisted of *en face* analysis of whole intact human skin (Figure 1) and the second analysis of cryosectioned skin (Figure 2). Both sets of data (Figures 1 and 2) were pseudocoloured based on  $\alpha_1\%$  0–100% (blue to red). The autofluorescent components of living skin, that is, NAD(P)H and keratin result in  $\alpha_1\%$  less than 95% and are subsequently pseudocoloured green, blue, and yellow (viable skin only) [8]. The gold nanoparticle luminescence result in high  $\alpha_1\%$  (95–100%) and is pseudocoloured orange to red. To determine any metabolic effects from the nanoparticles MPT-FLIM analysis was used to monitor NAD(P)H.

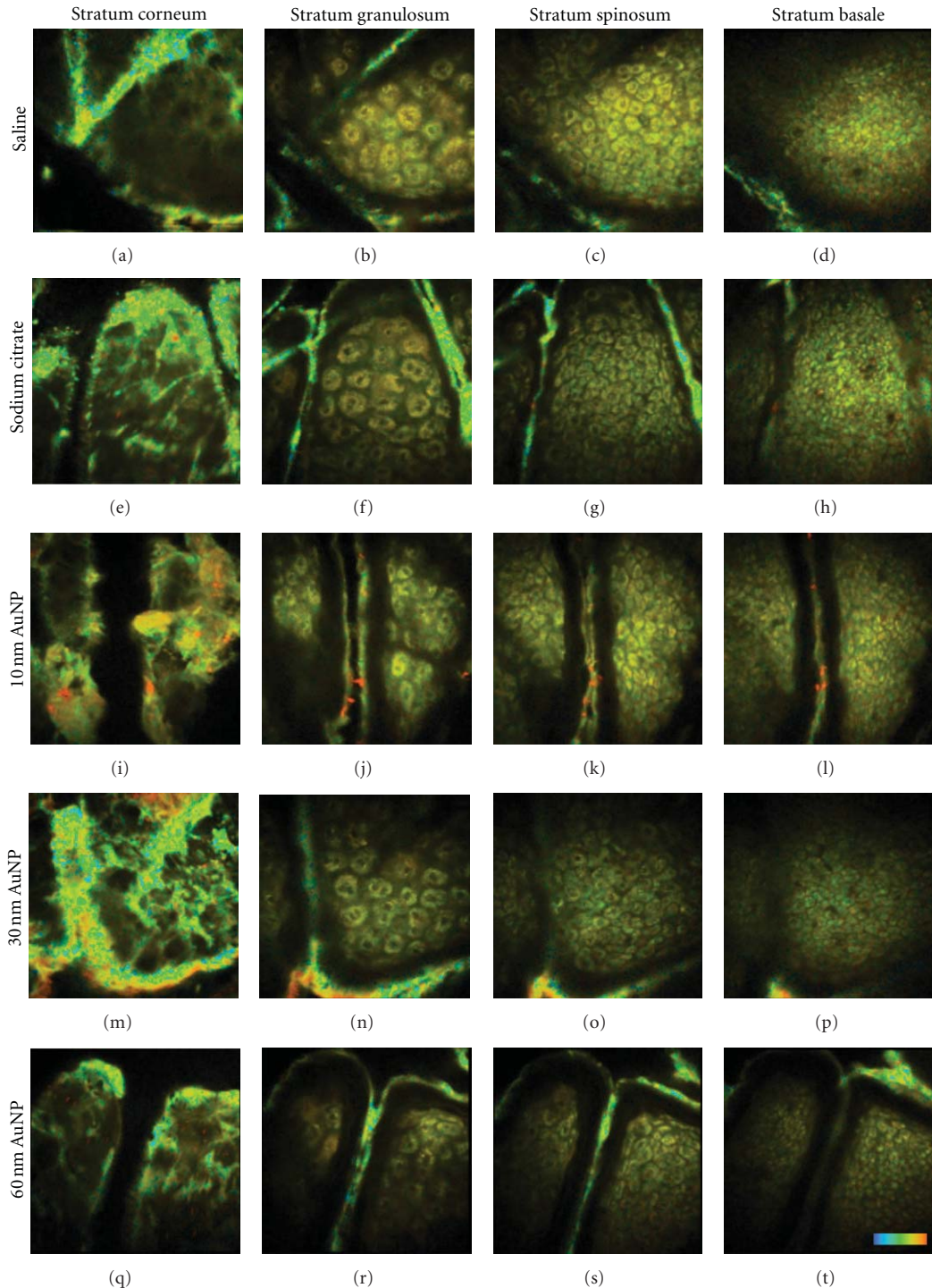


**FIGURE 1:** *En face* MPT-FLIM images of treated human viable skin. Multiphoton tomography fluorescence lifetime microscopy (FLIM) images showing the layers of excised full-thickness skin (stratum corneum, granulosum, spinosum, and basale) after 24-hour treatment with gold nanoparticles. Images are pseudocoloured based on  $\alpha_1\%$  signal (skin autofluorescence 0–95% and AuNPs 95–100% signal). No AuNP signal was detected in the saline control (a)–(d); however, deposits of high signal were detected in the stratum corneum of the sodium citrate control (sodium citrate crystal aggregates). The AuNP-treated groups, 10 nm (i)–(l), 30 nm (m)–(p), and 60 nm (q)–(t), resulted in signal throughout the stratum corneum. 10 nm AuNPs were also detected in the furrows. Scale bar indicates 50  $\mu$ m. Color bar, blue to red indicates  $\alpha_1\%$  0–100%.

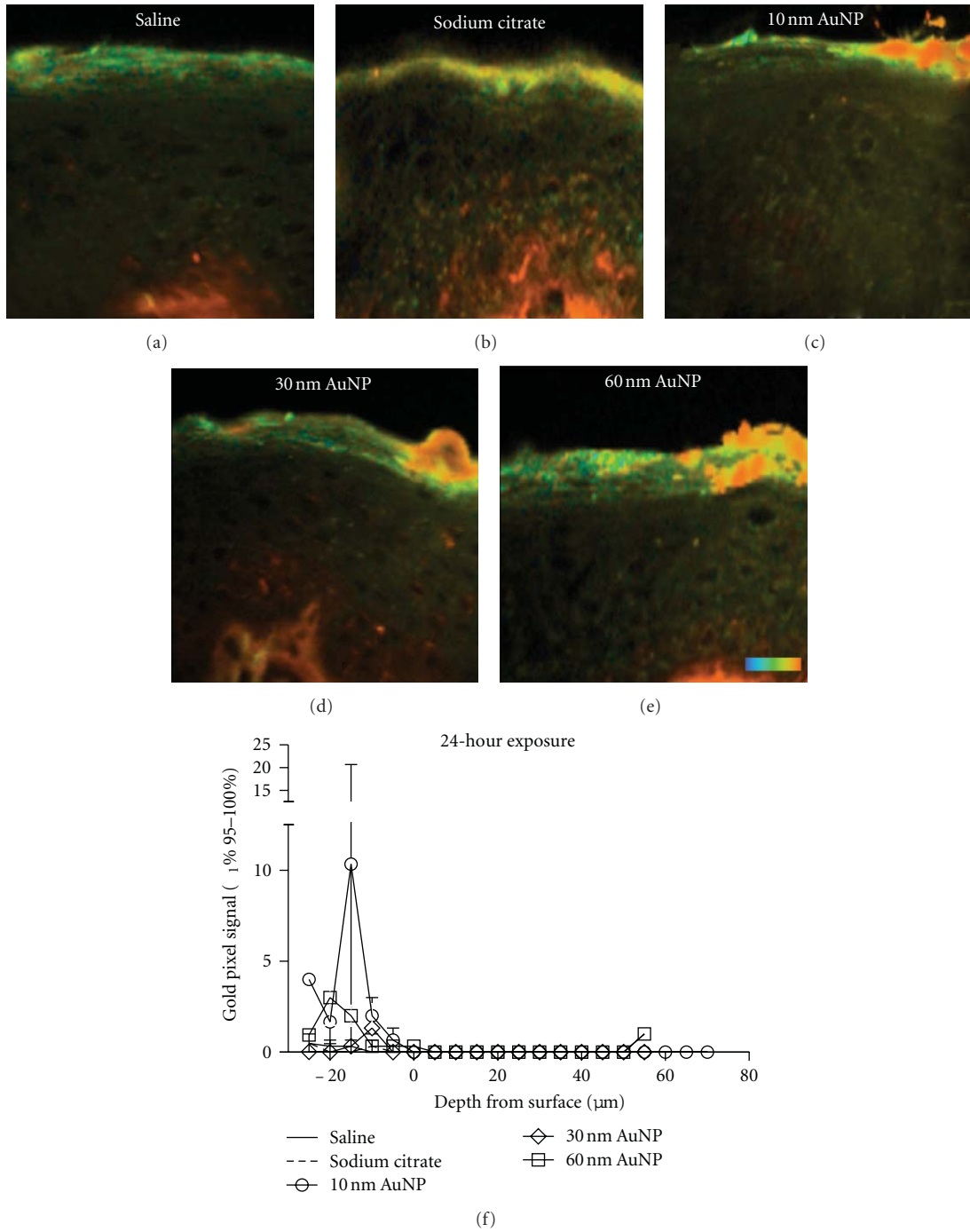


FIGURE 2: (a)–(e) Gold nanoparticle penetration in cryosectioned skin using MPT-FLIM and (f) gold nanoparticle luminescence skin depth profile. Cross-sectional images of the skin showing the superficial stratum corneum, viable epidermis and upper dermis. Images are pseudocoloured based on  $\alpha_1\%$  signal (skin autofluorescence 0–95% and AuNPs 95–100% signal). Both the saline (a) and sodium citrate buffer (b) controls show no AuNP signal. The 10 nm (c), 30 nm (d), and 60 nm (e) AuNP-treated groups resulted in high amounts of AuNP signal in the stratum corneum with no signal in the lower layers. High signal was detected in the upper dermis corresponding to second harmonic generation of dermal collagen. Scale bar indicates 50  $\mu\text{m}$ . Data from MPT-FLIM depth series (stratum corneum to basale of excised human skin) were processed to quantify gold nanoparticle luminescence intensity as a function of depth in non-furrow containing regions (i.e., AuNP penetration) (f). The top of the skin is at -20  $\mu\text{m}$ , whereas 0  $\mu\text{m}$  is the start of viable epidermis (stratum granulosum). These data were stacked from a depth series of *en face* images. Color bar, blue to red indicates  $\alpha_1\%$  0–100%.

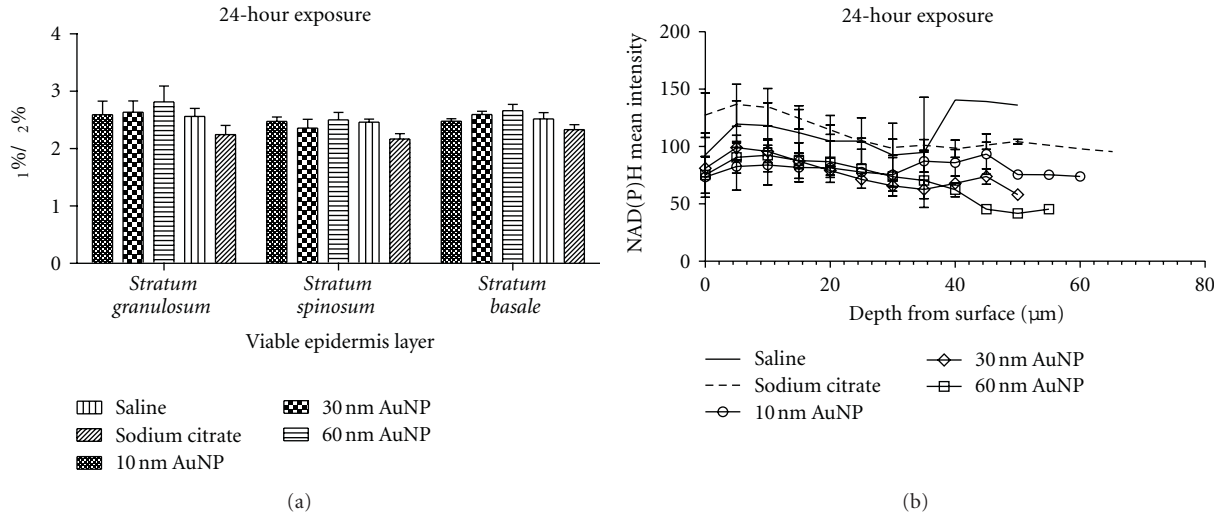


FIGURE 3: NAD(P)H effects from MPT-FLIM imaging. To assess the metabolic impact of AuNP penetration, NAD(P)H signals were analysed using  $\alpha_1\%/\alpha_2\%$  ratio and total NAD(P)H lifetime intensity using MPT-FLIM. The  $\alpha_1\%/\alpha_2\%$  ratio (a) is inversely related to the metabolic rate and was calculated for each of the treatment groups at 24 hours from stratum granulosum, spinosum, and basale. The total NAD(P)H lifetime intensities of selected area (b) were examined as a function of depth in non-furrow-containing regions. The beginning of viable epidermis is at 0  $\mu\text{m}$ .

**3.3. En Face MPT Analysis of Gold-Nanoparticle-Treated Skin.** Initial analysis of nanoparticle penetration consisted of qualitative MPT analysis of whole intact human skin (Figure 1 ( $n = 3$  per group)). The skin was optically sectioned at 5  $\mu\text{m}$  intervals from the stratum corneum through the stratum granulosum, stratum spinosum and down to the base of the stratum basale. To determine if there was any background noise associated with the nanoparticle buffers, both saline and sodium citrate were applied to the skin in separate experiments and analysed—resulting in low background signal in all of the layers (Figures 1(a)–1(h)). Skin treated with the 10 nm gold nanoparticles resulted in a significant increase in high  $\alpha_1\%$  signals throughout the stratum corneum compared to the controls (Figure 1(i)). There was no detection of AuNP signal in the stratum granulosum, spinosum, or basale. However, AuNP signal was detected on the surface within the furrows (Figures 1(j)–1(l)). Both the 30 and 60 nm gold nanoparticle groups showed similar penetration results to the 10 nm nanoparticles with AuNP signal detected only in the stratum corneum (Figures 1(i)–1(t)).

**3.4. Cross-Sectional Analysis of Gold Nanoparticle Penetration within Skin.** A second method using MPT analysis of cryo-sectioned skin was used to qualitatively assess the gold nanoparticle penetration. Representative images of each group are shown in Figure 2 resulting in a cross-sectional image of the stratum corneum (surface) down to the dermis. The control groups (Figures 2(a) and 2(b)) correlate with the results observed in Figure 1, with no AuNP signal detected within the upper layers of the skin. However,  $\alpha_1\%$  (95–100%) signal was detected within the dermis of not only the control groups but also the nanoparticle-treated samples (Figures 2(a), 2(b), 2(d), and 2(e)). This signal is attributed to second harmonic generation of dermal collagen. The gold-nanoparticle-treated groups also correlate with the data

observed in Figure 1, with AuNP signal detected only in the stratum corneum for all samples (Figures 2(c), 2(d), and 2(e)). However, the nanoparticles were distributed throughout the entire depth of the stratum corneum but not into the stratum granulosum. Overall, the two independent qualitative experiments analysing gold-nanoparticle-treated skin, resulted in AuNP signal in the stratum corneum layer with no significant nanoparticle signal in the lower layers.

**3.5. En Face MPT-FLIM Intensity Measurement of Gold Nanoparticle Luminescence in Human Viable Skin Depth Study.** Having qualitatively assessed the distribution and penetration profile of gold-nanoparticle-treated skin (Figures 1 and 2), the related gold fluorescence signal was then quantified using image software, Image J (National Institutes of Health, Bethesda, Washington, DC, USA) to analyse the number of pixels corresponding to AuNP signal and its depth within the skin (Figure 2(f)). This resulted in detection of a significantly higher concentration of AuNP signal within the stratum corneum in the 10 nm nanoparticle-treated group compared to the 30 nm and 60 nm nanoparticle-treated groups (Figure 2(f)). The AuNP signal below the stratum corneum did not differ significantly from the saline and sodium citrate negative controls. Overall, these data correlates with the qualitative experiments resulting in no significant penetration of the 10, 30, and 60 nm nanoparticles within the skin.

**3.6. MPT-FLIM Analysis of NAD(P)H after Gold Nanoparticle Treatment.** The metabolic profile of the skin was analysed using MPT-FLIM of total NAD(P)H in the epidermis of excised viable human skin. A depth study involving a series of stacked FLIM images of the treated groups was processed to quantify  $\alpha_1\%/\alpha_2\%$  ratio and total NAD(P)H lifetime intensity. The  $\alpha_1\%/\alpha_2\%$  ratio of NAD(P)H has been reported

to be inversely related to the metabolic rate [20]. Overall, there was no significant difference of the total NAD(P)H lifetime intensities between any of the groups (Figure 3).

## 4. Discussion and Conclusion

Human skin is regarded as the “gold standard” for skin penetration studies compared to animal model investigations [25]. The present study investigated 10, 30, and 60 nm gold nanoparticles penetration within excised viable human skin. An *en face* penetration profile provided gold nanoparticle distribution in excised skin from the stratum corneum to the basale in depth. Analysis of nanoparticle skin penetration involves a number of factors including the skin model, skin barrier integrity, and the inherent physicochemical attributes (size, shape, surface charge, etc.) of the nanoparticles and vehicle of the formulation. To assess the correlation of cell viability (metabolism) and nanoparticle penetration, experiments were conducted with intact human viable skin in an *ex vivo* diffusion cell system and tested within 24 hours after excision.

It has been previously reported, using spectrophotometry and TEM, that 15 nm gold nanoparticles suspended in an aqueous solution were capable of penetrating full thickness rat skin [15]. These results are consistent with a recent report by Filon et al. (2011) [14] who showed that 12.9 nm gold nanoparticles were capable of penetrating into thawed human skin within 24 hours of treatment. However, our study showed that 24-hour treatment of excised viable human skin with 10, 30, and 60 nm gold nanoparticles resulted in nanoparticle penetration into the stratum corneum only with no significant penetration into the lower layers (Figures 1 and 2). Based on the previous reports showing successful penetration of nanoparticles smaller than 15 nm, it was hypothesised that the 10 nm nanoparticle group would result in penetration into the viable epidermis. We hypothesise that the lack of penetration observed in our study of the 10, 30, and 60 nm nanoparticles is associated with the integrity and type of skin sample used (freshly excised viable human skin). As stated, Filon et al. used thawed excised human skin. The freezing and thawing process damaged the viable tissue resulting in increased penetration. We used MPT to detect gold nanoparticle penetration. This is a non-invasive method resulting in minimal disruption of the skin during sample analysis compared to other assays [26] and further emphasises the importance of maintaining skin integrity so as to not bias exposure assessment.

MPT-FLIM was used to assess the effect of gold nanoparticle-penetration on cell metabolism within the viable epidermis. There was no significant change in the total NAD(P)H lifetime intensities for any of the nanoparticle treated groups compared to the negative controls. These results (Figure 3) further support the results shown in Figures 1 and 2 where there was no significant penetration of the nanoparticles below the stratum corneum. Our results show that the stratum corneum protects the viable epidermis by preventing penetration of 10, 30, and 60 nm gold particles

within human skin. When comparing our results to those in literature, we hypothesise that nanoparticle penetration occurs more readily in animal models and nonviable human skin compared to freshly excised viable human skin or in people. Therefore, there should be careful consideration of the animal model and viability of tissue prior to conducting experiments on nanoparticle penetration. This is especially important for experiments analysing the biocompatibility and/or toxicity related to nanoparticle exposure.

## Acknowledgments

Jenny Ordóñez and Dr. Xin Liu are acknowledged for providing valuable laboratory assistance. All members of the TRC and DRC are thanked for their support. This work was supported by The United States Air Force, National Health and Medical Research Council of Australia, EpiDerm, and The University of Queensland Research Scholarship (DCL).

## References

- [1] M. S. Roberts, Y. Dancik, T. W. Prow et al., “Non-invasive imaging of skin physiology and percutaneous penetration using fluorescence spectral and lifetime imaging with multiphoton and confocal microscopy,” *European Journal of Pharmaceutics and Biopharmaceutics*, vol. 77, no. 3, pp. 469–488, 2011.
- [2] N. A. Monteiro-Riviere and C. L. Tran, *Nanotoxicology: Characterization, Dosing and Health Effects*, Informa Healthcare, New York, NY, USA, 2007.
- [3] X. R. Xia, N. A. Monteiro-Riviere, and J. E. Riviere, “Skin penetration and kinetics of pristine fullerenes ( $C_{60}$ ) topically exposed in industrial organic solvents,” *Toxicology and Applied Pharmacology*, vol. 242, no. 1, pp. 29–37, 2010.
- [4] S. Küchler, M. Abdel-Mottaleb, A. Lamprecht, M. R. Radowski, R. Haag, and M. Schäfer-Korting, “Influence of nano-carrier type and size on skin delivery of hydrophilic agents,” *International Journal of Pharmaceutics*, vol. 377, no. 1-2, pp. 169–172, 2009.
- [5] J. G. Rouse, J. Yang, J. P. Ryman-Rasmussen, A. R. Barron, and N. A. Monteiro-Riviere, “Effects of mechanical flexion on the penetration of fullerene amino acid-derivatized peptide nanoparticles through skin,” *Nano Letters*, vol. 7, no. 1, pp. 155–160, 2007.
- [6] L. J. Mortensen, G. Oberdörster, A. P. Pentland, and L. A. DeLouise, “In vivo skin penetration of quantum dot nanoparticles in the murine model: the effect of UVR,” *Nano Letters*, vol. 8, no. 9, pp. 2779–2787, 2008.
- [7] S. A. Coulman, A. Anstey, C. Gateley et al., “Microneedle mediated delivery of nanoparticles into human skin,” *International Journal of Pharmaceutics*, vol. 366, no. 1-2, pp. 190–200, 2009.
- [8] H. I. Labouta, D. C. Liu, L. L. Lin et al., “Gold nanoparticle penetration and reduced metabolism in human skin by toluene,” *Pharmaceutical Research*, vol. 28, pp. 2931–2944, 2011.
- [9] H. J. Johnston, G. Hutchison, F. M. Christensen, S. Peters, S. Hankin, and V. Stone, “A review of the *in vivo* and *in vitro* toxicity of silver and gold particulates: particle attributes and biological mechanisms responsible for the observed toxicity,” *Critical Reviews in Toxicology*, vol. 40, no. 4, pp. 328–346, 2010.

- [10] M. Schneider, F. Stracke, S. Hansen, and U. F. Schaefer, "Nanoparticles and their interactions with the dermal barrier," *Dermato-Endocrinology*, vol. 1, no. 4, pp. 197–206, 2009.
- [11] M. Crosera, M. Bovenzi, G. Maina et al., "Nanoparticle dermal absorption and toxicity: a review of the literature," *International Archives of Occupational and Environmental Health*, vol. 82, no. 9, pp. 1043–1055, 2009.
- [12] G. Cevc and U. Vierl, "Nanotechnology and the transdermal route. A state of the art review and critical appraisal," *Journal of Controlled Release*, vol. 141, no. 3, pp. 277–299, 2010.
- [13] T. W. Prow, J. E. Grice, L. L. Lin et al., "Nanoparticles and microparticles for skin drug delivery," *Advanced Drug Delivery Reviews*, vol. 63, no. 6, pp. 470–491, 2011.
- [14] F. L. Filon, M. Crosera, G. Adami et al., "Human skin penetration of silver nanoparticles through intact and damaged skin," *Toxicology*, vol. 255, no. 1-2, pp. 33–37, 2009.
- [15] G. Sonavane, K. Tomoda, A. Sano, H. Ohshima, H. Terada, and K. Makino, "In vitro permeation of gold nanoparticles through rat skin and rat intestine: effect of particle size," *Colloids and Surfaces B*, vol. 65, no. 1, pp. 1–10, 2008.
- [16] M. S. Roberts, M. J. Roberts, T. A. Robertson et al., "In vitro and in vivo imaging of xenobiotic transport in human skin and in the rat liver," *Journal of Biophotonics*, vol. 1, no. 6, pp. 478–493, 2008.
- [17] M. G. Lin, T. L. Yang, C. T. Chiang et al., "Evaluation of dermal thermal damage by multiphoton autofluorescence and second-harmonic-generation microscopy," *Journal of Biomedical Optics*, vol. 11, no. 6, Article ID 064006, 2006.
- [18] M. G. Lin, W. L. Chen, W. Lo et al., "Three-dimensional skin imaging using the combination of reflected confocal and multiphoton microscopy," in *Photonic Therapeutics and Diagnostics III*, vol. 6424 of *Proceedings of SPIE*, p. E4240, San Jose, Calif, USA, January 2007.
- [19] M. J. Levene, T. H. Chia, A. Williamson, and D. D. Spencer, "Multiphoton fluorescence lifetime imaging of intrinsic fluorescence in human and rat brain tissue reveals spatially distinct NADH binding," *Optics Express*, vol. 16, no. 6, pp. 4237–4249, 2008.
- [20] L. L. Lin, J. E. Grice, M. K. Butler et al., "Time-correlated single photon counting for simultaneous monitoring of zinc oxide nanoparticles and NAD(P)H in intact and barrier-disrupted volunteer skin," *Pharmaceutical Research*, vol. 28, pp. 2920–2930, 2011.
- [21] D. L. Kaiser, L. Robert, and J. Watters, National Institute of Standards & Technology Report of Investigation Reference Material 8011 Gold Nanoparticles, Nominal 10 nm Diameter. 10 p.
- [22] D. L. Kaiser, L. Robert, and J. Watters, National Institute of Standards & Technology Report of Investigation Reference Material 8012 Gold Nanoparticles, Nominal 30 nm Diameter. 10 p.
- [23] D. L. Kaiser, L. Robert, and J. Watters, National Institute of Standards & Technology Report of Investigation Reference Material 8013 Gold Nanoparticles, Nominal 60 nm Diameter. 10 p.
- [24] W. Y. Sanchez, T. W. Prow, W. H. Sanchez, J. E. Grice, and M. S. Roberts, "Analysis of the metabolic deterioration of ex vivo skin from ischemic necrosis through the imaging of intracellular NAD(P)H by multiphoton tomography and fluorescence lifetime imaging microscopy," *Journal of Biomedical Optics*, vol. 15, no. 4, Article ID 046008, 2010.
- [25] J. E. Seto, B. E. Polat, R. F. Lopez, D. Blankschtein, and R. F. Langer, "Effects of ultrasound and sodium lauryl sulfate on the transdermal delivery of hydrophilic permeants: Comparative in vitro studies with full-thickness and split-thickness pig and human skin," *Journal of Controlled Release*, vol. 145, no. 1, pp. 26–32, 2010.
- [26] K. König and I. Riemann, "High-resolution multiphoton tomography of human skin with subcellular spatial resolution and picosecond time resolution," *Journal of Biomedical Optics*, vol. 8, no. 3, pp. 432–439, 2003.

## Research Article

# Control of *In Vivo* Transport and Toxicity of Nanoparticles by Tea Melanin

Yu-Shiun Chen,<sup>1</sup> Yao-Ching Hung,<sup>2,3</sup> Meng-Yeng Hong,<sup>1</sup> Andrei Aleksandrovich Onischuk,<sup>4</sup> Jin Chern Chiou,<sup>5</sup> Irina V. Sorokina,<sup>6</sup> Tatiana Tolstikova,<sup>6</sup> and G. Steve Huang<sup>1</sup>

<sup>1</sup>Department of Materials Science and Engineering, National Chiao Tung University, Hsinchu 300, Taiwan

<sup>2</sup>Department of Obstetrics and Gynecology, China Medical University and Hospital, 91 Hsueh Shih Road, Taichung 404, Taiwan

<sup>3</sup>College of Medicine, China Medical University, Taichung 40402, Taiwan

<sup>4</sup>Institute of Chemical Kinetics & Combustion, Siberian Branch of Russian Academy of Sciences, Novosibirsk 630090, Russia

<sup>5</sup>Institute of Electrical Control Engineering, National Chiao Tung University, 1001 University Road, EE772, Hsinchu 300, Taiwan

<sup>6</sup>Institute of Organic Chemistry, Siberian Branch of Russian Academy of Sciences, Novosibirsk 630090, Russia

Correspondence should be addressed to G. Steve Huang, gstevehuang@mail.nctu.edu.tw

Received 5 April 2012; Accepted 14 May 2012

Academic Editor: Xiaoming Li

Copyright © 2012 Yu-Shiun Chen et al. This is an open access article distributed under the Creative Commons Attribution License, which permits unrestricted use, distribution, and reproduction in any medium, provided the original work is properly cited.

Nanoparticles are unfamiliar to researchers in toxicology. Toxicity may be generated simply due to the reduction in size. Compounds that prevent or cure toxic materials may not work on nanoparticles. Furthermore, as there are more and more applications of nanoparticles in drug delivery and *in vivo* imaging, controlling the transport and toxicity will be primary concerns for medical application of nanoparticles. Gold nanoparticles (GNPs) if injected intraperitoneally into mice can enter hippocampus and induce cognitive impairment. GNPs caused a global imbalance of monoamine levels, specifically affecting the dopaminergic and serotonergic neurons. Pretreatment of tea melanin significantly prevented the deposition of GNPs in mouse brains, especially in the hippocampus. Pretreatment of melanin completely alleviated GNP-induced impairment of cognition. Pre-administration of melanin stably maintained monoamines at normal profiles. Melanin completely prevented the invasion of GNPs into the Cornu Ammonis region of the hippocampus shown by coherent anti-Stoke Raman scattering microscopy. Here we show that the administration of tea melanin prevented the accumulation of Au in brain, the imbalance of monoamines, and the impairment of cognition in mice. The current study provides a therapeutic approach to toxicity of nanoparticles and a novel strategy to control the transport of GNP in mouse brain.

## 1. Introduction

Nanoparticles provide a novel platform for target-specific delivery of therapeutic agents [1–3]. Gold nanoparticles (GNPs) have recently been developed as an attractive candidate for use as carriers in drug and gene delivery, particularly because the gold core is essentially inert and nontoxic *in vitro* [4–7]. GNPs have been developed as drug carriers in pharmaceutical studies. This is largely due to the apparent benefits in targeting and medical image enhancement. Multiple conjugations can be achieved through the tight binding of sulfhydryl groups. In addition, GNPs are capable of passing both the blood-brain barrier and the blood-retinal barrier

[8]. However, neurotoxicity of GNPs has been reported to impair cognition in mice. In order to enhance the use of GNPs as drug carriers, the *in vivo* toxicity of nanoparticles must be minimized.

In general, GNPs exhibit very low cytotoxicity [9–16]. The cellular uptake of GNPs likely occurs through endocytosis, and is greatest for 50 nm particles [17]. The rare exception is that GNPs under 2 nm in diameter are toxic to many cell lines [18]. Furthermore, GNP uptake has been associated with damage to the cytoskeleton and cell adhesion [19].

GNPs show minor *in vivo* toxicity [20]. The tissue distribution of GNPs in rats and mice has been examined by inductively coupled plasma mass spectrometry (ICP-MS)

[21, 22]. GNPs 10 nm in diameter were present in the liver, spleen, kidney, testis, thymus, heart, lung, and brain, whereas GNPs larger than 50 nm were largely detected in the blood, liver, and spleen. GNPs ranging from 10 to 50 nm were found in the brain. In zebrafish embryos, silver nanoparticles produced almost 100% mortality, whereas GNPs induced minimal mortality at the same time point [23]. Previously, we have shown that GNPs can pass through the blood-retinal barrier and impair cognition in mice. To make better use of GNPs as a drug carrier to target the brain, the neurotoxicity must be eliminated.

We previously reported a polyphenolic antioxidant, of melanin nature, found in the black tea *Camellia sinensis* [24]. *Camellia sinensis* tea melanin comprises the high molecular weight portion of tea polyphenols [25]. Tea melanin has demonstrated a wide range of biochemical and pharmacological activities in animals including antioxidant activity, free radical scavenging, and immunomodulation [26–28]. Melanin also has revealed unexpected protective activity against various toxic substances, such as, benzidine, hydrazine, snake venoms, cisplatin, and acetaminophen [29–32].

In addition to antioxidant properties, one of the most significant properties of melanin is its chelating capability [33]. Melanin is capable of chelating heavy metals. In particular, melanin complexes with gadolinium (Gd) for use in Magnetic Resonance Imaging (MRI), thereby alleviating the *in vivo* toxicity of Gd [27]. In addition, melanin possesses paramagnetic properties due to a high concentration of free radicals conjugated to its polymeric matrix. The chelating and paramagnetic properties render melanin a promising candidate to scavenge GNPs *in vivo*.

## 2. Materials and Methods

**2.1. Materials.** HAuCl<sub>4</sub>, sodium citrate, NaBH<sub>4</sub>, HCl, HNO<sub>3</sub>, H<sub>2</sub>SO<sub>4</sub>, H<sub>2</sub>O<sub>2</sub>, scopolamine, and other chemicals of analytical grade were purchased from Sigma-Aldrich and Fisher (United States). H<sub>2</sub>O was obtained at >18 MΩ from a Milli-Q water purification system. Fully fermented black tea was purchased from local retail shops (Miaoli, Taiwan).

**2.2. Animal Treatment.** Animal treatments were performed following “The Guidelines for the Care and Use of Experimental Animals” of National Chiao Tung University, Taiwan. Four-week-old male BALB/c mice were housed at 22 ± 2°C with a 12 h light/dark cycle and were fed standard rodent chow and water *ad libitum*. Mice were randomly assigned to experimental or control groups consisting of 6–8 mice. The control group did not receive any treatment, and the experimental groups were as follows: a melanin-treated group, a 17 nm GNP-treated group, a 37 nm GNP-treated group, a melanin pretreated-plus 17 nm GNP-treated group, and a melanin pretreated-plus 37 nm GNP-treated group. GNPs were administered in a single dose intraperitoneally. For the passive avoidance test, an additional positive control that received scopolamine (1 mg/kg i.p.) was incorporated.

**2.3. Preparation of Gold Nanoparticles.** GNPs, with diameters of 17 and 37 nm, were synthesized as previously reported [34, 35]. The seed colloids were prepared by adding 1 mL of 0.25 mM HAuCl<sub>4</sub> to 90 mL of H<sub>2</sub>O and stirring for 1 min at 25°C. A 2 mL volume of 38.8 mM sodium citrate was stirred into the solution for 1 min, and then 0.6 mL of freshly prepared 0.1 M NaBH<sub>4</sub> in 38.8 mM sodium citrate was added. Different diameters of GNPs ranging from 3 to 100 nm were generated by altering the volume of added seed colloid. The solution was stirred for an additional 5–10 min at 0–4°C. Reaction temperatures and times were adjusted to obtain larger GNPs. All synthesized GNPs were characterized by UV absorbance. The size of the synthesized GNPs was verified by electron microscopy and atomic force microscopy. GNPs were dialyzed against phosphate buffered saline (pH 7.4) before injection into the animals.

**2.4. Extraction, Fractionation, and Characterization of Tea Melanin.** Isolation of tea melanin was performed according to a previous report [25]. Monomeric polyphenols were removed by treating the tea leaves with boiling water at a ratio of 1 : 10 (m/v) for 10 min followed by filtration. The obtained solid matter was immersed in 40°C water at a 1 : 10 (solid/liquid) ratio, and the pH was adjusted to 10.5 with 10% NH<sub>4</sub>OH. The extraction time was reduced to 12 h to avoid excessive oxidation of melanin. The extract was filtered and acidified to pH 2.5 using 2 N HCl and then centrifuged at 15,000 g for 15 min to form a pellet. Acid hydrolysis of the pellet was employed to remove carbohydrates and proteins. Organic solvents (chloroform, ethyl acetate, and ethanol) were used to remove lipids and related compounds. In addition, melanin was reduced by treatment with Ti<sup>+3</sup>. The reduced melanin was dialyzed against Milli-Q water to remove Ti<sup>+3</sup>. Finally, the reduced sample was suspended in distilled water, and 0.1 M NaOH was added drop wise to dissolve the melanin and to adjust the pH to 7.0. The solution was filtered through a Nalgene 0.45 μm filter. Melanin was fractioned on a Sephadex G-75 column (1.6 × 40 cm) at a 0.5 mL/min flow rate using 50 mM phosphate buffer (pH 7.5). Fractions were monitored by ultraviolet (UV) absorbance at 280 nm. All operations were conducted under N<sub>2</sub>. The physical and chemical characteristics of melanin were examined as described. UV absorption spectra were recorded on a JASCO V-530 UV-Visible Spectrophotometer. Infrared (IR) spectra were recorded on a Perkin Elmer spectrometer (Model 1600 FT). The purity of melanin was examined by thin layer chromatography (TLC) using silica gel as the stationary phase and chloroform/ethyl acetate/formic acid (6:4:1) as the mobile phase. Melanin was retained at the origin in TLC separation and did not produce any additional signals on the chromatogram. Comparisons with TLC separation of caffeine, catechin, epicatechin, epicatechin gallate, epigallocatechin, epigallocatechin gallate, and theaflavin assured that the melanin preparation was free from these components.

**2.5. Inductively Coupled Plasma Mass Spectrometry (ICP-MS).** For total element determinations, standard solutions were

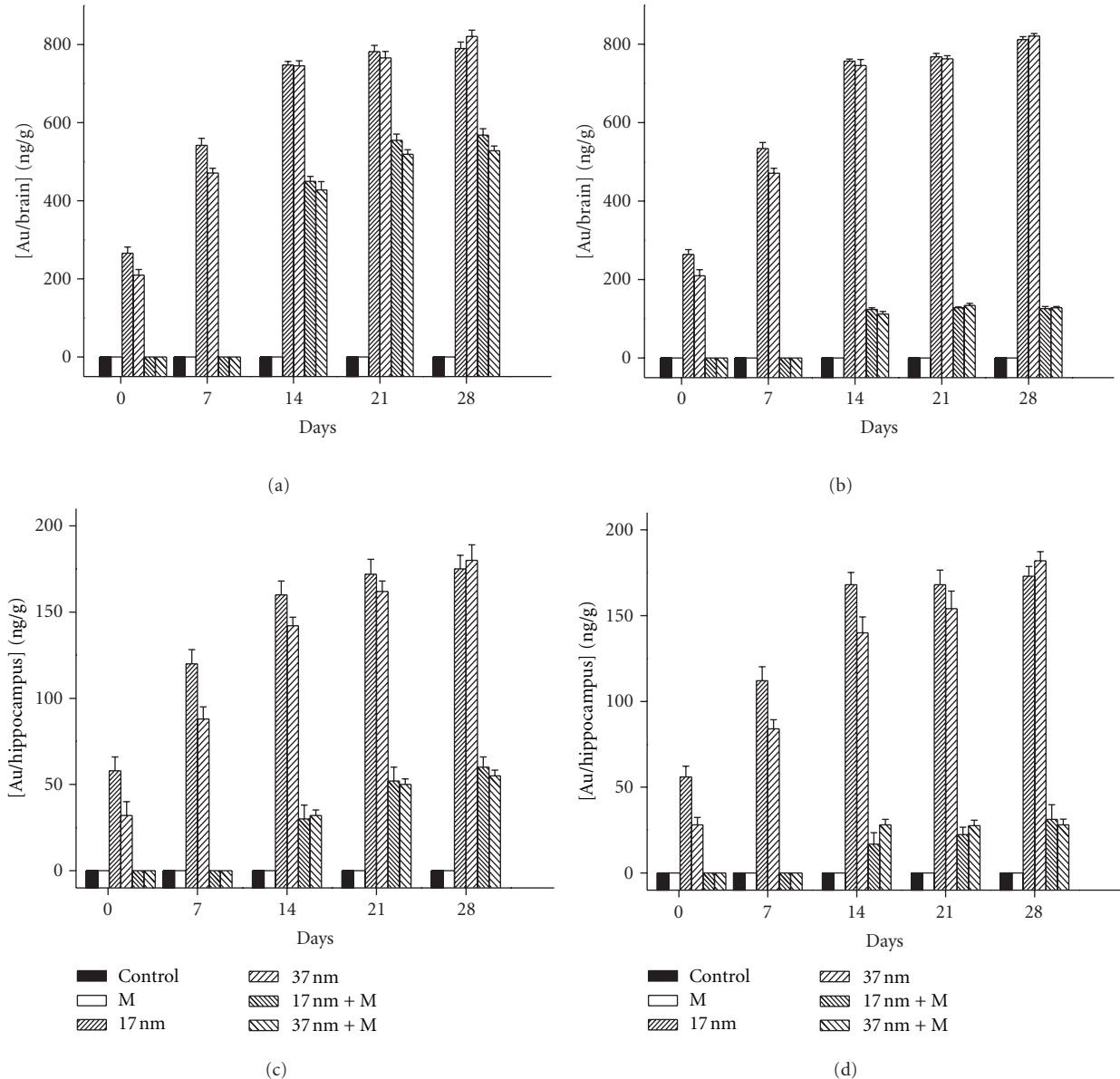


FIGURE 1: The effect of tea melanin on the accumulation of GNPs in the brain and hippocampus. Mice were divided into 6 groups: a control group receiving PBS; a melanin group receiving 0.3 or 0.5 mg/kg tea melanin; a 17 nm group receiving 10 mg/kg of 17 nm GNP; a 37 nm group receiving 10 mg/kg of 37 nm GNP; a 17 nm + M group receiving 10 mg/kg of 17 nm GNP and pretreated with 0.3 or 0.5 mg/kg melanin; a 37 nm + M group receiving 10 mg/kg of 37 nm GNP and pretreated with 0.3 or 0.5 mg/kg melanin. Each group included 30 mice. Six mice from each group were sacrificed on day 1, 7, 14, 21, and 28. The brain was carefully dissected and the hippocampus was separated. ICP-MS was performed to obtain the content of Au. (a) Deposition of Au in the hippocampus for mice receiving 0.3 mg/kg melanin. (b) Deposition of Au in the brain for mice receiving 0.3 mg/kg melanin. (c) Deposition of Au in the hippocampus for mice receiving 0.5 mg/kg melanin. (d) Deposition of Au in the brain for mice receiving 0.5 mg/kg melanin.

prepared by dilution of a multielement standard (1,000 mg/L in 1 M HNO<sub>3</sub>) obtained from Merck (Darmstadt, Germany). Nitric acid (65%), hydrochloric acid (37%), perchloric acid (70%), and hydrogen peroxide (30%) of Suprapur grade (Merck) were used to mineralize the samples. A size-exclusion column was connected to the ICP-MS apparatus. Brain section samples were homogenized in 25 mM tris(hydroxymethyl) aminomethane (Tris)-12.5 mM HCl

buffer solution at pH 8 and centrifuged at 13,000 rpm for 1 h. The supernatant was applied to the size-exclusion column of the HPLC system, which had been equilibrated with 25 mM Tris-12.5 mM HCl (containing 20 mM KCl) and eluted with the same buffer at a flow rate of 1 mL/min. The metal components of metal-binding proteins that were eluted from the HPLC system were detected by ICP-MS (Perkin Elmer, SCIEX ELAN 5000). The main instrumental operating

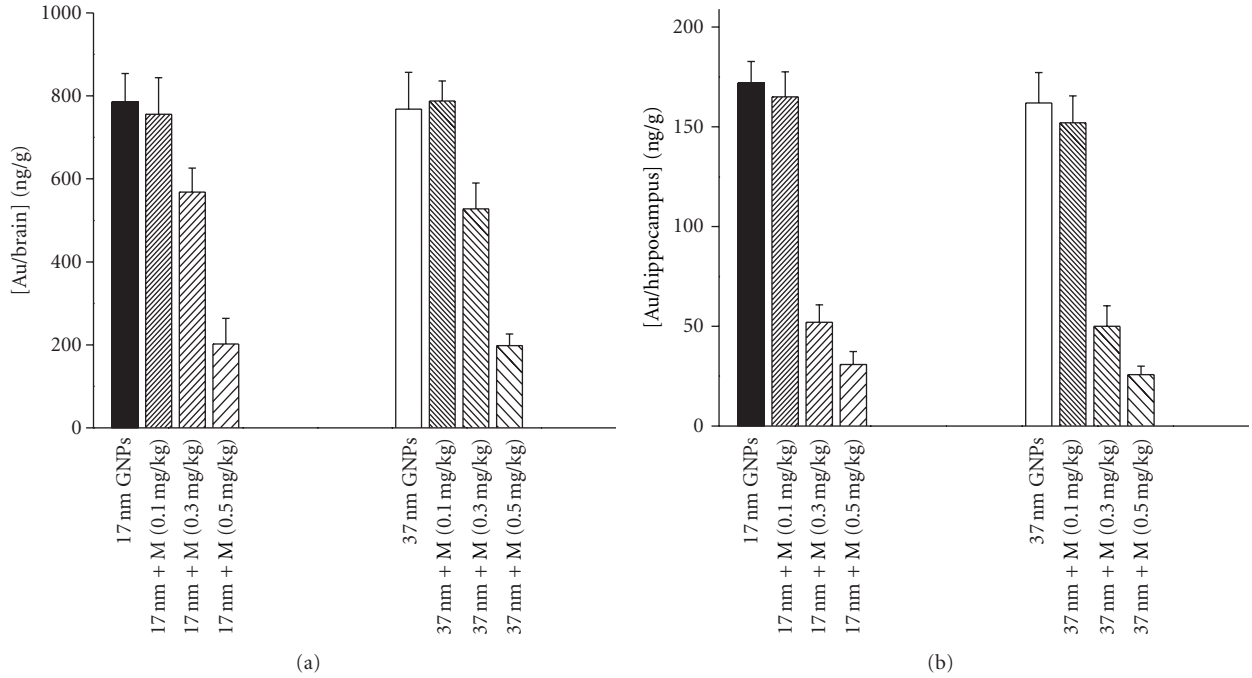


FIGURE 2: Dose-dependence for melanin-suppression of Au deposition in the brain and the hippocampus. Mice were pretreated with melanin at 0.1, 0.3, or 0.5 mg/kg and received 10 mg/kg 17 nm or 37 nm GNPs. The accumulation of Au on day 21 was obtained. (a) Accumulation of 17 nm GNP (left) and 37 nm GNP (right) in the brain. (b) Accumulation of 17 nm GNP (left) and 37 nm GNP (right) in the hippocampus.

conditions were as follows: RF power 1900 W, carrier gas flow 0.8 L/min Ar, and makeup gas flow 0.19 L/min Ar. 197 Au was used as the internal standard.

**2.6. Passive-Avoidance Test.** The passive-avoidance apparatus consisted of two compartments with a steel-rod grid floor (36 parallel steel rods, 0.3 cm in diameter, set 1.5 cm apart). One of the compartments ( $48 \times 20 \times 30$  cm) was equipped with a 20 W lamp located centrally at a height of 30 cm, and the other compartment was dark and of the same size, connected through a guillotine door (5 × 5 cm). The dark room was used during the experimental sessions that were conducted between 09:00 and 17:00 h. During the training trial, the guillotine door between the light and dark compartment was closed. When the mouse was placed in the light compartment with its back to the guillotine door, the door was opened, and the time until the mouse entered the dark compartment (step-through latency, STL) was measured with a stopwatch. After the mouse entered the dark compartment, the door was closed. An inescapable scrambled foot shock (1 mA for 2 s) was delivered through the grid floor. The mouse was removed from the dark compartment 5 s after the shock. Then, the mouse was put back into the home cage until the retention trial was carried out 24 hours later. The mouse was again placed in the light compartment, and as in the training trial, the guillotine door was opened and the STL was recorded and used as a measure of retention. If the mouse did not step through the door after 300 s, the experiment was terminated.

**2.7. Analysis of Monoamine and Acetylcholine Concentrations in the Mouse Brain.** Monoamine levels were determined as previously reported [36]. The mice were decapitated, and their brains were quickly removed. The brain samples were weighed and homogenized on ice using a polytron homogenizer (Kinematica, Lucern, Switzerland) at a maximum setting for 20 s in 10 volume equivalents of 0.2 M perchloric acid containing 100 mM Na<sub>2</sub>-EDTA and 100 ng/mL isoproterenol. The homogenate was centrifuged at 15,000 g for 30 min. The pH was adjusted to approximately 3.0 using 1 M sodium acetate. After filtration (0.45 μm), the samples were separated using high-performance liquid chromatography (HPLC). Monoamines and their metabolites were separated using HPLC at 30°C on a reverse-phase analytical column (ODS-80, 4.6 mm i.d. × 15 cm) and detected with an electrochemical detector (Model ECD-100, Eikom Co., Kyoto, Japan). The column was eluted with 0.1 M sodium acetate-citric acid buffer (pH 3.5) containing 15% methanol, 200 mg/L sodium 1-octanesulfonate, and 5 mg/L Na<sub>2</sub>-EDTA. The following monoamines and their metabolites were measured: norepinephrine (NE), 4-hydroxy-3-methoxyphenylglycol (MHPG), dopamine (DA), 3,4-dihydroxyphenylacetic acid (DOPAC), 5-hydroxytyramine (5-HT, serotonin), 5-hydroxyindoleacetic acid (5-HIAA), epinephrine (EPI), and homovanillic acid (HVA).

**2.8. Ex Vivo Coherent Anti-Stoke Raman Scattering (Cars) Microscopy.** Freshly excised hippocampi were dissected into thin slices, approximately 2 mm in thickness and immersed

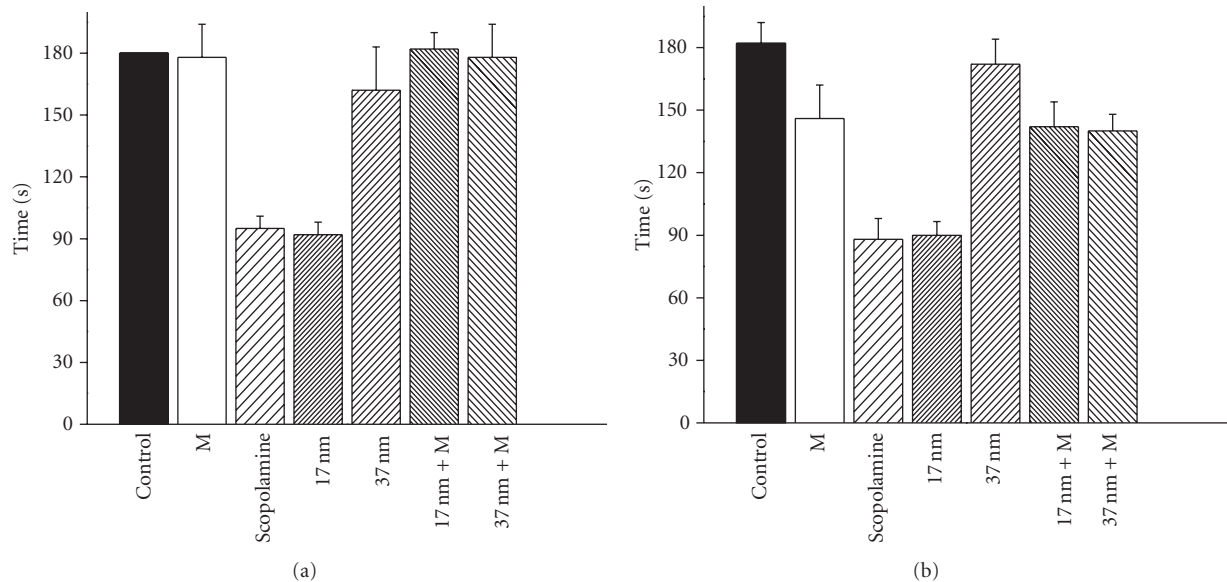


FIGURE 3: The effect of melanin pretreatment on GNP-induced cognition impairment. A passive avoidance test using light/dark rooms was performed. The latency time profiles on day 21 are shown for mice pretreated with 0.3 mg melanin/kg (a) and 0.5 mg melanin/kg (b). Each group of columns contains, in sequence, the averaged values from the control group (control), the melanin-treated only group (M), the scopolamine-treated group (scopolamine), the 17 nm GNP-treated group (17 nm), the 37 nm GNP-treated group (37 nm), the melanin pretreatment-plus 17 nm GNP-treated group (M + 17 nm), and the melanin pretreatment-plus 37 nm GNP-treated group (M + 37 nm). \*represents  $P < 0.05$  and \*\*represents  $P < 0.001$  from the student's  $t$ -test.

into a microchamber filled with PBS on a glass slide for examination. CARS microscopy was performed using a time constant of 3 ms, a scanning area of  $300 \times 300 \mu\text{m}$ , a step size of  $1 \mu\text{m}$ , a scanning size of  $300 \times 300$  pixels, a scanning velocity of  $1 \mu\text{m}/\text{ms}$ , and a sampling rate of 80 kHz. Laser power was set at 30 mW for 870 nm and 40 mW for 1,064 nm. The wavelengths of the Pump and the Stokes lasers (Pump = 870 nm and Stokes = 1,064 nm) were tuned to match a Raman shift ( $\sim 2100 \text{ cm}^{-1}$ ) that falls in the so-called “silent region” of the vibrational spectra of cells and tissues. As expected, the CARS images of the untreated hippocampus did not show appreciable contrast under the nonresonant condition. The CARS signals from GNP-treated specimens, however, were dramatically enhanced, that is, they appeared as scattered bright spots. The signal enhancement presumably resulted from strong scattering and large third-order polarizability of the GNPs [37–40].

**2.9. Statistical Analyses.** All data are presented as the mean  $\pm$  SD with a minimum of 6 mice per group. Concentrations of biogenic amines in mouse brains were analyzed using the unpaired Student's  $t$ -test. The criterion for statistical significance was set at  $P < 0.05$  for all statistical evaluations.

### 3. Results and Discussion

**3.1. Pretreatment of Melanin Reduced Au Accumulation in Brain and Hippocampus.** Accumulation of Au in the brain was investigated (Figure 1). Mice were divided into 6 groups

as follows: a control group receiving PBS; a melanin group receiving 0.5 mg/kg tea melanin; 17 nm GNP group receiving 10 mg/kg of 17 nm GNPs; 37 nm group receiving 10 mg/kg of 37 nm GNPs; 17 nm + M group receiving 10 mg/kg of 17 nm GNPs and 0.3 or 0.5 mg/kg melanin 3 hours prior to GNP treatment; 37 nm + M group receiving 10 mg/kg 37 nm GNPs and receiving 0.3 or 0.5 mg/kg melanin 3 hours prior to GNP treatment. Each group included 30 mice. Six mice from each group were sacrificed on day 1, 7, 14, 21, and 28. The brains were carefully dissected and the hippocampi were separated. ICP-MS was performed to obtain measurements for the accumulation of Au. Without melanin pretreatment, GNPs accumulated rapidly in the brain and reached a plateau of approximately 770 ng/g brain on day 14 (Figure 1(a)). The accumulation of 17 nm GNPs was apparently faster than that of 37 nm GNPs in the first 14 days. However, both GNPs reached the same plateau and remained unchanged at later time points. Pretreatment of 0.3 mg/kg melanin effectively suppressed the accumulation of Au in brains during the first 2 weeks. However, an abrupt increase in Au accumulation was observed in brains at later time points (440 ng/g brain for 17 nm GNPs and 420 ng/g brain for 37 nm GNPs). The amount of accumulation for melanin pretreated groups was approximately 65% compared to the control group on day 14. This ratio was slowly increased to 75% at the end of the experiment. Administration of 0.5 mg/kg melanin significantly reduced the accumulation of GNPs in the brain from  $\sim 420$  to 100 ng/g for 17 nm and 37 nm GNPs on day 14 (Figure 1(b)). The amount of Au was maintained at this level until the end of the experiment. Pretreatment of melanin at

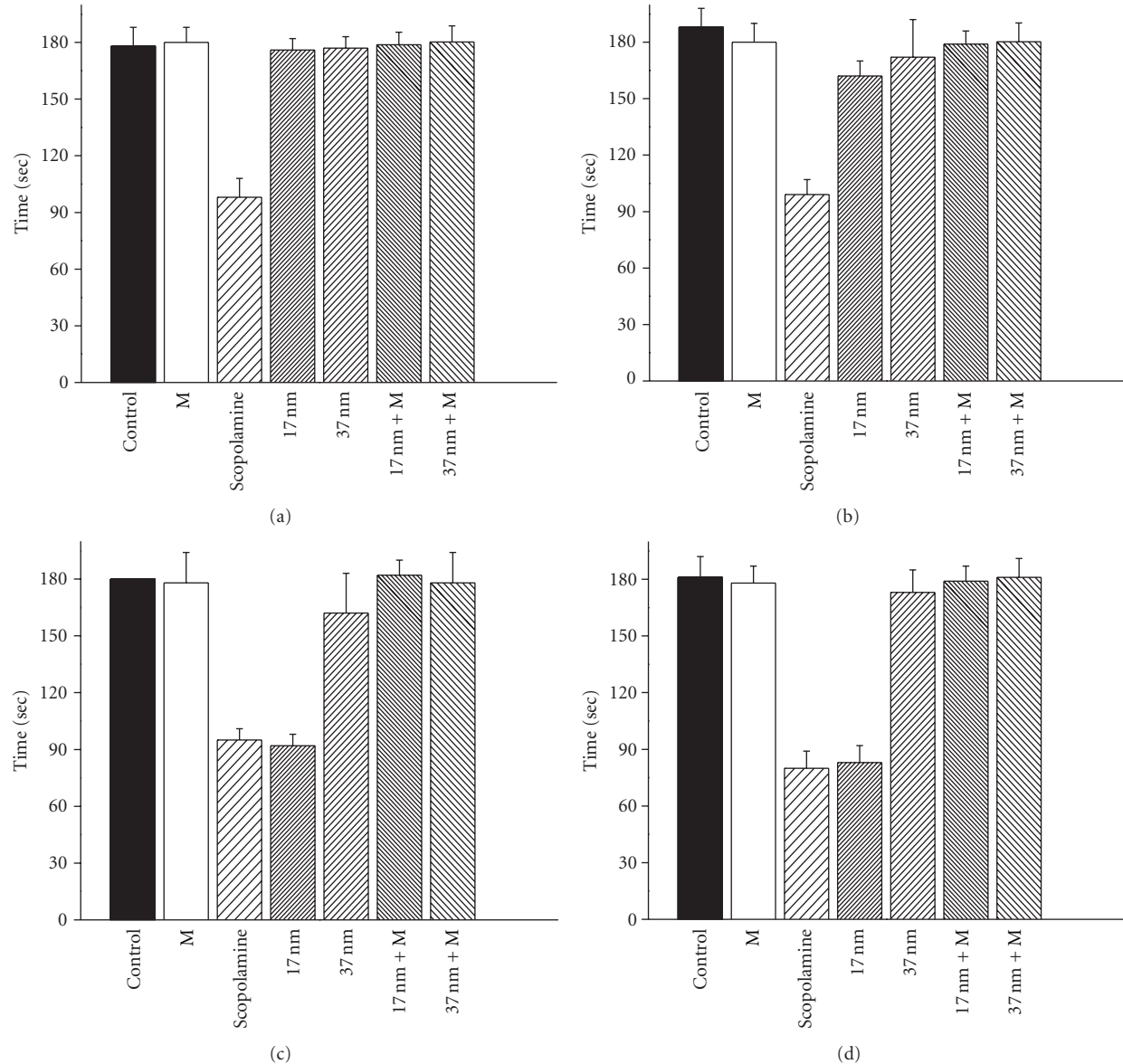


FIGURE 4: Time course of the passive-avoidance test performed on mice pretreated with melanin at 0.3 mg/kg. Mice were pretreated with melanin at 0.3 mg/kg followed by injection with 17 nm GNPs. The passive avoidance test was performed on day 7 (a), day 14 (b), day 21 (c), and day 28 (d).

0.5 mg/kg effectively suppressed the accumulation of GNPs in the brain.

In the hippocampus, the Au accumulation profile resembled that of the brain. The Au accumulation increased rapidly during the first two weeks and reached a plateau of ~160 ng/g of hippocampus on day 14. Pretreatment of melanin at 0.3 mg/kg decreased accumulated Au to a nondetectable level in two weeks (Figure 1(c)), but Au increased rapidly to 30 ng/g on day 14, reaching 60 ng/g on day 28. Pretreatment of melanin at 0.5 mg/kg decreased accumulated Au to a nondetectable level for the first two weeks (Figure 1(d)), but Au increased rapidly to 25 ng/g on day 14, remaining unchanged until day 28.

The suppression of Au accumulation by pretreatment of melanin was dose-dependent (Figure 2). On day 21, pre-treatment of 0.1 mg/kg melanin exhibited no influence on the suppression of Au accumulation in the brain (Figure 2(a)) and hippocampus (Figure 2(b)). Administration of 0.3 mg/kg melanin reduced Au accumulation by 30% for 17 nm GNPs and by 36% for 37 nm GNPs in the brain. Melanin at this dosage also reduced 71% Au accumulation for 17 nm and 37 nm GNPs in the hippocampus. Administration of 0.5 mg/kg melanin reduced 74% of Au accumulation for 17 nm GNPs and 37 nm GNPs in the brain. Melanin at this dosage also reduced Au accumulation by 82% for 17 nm GNPs and by 84% for 37 nm GNPs in the hippocampus.

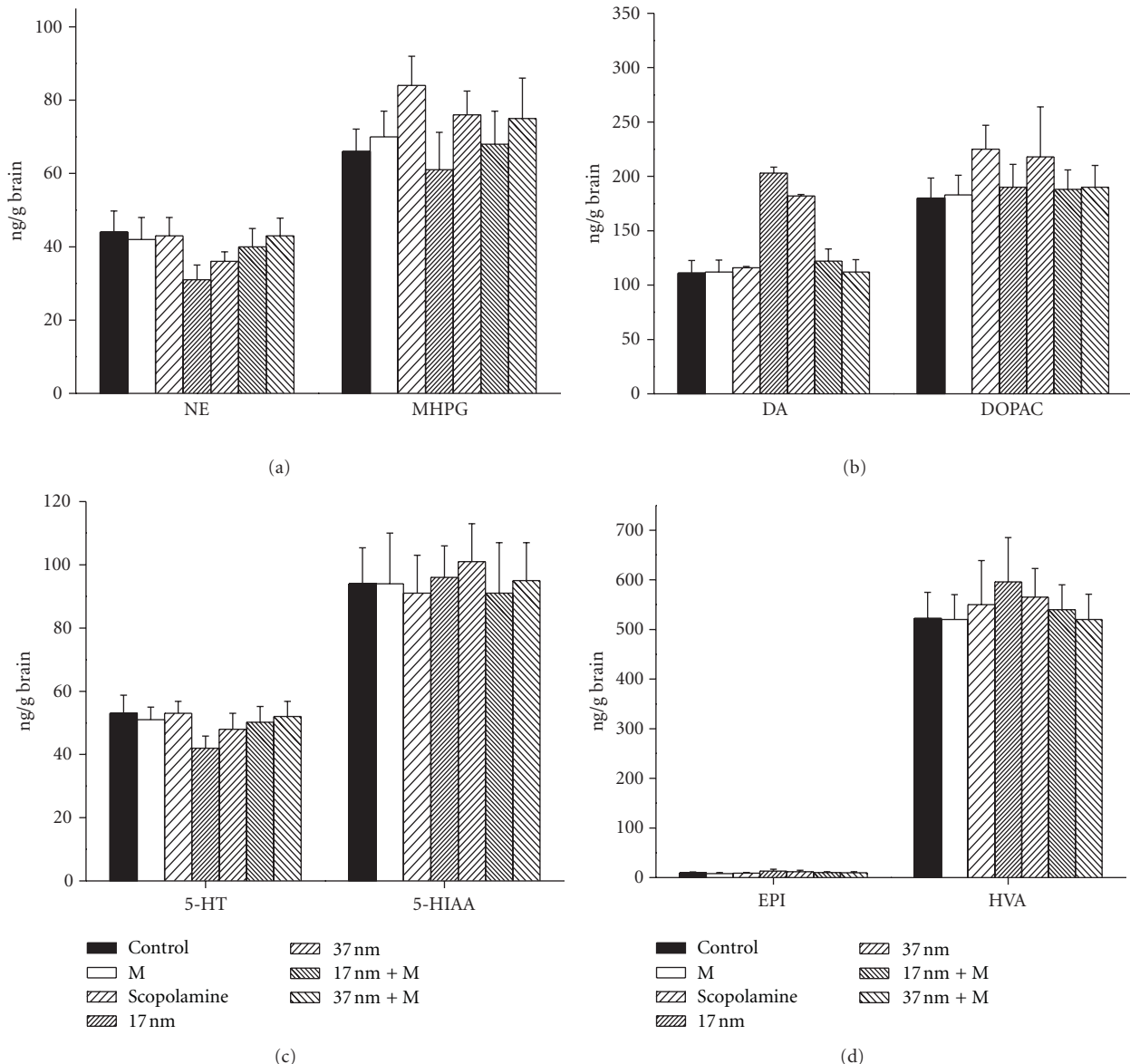


FIGURE 5: Melanin ameliorates the GNP-induced imbalance of neurotransmitter profiles. Immediately after the passive avoidance test, brain tissues were removed and the levels of monoamines were analyzed by HPLC. The levels of neurotransmitters and their metabolites are shown. (a) Norepinephrine (NE) and 4-hydroxy-3-methoxyphenylglycol (MHPG, metabolite). (b) Dopamine (DA) and 3,4-dihydroxyphenylacetic acid (DOPAC, metabolite). (c) 5-Hydroxytryptamine (5-HT, serotonin) and 5-hydroxyindoleacetic acid (5-HIAA, metabolite). (d) epinephrine (EPI) and homovanillic acid (HVA, metabolite). Each group of columns contains, in sequence, averaged values from the control group (control), the melanin-treated only group (M), the scopolamine-treated group (scopolamine), the 17 nm GNP-treated group (17 nm), the 37 nm GNP-treated group (37 nm), the melanin pretreatment-plus 17 nm GNP-treated group (M + 17 nm), and the melanin pretreatment-plus 37 nm GNP-treated group (M + 37 nm). \*represents  $P < 0.05$  and \*\*represents  $P < 0.001$  from the student's *t*-test.

**3.2. Melanin Ameliorated GNP-Induced Cognition Impairment in Mice.** GNP of 17 nm diameter impaired the cognition of mice, which was evident by the reduction in latency time measured for the passive avoidance test [41]. Pretreatment of melanin efficiently suppressed the accumulation of GNPs in mouse brains and hippocampi. However, it is not clear if the remaining GNPs would cause any physiological damage to the hippocampus. Mice were pretreated with 0.3 or 0.5 mg/kg melanin and injected with GNPs at

10 mg/kg. The passive-avoidance test was performed on day 21 (Figure 3). Scopolamine, serving as a positive control, shortened the latency time from 180 s to 90 s. Injection of 17 nm GNPs shortened the latency time from 180 s to 90 s. Pretreatment of melanin at a dosage of 0.3 mg/kg recovered the latency time to 180 s (Figure 3(a)). Melanin at 0.5 mg/kg also recovered the latency time to 140 s. Melanin is a mild sedative, and pretreatment with 0.5 mg/kg induced a minor neuronal disturbance, which was evident in the passive

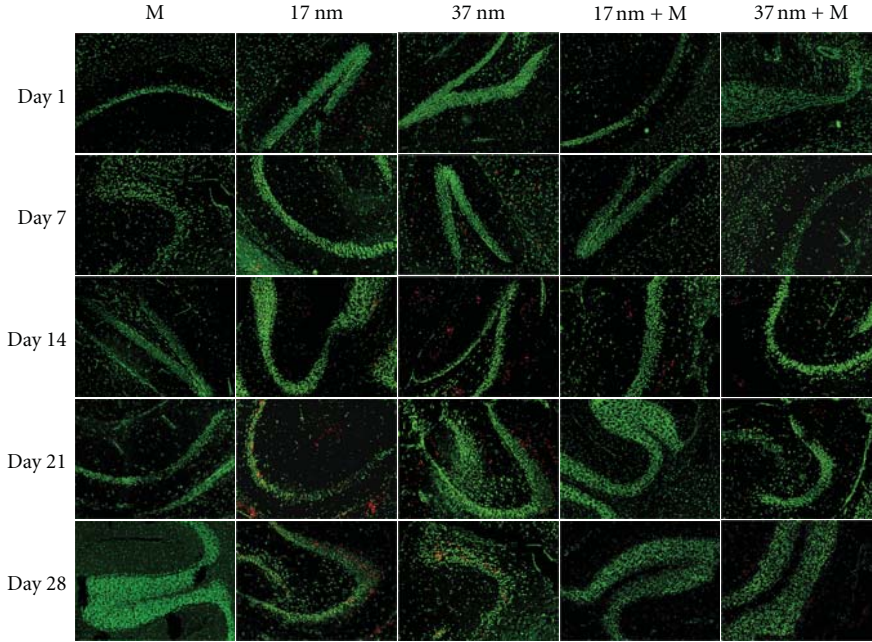


FIGURE 6: Time course examination by CARS microscopy of hippocampi isolated from mice in the melanin-treated only group (M), the 17 nm GNP-treated group (17 nm), the 37 nm GNP-treated group (37 nm), the melanin pretreatment-plus 17 nm GNP-treated group (M + 17 nm), and the melanin pretreatment-plus 37 nm GNP-treated group (M + 37 nm). The wavelengths of the Pump and Stokes lasers (Pump = 870 nm and Stokes = 1,064 nm) were tuned to match a Raman shift ( $\sim 2,100 \text{ cm}^{-1}$ ) that fell in the so-called “silent region” of the vibrational spectra of cells and tissues. To better visualize the location of GNPs, the enhanced bright spots are colored red in the final images. The green fluorescence is the auto-fluorescence emitted from the cells of the CA region of the hippocampus.

avoidance test. A 20% reduction in latency was observed for the melanin-treated group (Figure 3(b); M, M + 17 nm, and M + 37 nm). Although melanin at 0.5 mg/kg reduced the accumulation of Au more efficiently than melanin at 0.3 mg/kg, the lower dose was selected for the remaining experiments due to the lower neuronal toxicity.

Mice were treated with melanin at 0.3 mg/kg prior to the administration of 17 nm or 37 nm GNPs. The passive avoidance test was performed on day 7, 14, 21, and 28 (Figure 4). On day 14, mice treated with 17 nm GNPs started to show cognition impairment, which was pronounced by day 21. Injection of 37 nm GNP, however, never showed symptoms of neurotoxicity throughout the course of experiment. Pretreatment of melanin was sufficient to suppress the neurotoxicity induced by 17 nm GNP injection.

**3.3. Melanin Prevented the GNP-Induced Imbalance of Monoamines in Brain.** A global imbalance of neurotransmitters in the brain has been associated with GNP treatment [41]. In particular, analysis for monoamines from brain tissues has indicated that treatment with GNPs elevates dopamine levels and decreases serotonin levels. Administration of GNPs affected the mouse dopaminergic and serotonergic neurons. Mice were pretreated with 0.3 mg melanin/kg and then injected with GNPs at 10 mg/kg. The levels of monoamines were measured (Figure 5). The levels of norepinephrine (NE) and epinephrine (EPI) were undisturbed. GNP injection elevated the level of dopamine (DA), which was alleviated

by the pretreatment of melanin. GNP also decreased the level of 5-hydroxytyramine (5-HT, serotonin), which was also brought back to normal with melanin pretreatment (see Figure S1 in Supplementary Materials available online at doi:10.1155/2012/746960). The ameliorating effect of melanin pretreatment was validated by these monoamine profiles in the brain.

**3.4. Melanin Retarded the Invasion of GNPs into the Hippocampus.** The hippocampus is located in the medial temporal lobe of the brain, which belongs to the limbic system and plays major roles in short-term memory and spatial navigation. GNP injection impaired learning and memory in mice, and so the GNPs could have been transported through the blood, across the blood-brain barrier into the brain and into the hippocampus. Furthermore, 17 nm and 37 nm GNPs showed differential effects on the cognition impairment of mice, although the accumulation rate of both GNPs in the brain and hippocampus were strikingly similar. To localize GNPs, the freshly dissected hippocampi were examined using *ex vivo* CARS microscopy (Figure 6). GNPs are known to enhance the anti-Stoke Raman signal of nearby amino acids. Using the proper controls, enhancement visualized by CARS strongly indicated the presence of GNPs. Localized enhancement of the anti-Stoke Raman signal at an excitation wavelength of 817 nm was observed from the hippocampi removed from 17 nm and 37 nm GNP-treated mice. The Raman signal was completely absent from control

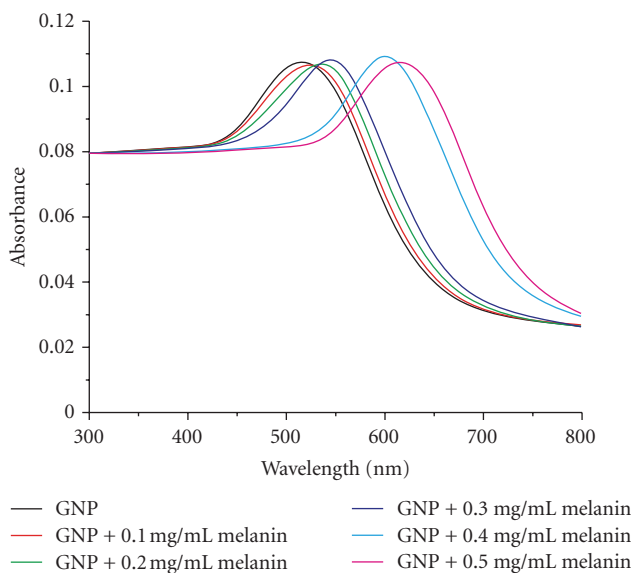


FIGURE 7: UV spectra for the titration of 17 nm GNP with melanin. Melanin is mixed with GNP at final concentrations of 0, 0.1, 0.2, 0.3, 0.4, and 0.5 mg/mL for melanin and 0.34 mM for GNP. UV absorbance of the binding reactions is shown. Red-shift of the absorbance peak indicates the increasing diameter of binding complex.

mouse tissues (mice pretreated with melanin). On day 21, the Raman signal of 17 nm GNPs was localized at the CA region of the hippocampus inside the cluster of neuronal cells, whereas 37 nm GNPs were less visible and scattered throughout the peripheral region. The distribution of 17 nm and 37 nm GNPs in the hippocampus suggests that the invasion of GNPs into the cluster of neuronal cells in the CA might have caused the learning impairment in the 17 nm GNP-treated mice. Accordingly, 37 nm GNPs were incapable of entering the neuronal cells, therefore causing only minimal deficits in learning and memory. The melanin-pretreated groups did not show scattered light throughout the whole study, which was consistent with our passive-avoidance test.

The *in vivo* toxicity of GNPs may very likely originate from the inability of the immune system to scavenge GNPs from organs. GNPs alone are biocompatible and stimulate a very minor immune response [42]. An overdose of GNPs, however, may cause a lethal effect in mice [20]. The lethality may be alleviated by the conjugation of immune-stimulating peptides to GNP.

The heavy metal chelating ability might play a role in the prevention of GNP nanotoxicity. Titration of 17 nm GNP by melanin was performed *in vitro* (Figure 7). In the titration experiment, melanin replaced citrate forming melanin-GNP complex. Melanin apparently has higher affinity than citrate to GNP binding. The melanin-GNP binding complex was stable in solution when heated up to 70°C for 10 min. Melanin is potentially capable of scavenging GNPs from blood stream.

Melanin is known to stimulate the immune system in mice [24]. The administration of melanin could enhance the ability of the mouse immune system to protect the invaded GNPs. However, it remains to be explored if this type of general immune response could protect the neuronal damage caused by GNPs' invasion into hippocampus.

## 4. Conclusion

Here we demonstrate the protective activity of tea melanin against GNP-induced neurotoxicity in mice. The administration of tea melanin was capable of retarding the accumulation of Au in the brain, recovering the imbalance of monoamines and preventing cognition impairment, thereby preventing GNP-induced neurotoxicity in mice.

## Acknowledgments

This study was supported in part by the National Science Counsel Grant 100-2923-B-009-001-MY3 and by the "Aim for the Top University Plan" of the National Chiao Tung University and Ministry of Education, Taiwan, R.O.C. The authors also acknowledge funding support from the Air Force Office of Scientific Research (AFOSR, FA2386-11-1-4094).

## References

- [1] M. Ferrari, "Cancer nanotechnology: opportunities and challenges," *Nature Reviews Cancer*, vol. 5, no. 3, pp. 161–171, 2005.
- [2] J.-C. Olivier, "Drug transport to brain with targeted nanoparticles," *NeuroRx*, vol. 2, no. 1, pp. 108–119, 2005.
- [3] T. C. Yih and M. Al-Fandi, "Engineered nanoparticles as precise drug delivery systems," *Journal of Cellular Biochemistry*, vol. 97, no. 6, pp. 1184–1190, 2006.
- [4] P. Ghosh, G. Han, M. De, C. K. Kim, and V. M. Rotello, "Gold nanoparticles in delivery applications," *Advanced Drug Delivery Reviews*, vol. 60, no. 11, pp. 1307–1315, 2008.
- [5] T. S. Hauck, A. A. Ghazani, and W. C. W. Chan, "Assessing the effect of surface chemistry on gold nanorod uptake, toxicity, and gene expression in mammalian cells," *Small*, vol. 4, no. 1, pp. 153–159, 2008.
- [6] G. F. Paciotti, L. Myer, D. Weinreich et al., "Colloidal gold: a novel nanoparticle vector for tumor directed drug delivery," *Drug Delivery*, vol. 11, no. 3, pp. 169–183, 2004.
- [7] N. L. Rosi, D. A. Giljohann, C. S. Thaxton, A. K. R. Lytton-Jean, M. S. Han, and C. A. Mirkin, "Oligonucleotide-modified gold nanoparticles for intracellular gene regulation," *Science*, vol. 312, no. 5776, pp. 1027–1030, 2006.
- [8] W. H. De Jong, W. I. Hagens, P. Krystek, M. C. Burger, A. J. A. M. Sips, and R. E. Geertsma, "Particle size-dependent organ distribution of gold nanoparticles after intravenous administration," *Biomaterials*, vol. 29, no. 12, pp. 1912–1919, 2008.
- [9] E. E. Connor, J. Mwamuka, A. Gole, C. J. Murphy, and M. D. Wyatt, "Gold nanoparticles are taken up by human cells but do not cause acute cytotoxicity," *Small*, vol. 1, no. 3, pp. 325–327, 2005.
- [10] C. M. Goodman, C. D. McCusker, T. Yilmaz, and V. M. Rotello, "Toxicity of gold nanoparticles functionalized with cationic

- and anionic side chains," *Bioconjugate Chemistry*, vol. 15, no. 4, pp. 897–900, 2004.
- [11] J. A. Khan, B. Pillai, T. K. Das, Y. Singh, and S. Maiti, "Molecular effects of uptake of gold nanoparticles in HeLa cells," *ChemBioChem*, vol. 8, no. 11, pp. 1237–1240, 2007.
- [12] K. B. Male, B. Lachance, S. Hrapovic, G. Sunahara, and J. H. T. Luong, "Assessment of cytotoxicity of quantum dots and gold nanoparticles using cell-based impedance spectroscopy," *Analytical Chemistry*, vol. 80, no. 14, pp. 5487–5493, 2008.
- [13] C. J. Murphy, A. M. Gole, J. W. Stone et al., "Gold nanoparticles in biology: beyond toxicity to cellular imaging," *Accounts of Chemical Research*, vol. 41, no. 12, pp. 1721–1730, 2008.
- [14] H. K. Patra, S. Banerjee, U. Chaudhuri, P. Lahiri, and A. K. Dasgupta, "Cell selective response to gold nanoparticles," *Nanomedicine: Nanotechnology, Biology, and Medicine*, vol. 3, no. 2, pp. 111–119, 2007.
- [15] R. Shukla, V. Bansal, M. Chaudhary, A. Basu, R. R. Bhonde, and M. Sastry, "Biocompatibility of gold nanoparticles and their endocytotic fate inside the cellular compartment: a microscopic overview," *Langmuir*, vol. 21, no. 23, pp. 10644–10654, 2005.
- [16] H. Takahashi, Y. Niidome, T. Niidome, K. Kaneko, H. Kawasaki, and S. Yamada, "Modification of gold nanorods using phosphatidylcholine to reduce cytotoxicity," *Langmuir*, vol. 22, no. 1, pp. 2–5, 2006.
- [17] B. D. Chithrani, A. A. Ghazani, and W. C. W. Chan, "Determining the size and shape dependence of gold nanoparticle uptake into mammalian cells," *Nano Letters*, vol. 6, no. 4, pp. 662–668, 2006.
- [18] Arnida, A. Malugin, and H. Ghandehari, "Cellular uptake and toxicity of gold nanoparticles in prostate cancer cells: a comparative study of rods and spheres," *Journal of Applied Toxicology*, vol. 30, no. 3, pp. 212–217, 2010.
- [19] Y. Pan, S. Neuss, A. Leifert et al., "Size-dependent cytotoxicity of gold nanoparticles," *Small*, vol. 3, no. 11, pp. 1941–1949, 2007.
- [20] Y. S. Chen, Y. C. Hung, I. Liau, and G. S. Huang, "Assessment of the in vivo toxicity of gold nanoparticles," *Nanoscale Research Letters*, vol. 4, no. 8, pp. 858–864, 2009.
- [21] N. Pernodet, X. Fang, Y. Sun et al., "Adverse effects of citrate/gold nanoparticles on human dermal fibroblasts," *Small*, vol. 2, no. 6, pp. 766–773, 2006.
- [22] Y. Qiu, Y. Liu, L. Wang et al., "Surface chemistry and aspect ratio mediated cellular uptake of Au nanorods," *Biomaterials*, vol. 31, no. 30, pp. 7606–7619, 2010.
- [23] R. G. Rayavarapu, W. Petersen, L. Hartsuiker et al., "In vitro toxicity studies of polymer-coated gold nanorods," *Nanotechnology*, vol. 21, no. 14, Article ID 145101, 2010.
- [24] V. M. Sava, B. N. Galkin, M. Y. Hong, P. C. Yang, and G. S. Huang, "A novel melanin-like pigment derived from black tea leaves with immuno-stimulating activity," *Food Research International*, vol. 34, no. 4, pp. 337–343, 2001.
- [25] V. M. Sava, S. M. Yang, M. Y. Hong, P. C. Yang, and G. S. Huang, "Isolation and characterization of melanic pigments derived from tea and tea polyphenols," *Food Chemistry*, vol. 73, no. 2, pp. 177–184, 2001.
- [26] Y.-C. Hung, V. M. Sava, S. Y. Makan, T.-H. J. Chen, M.-Y. Hong, and G. S. Huang, "Antioxidant activity of melanins derived from tea: comparison between different oxidative states," *Food Chemistry*, vol. 78, no. 2, pp. 233–240, 2002.
- [27] Y. C. Hung, V. M. Sava, C. L. Juang, T. C. Yeh, W. C. Shen, and G. S. Huang, "Gastrointestinal enhancement of MRI with melanin derived from tea leaves (*Thea sinensis* Linn.)," *Journal of Ethnopharmacology*, vol. 79, no. 1, pp. 75–79, 2002.
- [28] V. M. Sava, Y. C. Hung, B. N. Golkin, M. Y. Hong, and G. S. Huang, "Protective activity of melanin-like pigment derived from tea on *Drosophila melanogaster* against the toxic effects of benzidine," *Food Research International*, vol. 35, no. 7, pp. 619–626, 2002.
- [29] Y. C. Hung, G. S. Huang, L. W. Lin, M. Y. Hong, and P. S. Se, "Thea sinensis melanin prevents cisplatin-induced nephrotoxicity in mice," *Food and Chemical Toxicology*, vol. 45, no. 7, pp. 1123–1130, 2007.
- [30] Y.-C. Hung, G. S. Huang, V. M. Sava, V. A. Blagodarsky, and M.-Y. Hong, "Protective effects of tea melanin against 2,3,7,8-tetrachlorodibenzo-p-dioxin-induced toxicity: antioxidant activity and aryl hydrocarbon receptor suppressive effect," *Biological and Pharmaceutical Bulletin*, vol. 29, no. 11, pp. 2284–2291, 2006.
- [31] Y. C. Hung, V. M. Sava, V. A. Blagodarsky, M. Y. Hong, and G. S. Huang, "Protection of tea melanin on hydrazine-induced liver injury," *Life Sciences*, vol. 72, no. 9, pp. 1061–1071, 2003.
- [32] Y. C. Hung, V. M. Sava, S. Y. Makan, M. Y. Hong, and G. S. Huang, "Preventive effect of *Thea sinensis* melanin against acetaminophen-induced hepatic injury in mice," *Journal of Agricultural and Food Chemistry*, vol. 52, no. 16, pp. 5284–5289, 2004.
- [33] G. S. Huang, M.-T. Wang, C.-W. Su, Y.-S. Chen, and M.-Y. Hong, "Picogram detection of metal ions by melanin-sensitized piezoelectric sensor," *Biosensors and Bioelectronics*, vol. 23, no. 3, pp. 319–325, 2007.
- [34] K. R. Brown, D. G. Walter, and M. J. Natan, "Seeding of colloidal Au nanoparticle solutions. 2. Improved control of particle size and shape," *Chemistry of Materials*, vol. 12, no. 2, pp. 306–313, 2000.
- [35] F. K. Liu, C. J. Ker, Y. C. Chang, F. H. Ko, T. C. Chu, and B. T. Dai, "Microwave heating for the preparation of nanometer gold particles," *Japanese Journal of Applied Physics, Part 1*, vol. 42, no. 6 B, pp. 4152–4158, 2003.
- [36] M. T. Hsieh, C. R. Wu, and C. C. Hsieh, "Ameliorating effect of p-hydroxybenzyl alcohol on cycloheximide-induced impairment of passive avoidance response in rats: interactions with compounds acting at 5-HT(1A) and 5-HT2 receptors," *Pharmacology Biochemistry and Behavior*, vol. 60, no. 2, pp. 337–343, 1998.
- [37] C. J. Addison, S. O. Konorov, A. G. Brolo, M. W. Blades, and R. F. B. Turner, "Tuning gold nanoparticle self-assembly for optimum coherent anti-Stokes Raman scattering and second harmonic generation response," *Journal of Physical Chemistry C*, vol. 113, no. 9, pp. 3586–3592, 2009.
- [38] C. L. Evans, E. O. Potma, M. Puoris'haag, D. Côté, C. P. Lin, and X. S. Xie, "Chemical imaging of tissue in vivo with video-rate coherent anti-Stokes Raman scattering microscopy," *Proceedings of the National Academy of Sciences of the United States of America*, vol. 102, no. 46, pp. 16807–16812, 2005.
- [39] N. Hayazawa, T. Ichimura, M. Hashimoto, Y. Inouye, and S. Kawata, "Amplification of coherent anti-Stokes Raman scattering by a metallic nanostructure for a high resolution vibration microscopy," *Journal of Applied Physics*, vol. 95, no. 5, pp. 2676–2681, 2004.
- [40] X. Qian, X. H. Peng, D. O. Ansari et al., "In vivo tumor targeting and spectroscopic detection with surface-enhanced Raman nanoparticle tags," *Nature Biotechnology*, vol. 26, no. 1, pp. 83–90, 2008.
- [41] Y.-S. Chen, Y.-C. Hung, L.-W. Lin, I. Liau, M.-Y. Hong, and G. S. Huang, "Size-dependent impairment of cognition in mice caused by the injection of gold nanoparticles," *Nanotechnology*, vol. 21, no. 48, Article ID 485102, 2010.

- [42] Y.-S. Chen, Y.-C. Hung, W.-H. Lin, and G. S. Huang, "Assessment of gold nanoparticles as a size-dependent vaccine carrier for enhancing the antibody response against synthetic foot-and-mouth disease virus peptide," *Nanotechnology*, vol. 21, no. 19, Article ID 195101, 2010.

## Review Article

# Biocompatibility and Toxicity of Nanoparticles and Nanotubes

Xiaoming Li,<sup>1</sup> Lu Wang,<sup>1</sup> Yubo Fan,<sup>1</sup> Qingling Feng,<sup>2</sup> and Fu-zhai Cui<sup>2</sup>

<sup>1</sup> Key Laboratory for Biomechanics and Mechanobiology of Ministry of Education, School of Biological Science and Medical Engineering, Beihang University, Beijing 100191, China

<sup>2</sup> State Key Laboratory of New Ceramic and Fine Processing, Tsinghua University, Beijing 100084, China

Correspondence should be addressed to Xiaoming Li, x.m.li@hotmail.com and Yubo Fan, yubofan@buaa.edu.cn

Received 27 February 2012; Accepted 3 April 2012

Academic Editor: Shuming Zhang

Copyright © 2012 Xiaoming Li et al. This is an open access article distributed under the Creative Commons Attribution License, which permits unrestricted use, distribution, and reproduction in any medium, provided the original work is properly cited.

In recent years, nanoparticles (NPs) have increasingly found practical applications in technology, research, and medicine. The small particle size coupled with their unique chemical and physical properties is thought to underline their exploitable biomedical activities. Its form may be latex body, polymer, ceramic particle, metal particles, and the carbon particles. Due to their small size and physical resemblance to physiological molecules such as proteins, NPs possess the capacity to revolutionise medical imaging, diagnostics, therapeutics, as well as carry out functional biological processes. But these features may also underline their toxicity. Indeed, a detailed assessment of the factors that influence the biocompatibility and toxicity of NPs is crucial for the safe and sustainable development of the emerging NPs. Due to the unique structure, size, and shape, much effort has been dedicated to analyzing biomedical applications of nanotubes. This paper focuses on the current understanding of the biocompatibility and toxicity of NPs with an emphasis on nanotubes.

## 1. Introduction

First of all, we would better have a clear understanding of the definition of biocompatibility and toxicity. In 2008, Williams redefined biocompatibility as follows [1]: biocompatibility refers to the ability of a biomaterial to perform its desired function with respect to a medical therapy, without eliciting any undesirable local or systemic effects in the recipient or beneficiary of that therapy, but generating the most appropriate beneficial cellular or tissue response in that specific situation, and optimising the clinically relevant performance of that therapy. And his definition has been recognised. In this context, NP toxicity refers to the ability of the particles to adversely affect the normal physiology as well as to directly interrupt the normal structure of organs and tissues of humans and animals. It is widely accepted that toxicity depends on physiochemical parameters such as particle size, shape, surface charge and chemistry, composition, and subsequent NPs stability.

The size of NPs is not more than 100 nm micro. They can be obtained by many ways: wet chemical treatment (chemical reactions in solution), mechanical processing (milling and grinding technology), vacuum deposition, and gas phase

synthesis. Its form may be latex body, polymer, ceramic particle, metal particles, and the carbon particles. According to the different preparation methods, those NPs can have different size, chemical composition, and shape and can be with or without surface coating. Each of these factors can affect the interactions between the nanomaterials and cells or tissues. NPs can permeate membrane cells, and spread along the nerve cells synapses, blood vessels, and lymphatic vascular. At the same time, NPs selectively accumulate in the different cells and certain cellular structure. NPs of strong permeability not only provide the effectiveness for the use of drugs, at the same time, but also give rise to potential threats on the health of human body.

The development of NPs for biomedical applications including medical imaging, magnetic hyperthermia, and gene or drug delivery is currently undergoing a dramatic expansion. For biomedical applications, emerging nano-structures requires stringent evaluations for their biological security. There are a number of different classes of NPs promising for biomedical purposes.

Due to the unique structure, size, and shape, much effort has been dedicated to analyzing biomedical applications of nanotubes. At present, nanotubes for biomedical application

include carbon nanotubes, silicon dioxide nanotubes, boron nitride nanotubes, titanium dioxide nanotubes, and organic nanotubes, of which carbon nanotubes are the most widely used materials.

Here, we will focus on the current understanding of the biocompatibility and toxicity of NPs and nanotubes. This paper proceeds as follows. In later sections, the NPs and nanotubes are reviewed in two separate sections. Section 2 reviews the biocompatibility and toxicity of NPs in the aspect of hemocompatibility, histocompatibility, cytotoxicity, and neurotoxicity. Section 3 is a description of main types of nanotubes. Considering the attention that carbon nanotube has received, the section of nanotubes is structured a little differently from that of the NPs.

## 2. Biocompatibility and Toxicity of Nanoparticles

**2.1. Biocompatibility of Nanoparticles.** For biomedical applications, those NPs enter the body and contact with tissues and cells directly, thus it is necessary for exploring their biocompatibility.

**2.1.1. Hemocompatibility.** NPs are used as vectors for the applications in drug delivery, gene delivery, or as biosensors, where a direct contact with blood occurs. Here some NPs are examined for their blood-compatible behaviors.

Recently, blood cell aggregation and haemolysis studies, coagulation behaviors experiments have been carried out evaluating blood compatibility of NPs *in vitro* conditions, of which hemolysis is considered to be a simple and reliable measure for estimating blood compatibility of materials [2].

Chouhan and Bajpai [3] has adopted Hemolysis assay to judge the *in vitro* blood compatibility of the prepared PHEMA NPs. Hemolysis assay experiments were performed on the surfaces of the prepared particles. The results indicate that for NPs with 12.37 mM HEMA and 1.06 mM EGDMA percentage hemolysis is lowest. This clearly suggests a moderate level of biocompatibility.

Sanoj Rejinold et al. [4] have studied the formulation of curcumin with biodegradable thermoresponsive chitosan-g-poly (N-vinyl caprolactam) NPs (TRC-NPs) for cancer drug delivery. Fresh human blood was used in this study. Hemolysis assay was carried out to evaluate the blood compatibility of bare and curcumin-loaded TRC-NPs. The results showed that the hemolytic ratio of the sample was within the range of less than 5%, the critical safe hemolytic ratio for biomaterials according to ISO/TR 7406, which indicated that the damage of the sample on the erythrocytes was little.

The blood compatibility of the carrier MSNs-RhB was evaluated by investigating the hemolysis and coagulation behaviors in a broad concentration range ( $50\text{--}500 \text{ mg mL}^{-1}$ ) under *in vitro* conditions [5]. The results suggested that MSNs-RhB possessed good blood compatibility and also, SEM and TEM analyses in Figure 1 indicated that both MSNs and MSNs-RhB had a subsphaeroidal morphology, a high dispersivity and uniform particle size of about 400 nm. In

this work, He et al. [5] evaluated the blood compatibility of SBA-15-type MSNs and MSNs-RhB with negative and positive surface potentials, respectively, by investigating their hemolysis and coagulation behaviors. As to their coagulation behaviors, PT was used to evaluate the extrinsic and common coagulation pathways, APTT was used to evaluate the intrinsic and common coagulation pathways, and Fib was used to evaluate the abnormality of coagulation factor I. The hemolytic phenomena of SBA-15-type MSNs and MSNs-RhB are almost invisible by direct observation.

This is utterly different from the dry mesoporous silica powder previously reported by Dai et al. [6], because all hydrophilic mesoporous channels of MSNs and MSNs-RhB have been fully filled with PBS during experimental operation in the present study, and no space is left for further water absorption when mixed with plasma. Thus both MSNs and MSNs-RhB had not effected the normal coagulation/anti-coagulation functions of plasma, that is, the blood compatibility of SBA-15-type MSNs-RhB is satisfactory. The aggregations of the blood cells on interaction with the NPs are shown for RBCs, WBCs, and platelets. It revealed no aggregation of blood cells on incubation of NPs at a higher interaction ratio of 10 mg/mL. Polyethylene imine (PEI) which was used as positive control showed aggregation whereas saline used as negative control did not show any aggregation. Citrate-capped NPs also revealed no aggregation of blood cells on incubation with blood as reported earlier [7]. The same was visible with the haemolytic property of the NPs. The haemolysis induced by gold NPs is shown which were well within the acceptable limits of 1% [8]. Stability in physiologically relevant media, where saline levels are high, is a significant issue for the use of gold NPs in biological applications and assays. Therefore, stability in PBS may be taken as an initial screening test for compatibility with physiological conditions [9]. Regarding the application of gold NPs in biomedicine (sensing and drug delivery applications), they should be easily dispersible at neutral pH and should be stable.

Most studies are aimed at attempting to understand the blood compatibility of foreign materials and their investigation have shown that the blood compatibility was affected by various properties of the material surface. The response of blood in contact with the material depends on physicochemical features such as surface area, surface charge, hydrophobicity/hydrophilicity, and so forth. As for NPs, the size effect, structure, and surface are the decisive factors in these responses [10].

**2.1.2. Histocompatibility.** Targeted drug delivery is one of the most intensively explored areas of research and the use of NPs for diagnostic purposes has already entered the biomedical field. The current review is focused on biocompatibility of several representative types of nanomaterials: super paramagnetic iron oxides (SPION), dendrimers, mesoporous silica particles, gold NPs, and carbon nanotubes (CNTs).

In general, SPION are classified as biocompatible, showing no severe toxic effects *in vitro* or *in vivo* [11]. In primary human macrophages, no immunomodulatory effects

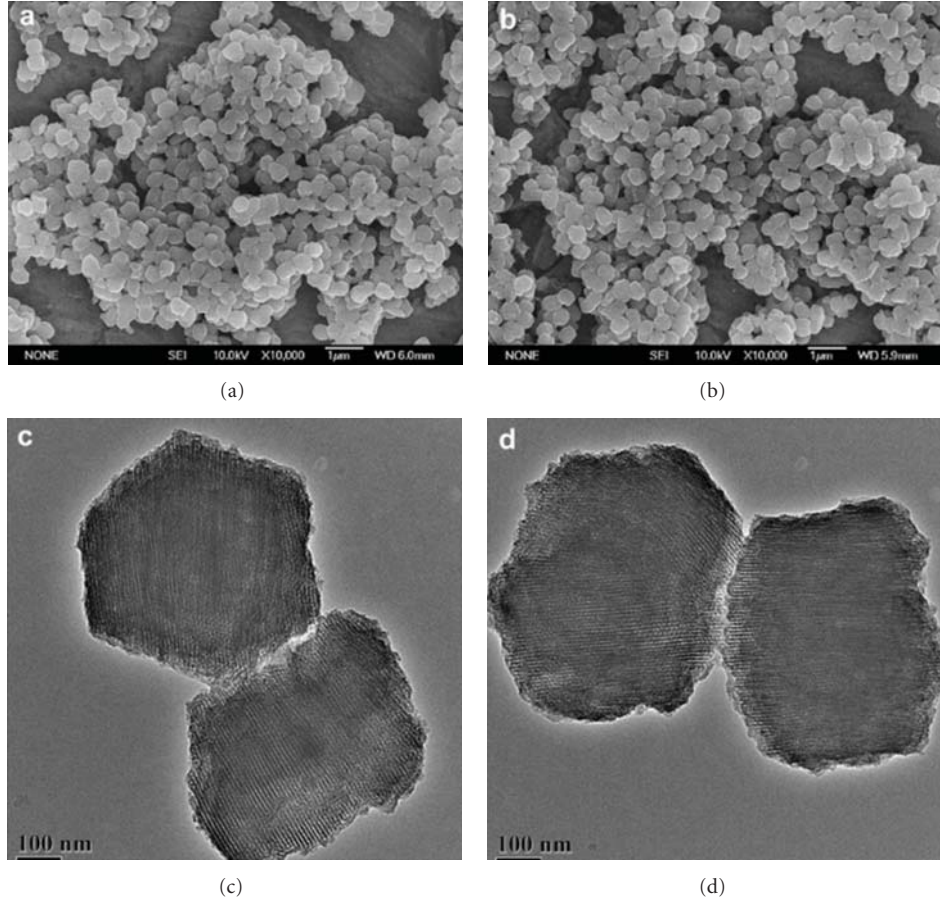


FIGURE 1: SEM and TEM images of samples MSNs ((a) and (c), resp.) and MSNs-RhB ((b) and (d), resp.). The scale bars of (a), (b), (c) and (d) correspond to 1 mm, 1 mm, 100 nm and 100 nm, respectively [5].

were observed when cells were exposed to 30 nm dextran-coated SPION [11]. However, when primary peritoneal macrophages from rats and mice were exposed to 20 nm and 60 nm dextran-coated SPION, an increased secretion of anti-inflammatory cytokines, and reduced production of proinflammatory cytokines occurred [12]. In contrast, an increase in proinflammatory cytokines in a murine macrophage cell line was observed, accompanied by a decrease in the phagocytic function of these cells upon exposure to dextran-coated SPION [13]. These studies underline the importance of using different cellular systems for nanotoxicological studies, including primary human cell types. Jain et al. [14] have reported that SPION neither cause any effect in liver function when administered *in vivo* in rats nor do the particles induce oxidative stress. Our own studies demonstrate that dextran-coated SPION are nontoxic to primary human monocyte-derived macrophages and dendritic (antigen-presenting) cells (Kunzmann et al., unpublished observations).

Dendrimers exhibit a generation-dependent toxicity with higher generation dendrimers being the most toxic. The extent of cytotoxicity induced by dendrimers also depends on surface charge, whereby cationic dendrimers are more toxic than anionic dendrimers. A marked decrease

in cytotoxicity can also be achieved when the surface is modified with PEG. Cationic dendrimers induce disruption including formation of pores in membranes [15]. They can induce apoptosis caused by mitochondrial dysfunction [16]. Cationic dendrimers can cause substantial changes in red blood cell morphology and hemolysis in a generation-dependent manner, whereas anionic dendrimers have no such effect. Cationic dendrimers were shown to induce caspase-dependent apoptosis and negatively influence proliferation in a murine macrophage cell line [17]. These effects could not be observed in two other murine cell lines, highlighting the importance of cell type specific differences. PAMAM dendrimers of generation 3.5 (G3.5) were shown to affect mitochondrial membrane potential in isolated rat liver mitochondria [18]. Glucosamine-conjugated dendrimers inhibit the synthesis of proinflammatory cytokines in LPS-treated human dendritic cells and macrophages. These dendrimer conjugates also have an inhibitory effect on toll-like receptor 4 (TLR4), a receptor that triggers LPS-induced stimulation of immune-competent cells [19]. Shaunik et al. evaluated the dendrimer conjugates in a rabbit model of scar tissue formation after glaucoma filtration surgery and found that the long-term success of the surgery increased from 30% to 80% [19]. The authors suggested that these

dendrimer conjugates could be utilized to prevent scar tissue formation. The transcriptional profile of monocytes exposed to phosphorylated dendrimers revealed over expression of genes involved in anti-inflammatory responses [20]. Anti-inflammatory effects were also reported *in vivo* when simple modified PAMAM dendrimers were injected into rats [21]. However, the detailed mechanisms are still unknown.

Silica-NPs-demonstrated a good degree of biocompatibility [22, 23]. Silica-coated NPs, or silica NPs, have been demonstrated to enter the cell without affecting cell survival. These insights push research toward the development of silica NPs based drug delivery systems and biosensors [24–26]. Bardi et al. [27], developed and characterized NH<sub>2</sub> functionalized CdSe/ZnS quantum dot (QD)-doped SiO<sub>2</sub> NPs with both imaging and gene carrier capabilities. They show that QD-doped SiO<sub>2</sub> NPs are internalized by primary cortical neural cells without inducing cell death *in vitro* and *in vivo*. Moreover, the ability to bind, transport, and release DNA into the cell allows GFP-plasmid transfection of NIH-3T3 and human neuroblastoma SH-SY5Y cell lines. QD-doped SiO<sub>2</sub> NPs properties make them a valuable tool for future nanomedicine application.

The use of colloidal gold has a long history in coatings and glassware as a result of their high scattering power, variability of bright and intense colors, and stability. Furthermore, gold NPs can be readily functionalized with probe molecules such as antibodies, enzymes, and nucleotides. These hybrid organic-inorganic nanomaterials are the active elements of a number of biosensor assays, drug and gene delivery systems, laser confocal microscopy diagnostic tools, and other biomaterial-based imaging systems [28]. There have been many studies on the biocompatibility of gold NPs. In an attempt to mimic the respiratory tract after inhalation, Brandenberger et al. [29] devised an epithelial-airway model consisting of alveolar epithelial-like cells (the A549 lung carcinoma cell line), human monocyte-derived macrophages, and dendritic cells. After exposure to 15 nm gold NPs using an air-liquid interface exposure system, no induction of oxidative stress or inflammatory responses was noted. However, the system was responsive to proinflammatory LPS. No synergistic or suppressive effect was seen in the presence of gold NPs, suggesting that the gold NPs do not elicit immune reactions. On the other hand, gold NPs conjugated with peptides were recognized by primary murine macrophages and induced an immune response as evidenced by secretion of IL-6, IL- $\beta$ , and TNF- $\alpha$  [30]. Therefore, the peptide coating on gold NPs is an important factor to enhance the immune response. Indeed, recent studies have shown that the conjugation of peptides on the surface of NPs may enhance the immune response [30]. Murine bone marrow macrophages were thus found to be able to recognize gold NP-peptide conjugates, while peptides or NPs alone were not recognized. The latter studies shed light on the design of NPs conjugates for modulation of immune responses in the fight against allergies, cancer, and autoimmune diseases. The role of plasma proteins attaching to NPs following entry into circulation also merits attention as this could potentially interfere with or modulate the presentation of other ligands attached to the particles.

## 2.2. Toxicity of Nanoparticles

**2.2.1. Toxicology of Nanoparticles [31].** Interaction mechanisms between NPs and living systems are not yet fully understood. The complexity comes with the particles' ability to bind and interact with biological matter and change their surface characteristics, depending on the environment they are in. Scientific knowledge about NPs cell-interaction mechanisms has been accumulating in recent years, indicating that cells readily take up NPs via either active or passive mechanisms. Intracellularly, however, mechanisms and pathways are more difficult to understand. Even particles of the same material can show completely different behaviour due to, for example, slight differences in surface coating, charge, or size. This makes the categorisation of NPs behaviour, when in contact with biological systems, intricate and thus nanoparticle hazard identification is not straightforward. This is one of the main distinctions between nanotoxicology and classical toxicology where, in the latter, characterisation of toxicants is, in general, protocolised with a well-established set of methodologies available, employing a mass-based dose metric. However, with NPs the dose metric is not straightforward, as discussed below. Furthermore the protocolization of bioassays involving nanomaterials is still under development and has, in general, not yet been internationally validated. In addition, there are many more variables to consider when working with nanomaterials and these include material, size, shape, surface, charge, coating, dispersion, agglomeration, aggregation, concentration, and matrix.

The complexity increases when moving from *in vitro* to *in vivo* models. Hazard identification on the *in-vivo* level, with regards to nanomaterials, is still at an early stage. Major entry routes (lung, gut, and possibly skin) as well as putative targets (lung, liver, heart, and brain) have been identified. However, more research is required to understand mechanisms and pathways in the body. What seems clear is that exposure to insoluble nanoscale particles of b50 nm appears to be "new," when compared to the evolutionary history of the preindustrial world. Furthermore, such NPs appear to be able to hijack a preexisting transport mechanism through the body using endocytotic mechanisms, in the same manner that viruses employ. Therefore, because widespread translation of NPs within the body seems to be likely if the body is exposed, we need to take any toxicological risks seriously.

**2.2.2. Cytotoxicity.** Depending on the mode of administration and sites of deposition, toxicity may vary in severity. Therefore, to maintain clinical relevance, information on toxicity is presented using a system-based approach focusing on lung, dermal, liver, and nervous system targets. Figure 2 summarizes the advantages and disadvantages of each of the routes.

All eukaryotic cells (such as lung cells) contain functionally distinct, membrane-enclosed compartments. The main types are the nucleus and the organelles which include mitochondria, endoplasmic reticulum, Golgi apparatus, peroxisomes, lysosomes, and endosomes. Nucleus and

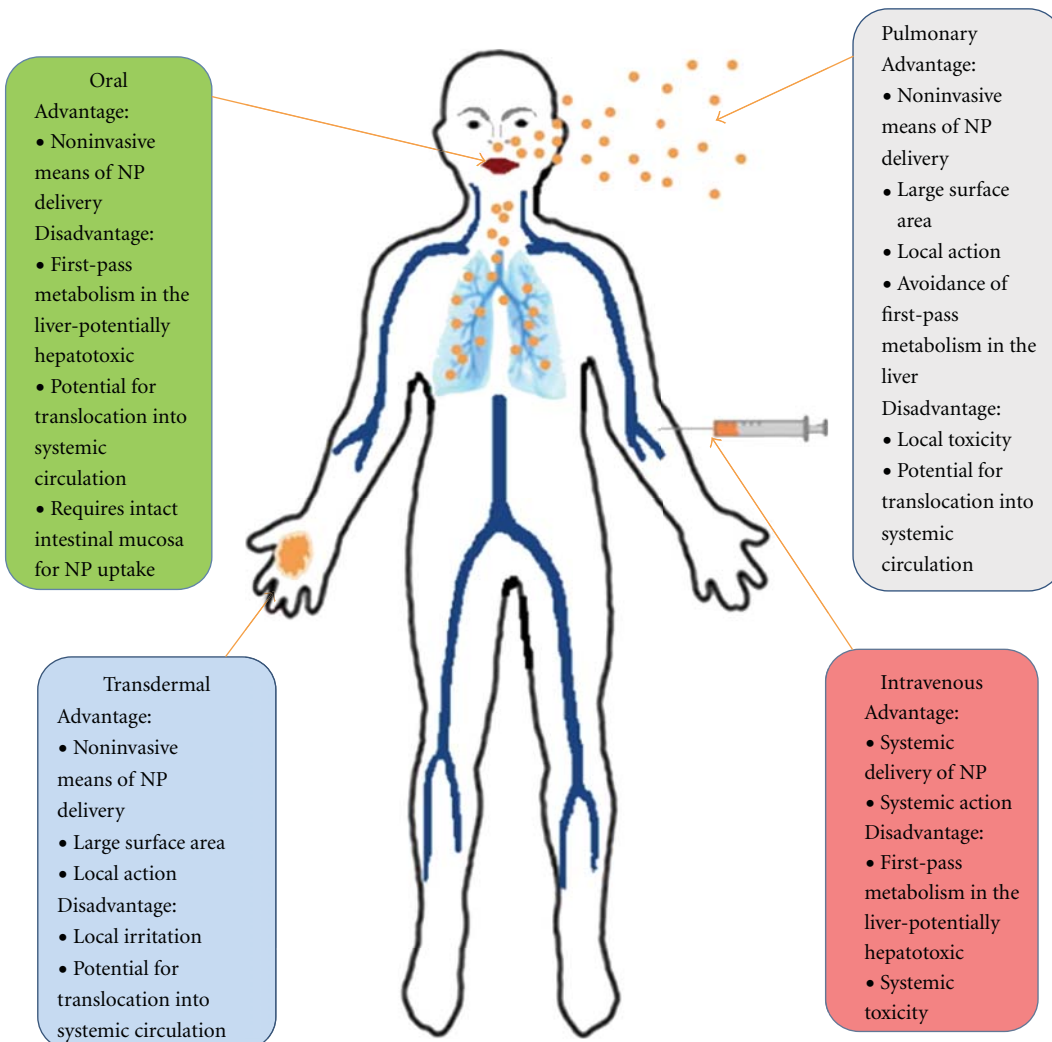


FIGURE 2: Routes of administration of nanoparticles and their advantages and disadvantages [32].

organelles are enclosed by a lipid bilayer containing distinct proteins. NPs can cross the membranes of organelles since they have been localized in lysosomes, mitochondria, and the nucleus, the mechanisms of internalization are, however, not known so far.

In this paper we focus on the cytotoxic effects of frequently used NPs, such as Metal and metallic oxide NPs, Polymeric NPs, Quantum dots, Silica ( $\text{SiO}_2$ ) NPs, to explain this topic.

**Lung Cells.** As NPs get in contact with the skin, the gastrointestinal tract, and the respiratory tract, these biological compartments are “designed” to act as barriers to the passage of nanosized materials into the organism. Because the lung is considered by far the most important portal of entry for NPs into the human body this overview will mainly focus on the lung as a potential barrier for inhaled NPs. It should however be noted that evidence has been published that NPs can also deposit on the olfactory epithelium and directly be translocated to the brain [33]. Current related researches are mainly focused on the impact of NPs on alveolar macrophages and

fibroblasts and bronchial epithelial cells. Studies have already shown that NPs can remarkably weaken the phagocytic capacity of macrophages, which causes decline in lung’s clearance ability. Nanocarrier systems (polymeric NPs, silica ( $\text{SiO}_2$ ) NPs, silver NPs, carbon nanotubes) for pulmonary drug delivery have several advantages which can be exploited for therapeutic reasons and, thus, intensively studied

Polymeric NPs are biocompatible, surface modifiable, and capable of sustained drug release. They show potential for applications in the treatment of various pulmonary conditions such as asthma, chronic obstructive pulmonary disease (COPD), tuberculosis (TB), and lung cancer as well as extra pulmonary conditions such as diabetes [34–36]. Already, there is a multitude of organic nanopolymers including collagen, gelatin, chitosan, alginate, and bovine serum albumin (BSA). Furthermore, the last three decades has seen a rise in the development of synthetic polymers such as the biocompatible and biodegradable poly(lactic-co-glycolic acid) (PLGA) for use as drug carrier devices [37, 38]. While such drug-loaded nanoconfigurations demonstrate promising alternatives to current cancer treatment,

cytotoxicity needs to be evaluated. PLGA NPs successfully improve therapeutic outcome and reduce adverse effects via sustained and targeted drug delivery. Additionally, the use of biological capping materials such as chitosan or BSA further reduce toxicity while their biocompatibility and biodegradative capacity making them an intuitive choice for NPs surface modification. Romero et al. demonstrated a reduction in cytotoxicity of PLGA NPs stabilized with BSA compared to synthetic coating materials in cultured lung cancer cells [37]. Albumin, the most abundant serum protein, was found to be highly biocompatible making it a useful stabilizer for drug delivery vehicles. Similarly, chitosan-stabilization resulted in near-total cellular preservation and improved pulmonary mucoadhesion in an *in vivo* lung cancer model [39]. Biological capping materials reduce cytotoxicity by mimicking the physiological environment, thus “hiding” from the immune system. However, the possibility of enzymatic degradation due to biophysical resemblance needs further investigation.

Silica ( $\text{SiO}_2$ ) NPs have found extensive applications in chemical, mechanical polishing, and as additives to drugs, cosmetics, printer toners, varnishes, and food. Recently, the use of silica NPs has been extended to biomedical and biotechnological fields, such as biosensors for simultaneous assay of glucose, lactate, L-glutamate, and hypoxanthine levels in rat striatum, biomarkers for leukemia cell identification using optical microscopy imaging, cancer therapy, DNA delivery, drug delivery, and enzyme immobilization. Silica NPs have been shown to have a low toxicity when administered in moderate doses [40]. Unfortunately, silica NPs also tend to agglomerate and have been demonstrated to lead to protein aggregation *in vitro* at dose of  $25 \mu\text{g/mL}$  [41]. Oxidative stress has been implicated as an explanation behind silica NPs cytotoxicity both *in vitro* and *in vivo* [42–45]. All these studies have reported cytotoxicity and oxidative stress, as determined by increasing lipid peroxidation (LPO), reactive oxygen species (ROS), and decreasing cellular glutathione (GSH level), but no similarity exists regarding dose-response. In the present study, we did not find significant difference in the cytotoxicity and oxidative stress caused by the two sizes 10 nm and 80 nm of amorphous silica NPs. A similar result was observed for 15 nm and 46 nm silica NPs by Lin et al. [46]. Present studies suggest that it is theoretically feasible and within acceptable safety limits to use moderate doses of silica NPs; however, high-dose toxicity profiles warrant further investigations.

The most common route of pulmonary exposure to silver NPs (AgNP) is via the occupational inhalation of airborne particles during manufacturing. The current American Conference of Governmental Industrial Hygienist's (ACGIH) limit for silver dust exposure is  $100 \mu\text{g/m}^3$ . In order to evaluate potentially acute and delayed adverse pulmonary effects of AgNP, Sung et al. have carried out a series of inhalation studies focusing on the acute, subacute (28 days) and subchronic (90 days) toxicity of AgNP in rats [47–49]. In the acute setting, rats were exposed to different particle concentrations in a whole-body inhalation chamber for 4 consecutive hours and were subsequently observed for a further 2 weeks. At the highest concentration used ( $750 \mu\text{g/m}^3$ ; 7.5 times higher than the limit), no significant body weight

changes or clinical changes were observed. Furthermore, lung function tests revealed no statistical differences between exposed and control groups. Repeated administration of AgNP for 4 weeks showed similar results. In contrast, subchronic inhalation for 13 weeks at a maximum concentration of  $515 \mu\text{g/m}^3$  (5 times the limit) revealed time- and dose-dependent alveolar inflammatory and granulomatous changes as well as decreased lung function [50]. Such results suggest that while high-dose chronic exposure to AgNP has the potential to cause harm, under current guidelines and limits, such excessive particle inhalation would seem unrealistic.

**Dermal Cells.** The skin is the largest organ of the body and functions as the first-line barrier between the external environment and the internal organs of the human body. Consequently, it is exposed to a plethora of nonspecific environmental assault within the air as well as to distinct and potentially toxic substances within creams, sprays, or clothing. Topically applied NPs can potentially penetrate the skin and access the systemic circulation and exert adverse effects on a systemic scale. In this part, we will explain cytotoxic effects of  $\text{TiO}_2$  NPs and gold NPs.

$\text{TiO}_2$  NPs have several properties which make them an advantageous ingredient for commercial sunscreens and cosmetics. They exhibit UV-light blocking properties and confer better transparency and aesthetics to creams. *In vitro* studies demonstrated cell type-dependent  $\text{TiO}_2$  toxicity affecting cellular functions such as cell proliferation, differentiation, mobility, and apoptosis [51, 52]. Such adverse effects, however, could not be replicated *in vivo*. In order to assess penetrative capacities, dermal infiltration studies have been carried out on human volunteers using different investigative techniques. Lademann et al. investigated the penetrative effect of repeated administration of  $\text{TiO}_2$ -containing sunscreen on the skin of volunteers [53]. Tape stripping and histological appraisal of skin biopsies revealed that  $\text{TiO}_2$  penetrated into the open part of a hair follicle as opposed to the viable layers of the epidermis or dermis. Furthermore, the titanium amount in any given follicle was less than 1% of the applied total amount of sunscreen. Surface penetration via hair follicles or pores was also suggested by a study conducted by Bennat and Muller-Goymann where skin permeation was greater when sunscreen was applied to relatively hairy skins [54]. Mavon et al. demonstrated near total recovery of sunscreen after 15 tape stripplings with no  $\text{TiO}_2$  deposition in hair follicles or skin layers [55]. It could be argued that different degrees of permeation and toxicity correlate with surface coatings and functionalizations of  $\text{TiO}_2$  NPs as well as with the number of follicular pores within the skin facilitating particle uptake.

Due to facile means of synthesis and the potential for biofunctionalization, gold NPs (AuNP) are being investigated for clinical applications including dermal drug-delivery [56]. Sonavane et al. demonstrated size-dependent permeation on excised rat skin after topical application of differently sized AuNP (15, 102 and 198 nm) [57]. Smaller NPs penetrated deeper into the tissue than larger ones which

were mainly accumulated in the more superficial epidermis and dermis. These findings may have important implications with regards to efficient NP-based dermal drug delivery. Au compounds are generally considered safe and have been in routine clinical use for many years, for example, in the treatment of rheumatoid arthritis [58]. However, once reduced to nanometer scale, particles are known to undergo profound changes in terms of their biochemical properties which necessitates renewed investigations into their cytotoxic profile. Despite the relative wealth of toxicity studies focusing on AuNP, contradictory results remain the main obstacle to transition into the clinical setting. Several studies have demonstrated cellular uptake of AuNP to be a function of time, particle size, and concentration. In a study by Murphy et al., human dermal fibroblasts were exposed to AuNP for a period of up to 6 days [58]. Three sets of NP concentrations were obtained for each of two different sizes. Larger particles, 45 nm, exhibited marked cytotoxicity at a concentration of 10 µg/mL compared to smaller particles, 13 nm in size, which only displayed cytotoxic signs at the much higher concentration of 75 µg/mL. These results conflict with those obtained by Mironava et al. who reported maximum toxicity for a particle size of 1.4 nm [59]. Such differences may be explained by the distribution pattern of particles within cells and require more research.

**Liver Cells.** Being the site for first-pass metabolism, the liver is particularly vulnerable to NP toxicity and has consistently been shown to accumulate administered substances, even long after cessation of exposure. Thorough evaluation of NP-mediated hepatocellular toxicity thus remains of prevailing importance. Lipid peroxidation assay, comet assay, and oxidative DNA damage are commonly used to study the impact of NPs on liver cells. Gold NPs, silver NPs, silica NPs, and QDs have been intensively studied for clinically application reasons. The effect of surface structure and surface modification of NPs are important factors of their interaction with cells. Here we use QDs to elaborate it.

Semiconductor nanocrystals, or QDs, may be used in a variety of biomedical applications. The general structure of QDs comprises an inorganic core-shell and an organic coating to which biomolecules may be conjugated to enable targeting to specific areas within the body. Such close proximity and interaction with the physiological environment necessitates toxicological evaluation of these particles. Cell-based studies focusing on QD-induced adverse effects that found that toxicity most likely arises from the liberation of metal ions released from the heavy metal core [60]. Oxidative environments further promote degradation and metal-ion leaching. The liver is of particular importance with regards to bio-toxicity because of first-pass metabolism and potential accumulation and deposition within the organ, as shown by Derfus et al. [61]. QD size was also postulated to be a major parameter in organ-specific deposition with smaller particles (<20 nm) extravagating through capillary fenestrae that are large enough in the liver (~100 nm in size) [62]. The long half-life clearly has implications for organ toxicity, particularly in view of the liver's untoward propensity to heavy metal ion poisoning which makes exposure to QDs

potentially very hazardous. Surface coating to protect the core from degradation has been shown to reduce toxicity [63]. Conventionally, QDs are coated with a layer of zinc sulphide (ZnS) or mercaptoacetic acid. However, evidence of continued cellular toxicity after prolonged periods of time suggests either inadequate core coverage or the need for a different type of coating material [64]. Das et al. carried out a series of experiments assessing additional surface coatings for their respective cytotoxicities [65]. CdTe/CdSe cored QDs with a ZnS shell were additionally covered with organic, carboxylated (COOH), amino (NH<sub>2</sub>), or poly(ethylene glycol) (PEG) coatings. Cytotoxicity was tested on exposure to each type separately by measurement of macrophage cell viability and LDH release. All QDs were shown to induce significant cytotoxicity after 48 h and coating materials as well as liberated Cd ions were suggested to be the causative agents. It is likely that a breakdown of physically labile surface material resulted in ion liberation and subsequent toxicity. Recently, Seifalian and colleagues have demonstrated that the novel synthetic nanomaterial polymeric oligoheptad silsesquioxane (POSS), when incorporated onto CdTe-cored QDs, shows significantly enhanced cytocompatibility more than conventionally used materials, even without ZnS shelling (unpublished data). POSS was shown to be nontoxic by preventing ion leakage from the core. These results underline the importance of the type of coating material used and suggest that the most important factor influencing QD toxicity remains heavy metal-ion leakage from the core due to inadequate surface coverage.

**2.2.3. Neurotoxicity.** The central nervous system is composed of two parts: the brain and the spinal cord. Both of them are delicate organs in human body which must be protected from the injury to xenobiotics. Recent observations suggest that several NPs, such as polysorbate 80-coated PBCA NPs and pegylated PLA immunonanoparticles, are able to cross BBB [66, 67] through intravenous administration and followed by the accumulation in the brain. However, due to their special physicochemical properties, such as large surface area, the NPs may cause neurotoxicity after entering into the brain. Therefore, the evaluation of the potential neurotoxic effects of these NPs on CNS function is required, as specific mechanisms and pathways through which NPs may exert their toxic effects remain largely unknown. So far, there are already some reports, but not many, which observed the neurotoxicity of NPs both in vitro and in vivo [68, 69]. As a large variety of colloidal dispersions of super paramagnetic iron oxide nanoparticles (SPIONs) have been developed and explored for a range of new biological, biomedical, and diagnostic applications with regard to their magnetic properties [70, 71]. Here we will give a description of the toxicity effect of super paramagnetic NPs on the brain.

SPIONs and ultrasmall SPION nanoparticles (USPIONs) consist of an iron oxide core and a variable carbohydrate coating which determines cellular up take and biological half-life. The degree of surface coverage has been postulated to be the main parameter in cellular uptake as incomplete surface coverage was shown to promote opsonization and rapid endocytosis whereas fully coated SPION escaped

opsonization which, as a result, prolonged plasma half-life [72]. However, more recently, particle size as opposed to coating degree has been suggested to exert chief influence on the rates of uptake by macrophages [73]. Being one of the few FDA approved NPs for the use in MRI, SPIONs most commonly find applications in the imaging of the vasculature and lymph nodes [74–77]. However, recent reports from both animal models and human subjects have shown their efficacy in visualizing intracerebral malignancies and neurological lesions within the CNS [78]. Despite such routine use of SPION, the long-term effects and potential neurotoxicity have, as yet, not been evaluated extensively. The unique physiochemical properties shared by all NPs, such as nanometer size and a large surface area to volume ratio, make SPION particularly valuable for novel therapeutic and diagnostic applications. However, such dimensional reductions may potentially induce cytotoxicity and interfere with the normal components and functions of the cell [79]. Previous in vitro studies have shown the capacity for SPION to induce ROS generation, impair mitochondrial function and cause leakage of LDH—all of which could incite neurotoxicity as well as potentially aggravate pre-existing neuronal damage [80]. Furthermore, toxicity reports demonstrated an association between particle size, type of surface coating and breakdown products, concentration, and the degree of opsonization and cytotoxicity in cultured cells [81]. For example, Berry et al. utilized fibroblast cultures to demonstrate the ability to tune particle toxicity according to particle coating. They compared the in vitro toxicity of plain uncoated magnetic iron oxide NPs (P particles) with either dextran-derivatized (DD) or albumin-derivatized (AD) NPs. P particles as well as DD particles exhibited similar toxicities, whereas AD particles managed to induce cell proliferation [82]. In a study by Muldoon et al., the distribution, cellular uptake, and toxicity of three FDA-approved SPION of different sizes and surface coatings were compared to each other and to a laboratory reagent [83]. Firstly, inoculation of ferumoxtran-10 (USPION: 20–50 nm in size, complete surface coverage with native dextran), ferumoxytol (USPION: 20–50 nm in size, complete surface coverage with semisynthetic carbohydrate) and ferumoxide (SPION: 60–185 nm in size, incompletely coated with dextran) as well as the lab reagent MION-46 into tumor-bearing rat brains demonstrated direct uptake of ferumoxtran-10 into tumor tissue and long-term retention within the cancerous lesion (5 days). However, uptake seemed NP dependent. Ferumoxide inoculation did not yield tumor enhancement which suggests size and surface coverage dependence. The second step involving osmotic BBB disruption to evaluate transvascular SPION delivery and neurotoxicity displayed no evidence of gross pathology implying the feasibility of intracerebral injection of clinical USPION into humans.

### 3. Biocompatibility and Toxicity of Nanotubes

At present, nanotubes for biomedical application include carbon nanotubes, silicon dioxide nanotubes, boron nitride nanotubes, titanium dioxide nanotubes, and organic nanotubes, of which carbon nanotubes are the most widely

used materials. So far, there have been many great studies into it.

**3.1. Carbon Nanotubes.** Carbon nanotubes are made from rolled up sheets of graphene and are classified as single-walled (SWCNTs) or multiwalled carbon nanotubes (MWCNTs) (as shown in Figure 3) depending on the constituent numbers of graphene layers. Due to their unique size and shape, much effort has been dedicated to analyzing biomedical applications of CNTs. Such extensive potential requires the meticulous evaluation of toxicity. This widespread use of different types of NPs in the biomedical field raises concerns over their increasing access to tissues and organs of the human body and, consequently, the potential toxic effects. Carbon nanotubes (CNTs) are cylindrical graphene sheets. Due to their unique structure, CNTs can be used for hyperthermic ablation of cancer cells due of their strong optical absorption in the NIR wavelength region, as well as for drug delivery to cancer cells owing to their high surface areas.

CNTs are hydrophobic in nature and thus insoluble in water, which limits their application in biomedical and medicinal chemistry. Therefore, various functionalization methods like adsorption, electrostatic interaction, and covalent bonding are being utilized with a number of compounds and polymers to render a hydrophilic character to CNTs so as to avoid their aggregation and to facilitate their use in biomedical applications. Recent developments with CNTs span the areas of gene therapy, drug delivery, thermotherapy, imaging, and anticancer treatments.

**3.1.1. Biocompatibility of Carbon Nanotubes.** Carbon nanotubes (CNTs) have attracted broad attention because of their excellent electrochemical, mechanical, and electrical characteristics. In recent years, many research efforts have focused on the exploration of the application of both single-wall (SWCNT) and multiwall (MWCNT) carbon nanotubes in the biological and biomedical field as nerve cell stimuli, diabetes sensors, cancer therapy, drug delivery carrier, bone scaffold materials, and so forth [85, 86].

**Interaction with Cells.** Among CNTs, single-wall CNTs consist of a single layer of graphite lattice rolled into a perfect cylinder, whereas sets of concentric cylindrical graphite shells form multiwall CNTs (MWCNTs). Neurobiology is one of the fields where the potential applications seem to be very promising [87]. Neurons and neuronal cell lines can grow and differentiate on CNT substrates [88, 89].

It is known that the functionalized CNTs (f-CNTs) can be used to control the number of growth cones, neurite outgrowth, length, and branching during neuronal cell growth on f-CNTs [90]. The neuronal environment with positively charged multiwalled carbon nanotubes (MWCNTs) has improved neurite outgrowth and branching compared to neutral or negatively charged MWCNTs [91, 92].

Bardi et al. [93] show that multiwall CNTs (MWCNTs) coated with Pluronic F127 (PF127) surfactant can be injected in the mouse cerebral cortex without causing degeneration

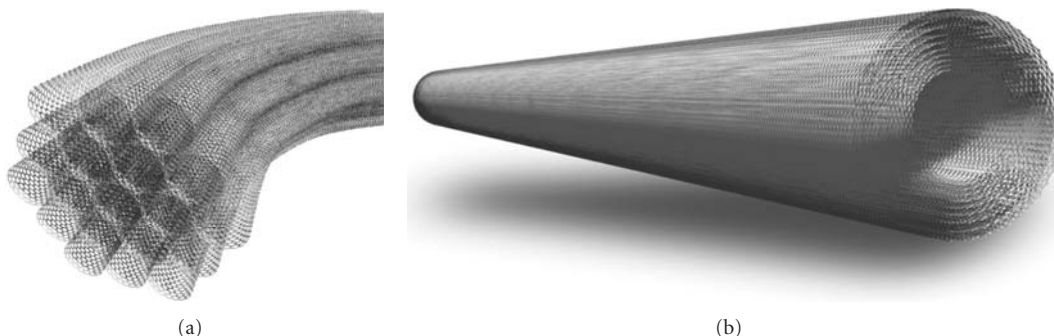


FIGURE 3: (a) Single-walled carbon nanotubes (SWCNTs); (b) multiwalled carbon nanotubes (MWCNTs) [84].

of the neurons surrounding the site of injection. These results suggest that PF127-coated MWCNTs do not induce apoptosis of cortical neurons. Moreover, the presence of MWCNTs can reduce PF127 toxicity.

In 2011, to evaluate the effects of the surface roughness and functionalization modifications of the SWCNT papers, Yoon et al. and so forth [94] investigated the neuronal morphology, mitochondrial membrane potential, and acetylcholine/acetylcholinesterase levels of human neuroblastoma during SH-SY5Y cell growth on the treated SWCNT papers. Their results demonstrated that the plasma-chemical functionalization caused changes in the surface charge states with functional groups with negative and positive charges and then the increased surface roughness enhanced neuronal cell adhesion, mitochondrial membrane potential, and the level of neurotransmitter in vitro. The cell adhesion and mitochondrial membrane potential on the negatively charged SWCNT papers were improved more than on the positively charged SWCNT papers. Also, measurements of the neurotransmitter level showed an enhanced acetylcholine level on the negatively charged SWCNT papers compared to the positively charged SWCNT papers.

It has been demonstrated that CNT support the growth of osteoblastic cells by stimulating the production of extracellular matrix (ECM), a central step during the formation of bone tissue [95].

In order to investigate the interaction of cells with modified multiwalled carbon nanotubes (MWCNTs) for their potential biomedical applications, the MWCNTs were chemically modified with carboxylic acid groups ( $-COOH$ ), polyvinyl alcohol (PVA) polymer and biomimetic apatite on their surfaces [96]. In this study, human osteoblast MG-63 cells were cultured in the presence of the surface-modified MWCNTs. There were no obvious changes in cell morphology in osteoblastic MG-63 cells cultured in the presence of these chemically modified MWCNTs. The surface modification of MWCNTs with apatite achieves an effective enhancement of their biocompatibility. Recently, a new study [97] indicated that MWCNTs might stimulate inducible cells in soft tissues to form inductive bone by concentrating more proteins, including bone-inducing proteins. In this study, they evaluated human adipose-derived MSCs (HASCs) cultured on MWCNTs compacts, comparing on graphite compacts, with and without the adsorption of

FBS and recombinant human bone morphogenetic protein-2 (rhBMP-2) in advance in order to find out how CNTs affect differentiation of HASCs. Larger mineral content was found on the MWNTs compacts than on the GP compacts at day 7. In vivo experiment showed that the MWNTs could induce ectopic bone formation in the dorsal musculature of ddY mice while GP could not.

Surface-coating treatment with multiwalled carbon nanotubes (MWCNTs) was applied to 3D collagen scaffold for bone tissue engineering. In Hirata et al. [98] study, the effect of the MWCNT coating on differentiation of rat primary osteoblasts and the tissue response around MWCNT-coated sponges were investigated. Rat primary osteoblasts (ROBs) were cultured on an MWCNT-coated collagen sponge (MWCNT-coated sponge) in a 3D dynamic flow cell culture system and differentiation markers were measured. Significantly more bone formation was observed around the MWCNT-coated sponges than around the uncoated sponges and new bone attached to MWCNTs directly at 28 and 56 days after implantation in the femur. Moreover, at 28 days after implantation of the MWCNT-coated sponge with osteoblasts cultured for 1 day, bone tissues were successfully formed in the pores according to its honeycomb structure. Therefore, MWCNT coating appears to be effective for bone tissue engineering.

*As Drug and Vaccine Delivery Vehicles.* Carbon nanotubes (CNTs) could be one of the most advanced nanovectors for the highly efficient delivery of drugs and biomolecules owing to their large surface with unique optical and electrical properties. They can be conjugated noncovalently or covalently with drugs, biomolecules and NPs towards the development of a new-generation delivery system for drugs and biomolecules.

CNTs can interact with mammalian cells and enter cells via cytoplasmic translocation [99–102]; they therefore can deliver a range of therapeutic reagents into the cell. For example, plasmid DNA has been internalized by the cell, and the expression of the plasmid-carried marker genes has been enhanced [102–105]. Other macromolecules, including proteins [106], polymers [107], and single-stranded DNA [108] have also been internalized by coating onto CNTs and through the interaction of CNTs with mammalian cells.

Based on the dosage differences in target organelles, Yang et al. [109] successfully used SWCNTs to deliver acetylcholine into brain for treatment of experimentally induced Alzheimer disease with a moderate safety range by precisely controlling the doses, ensuring that SWCNTs preferentially enter lysosomes, the target organelles, and not mitochondria, the target organelles for SWCNT cytotoxicity.

To evaluate the acute response of blood leukocytes to CNTs *in vitro*, Medepalli et al. [110] recreated two specific events: (a) a direct-exposure event that may occur due to presence of CNTs in circulation and (b) presentation of CNTs to blood leukocytes via antigen presenting cells. The potential for activation of different leukocyte subpopulations was then evaluated by profiling various early activation markers using flow cytometry. To ensure relevance to gene and drug delivery, these experiments utilized single-walled CNTs (SWCNTs) functionalized with single-stranded (ss)-DNA fragments consisting of guanine-thymine (GT) repeated sequences, which have potential to serve as a backbone for transport of biomolecules and also as a surfactant to prevent aggregation. Results from this study demonstrate that ss-DNA-functionalized SWCNTs does not elicit an acute immune response from blood leukocytes through either direct or indirect interactions as verified by the expression of early leukocyte activation markers.

**As Biosensors.** Carbon nanotubes show great potential for use as highly sensitive electronic (bio)sensors. Single-walled carbon nanotubes (SWNTs) arguably are the ultimate nanosensor in this class for a number of reasons: SWNTs have the smallest diameter ( $\sim 1 \text{ nm}$ ), directly comparable to the size of single molecules and to the electrostatic screening length in physiological solutions [111]. Furthermore, the low charge-carrier density of SWNTs [112] is directly comparable to the surface charge density of proteins, which intuitively makes SWNTs well suited for electronic detection that relies on electrostatic interactions with analyte (bio)molecules. Finally, the SWNT consists solely of surface such that every single carbon atom is in direct contact with the environment, allowing optimal interaction with nearby molecules. Although an appreciable amount of biosensing studies has been conducted using carbon nanotube transistors, the physical mechanism that underlies sensing is still under debate [113]. Several suggested that mechanisms are electrostatic gating [114], changes in gate coupling, carrier mobility changes, and Schottky barrier effects [115].

Recently, Zelada-Guillén et al. [116] have reported the first biosensor that is able to detect *Staphylococcus aureus* in real time. A network of single-walled carbon nanotubes (SWCNTs) acts as an ion-to-electron potentiometric transducer and anti-*S. aureus* aptamers are the recognition element. In this study, both biosensor types demonstrated great versatility in selectivity assays, which suggests the applicability of SWCNT/aptamer-based potentiometric biosensors in the highly selective identification of *S. aureus*.

**3.1.2. Toxicity of Carbon Nanotubes.** CNTs has certain toxicity, including lung toxicity and embryonic toxicity. Through covalent modification and adding surfactants to the CNTs,

the improvement of the living creature exploitation degree, and reducing the biological toxicity can be achieved.

CNTs may eliminate quickly *in vivo* from the blood, is mainly detained in the liver, the spleen and the lung.

Liver is the dominant site of accumulation after intravenous (iv) or intraperitoneal (ip) administration of CNTs, but only few studies were conducted in order to establish the impact of CNTs over the liver [117]. Also, only few studies have been conducted regarding ip delivery of CNTs [118]. Last year, Clichici et al. and so forth [119] have found that ss-DNA-MWCNTs induce oxidative stress in plasma and liver, with the return of the tested parameters to normal values, 6 h after ip injection of nanotubes, with the exception of reduced glutathione in plasma. Results demonstrate that ss-DNA-MWCNTs produce oxidative stress and inflammation, but with a transient pattern. Given the fact that antioxidants modify the profile not only for oxidative stress, but also of inflammation, the dynamics of these alterations may be of practical importance for future protective strategies.

The research [120] indicated that in 2 months water-soluble SWCNTs does not cause the mouse spleen organization refining various biochemistry target change, the histopathology inspects the nonspleen damage; But along with detection time's extension, possibly causes spleen's immune response.

Porter et al. [121] conducted an *in vivo* dose-response and time course study of MWCNT in mice in order to assess their ability to induce pulmonary inflammation, damage, and fibrosis using doses that approximate estimated human occupational exposures. The data reported indicate that MWCNT exposure rapidly produces significant adverse health outcomes in the lung. Furthermore, the observation that MWCNT reach the pleura after aspiration exposure indicates that more extensive investigations are needed to fully assess if pleural penetration results in any adverse health outcomes.

Recently, Pietrojasti et al. [122] have tested the effect of pristine and oxidized single-wall carbon nanotubes (SWCNTs) on the development of the mouse embryo. No fetal and placental abnormalities were ever observed in control animals. In parallel, SWCNT embryo toxicity was evaluated using the embryonic stem cell test (EST), a validated *in vitro* assay developed for predicting embryo toxicity of soluble chemical compounds, but never applied in full to NPs. The EST predicted the *in vivo* data, identifying oxidized SWCNTs as the more toxic compound.

Toxicity of CNTs and its mechanism have been widely investigated, which is differing from composition, length, diameter and sizes. Exposure to pristine CNT has been shown to cause minimal cytotoxicity at higher concentrations (both *in vivo* and *in vitro*), while chemically functionalized CNT enhanced for drug delivery has not demonstrated any toxicity thus far. However, CNT aggregation has plagued research in this area and the impact of this key variable is unclear at this stage.

**3.2. Other Nanotubes.** Silicon dioxide nanotubes, boron nitride nanotubes, titanium dioxide nanotubes, organic nanotubes are emerging used nanotubes. Until now, reports

about their biomedical application are still not sufficient. Simple descriptions of their biomedical studies are given here to help us get a better understanding about them.

**3.2.1. Silicon Dioxide Nanotubes.** Silica nanotubes (SNTs) have become a promising material in biomedical applications, owing to their unique properties. The tube-structured SNTs are endowed with two physically distinct domains: the inner void and the outer surface. Differential functionalization of the inner and outer surfaces of SNT could provide a facile and effective means to integrate multifunctionality with SNT technology [123]. For example, various nanosized biomaterials and therapeutics, such as magnetic particles, imaging agents, and drugs, can be loaded inside the vacant inner space of SNT to make them potent multifunctional materials. Figure 4(a) shows a TEM micrograph of MSNTs with a length of 6–10  $\mu\text{m}$  and a diameter in the range 400–600 nm. From the TEM image of NH<sub>2</sub>-MSNTs (Figure 4(b)) it can be seen that the samples retained the same morphology as the as prepared MSNTs after modification with APTS. A TEM micrograph of MSNTs coated with PAH/PSS multilayers is presented in Figure 4(c). Similar results for the thickness of the ALG/CHI multilayer assembled on NH<sub>2</sub>-MSNTs can be determined from the TEM micrograph of Figure 4(d).

Biocompatibility and facile modification through well-known silane chemistry [125–127] make SNTs even more attractive tools in various biomedical applications, such as in drug or gene delivery vehicles. Nevertheless, SNTs have encountered a fundamental impediment in gene delivery as they acquire a negative charge in aqueous solution due to the presence of a large number of hydroxyl groups on their surface. Therefore, to achieve efficient gene delivery, the surface of the SNT must be rendered positive by conjugating cationic materials. These cationic materials then condense and load DNA, having a negatively charged phosphate backbone and transport it to the target sites, especially intracellular regions.

The Wu group was the first to introduce SNT as a therapeutic cargo for gene delivery [128]. In their report, the inner surface of SNT was functionalized with 3-(aminopropyl)trimethoxysilane to generate a polycationic surface and, as per confocal microscopy, 60e 70% of the cells were transfected during incubation. The Ran group [129] have functionalized SNT with a magnetic-fluorescent nanocomposite and LMW BPEI to construct a device that can act as an efficient gene delivery carrier and as a MRI agent. The success of this dual-modality nanoconstruct should drive further research into multipurpose therapeutic biomaterials.

**3.2.2. Boron Nitride Nanotubes.** A boron nitride nanotube (BNNT) is a structural analog of a carbon nanotube: alternating B and N atoms entirely substitute for C atoms in a graphitic-like sheet with almost no change in atomic spacing [130]. Despite this structural similarity with carbon nanotubes (CNTs), BNNTs own superior mechanical, chemical, and electrical properties [131, 132]. In the latest years, several examples of CNT exploitation in biotechnology have

been proposed [133], while the biomedical applications of BNNTs have remained largely unexplored [134], having the first study about BNNT-cell interactions been performed by Ciofani et al. [135].

Figure 5 shows the SEM and TEM images of the as-received BNNTs SEM image shows nice clean BNNTs, whereas TEM picture shows the presence of both long cylindrical tubes and bamboo type structures. BNNTs have excellent elastic modulus of 1.22 TPa (similar to CNTs) and are thus a potential candidate as reinforcement. A recent study through the molecular dynamic approach has shown the tensile strength of single-walled BNNTs to be P24 GPa [137]. Also, BNNTs are very flexible and hence their reinforcement will not adversely affect the ductility of the scaffolds [138]. BNNTs were first synthesized in 1995 but there are very few studies [139–144] on BNNT reinforced composites. Researchers have used BNNTs as reinforcement in glasses mainly to increase the strength and fracture toughness [139, 140]. Only one report is available on ceramic-BNNT composite [141], where enhanced superplasticity in Al<sub>2</sub>O<sub>3</sub> and Si<sub>3</sub>N<sub>4</sub> with BNNT addition is observed. Few studies on polymer-BNNT composites have been reported including nonbiodegradable polymers like polyaniline [142], polystyrene [143], and copolymer of vinylidene chloride and acrylonitrile [144]. These studies have justified the role of BNNT in terms of improvement in mechanical and optical properties. BNNTs have higher chemical stability than CNTs in oxidative atmosphere, with their oxidation starting at 1223 K compared to CNTs at 773 K [145]. Although human body temperature is 310 K, the chemical inertness of BNNTs may still be an added advantage when they are exposed in the living body.

Given its proposed biomedical application, cytotoxicity of BNNTs is a very important issue. Recently, Chen et al. [146] have shown BNNTs to be noncytotoxic to human embryonic kidney cells (HEK-293) and reported that BNNTs do not inhibit cell proliferation even after 4 days. Ciofani et al. [147] demonstrated good cytocompatibility and cellular uptake of polyethyleneimine- (PEI-) coated BNNTs in a human neuroblastoma cell line (SH-SY5Y). Both these studies indicate safe use of BNNTs in bioapplication. The application of BNNTs in orthopedic scaffold material requires their cytotoxic behavior to be investigated with bone cells, for example, osteoblasts. Since PLC matrix is biodegradable, BNNTs may get exposed to the bloodstream after the scaffold degrades. BNNTs, exposed in the bloodstream, interact first with macrophages. Macrophages internalize the foreign elements entering in the bloodstream to prevent any harmful reaction. Hence, the cytotoxicity test of BNNTs on macrophages is also very important. No studies have yet been performed on cytotoxicity of BNNTs with osteoblasts or macrophages. It must also be emphasized that no report exists on any biodegradable polymer-BNNT composites up to now.

**3.2.3. Titanium Dioxide Nanotubes.** In 2001, Gong and coworkers [148] reported the fabrication of vertically oriented highly ordered TiO<sub>2</sub> nanotube arrays up to

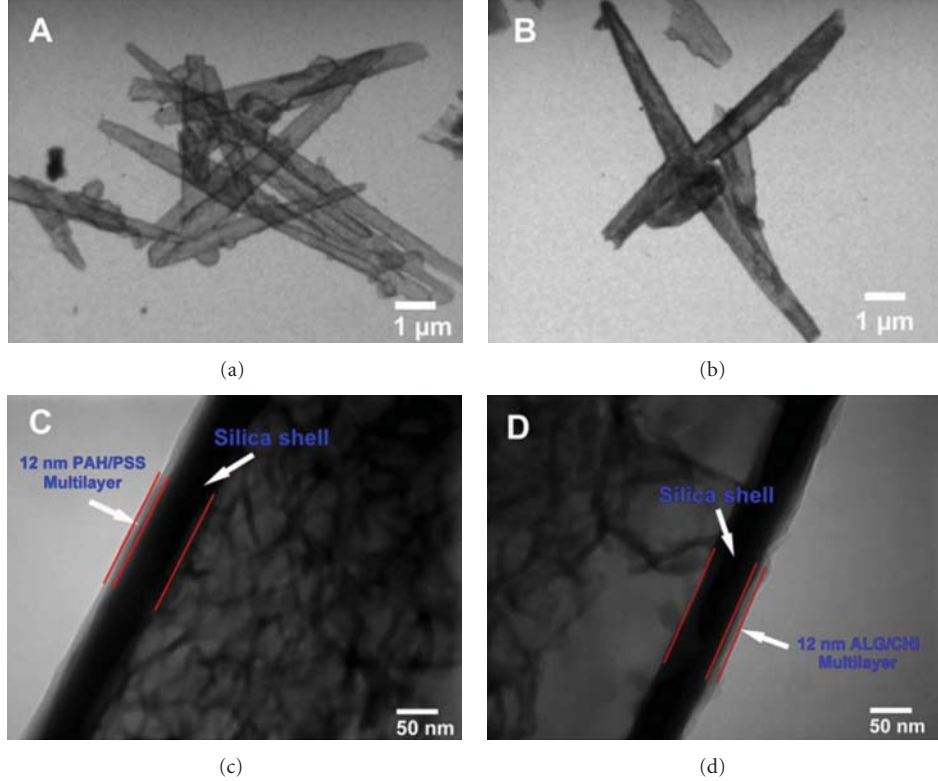


FIGURE 4: TEM images of (a) MSNTs, (b) NH<sub>2</sub>-MSNTs, (c) PAH/PSS-MSNTs, and (d) ALG/CHI-NH<sub>2</sub>-MSNTs [124].

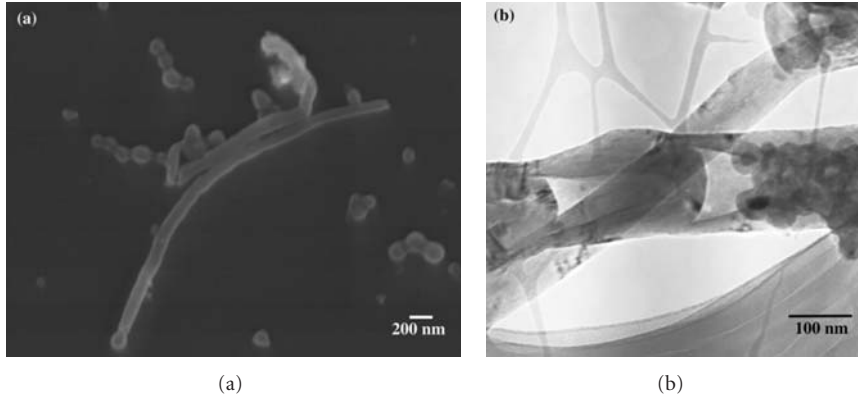


FIGURE 5: (a) SEM image of the as-received BNNTs. (b) TEM images of the as-received BNNTs showing the presence of both tubular- and bamboo-type structures [136].

approximately 500 nm length by anodization of titanium foil in an aqueous HF electrolyte. Since then, substantial efforts have been devoted to the self organisation and growth of TiO<sub>2</sub> [149]. Titanium dioxide nanotube layers are used as photocatalysts in water and environmental purification, as well as biological and biomedical applications [150–152]. In particular, titanium dioxide nanotubes are used as a biomaterial for implants, drug delivery platforms, tissue engineering, and bacteria killing [153–155]. Another interesting property of TiO<sub>2</sub> is its tunable wettability effect [156]. The ability to modify surface topography and to control wetting behavior is useful for biomedical applications. Surface roughness,

contact angle, and surface energy are the main factors in understanding the biology media and material interaction. We can see the SEM images of the ordered anodized titanium oxide nanotube arrays in Figures 6(a) and 6(b). Figure 6(c) shows Silica coated TiO<sub>2</sub> nanotubes prepared on the above anodized TiO<sub>2</sub> via a sol-gel method.

In 2010, Feschet-Chassot et al. [158] used the ciliated protozoan *T. pyriformis* to predict the toxicity of titanium dioxide nanotube layers towards biological systems. The contact angle measurements show clearly the correlation between surface topography and surface wettability. They have shown the ability of the titanium dioxide nanotube

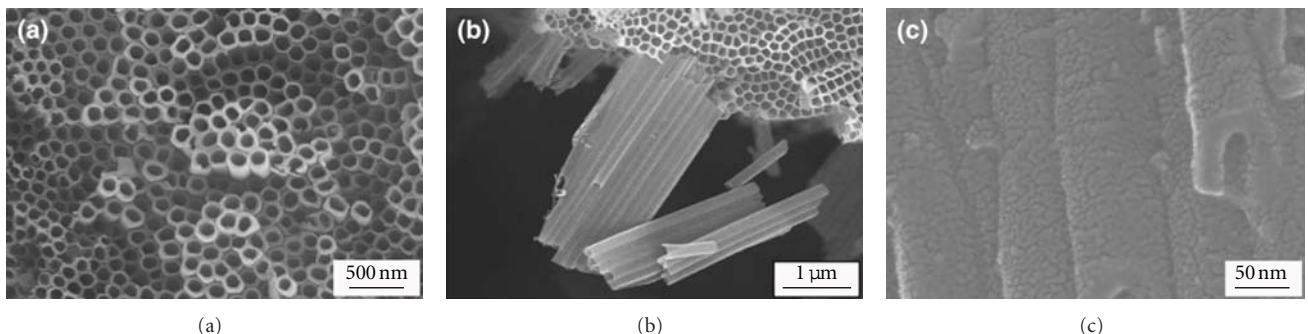


FIGURE 6: SEM images of  $\text{TiO}_2$  nanotube arrays anodized at constant potential. (a) Top view, (b) side view, and (c) silica-coated titania nanotube [157].

layers to degrade AO7. Such surfaces do not show any characteristic in vitro toxicity effect in a biological system.

**3.2.4. Organic Nanotubes.** Organic nanotubes (ONTs) self-assembled from amphiphiles are one of the tubular nanomaterials that have attracted many interest in the field of nanotechnology because of their uniform tubular morphology with a hollow nanospace and a hydrophilic biocompatible surface [159]. Application of pristine ONTs has been found in nanopipettes, photovoltaic devices, and nanocontainer for gene. Furthermore, the surface functionalization of ONTs has become a key methodology to utilize them for many purposes, such as sensor for guest protein, pathogen detection chips, and biomimetic catalyst [160].

In the meantime, the use of tubular nanomaterials as nonviral gene transfer vector has been growing fast. Inorganic ones, mainly carbon and silica nanotubes, were functionalized with various positive materials and their gene transfer ability has been extensively investigated. To the best of knowledge, two attempts on the usage of ONTs in gene delivery have been reported. In the first example, lipid microtubules were embedded in an agarose gel as a reservoir for the sustained release of plasmid DNA, but not as a DNA transfer vector [162]. In the second example, cationic nanotubes self-assembled from dipeptide were able to associate single-stranded DNA on their outer surface for the intracellular delivery [163]; however, they were transformed to spherical vesicles under dilute condition before cellular internalization. These limited reports indicated that the utility of ONTs as nonviral tubular gene transfer vectors has not been fully demonstrated.

The drug loading of ONTs was susceptible to the effect of ionic strength and  $\text{H}^+$  concentration in the medium, and drug release from ONTs was promoted at lower pH, which is favorable for the release of drugs in the endosome after cellular uptake [161] and Figure 7 shows that ONT1 was taken up to the cells. Moreover, ONT could be modified chemically with folate by simply mixing with a folate-conjugate lipid. Also in 2011, another study [164] demonstrated the usefulness of functionalized ONT in gene delivery, and the functionalized ONT represents a novel type of tubular nonviral gene transfer vector. These novel, biodegradable organic nanotubes have the potential to be

used as drug carriers for controlled and targeting drug delivery.

#### 4. Conclusions

Nanoparticles, of large surface area and high specific surface energy, are thermodynamically unstable system. After the NPs enter the organism by various means, they will agglomerate, dissolve, and meet with other changes as a result of the environmental impact of the body (such as protein concentration and high ionic strength, high acidity). When NPs agglomerate, the physical and chemical properties may change, thus affect the biological effects. For metal and metallic oxide NPs, solubility problems are more important. The release of metal ions of dissolved NPs, at least part of them contributes to the toxicity that we observed. The biological characteristics which NPs demonstrated have significant correlations with structures and the nature of their own. Therefore, people are considering changes in NPs themselves to reduce their toxicity and improve the biocompatibility.

Surface modification of NPs and artificial control of NPs size and shape, are effective ways to reduce the toxicity of NPs. But some scholars believe that artificially coated and modified NPs have lost their original features, which from a fundamental sense not the original NPs can be compared with. Surface modification methods can be divided into the surface coating and chemical modification. Through the surface modification of NPs, the inherent toxicity of NPs can be reduced, which also can greatly improve the biocompatibility of NPs.

To use NPs safely in biomedicine, a detailed understanding of biocompatibility and toxicity of NPs is needed. As we can see, more and more data are becoming available regarding NPs toxicity, but highly effort is still required in order to truly advance our knowledge in this field. Currently, researchers may carry out these studies from these aspects: considering various forms of particles respectively, considering the dose-response relationship, in vivo and in vitro experiments, setting about establishing a database of toxic nanoscale to further clarify the division of nanoscale toxic nanosize range. Meantime, deep studies about the

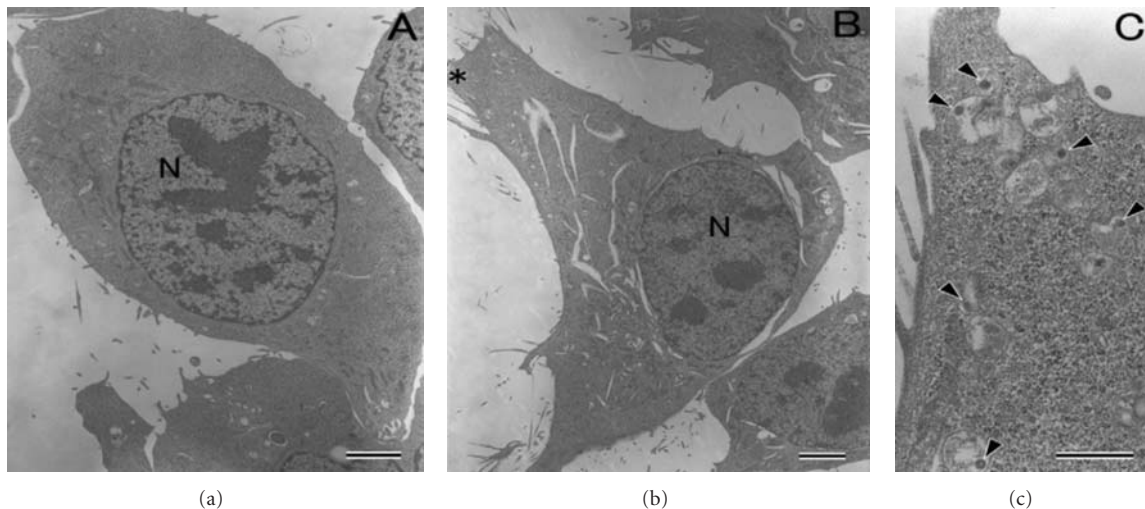


FIGURE 7: Transmission electron micrographs showing untreated C26 cells (a) and C26 cells incubated with ONT1 for 24 h (b) and a high magnification image of the surrounding cell (indicated by an asterisk in (b)) (c). N: nucleus; arrowhead: ONT1, bars = 2  $\mu$ m (a) and (b) and 500 nm (c) [161].

interaction between cells from different tissues and NPs are also necessary.

As a novel kind of nanomaterials with wide potential applications, adverse effects of carbon nanotubes (CNTs) have recently received significant attention after respiratory exposure. Toxicity of CNTs and its mechanism have been widely investigated, which is differing from composition, length, diameter, and sizes. Exposure to pristine CNT has been shown to cause minimal cytotoxicity at higher concentrations (both *in vivo* and *in vitro*), while chemically functionalized CNT enhanced for drug delivery have not demonstrated any toxicity thus far. However, CNT aggregation has plagued research in this area and the impact of this key variable is unclear at this stage.

## Acknowledgments

The authors acknowledge the financial supports from the National Natural Science Foundation of China (no. 31000431 and 10925208), the Beijing Nova Program (no. 2010B011), State Key Laboratory of New Ceramic and Fine Processing (Tsinghua University), and Program for New Century Excellent Talents (NCET) in University from Ministry of Education of China.

## References

- [1] D. F. Williams, "On the mechanisms of biocompatibility," *Biomaterials*, vol. 29, pp. 2941–2953, 2008.
- [2] D. W. Lee, K. Powers, and R. Baney, "Physicochemical properties and blood compatibility of acylated chitosan nanoparticles," *Carbohydrate Polymers*, vol. 58, no. 4, pp. 371–377, 2004.
- [3] R. Chouhan and A. K. Bajpai, "Release dynamics of ciprofloxacin from swellable nanocarriers of poly(2-hydroxyethyl methacrylate): an *in vitro* study," *Nanomedicine*, vol. 6, no. 3, pp. 453–462, 2010.
- [4] N. Sanoj Rejinold, M. Muthunarayanan, V. V. Divyaratne et al., "Curcumin-loaded biocompatible thermoresponsive polymeric nanoparticles for cancer drug delivery," *Journal of Colloid and Interface Science*, vol. 360, no. 1, pp. 39–51, 2011.
- [5] Q. He, J. Zhang, F. Chen, L. Guo, Z. Zhu, and J. Shi, "An anti-ROS/hepatitis drug delivery system based on salvianolic acid B loaded mesoporous silica nanoparticles," *Biomaterials*, vol. 31, no. 30, pp. 7785–7796, 2010.
- [6] C. Dai, Y. Yuan, C. Liu et al., "Degradable, antibacterial silver exchanged mesoporous silica spheres for hemorrhage control," *Biomaterials*, vol. 30, pp. 5364–5375, 2009.
- [7] N. Nimi, W. Paul, and C. P. Sharma, "Blood protein adsorption and compatibility studies of gold nanoparticles," *Gold Bulletin*, vol. 44, pp. 15–20, 2011.
- [8] ASTM Standard, "Standard practice for assessment of hemolytic properties of materialss," Tech. Rep. F756-08, 2008.
- [9] T. J. Cho, R. A. Zangmeister, R. I. MacCuspie, A. K. Patri, and V. A. Hackley, "Newkome-type dendron-stabilized gold nanoparticles: synthesis, reactivity, and stability," *Chemistry of Materials*, vol. 23, no. 10, pp. 2665–2676, 2011.
- [10] N. N. Reddy, K. Varaprasad, S. Ravindra et al., "Evaluation of blood compatibility and drug release studies of gelatin based magnetic hydrogel nanocomposites," *Colloids and Surfaces A*, vol. 385, no. 1–3, pp. 20–27, 2011.
- [11] K. Muller, J. N. Skepper, M. Posfai et al., "Effect of ultrasmall superparamagnetic iron oxide nanoparticles (Ferumoxtran-10) on human monocyte-macrophages *in vitro*," *Biomaterials*, vol. 28, pp. 1629–1642, 2007.
- [12] I. Siglienti, M. Bendszus, C. Kleinschmitz, and G. Stoll, "Cytokine profile of iron-laden macrophages: implications for cellular magnetic resonance imaging," *Journal of Neuroimmunology*, vol. 173, pp. 166–173, 2006.
- [13] J. K. Hsiao, H. H. Chu, Y. H. Wang et al., "Macrophage physiological function after superparamagnetic iron oxide labeling," *NMR in Biomedicine*, vol. 21, pp. 820–829, 2008.
- [14] T. K. Jain, M. K. Reddy, M. A. Morales, D. L. Leslie-Pelecky, and V. Labhasetwar, "Biodistribution, clearance, and biocompatibility of iron oxide magnetic nano-particles in rats," *Molecular Pharmacology*, vol. 5, pp. 316–327, 2008.

- [15] P. R. Leroueil, S. A. Berry, K. Duthie et al., "Wide varieties of cationic nanoparticles induce defects in supported lipid bilayers," *Nano Letters*, vol. 8, pp. 420–424, 2008.
- [16] J. H. Lee, K. E. Cha, M. S. Kim et al., "Nanosized polyamidoamine (PAMAM) dendrimer-induced apoptosis mediated by mitochondrial dysfunction," *Toxicology Letters*, vol. 190, pp. 202–207, 2009.
- [17] J. H. Kuo, M. S. Jan, and H. W. Chiu, "Mechanism of cell death induced by cationic dendrimers in RAW264.7 murine macrophage-like cells," *Journal of Pharmacy and Pharmacology*, vol. 57, pp. 489–495, 2005.
- [18] M. Labieniec and T. Gabryelak, "Preliminary biological evaluation of poly(amideamine) (PAMAM) dendrimer G3.5 on selected parameters of rat liver mitochondria," *Mitochondrion*, vol. 8, pp. 305–312, 2008.
- [19] S. Shaunik, S. Thomas, E. Gianasi et al., "Polyvalent dendrimer glucosamine conjugates prevent scar tissue formation," *Nature Biotechnology*, vol. 22, pp. 977–984, 2004.
- [20] S. Fruchon, M. Poupot, L. Martinet et al., "Anti-inflammatory and immunosuppressive activation of human monocytes by a bioactive dendrimer," *Journal of Leukocyte Biology*, vol. 85, pp. 553–562, 2009.
- [21] A. S. Chauhan, P. V. Diwan, N. K. Jain, and D. A. Tomalia, "Unexpected *in vivo* anti-inflammatory activity observed for simple, surface functionalized poly(amideamine) dendrimers," *Biomacromolecules*, vol. 10, pp. 1195–1202, 2009.
- [22] T. H. Chung, S. H. Wu, M. Yao et al., "The effect of surface charge on the uptake and biological function of mesoporous silica nano-particles in 3T3-L1 cells and human mesenchymal stem cells," *Biomaterials*, vol. 28, no. 19, pp. 2959–2966, 2007.
- [23] G. Bhakta, R. K. Sharma, N. Gupta et al., "Multifunctional silica nanoparticles with potentials of imaging and gene delivery," *Nanomedicine*, vol. 7, no. 4, pp. 472–479, 2011.
- [24] W. Sun, N. Fang, B. G. Trewyn, M. Tsunoda, I. I. Slowing, V. S. Lin et al., "Endocytosis of a single mesoporous silica nanoparticle into a human lung cancer cell observed by differential interference contrast microscopy," *Analytical and Bioanalytical Chemistry*, vol. 391, no. 6, pp. 2119–2125, 2008.
- [25] B. G. Trewyn, S. Giri, I. I. Slowing, and V. S. Lin, "Mesoporous silica nanoparticle based controlled release, drug delivery, and biosensor systems," *Chemical Communications*, vol. 31, pp. 3236–3245, 2007.
- [26] Y. Zhao, B. G. Trewyn, I. I. Slowing, and V. S. Lin, "Mesoporous silica nanoparticle-based double drug delivery system for glucose-responsive controlled release of insulin and cyclic AMP," *Journal of the American Chemical Society*, vol. 131, no. 24, pp. 8398–8400, 2009.
- [27] G. Bardia, M. A. Malvindib, L. Gherardinia et al., "The biocompatibility of amino functionalized CdSe/ZnS quantum-dot-Doped SiO<sub>2</sub> nanoparticles with primary neural cells and their gene carrying performance," *Biomaterials*, vol. 31, pp. 6555–6566, 2010.
- [28] C. Loo, L. Hirsch, M. Lee et al., "Gold nanoshell bioconjugates form molecular imaging in living cells," *Optics Letters*, vol. 30, pp. 1012–1014, 2005.
- [29] C. Brandenberger, B. Rothen-Rutishauser, C. Muhlfeld et al., "Effects and uptake of gold nanoparticles deposited at the air–liquid interface of a human epithelial airway model," *Toxicology and Applied Pharmacology*, vol. 242, pp. 56–65, 2010.
- [30] N. G. Bastus, E. Sanchez-Tillo, S. Pujals et al., "Homogeneous conjugation of peptides onto gold nanoparticles enhances macrophage response," *American Chemical Society Nano*, vol. 3, pp. 1335–1344, 2009.
- [31] A. Elsaesser and C. V. Howard, "Toxicology of nanoparticles," *Advanced Drug Delivery Reviews*, vol. 64, no. 2, pp. 129–137, 2012.
- [32] L. Yildirim, N. T. K. Thanh, M. Loizidou et al., "Toxicological considerations of clinically applicable nanoparticles," *Nano Today*, vol. 6, pp. 585–607, 2011.
- [33] H. R. Paur, F. R. Cassee, J. Teeguarden et al., "In-vitro cell exposure studies for the assessment of nanoparticle toxicity in the lung-A dialog between aerosol science and biology," *Journal of Aerosol Science*, vol. 42, no. 10, pp. 668–692, 2011.
- [34] A. Sosnik, A. M. Carcaboso, R. J. Glisoni, M. A. Moreton, and D. A. Chiappetta, "New old challenges in tuberculosis: potentially effective nanotechnologies in drug delivery," *Advanced Drug Delivery Reviews*, vol. 62, no. 4–5, pp. 547–559, 2010.
- [35] G. Sarfati, T. Dvir, M. Elkabets, R. N. Apte, and S. Cohen, "Targeting of polymeric nanoparticles to lung metastases by surface-attachment of YIGSR peptide from laminin," *Biomaterials*, vol. 32, no. 1, pp. 152–161, 2011.
- [36] J. S. Rink, K. M. McMahon, X. Chen, C. A. Mirkin, C. S. Thaxton, and D. B. Kaufman, "Transfection of pancreatic islets using polyvalent DNA-functionalized gold nanoparticles," *Surgery*, vol. 148, no. 2, pp. 335–345, 2010.
- [37] G. Romero, I. Estrela-Llopis, J. Zhou et al., "Surface engineered poly(lactide-co-glycolide) nanoparticles for intracellular delivery: uptake and cytotoxicity—a confocal raman microscopic study," *Biomacromolecules*, vol. 11, pp. 2993–2999, 2010.
- [38] R. Yang, S. G. Yang, W. S. Shim et al., "Lung-specific delivery of paclitaxel by chitosan-modified PLGA nanoparticles via transient formation of microaggregates," *Journal of Pharmaceutical Sciences*, vol. 98, no. 3, pp. 970–984, 2009.
- [39] K. Tahara, T. Sakai, H. Yamamoto, H. Takeuchi, N. Hirashima, and Y. Kawashima, "Improved cellular uptake of chitosan-modified PLGA nanospheres by A549 cells," *International Journal of Pharmaceutics*, vol. 382, no. 1–2, pp. 198–204, 2009.
- [40] H. Yang, C. Liu, D. Yang, H. Zhangs, and Z. Xi, "Comparative study of cytotoxicity, oxidative stress and genotoxicity induced by four typical nanomaterials: the role of particle size, shape and composition," *Journal of Applied Toxicology*, vol. 29, pp. 69–78, 2009.
- [41] M. Chen and A. von Mikecz, "Formation of nucleoplasmic protein aggregates impairs nuclear function in response to SiO<sub>2</sub> nanoparticles," *Experimental Cell Research*, vol. 305, pp. 51–62, 2005.
- [42] V. Christen and K. Fent, "Silica nanoparticles and silver-doped silica nanoparticles induce endoplasmatic reticulum stress response and alter cytochrome P4501A activity," *Chemosphere*, vol. 87, no. 4, pp. 423–434, 2012.
- [43] J. S. Chang, K. L. Chang, D. F. Hwang, and Z. L. Kong, "In vitro cytotoxicity of silica nanoparticles at high concentrations strongly depends on the metabolic activity type of the cell line," *Environmental Science & Technology*, vol. 41, pp. 2064–2068, 2007.
- [44] Y. Jin, S. Kannan, M. Wu, and J. X. Zhao, "Toxicity of luminescent silica nanoparticles to living cells," *Chemical Research in Toxicology*, vol. 20, pp. 1126–1133, 2007.
- [45] F. Wang, F. Gao, M. Lan, H. Yuan, Y. Huang, and J. Liu, "Oxidative stress contributes to silica nanoparticle-induced cytotoxicity in human embryonic kidney cells," *Toxicology in vitro*, vol. 23, pp. 808–815, 2009.

- [46] W. Lin, Y. W. Huang, X. D. Zhou, and Y. Ma, “*In vitro* toxicity of silica nanoparticles in human lung cancer cells,” *Toxicology and Applied Pharmacology*, vol. 217, pp. 252–259, 2006.
- [47] J. H. Sung, J. H. Ji, K. S. Song et al., “Acute inhalation toxicity of silver nanoparticles,” *Toxicology and Industrial Health*, vol. 2, pp. 34–38, 2010.
- [48] J. H. Ji, J. H. Jung, S. S. Kim et al., “Twenty-eight-day inhalation toxicity study of silver nanoparticles in Sprague-Dawley rats,” *Inhalation Toxicology*, vol. 19, pp. 857–871, 2007.
- [49] J. H. Sung, J. H. Ji, J. D. Park et al., “Subchronic inhalation toxicity of silver nanoparticles,” *Toxicological Sciences*, vol. 108, pp. 452–461, 2009.
- [50] J. H. Sung, J. H. Ji, J. U. Yoon et al., “Lung function changes in Sprague-Dawley rats after Prolonged inhalation exposure to silver nanoparticles,” *Inhalation Toxicology*, vol. 20, pp. 567–574, 2008.
- [51] B. Kiss, T. Biro, G. Czifra et al., “Investigation of micronized titanium dioxide penetration in human skin xenografts and its effect on cellular functions of human skin-derived cells,” *Experimental Dermatology*, vol. 17, pp. 659–667, 2008.
- [52] Z. Pan, W. Lee, L. Slutsky, R. A. Clark, N. Pernodet, and M. H. Rafailovich, “Adverse effects of titanium dioxide nanoparticles on human dermal fibroblasts and how to protect cells,” *Small*, vol. 5, pp. 511–520, 2009.
- [53] J. Lademann, H. Weigmann, C. Rickmeyer et al., “Penetration of titanium dioxide microparticles in a sunscreen formulation into the horny layer and the follicular orifice,” *Skin Pharmacology and Physiology*, vol. 12, pp. 247–256, 1999.
- [54] C. Bennat and C. C. Muller-Goymann, “Skin penetration and stabilization of formulations containing microfine titanium dioxide as physical UV filter,” *International Journal of Cosmetic Science*, vol. 22, no. 4, pp. 271–283, 2000.
- [55] A. Mavon, C. Miquel, O. Lejeune, B. Payre, and P. Moretto, “*In vitro* percutaneous absorption and *in vivo* stratum corneum distribution of an organic and a mineral sunscreen,” *Skin Pharmacology and Physiology*, vol. 20, no. 1, pp. 10–12, 2007.
- [56] D. Pornpattananangkul, S. Olson, S. Aryal et al., “Stimuli-responsive liposome fusion mediated by gold nanoparticles,” *ACS Nano*, vol. 4, no. 4, pp. 1935–1942, 2010.
- [57] G. Sonavane, K. Tomoda, A. Sano, H. Ohshima, H. Terada, and K. Makino, “*In vitro* permeation of gold nanoparticles through rat skin and rat intestine: effect of particle size,” *Colloids and Surfaces B*, vol. 65, pp. 1–10, 2008.
- [58] C. J. Murphy, A. M. Gole, J. W. Stone et al., “Gold nanoparticles in biology: beyond toxicity to cellular imaging,” *Accounts of Chemical Research*, vol. 41, pp. 1721–1730, 2008.
- [59] T. Mironava, M. Hadjihargyrou, M. Simon, V. Jurukovski, and M. H. Rafailovich, “Gold nanoparticles cellular toxicity and recovery: effect of size, concentration and exposure time,” *Nanotoxicology*, vol. 4, pp. 120–137, 2010.
- [60] Y. Pan, S. Neuss, A. Leifert, M. Fischler, F. Wen, U. Simon et al., “Size-dependent cytotoxicity of gold nanoparticles,” *Small*, vol. 3, pp. 1941–1949, 2007.
- [61] A. M. Derfus, W. C. W. Chan, and S. N. Bathia, “Intracellular delivery of quantum dots for live cell labeling and organelle tracking,” *Advanced Materials*, vol. 16, pp. 961–966, 2004.
- [62] R. S. Yang, L. W. Chang, J. P. Wu et al., “Persistent tissue kinetics and redistribution of nanoparticles, Quantum Dot 705, in Mice: ICP-MS quantitative assessment,” *Environmental Health Perspectives*, vol. 115, no. 9, pp. 1339–1343, 2007.
- [63] P. Lin, J. W. Chen, L. W. Chang et al., “Computational and ultrastructural toxicology of a nanoparticle, Quantum Dot 705, in mice,” *Environmental Science and Technology*, vol. 42, no. 16, pp. 6264–6270, 2008.
- [64] B. R. Prasad, N. Nikolskaya, D. Connolly et al., “Long-term exposure of CdTe quantum dots on PC12 cellular activity and the determination of optimum non-toxic concentrations for biological use,” *Journal of Nanobiotechnology*, vol. 8, article 7, 2010.
- [65] G. K. Das, P. P. Y. Chan, A. Teo, J. S. C. Loo, J. M. Anderson, and T. T. Y. Tan, “*In vitro* cytotoxicity evaluation of biomedical nanoparticles and their extracts,” *Journal of Biomedical Materials Research A*, vol. 93, no. 1, pp. 337–346, 2010.
- [66] M. J. Clift, J. Varet, S. M. Hankin, B. Brownlee, A. M. Davidson, and C. Brandenberger, “Quantum dot cytotoxicity in vitro: an investigation into the cytotoxic effects of a series of different surface chemistries and their core/shell materials,” *Nanotoxicology*, vol. 5, no. 4, pp. 664–674, 2011.
- [67] J. C. Olivier, “Drug transport to brain with targeted nanoparticles,” *NeuroRx*, vol. 2, pp. 108–119, 2005.
- [68] H. S. Sharma and A. Sharma, “Nanoparticles aggravate heat stress induced cognitive deficits, blood-brain barrier disruption, edema formation and brain pathology,” *Progress in Brain Research*, vol. 162, pp. 245–273, 2007.
- [69] Y. S. Kim, J. S. Kim, H. S. Cho et al., “Twenty-eight-day oral toxicity, genotoxicity, and gender-related tissue distribution of silver nanoparticles in Sprague-Dawley rats,” *Inhalation Toxicology*, vol. 20, pp. 575–583, 2008.
- [70] F. Cengelli, D. Maysinger, F. Tschudi-Monnet et al., “Interaction of functionalized super-paramagnetic iron oxide nanoparticles with brain structures,” *Journal of Pharmacology and Experimental Therapeutics*, vol. 318, pp. 108–116, 2006.
- [71] C. Corot, K. G. Petry, R. Trivedi et al., “Macrophage imaging in central nervous system and in carotid atherosclerotic plaque using ultrasmall superparamagnetic iron oxide in magnetic resonance imaging,” *Investigative Radiology*, vol. 39, no. 10, pp. 619–625, 2004.
- [72] C. W. Jung and P. Jacobs, “Physical and chemical properties of superparamagnetic iron oxide MR contrast agents: ferumoxides, ferumoxtran, ferumoxsil,” *Magnetic Resonance Imaging*, vol. 13, no. 5, pp. 661–674, 1995.
- [73] I. Raynal, P. Prigent, S. Peyramaure, A. Najid, C. Rebuzzi, and C. Corot, “Macrophage endocytosis of superparamagnetic iron oxide nanoparticles: mechanisms and comparison of Ferumoxides and Ferumoxtran-10,” *Investigative Radiology*, vol. 39, no. 1, pp. 56–63, 2004.
- [74] D. Baumjohann, A. Hess, L. Budinsky, K. Brune, G. Schuler, and M. B. Lutz, “*In vivo* magnetic resonance imaging of dendritic cell migration into the draining lymph nodes of mice,” *European Journal of Immunology*, vol. 36, no. 9, pp. 2544–2555, 2006.
- [75] M. G. Harisinghani, J. Barentsz, P. F. Hahn, W. M. Deserno, S. Tabatabaei, C. H. van de Kaa et al., “Noninvasive detection of clinically occult lymph-node metastases in prostate cancer,” *The New England Journal of Medicine*, vol. 348, pp. 2491–2499, 2003.
- [76] M. E. Kooi, V. C. Cappendijk, K. B. Cleutjens, A. G. Kessels, P. J. Kitslaar, M. Borgers et al., “Accumulation of ultra-small superparamagnetic particles of iron oxide in human atherosclerotic plaques can be detected by *in vivo* magnetic resonance imaging,” *Circulation*, vol. 107, pp. 2453–2458, 2003.

- [77] S. G. Ruehm, C. Corot, P. Vogt, S. Kolb, and J. F. Debatin, "Magnetic resonance imaging of atherosclerotic plaque with ultrasmall superparamagnetic particles of iron oxide in hyperlipidemic rabbits," *Circulation*, vol. 103, pp. 415–422, 2001.
- [78] N. Beckmann, C. Gerard, D. Abramowski, C. Cannet, and M. Staufenbiel, "Noninvasive magnetic resonance imaging detection of cerebral amyloid angiopathy-related microvascular alterations using superparamagnetic iron oxide particles in APP transgenic mouse models of Alzheimer's disease: application to passive Abeta immunotherapy," *Journal of Neuroscience*, vol. 31, pp. 1023–1031, 2011.
- [79] G. Oberdorster, V. Stone, and K. Donaldson, "Toxicology of nanoparticles: a historical perspective," *Nanotoxicology*, vol. 1, pp. 2–25, 2007.
- [80] U. O. Hafeli, J. S. Riffle, L. Harris-Sekhawat, A. Carmichael-Baranauskas, F. Mark, J. P. Dailey et al., "Cell uptake and *in vitro* toxicity of magnetic nanoparticles suitable for drug delivery," *Molecular Pharmacology*, vol. 6, pp. 1417–1428, 2009.
- [81] M. Mahmoudi, A. Simchi, M. Imani, M. A. Shokrgozar, A. S. Milani, U. O. Hafeli et al., "A new approach for the *in vitro* identification of the cytotoxicity of superparamagnetic iron oxide nanoparticles," *Colloids and Surfaces B*, vol. 75, pp. 300–309, 2010.
- [82] C. C. Berry, S. Wells, S. Charles, and A. S. Curtis, "Dextran and albumin derivatised iron oxide nanoparticles: influence on fibroblasts *in vitro*," *Biomaterials*, vol. 24, pp. 4551–4557, 2003.
- [83] L. L. Muldoon, M. Sandor, K. E. Pinkston, and E. A. Neuweit, "Imaging, distribution, and toxicity of superparamagnetic iron oxide magnetic resonance nanoparticles in the rat brain and intracerebral tumor," *Neurosurgery*, vol. 57, pp. 785–796, 2005.
- [84] X. Li, Y. Fan, and F. Watari, "Current investigations into carbon nanotubes for biomedical application," *Biomedical Materials*, vol. 5, no. 2, Article ID 022001, 12 pages, 2010.
- [85] A. V. Liopo, M. P. Stewart, J. Hudson, J. M. Tour, and T. C. Pappas, "Biocompatibility of native and functionalized single-walled carbon nanotubes for neuronal interface," *Journal of Nanoscience and Nanotechnology*, vol. 6, no. 5, pp. 1365–1374, 2006.
- [86] W. Yang, P. Thordarson, J. J. Gooding, S. P. Ringer, and F. Braet, "Carbon nanotubes for biological and biomedical applications," *Nanotechnology*, vol. 18, no. 41, Article ID 412001, 2007.
- [87] E. B. Malarkey and V. Parpura, "Applications of carbon nanotubes in neurobiology," *Neurodegenerative Diseases*, vol. 4, pp. 292–299, 2007.
- [88] P. Galvan-Garcia, E. W. Keefer, F. Yang, M. Zhang, S. Fang, A. A. Zakhidov et al., "Robust cell migration and neuronal growth on pristine carbon nanotube sheets and yarns," *Journal of Biomaterials Science, Polymer Edition*, vol. 18, pp. 1245–1261, 2007.
- [89] E. Jan and N. A. Kotov, "Successful differentiation of mouse neural stem cells on layer-by-layer assembled single-walled carbon nanotube composite," *Nano Letters*, vol. 7, pp. 1123–1128, 2007.
- [90] M. A. Correa-Duarte, M. Wagner, J. Rojas-Chapana, C. Morsczeck, M. Thie, and M. Giersig, "Fabrication and biocompatibility of carbon nanotube-based 3D net-works as scaffolds for cell seeding and growth," *Nano Letters*, vol. 4, pp. 2233–2236, 2004.
- [91] H. Hu, Y. Ni, S. K. Mandal et al., "Polyethyleneimine functionalized single-walled carbon nanotubes as a substrate for neuronal growth," *Journal of Physical Chemistry B*, vol. 109, pp. 4285–4289, 2005.
- [92] H. Hu, Y. Ni, V. Montana, R. C. Haddon, and V. Parpura, "Chemically functionalized carbon nanotubes as substrates for neuronal growth," *Nano Letters*, vol. 4, pp. 507–511, 2005.
- [93] G. Bardi et al., "Pluronic-coated carbon nanotubes do not induce degeneration of cortical neurons *in vivo* and *in vitro*," *Nanomedicine*, vol. 5, pp. 96–104, 2009.
- [94] O. K. Ja Yoon et al., "Effects of O<sub>2</sub> and N<sub>2</sub>/H<sub>2</sub> plasma treatments on the neuronal cell growth on single-walled carbon nanotube paper scaffolds," *Applied Surface Science*, vol. 257, pp. 8535–8541, 2011.
- [95] X. Li, H. Gao, M. Uo et al., "Maturation of osteoblast-like Saos<sub>2</sub> induced by carbon nanotubes," *Biomedical Materials*, vol. 4, no. 1, Article ID 015005, 2009.
- [96] F. Zhang, A. Weidmann, J. B. Nebe, and E. Burkert, "Osteoblast cell response to surface-modified carbon nanotubes," *Materials Science and Engineering C*, vol. 32, no. 5, pp. 1057–1061, 2012.
- [97] X. M. Li, H. F. Liu, X. F. Niu et al., "The use of carbon nanotubes to induce osteogenic differentiation of human adipose-derived MSCs *in vitro* and ectopic bone formation *in vivo*," *Biomaterials*, vol. 33, no. 19, pp. 4818–4827, 2012.
- [98] E. Hirata, M. Uo, and H. Takita, "Multiwalled carbon nanotube-coating of 3D collagen scaffolds for bone tissue engineering," *Carbon*, vol. 49, pp. 3284–3291, 2011.
- [99] A. E. Porter, M. Gass, K. Muller, J. N. Skepper, P. Midgley, and M. Welland, "Direct imaging of single-walled carbon nanotubes in cells," *Nature Nanotechnology*, vol. 2, pp. 713–717, 2007.
- [100] M. Tanaka, Y. Nishigaki, N. Fuku, T. Ibi, K. Sahashi, and Y. Koga, "Therapeutic potential of pyruvate therapy for mitochondrial diseases," *Mitochondria*, vol. 7, pp. 399–403, 2007.
- [101] K. Kostarelos, L. Lacerda, G. Pastorin, W. Wu, S. Wieckowski, J. Luangsivilay et al., "Cellular uptake of functionalized carbon nanotubes is independent of functional group and cell type," *Nature Nanotechnology*, vol. 2, pp. 108–113, 2007.
- [102] D. Pantarotto, J. P. Briand, M. Prato, and A. Bianco, "Translocation of bioactive peptides across cell membranes by carbon nanotubes," *Chemical Communications*, vol. 2004, pp. 16–17, 2004.
- [103] D. Pantarotto, R. Singh, D. McCarthy, M. Erhardt, J.-P. Briand, M. Prato et al., "Functionalized carbon nanotubes for plasmid DNA gene delivery," *Angewandte Chemie International Edition*, vol. 43, pp. 5242–5246, 2004.
- [104] D. Cai, M. M. Jennifer, Z.-H. Qin, Z. Huang, J. Huang, T. C. Chiles et al., "Highly efficient molecular delivery into mammalian cells using carbon nanotube spearing," *Nature Methods*, vol. 2, pp. 449–454, 2005.
- [105] L. Gao, L. Nie, T. Wan, Y. Qin, Z. Guo, D. Yang et al., "Carbon nanotube delivery of the GFP gene into mammalian cells," *ChemBioChem*, vol. 7, pp. 239–242, 2006.
- [106] Y. Liu, D.-C. Wu, W.-D. Zhang, X. Jiang, C.-B. He, T.-S. Chung et al., "Polyethyleneimine-grafted multiwalled carbon nanotubes for secure noncovalent immobilization and efficient delivery of DNA," *Angewandte Chemie International Edition*, vol. 44, pp. 4782–4785, 2005.
- [107] N. W. S. Kam and H. J. Dai, "Carbon nanotubes as intracellular protein transporters: generality and biological

- functionality," *Journal of the American Chemical Society*, vol. 127, pp. 6021–6026, 2005.
- [108] P. Cherukuri, S. Bachilo, S. Litovsky, and R. Weisman, "Near-infrared fluorescence microscopy of single-walled carbon nanotubes in phagocytic cells," *Journal of the American Chemical Society*, vol. 126, pp. 15638–15639, 2004.
- [109] Z. Yang, Y. Zhang, Y. Yang et al., "Pharmacological and toxicological target organelles and safe use of single-walled carbon nanotubes as drug carriers in treating Alzheimer disease," *Nanomedicine*, vol. 6, pp. 427–441, 2010.
- [110] K. Medepalli, B. Alphenaar, A. Raj et al., "Evaluation of the direct and indirect response of blood leukocytes to carbon nanotubes (CNTs)," *Nanomedicine*, vol. 7, pp. 983–991, 2011.
- [111] A. Maroto, K. Balasubramanian, M. Burghard, and K. Kern, "Functionalized metallic carbon nanotube devices for pH sensing," *ChemPhysChem*, vol. 8, no. 2, pp. 220–223, 2007.
- [112] I. Heller, J. Kong, K. A. Williams, C. Dekker, and S. G. Lemay, "Electrochemistry at single-walled carbon nanotubes: the role of band structure and quantum capacitance," *Journal of the American Chemical Society*, vol. 128, pp. 7353–7359, 2006.
- [113] B. L. Allen, P. D. Kichambarre, and A. Star, "Carbon nanotube field-effect-transistor-based biosensors," *Advanced Materials*, vol. 19, no. 11, pp. 1439–1451, 2007.
- [114] E. L. Gui, L. J. Li, K. Zhang, Y. Xu, X. Dong, X. Ho et al., "DNA sensing by field-effect transistors based on networks of carbon nanotubes," *Journal of the American Chemical Society*, vol. 129, pp. 14427–14432, 2007.
- [115] H. R. Byon and H. C. Choi, "Network single-walled carbon nanotube-field effect transistors (SWNT-FETs) with increased Schottky contact area for highly sensitive biosensor applications," *Journal of the American Chemical Society*, vol. 128, no. 7, pp. 2188–2189, 2006.
- [116] G. A. Zelada-Guillén, J. L. Sebastián-Avila, P. Blondeau et al., "Label-free detection of *Staphylococcus aureus* in skin using real-time potentiometric biosensors based on carbon nanotubes and aptamers," *Biosensors and Bioelectronics*, vol. 31, pp. 226–232, 2012.
- [117] A. Patlolla, B. McGinnis, and P. Tchounwou, "Biochemical and histopathological evaluation of functionalized single-walled carbon nanotubes in Swiss-Webster mice," *Journal of Applied Toxicology*, vol. 31, no. 1, pp. 75–83, 2011.
- [118] G. Liang, L. Yin, J. Zhang et al., "Effects of subchronic exposure to multi-walled carbon nanotubes on mice," *Journal of Toxicology and Environmental Health A*, vol. 73, no. 7, pp. 463–470, 2010.
- [119] S. Clichici, A. R. Biris, F. Tabaran et al., "Transient oxidative stress and inflammation after intraperitoneal administration of multiwalled carbon nanotubes functionalized with single strand DNA in rats," *Toxicology and Applied Pharmacology*, vol. 259, pp. 281–292, 2012.
- [120] X. Y. Deng, F. Wu, Z. Liu et al., "The splenic toxicity of water soluble multi-walled carbon nanotubes in mice," *Carbon*, vol. 47, no. 6, pp. 1421–1428, 2009.
- [121] D. W. Porter, A. F. Hubbs, R. R. Mercer et al., "Mouse pulmonary dose- and time course-responses induced by exposure to multi-walled carbon nanotubes," *Toxicology*, vol. 269, pp. 136–147, 2010.
- [122] A. Pietrojasti, M. Massimiani, I. Fenoglio et al., "Low doses of pristine and oxidized single-wall carbon nanotubes affect mammalian embryonic development," *ACS Nano*, vol. 5, no. 6, pp. 4624–4633, 2011.
- [123] S. J. Son, J. Reichel, B. He, M. Schuchman, and S. B. Lee, "Magnetic nanotubes for magnetic-field-assisted bioseparation, biointeraction, and drug delivery," *Journal of the American Chemical Society*, vol. 127, pp. 7316–7317, 2005.
- [124] Y.-J. Yang, X. Tao, and Q. Hou, "Mesoporous silica nanotubes coated with multilayered polyelectrolytes for pH-controlled drug release," *Acta Biomaterialia*, vol. 6, pp. 3092–3100, 2010.
- [125] I. I. Slowing, J. L. Vivero-Escoto, C. W. Wu, and V. S. Lin, "Mesoporous silica nanoparticles as controlled release drug delivery and gene transfection carriers," *Advanced Drug Delivery Reviews*, vol. 60, pp. 1278–1288, 2008.
- [126] C. W. Lu, Y. Hung, J. K. Hsiao, M. Yao, T. H. Chung, Y. S. Lin et al., "Bifunctional magnetic silica nanoparticles for highly efficient human stem cell labeling," *Nano Letters*, vol. 7, pp. 149–154, 2007.
- [127] C. A. Barnes, A. Elsaesser, J. Arkusz, A. Smok, J. Palus, and A. Lesniak, "Reproducible comet assay of amorphous silica nanoparticles detects no genotoxicity," *Nano Letters*, vol. 8, pp. 3069–3074, 2008.
- [128] C.-C. Chen, Y.-C. Liu, C.-H. Wu, C.-C. Yeh, M.-T. Su, and Y.-C. Wu, "Preparation of fluorescent silica nanotubes and their application in gene delivery," *Advanced Materials*, vol. 17, pp. 404–407, 2005.
- [129] R. Namgung, Y. Zhang, Q. L. Fang et al., "Multifunctional silica nanotubes for dual-modality gene delivery and MR imaging," *Biomaterials*, vol. 32, pp. 3042–3052, 2011.
- [130] N. G. Chopra, R. J. Luyken, K. Cherrey et al., "Boron nitride nanotubes," *Science*, vol. 269, pp. 966–967, 1995.
- [131] V. Nirmala and P. Kolandaivel, "Structure and electronic properties of armchair boron nitride nanotubes," *Journal of Molecular Structure*, vol. 817, pp. 137–145, 2007.
- [132] M. Terrones, J. M. Romo-Herrera, E. Cruz-Silva et al., "Pure and doped boron nitride nanotubes," *Materials Today*, vol. 10, pp. 30–38, 2007.
- [133] L. Lacerda, A. Bianco, M. Prato, and K. Kostarelos, "Carbon nanotubes as nanomedicines: from toxicology to pharmacology," *Advanced Drug Delivery Reviews*, vol. 58, pp. 1460–1470, 2006.
- [134] G. Ciofani, V. Raffa, A. Menciassi, and A. Cuschieri, "Boron nitride nanotubes: an innovative tool for nanomedicine," *Nano Today*, vol. 4, pp. 8–10, 2009.
- [135] G. Ciofani, V. Raffa, A. Menciassi, and A. Cuschieri, "Cytocompatibility, interactions and uptake of polyethyleneimine-coated boron nitride nanotubes by living cells: confirmation of their potential for biomedical applications," *Biotechnology and Bioengineering*, vol. 101, pp. 850–858, 2008.
- [136] D. Lahiria, F. Rouzaud, T. Richard et al., "Boron nitride nanotube reinforced polylactide-polycaprolactone copolymer composite: Mechanical properties and cytocompatibility with osteoblasts and macrophages *in vitro*," *Acta Biomaterialia*, vol. 6, pp. 3524–3533, 2010.
- [137] H. Shen, "Thermal-conductivity and tensile-properties of BN, SiC and Ge nanotubes," *Computational Materials Science*, vol. 47, pp. 220–224, 2009.
- [138] D. Golberg, X. D. Bai, M. Mitome, C. C. Tang, C. H. Zhi, and Y. Bando, "Structural peculiarities of *in situ* deformation of a multi-walled BN nanotube inside a high-resolution analytical transmission electron microscope," *Acta Materialia*, vol. 55, pp. 1293–1298, 2007.
- [139] N. P. Bansal, J. B. Hurst, and S. R. Choi, "Boron nitride nanotubes-reinforced glass composites," *Journal of the American Ceramic Society*, vol. 89, no. 1, pp. 388–390, 2006.

- [140] S. R. Choi, N. P. Bansal, and A. Garg, "Mechanical and microstructural characterization of boron nitride nanotubes-reinforced SOFC seal glass composite," *Materials Science and Engineering A*, vol. 460-461, pp. 509–515, 2007.
- [141] Q. Huang, Y. Bando, X. Xu et al., "Enhancing superplasticity of engineering ceramics by introducing BN nanotubes," *Nanotechnology*, vol. 18, no. 48, Article ID 485706, 2007.
- [142] C. Zhi, Y. Bando, C. Tang, S. Honda, K. Sato, H. Kuwahara et al., "Characteristics of boron nitride nanotube—polyaniline composites," *Angewandte Chemie International Edition*, vol. 44, pp. 7929–7932, 2005.
- [143] C. Zhi, Y. Bando, C. Tang, S. Honda, H. Kuwahara, and D. Golberg, "Boron nitride nanotubes/polystyrene composites," *Journal of Materials Research*, vol. 21, no. 11, pp. 2794–2800, 2006.
- [144] J. Ravichandran, A. G. Manoj, J. Liu, I. Manna, and D. L. Carroll, "A novel polymer nanotube composite for photovoltaic packaging applications," *Nanotechnology*, vol. 19, no. 8, Article ID 085712, 2008.
- [145] D. Golberg, Y. Bando, C. Tang, and C. Zhi, "Boron nitridenanotubes," *Advanced Materials*, vol. 19, pp. 2413–2432, 2007.
- [146] X. Chen, P. Wu, M. Rousseas, D. Okawa, Z. Gartner, A. Zettl et al., "Boron nitride nanotubes are noncytotoxic and can be functionalized for interaction with proteins and cells," *Journal of the American Chemical Society Communications*, vol. 131, pp. 890–891, 2009.
- [147] G. Ciofani, V. Raffa, A. Menciassi, and A. Cuschieri, "Cytocompatibility, interactions, and uptake of polyethyleneimine-coated boron nitride nanotubes by living cells: confirmation of their potential for biomedical applications," *Biotechnology and Bioengineering*, vol. 101, pp. 850–858, 2008.
- [148] D. Gong, C. A. Grimes, O. K. Varghese et al., "Titanium oxide nanotube arrays prepared by anodic oxidation," *Journal of Materials Research*, vol. 16, no. 12, pp. 3331–3334, 2001.
- [149] J. M. Macak, M. Zlamal, J. Krysa, and P. Schmuki, "Self-organized TiO<sub>2</sub> nanotube layers as highly efficient photocatalysts," *Small*, vol. 3, no. 2, pp. 300–304, 2007.
- [150] K. O. Awitor, S. Rafqah, G. Géranton et al., "Photocatalysis using titanium dioxide nanotube layers," *Journal of Photochemistry and Photobiology A*, vol. 199, no. 2-3, pp. 250–254, 2008.
- [151] K. Sasaki, K. Asanuma, K. Johkura et al., "Ultrastructural analysis of TiO<sub>2</sub> nanotubes with photodecomposition of water into O<sub>2</sub> and H<sub>2</sub> implanted in the nude mouse," *Annals of Anatomy*, vol. 188, no. 2, pp. 137–142, 2006.
- [152] K. Vasilev, Z. Poh, K. Kant, J. Chan, A. Michelmore, and D. Losic, "Tailoring the surface functionalities of titania nanotube arrays," *Biomaterials*, vol. 31, no. 3, pp. 532–540, 2010.
- [153] S. D. Puckett, E. Taylor, T. Raimondo, and T. J. Webster, "The relationship between the nanostructure of titanium surfaces and bacterial attachment," *Biomaterials*, vol. 31, no. 4, pp. 706–713, 2010.
- [154] I. Romana, C. Fratila, E. Vasile, A. Petre, and M.-L. Soare, "Achievement and evaluation of some ceramic nanostructured titanium oxide-layers," *Materials Science and Engineering B*, vol. 165, no. 3, pp. 207–211, 2009.
- [155] C. Yao and T. J. Webster, "Prolonged antibiotic delivery from anodized nanotubular titanium using a co-precipitation drug loading method," *Journal of Biomedical Materials Research B*, vol. 91, no. 2, pp. 587–595, 2009.
- [156] Y.-Y. Song, F. Schmidt-Stein, S. Bauer, and P. Schmuki, "Amphiphilic TiO<sub>2</sub> nanotube arrays: An actively controllable drug delivery system," *Journal of the American Chemical Society*, vol. 131, no. 12, pp. 4230–4232, 2009.
- [157] S. J. Cho, H. J. Kim, J. H. Lee et al., "Silica coated titania nanotubes for drug delivery system," *Materials Letters*, vol. 64, pp. 1664–1667, 2010.
- [158] E. Feschet-Chassot, V. Raspal, Y. Sibaud et al., "Tunable functionality and toxicity studies of titanium dioxide nanotube layers," *Thin Solid Films*, vol. 519, pp. 2564–2568, 2011.
- [159] N. Kameta, H. Minamikawa, and M. Masuda, "Supramolecular nanotubes: how to utilize the inner nanospace and the outer space," *Soft Matter*, vol. 7, pp. 4539–4561, 2011.
- [160] Y. Tang, L. Zhou, J. Li et al., "Giant nanotubes loaded with artificial peroxidase centers: self-assembly of supramolecular amphiphiles as a tool to functionalize nanotubes," *Angewandte Chemie International Edition*, vol. 49, pp. 3920–3924, 2010.
- [161] A. Wakasugi, M. Asakawa, M. Kogiso et al., "Organic nanotubes for drug loading and cellular delivery," *International Journal of Pharmaceutics*, vol. 413, pp. 271–278, 2011.
- [162] N. J. Meilander, M. K. Pasumarty, T. H. Kowalczyk, M. J. Cooper, and R. V. Bellamkonda, "Sustained release of plasmid DNA using lipid microtubules and agarose hydrogel," *Journal of Controlled Release*, vol. 88, no. 2, pp. 321–331, 2003.
- [163] X. Yan, Q. He, K. Wang, L. Duan, Y. Cui, and J. Li, "Transition of cationic dipeptide nanotubes into vesicles and oligonucleotide delivery," *Angewandte Chemie International Edition*, vol. 46, pp. 2431–2434, 2007.
- [164] W. Ding, M. Wada, N. Kameta et al., "Functionalized organic nanotubes as tubular nonviral gene transfer vector," *Journal of Controlled Release*, vol. 156, pp. 70–75, 2011.

## Research Article

# Biocompatibility of Nanoporous TiO<sub>2</sub> Coating on NiTi Alloy Prepared via Dealloying Method

Jin Huang,<sup>1</sup> Junqiang Wang,<sup>1</sup> Xiangdong Su,<sup>2</sup> Weichang Hao,<sup>2</sup> Tianmin Wang,<sup>2</sup> Yayi Xia,<sup>3</sup> Guozu Da,<sup>4</sup> and Yubo Fan<sup>1</sup>

<sup>1</sup> Key Laboratory for Biomechanics and Mechanobiology of Ministry of Education, School of Biological Science and Medical Engineering, Beihang University, Beijing 100191, China

<sup>2</sup> Center of Material Physics and Chemistry, Beihang University, Beijing 100191, China

<sup>3</sup> Orthopedic Institute and The Second Hospital of Lanzhou University, Lanzhou 730030, China

<sup>4</sup> Research Division, Gansu Seemine Material High-Tech Co. Ltd., Lanzhou 730030, China

Correspondence should be addressed to Weichang Hao, cmpe@buaa.edu.cn and Yubo Fan, yubofan@buaa.edu.cn

Received 2 March 2012; Accepted 30 March 2012

Academic Editor: Xiaoming Li

Copyright © 2012 Jin Huang et al. This is an open access article distributed under the Creative Commons Attribution License, which permits unrestricted use, distribution, and reproduction in any medium, provided the original work is properly cited.

This paper investigated the biocompatibility of nanoporous TiO<sub>2</sub> coating on NiTi shape-memory alloy (SMA) prepared via dealloying method. Our previous study shows that the dealloying treatment at low temperature leads to 130 nm Ni-free surface titania surface layer, which possesses good bioactivity because of the combination of hydroxyl (OH<sup>-</sup>) group in the process of dealloying treatment simultaneously. In this paper, the biological compatibility of NiTi alloy before and after dealloying treatment was evaluated and compared by direct contact method with dermal mesenchymal stem cells (DMSCs) by the isolated culture way. The interrelation between the biological compatibility and surface change of material after modification was systematically analyzed. As a consequence, the dealloying treatment method at low temperature could be of interest for biomedical application, as it can avoid sensitization and allergies and improve biocompatibility of NiTi shape-memory alloys. Thus it laid the foundation of the clinical trials for surface modification of NiTi memory alloy.

## 1. Introduction

Nowadays, nickel-titanium (NiTi) shape-memory alloy (SMA) becomes one of important biomedical metal materials because of its special shape-memory effect, the hyperelasticity, and excellent biocompatibility [1, 2]. However, NiTi alloy containing high-concentration nickel (atomic ratio at 50%) can have a large number of nickel ions dissolved out after corrosion; especially in body fluid containing chlorine ion, point corrosion-resistant performance is not ideal, which will cause larger chronic host negative response, such as sensitization, teratogenicity, and even carcinogenic change [3]. These negative properties make NiTi alloy in the body of safety questioned, and patients are worried, which become one of the obstacles for NiTi alloy biomedical application. In view of the above questions, researchers have done a lot of work, the use of physical, chemical, and electrochemical, and so forth diversified method on NiTi shape-memory alloy surface modification [4, 5]. Recently

our research team have used dealloying technology at low temperature to realize the surface Ni ions removal and obtained the titanium oxide of porous structure on the surface [6–10]. Li et al. studies show that the formation of the porous structure is beneficial to cell compatibility [11, 12]. The nanoporous surface can obviously improve the cellular compatibility [13].

Stem cell with the capacity of quick proliferation and itself renewal can be differentiated into many different target cells, and its potential of multilineage differentiation brought new chance for biological tissue engineering [11, 14–16]. Dermal mesenchymal stem cells (DMSCs) as a part of the stem cells, compared with other mesenchymal stem cells, are characterized by drawing materials conveniently, unrestricted position, and the advantages of fast growth and renewal; yet they are able to keep those characteristics in vitro culture. Jean et al. have confirmed dermal sources of stem cells with differentiation potential to be the fat, cartilage,

and bone, which starts the important role of dermal stem cells in the connective tissue repair for recognizing [17–22]. In this paper, first of all, the dermal stem cells were separated and subcultured by the traditional program successfully, then used direct contact method to the evaluation and comparison of NiTi alloy biological compatibility with that before and after dealloying treatment and performed a systematic analysis of the relationship between the nature change of material surface after modification and the biological compatibility. Thus it is laid the foundation of the clinical trials for surface modification of NiTi SMA.

## 2. Experiments

**2.1. Dealloying NiTi Alloy.** NiTi shape-memory alloy performance for experiment reaches the country demanding on “using NiTi shape memory alloy to processing material standard in medical equipment and surgical implants”; the alloy components are Ni: 50.7% and Ti: 49.3%. Sample was processed into  $20\text{ mm} \times 10\text{ mm} \times 2\text{ mm}$ , grinded and polished gradually with metallographic sand paper from  $400\times$  to  $1200\times$ , and then put, respectively, into acetone and anhydrous alcohol with ultrasonic cleaning. The 200 mL self-developed dealloying treatment liquid (a typical formula as follows: nitro diethyl phthalate :  $\text{H}_2\text{O}_2$  : HCl :  $\text{H}_2\text{SO}_4 = 4:1:2:3$ , volume ratio) was held in the beaker with sample and stirred at  $50^\circ\text{C}$ , low temperature for 15 h. The sample was taken out to clean with deionized water and dry. The dealloyed sample was heated treatment at  $400^\circ\text{C}$  for an hour and prepared for use.

**2.2. Structure Characterization.** Nano Indenter DCM system test analyzed mechanical performance to be on submicron scale on the surface of NiTi memory alloy, taken off the nickel by process of dealloying. Test adopted the pyramid pressure head and pressed in the maximum depth of 500 nm. The maximum load was 500 mN, but the displacement and loading precision are 0.01 nm and 50 nN, respectively. The place of 70% maximum load maintained 60 s of the thermal drift correction after unloading. The Oliver and Pharr method was used to calculate H and E value.

**2.3. Cellular Compatibility Experiments.** The New Zealand rabbit, 2–5 days old, was twisted off neck to lead to death and was put on asepsis platform after body disinfection with 75% alcohol. After clipping the whole layer of the backside skin, we removed the subcutaneous tissue by sterile blade and operated separation dermis by the mechanical method (biopsy). DMSCs were separated and subcultured by the traditional program successfully. DMSCs in passage 3 were seeded at a final concentration of  $1 \times 10^5$  cells per mL to the glass slides coated with polylysine in a 6-well plate. Cells detected positively of Vimentin, cytokeratin, nestin, CD34, and FVIII factors by the SABC method were considered as DMSCs.

The NiTi memory alloy after surface treatment by crystallization at  $400^\circ\text{C}$  for 1.5 h was group A, the untreated alloy was group B, and pure DMSCs was control group.

The sample specifications of NiTi memory alloy were width 10 mm, length 15 mm, and height 2 mm, then 40 pieces sample of group B or 40 pieces sample of group A, and DMSCs were developed together in vitro. Compared with the control group, NiTi memory allos from group A and B were put on the preset against taking off microslides within 12-well plate, respectively. Every hole was covered by cell suspension with the same volume and density. DMSCs were counted by the flow cytometry, and cell growth curves were drawn after cell growth situation was observed for 1 d, 5 d, and 8 d. The hydroxyproline and alkaline phosphatase of cells with group A or B were measured for 1 d, 5 d, 8 d (the kit was provided by the Nanjing Jiancheng Biotechnology Company). The content of nickel ion in cell culture medium. The content of nickel ions in cell culture medium from three groups was determined by AA-800 type graphite furnace atomic absorption spectrophotometer.

## 3. The Results and Discussion

**3.1. Porous Structure and Properties of  $\text{TiO}_2$  Coating.** The surface morphology of NiTi alloy after the different treatment time via amino oxidation method at  $55^\circ\text{C}$  is shown as Figure 1. It clearly shows that NiTi memory alloy began gradually to form the porous structure in the dealloying process for 4 h, at last in the porous alloy surface won a porous nanogrid structure, which is a typical characteristics after dealloying. The grid structure is constituted by the rest undissolved element after one-element selectivity dissolution from the alloy components. XRD research shows that because of the thinner membrane formation after dealloying the diffraction peak of alloy substrate phase remained predominant, but having the titanium dioxide diffraction peak of faint sharp titanium ore phase and rutile phase appeared after processing, then surface formed the titanium oxide.

Figure 2 shows mechanical properties of NiTi alloy after dealloying. We can see that the elastic modulus of 120 nm depth frontal film is lower, and the elastic modulus of 50 nm depth frontal film is lower than 20 GPa, which is almost equal to the elastic modulus of human body cortical bone. Hence, this layer film with low modulus of elasticity will benefit to weaken stress shelter effect from alloy in the course of the bone tissue growth. The elastic modulus of 120 nm depth has already reached the highest 71 GPa, after that basically remained level, which illustrates that it is already the elastic modulus value of matrix NiTi austenitic parent phase. The nanohardness-displacement change on the surface layer of test sample is seen Figure 2(b). It can be seen that the nanohardness of alloy increases gradually from the exterior to the interior and mutations does not appear, beginning to appear slow flat after a depth of about 300 nm and a maximum value 4.7 GPa. From the outside to the inside, hardness value with the slow continuous increase the gradient transition is between that membrane layer, and matrix, and the stress is smaller with good combination. In the load-displacement curve as shown in Figure 2(c), both loading curve and unloading curve are nonlinear, then the

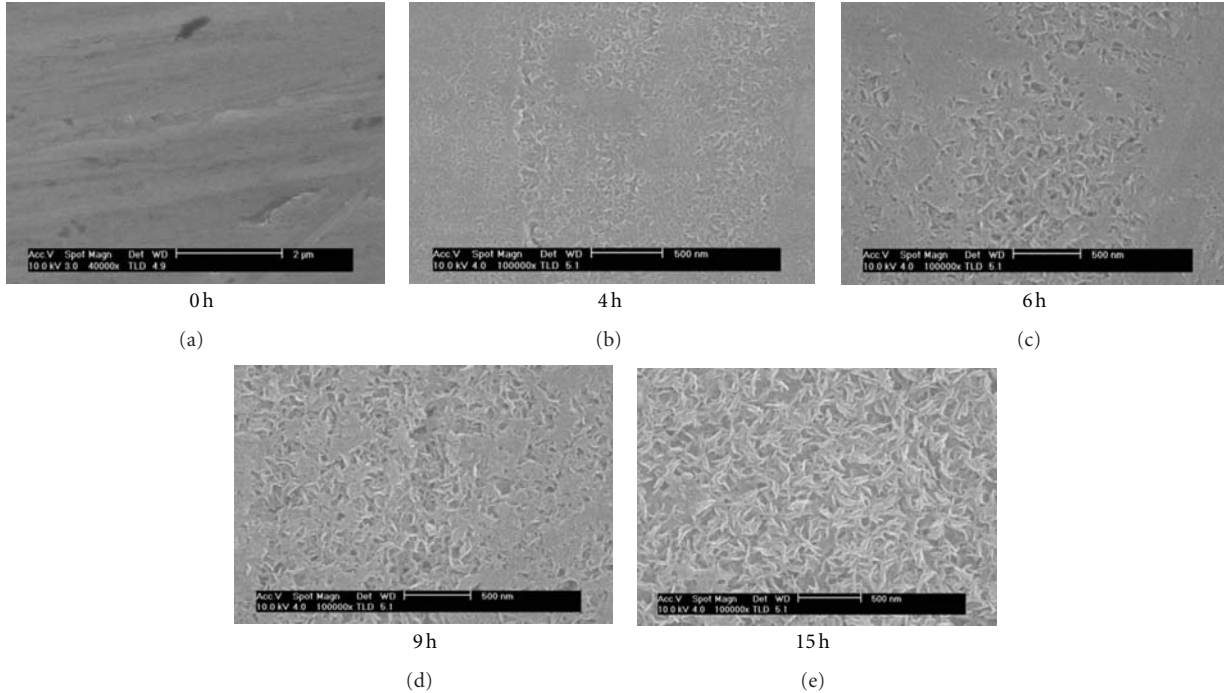


FIGURE 1: SEM images of the surface morphologies of NiTi alloy dealloyed for 0 h, 4 h, 6 h, 9 h, and 15 h.

maximal displacement of the pressure head including both elasticity and plastic deformation parts, while unloading produces elastic recovery and elastic recovery reaches 44.4%, the residual displacement depends on the elastic deformation mainly, which shows obvious characteristics of ceramic material. Electrochemical test results in Hank's simulation body solution ( $\text{pH} = 7.45$ ) are shown in Figure 3. Compared to the NiTi memory alloys without surface treatment, the self-corrosion potential of dealloying NiTi sample gets bigger enhancement from 0.05 V to 0.92 V.

### 3.2. Cells Compatibility

**3.2.1. Cell Proliferation.** DMSCs grow well in control group, but DMSCs cultured in groups A and B have difference forms as shown in Figure 4. DMSCs in group A have uniform, long fusiform and their cytoplasm is abundant, then cell culture flask is almost full of DMSCs after two days, which is close to control groups. However, most of the DMSCs in group B are polygonal, with significant morphological differences and less cytoplasm. In Figure 5, the amount of DMSCs increases sharply in two days and begins to reduce after two days gradually; moreover all data are significantly less than those of control group or group A which have less influence on DMSCs proliferation.

**3.2.2. Determination of Hydroxyproline and Alkaline Phosphatase in Cell Culture Medium.** *Hydroxyproline content analysis results as Table 1 shows.* The content of hydroxyproline in the culture medium of group B reduced gradually, which has close relationship to DMSCs growth. It shows that cell growth is slow, so absorption of hydroxyproline is also

TABLE 1: The content of hydroxyproline in cell culture medium (mg/L).

Group	Initial content	1 d	5 d	8 d
B	20.00	12.07 + 0.13	11.40 + 0.08	6.47 + 0.04
		39.6%	43%	67.6%
A	20.00	5.34 + 0.21	2.89 + 0.29	2.51 + 0.35
		73.3%	85.5%	87.5%

slow which led to the content decrease slow. However, the content of hydroxyproline in group A declined dramatically, which shows that cell growth is quick. The decrease of hydroxyproline results from its consumption of the collagen synthesis process.

*The results of alkaline phosphatase content analysis as Table 2 shows.* The content of alkaline phosphatase in the culture medium of group A declined gradually, and in the culture medium of group B the content of alkaline phosphatase also gradually declined, but all data of group B are lower than those of group A, because, after the surface modification the NiTi memory alloy is the slow release of the nickel ions which have less influence on cell metabolism.

**3.2.3. Determination of Nickel Ions in Cell Culture Medium.** As indicated in Table 3, the content of nickel ions release in cell culture medium increases with time; the amount of nickel ion in group A after 5 days is greatly below the amount of group B. The change is slight after 8 days, and the incremental quantity is smaller. In addition, in cell culture medium of group B, the concentration of nickel ion is about 3.7 times higher than that of the group A significantly after

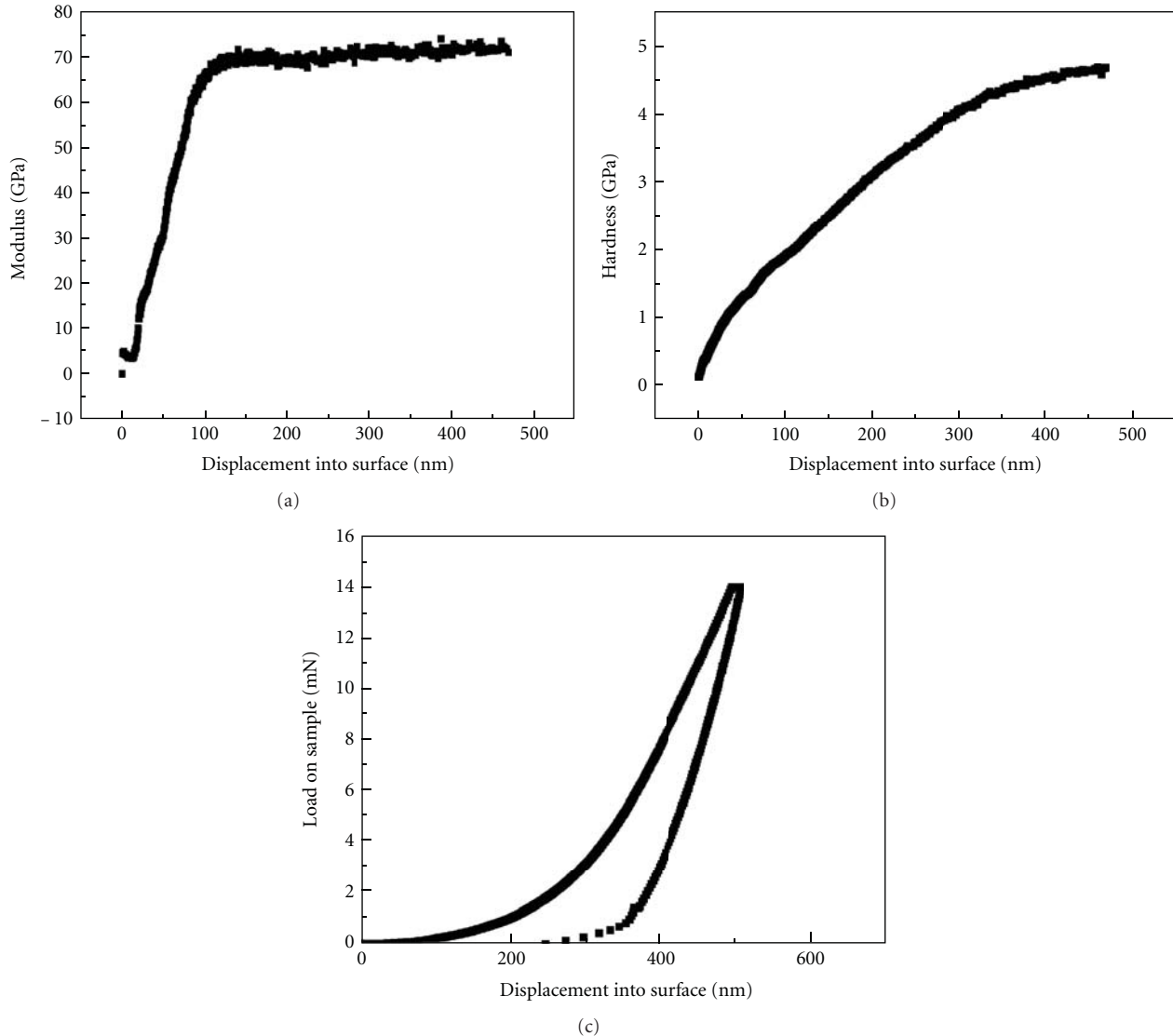


FIGURE 2: NiTi memory alloy surface dealloying and surface nanocreasing test.

TABLE 2: The content of alkaline phosphatase in culture medium (U/g prot).

AKP	1 d	5 d	8 d
Group A	8.35 + 0.62	5.71 + 0.43	4.25 + 1.30
Group B	7.06 + 1.13	4.27 + 1.09	3.61 + 1.52

5 days, which is a leading cause of affecting cell proliferation. The much more nickel ions from NiTi shape-memory alloy in group B may occur in corrosion within the body and have biological system damage on the body.

**3.3. Discussion.** After calculated the dealloying conditions of thermodynamics, a dealloying treatment method was applied to nearly equiatomic NiTi alloy so as to remove the harmful element of nickel selectively from NiTi alloys and form a Ni-free titanium oxide layer on the surface [23]. The results show that the dealloying treatment at

TABLE 3: The content of nickel ions in cell culture medium (ng/mL).

Group	Time		
	1 d	5 d	8 d
Group A	28.7	46.8	50
Group B	31.1	173	177.5
Control	1.97	1.97	1.97

low temperature leads to 130 nm Ni-free surface layer that possesses a nanometer structure and in situ formation of titania surface that possesses a degree of bioactivity because of the combination of hydroxyl ( $\text{OH}^-$ ) group in the process of dealloying treatment simultaneously. This dealloying treatment can avoid sensitization and allergies and improve biocompatibility of NiTi shape-memory alloys. It will be a good news to biomedical application. DMSCs can timely, accurately reflect the early nickel ions adverse effects which are the influence of growth and cell metabolism

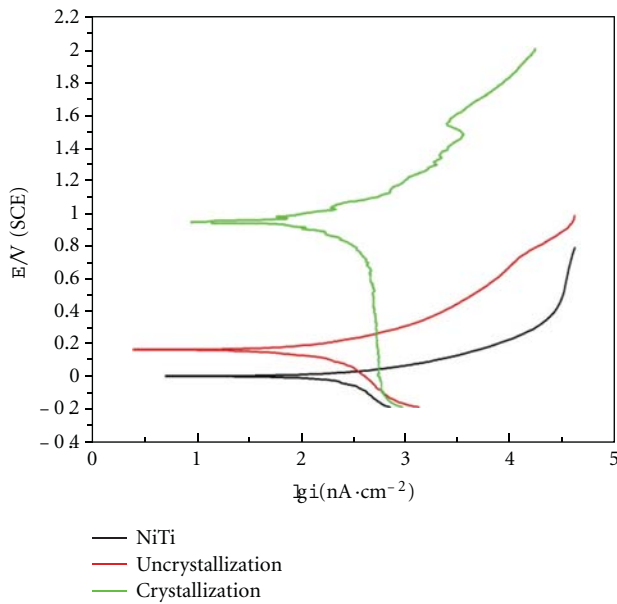


FIGURE 3: Electrokinetic potential polarization curve of NiTi after dealloying treatment in Hank's simulation body fluids ( $\text{pH} = 7.45$ ) and crystallization in  $500^\circ\text{C}$  for 1 h.

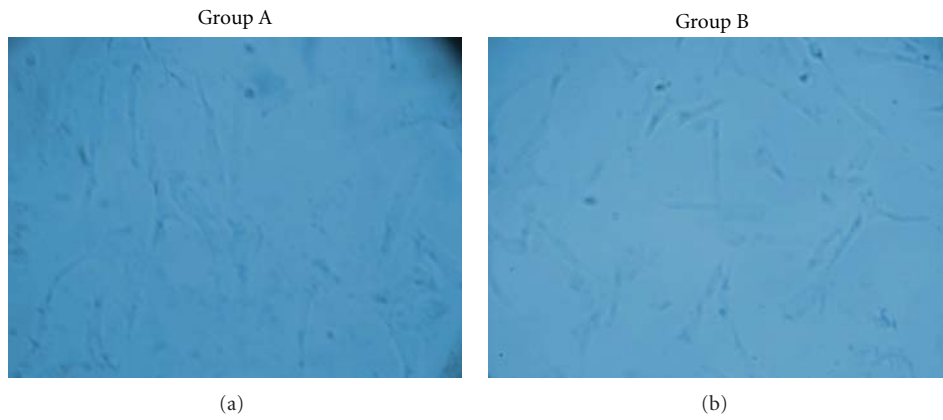


FIGURE 4: NiTi memory alloy and DMSCs culture in vitro.

nickel ions give to. The NiTi memory alloys after surface modification or without surface modification and leather stem cells in culture in vitro observe the influence on leather stem cells and determin concentration of nickel ions, the content of hydroxyproline and alkaline phosphatase in cell culture medium, thus compare the cell compatibility difference between surface modified NiTi memory alloy and NiTi memory alloy without surface modification.

From cell count detection result in the incubation, logarithmic growth, and the platform period of the cells, NiTi memory alloy without the surface modification does have influence on the proliferation of the cells, but the NiTi memory alloy after surface modification reduced greatly the influence of cell proliferation. The content of alkaline phosphatase in cell culture medium of group A declined gradually and in group B has same trend, but all of values are below those of group A. The pure  $\text{TiO}_2$  coating free of nickel ions within the hundreds of nanometers of surface of NiTi memory alloy after surface modification blocked the

diffusion of nickel ions in the alloy matrix. The low level of nickel ions in cell culture medium has less effect on cell metabolism. It has been proved that the NiTi memory alloy after surface modification at low temperature process can effectively prevent the spread, dissolution, and release of the nickel ions.

Hydroxyproline is the main raw material of collagen synthesis in cells, so the number of hydroxyproline can reflect the collagen synthesis. In the cell culture medium of group B, the content of hydroxyproline is slow decline, which is in proportion to cell growth to explain the slow growth of cells and less collagen synthesis. So the slow absorption of hydroxyproline in culture liquids results in hydroxyproline content dropping gradually. The level of hydroxyproline in group A dropped sharply; it shows the rapid growth of cells and the more amount of collagen, which also prove the fact that the modified surface can effectively improve the tissue compatibility of alloy.

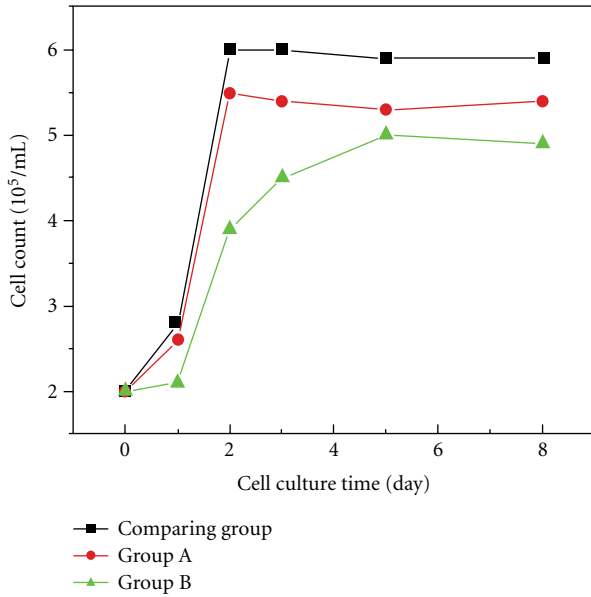


FIGURE 5: Flow cytometric cell count analysis.

## 4. Conclusions

Nanoporous TiO<sub>2</sub> coatings on NiTi alloy were prepared via dealloying method. The hydroxyl (OH<sup>-</sup>) group was introduced into the surface of TiO<sub>2</sub> during the process of dealloying treatment simultaneously. The direct contact method was used for the evaluation and comparison of biological compatibility between NiTi alloy and samples after dealloying treatment. Research results indicate that the dealloying treatment method at low temperature could be of interest for biomedical application, as it can avoid sensitization and allergies and improve biocompatibility of NiTi shape memory alloys. This paper led to the foundation of the clinical trials for surface modification of NiTi memory alloy.

## Acknowledgments

The word is changed into "This work was financially supported by the National Basic Research Program of China (973 program, 2011CB710901), the National Natural Science Foundation of China (Grants no. 11120101001, 10925208, 51072012), and the Fundamental Research Funds for the Central Universities (Grant no. YWF-1-03 Q- 079).

## References

- [1] J. Ryhanen, M. Kallioinen, J. Tuukkanen et al., "In vivo biocompatibility evaluation of nickel-titanium shape memory metal alloy: muscle and perineural tissue responses and encapsule membrane thickness," *Journal of Biomedical Materials Research*, vol. 41, no. 3, pp. 481–488, 1998.
- [2] J. Ryhanen, E. Niemi, W. Serlo et al., "Biocompatibility of nickel-titanium shape memory metal and its corrosion behavior in human cell cultures," *Journal of Biomedical Materials Research*, vol. 35, no. 4, pp. 451–457, 1997.
- [3] J. Ryhanen, M. Kallioinen, W. Serlo et al., "Bone healing and mineralization, implant corrosion, and trace metals after nickel-titanium shape memory metal intramedullary fixation," *Journal of Biomedical Materials Research*, vol. 47, no. 4, pp. 472–480, 1999.
- [4] Q. Li, Y. Zeng, and X. Tang, "The applications and research progresses of nickel-titanium shape memory alloy in reconstructive surgery," *Australasian Physical and Engineering Sciences in Medicine*, vol. 33, no. 2, pp. 129–136, 2010.
- [5] Q. Li, Y. Y. Xia, J. C. Tang, R. Y. Wang, C. Y. Bei, and Y. Zeng, "In vitro and in vivo biocompatibility investigation of diamond-like carbon coated nickel-titanium shape memory alloy," *Artificial Cells, Blood Substitutes, and Biotechnology*, vol. 39, no. 3, pp. 137–142, 2011.
- [6] X. Su, R. Lin, W. Hao, and T. Wang, "Molybdenum disilicide oxidation protective coating for silicon carbide heating element at high-temperature condition," *Rare Metal Materials and Engineering*, vol. 35, no. 1, pp. 123–126, 2006.
- [7] X. D. Su, T. M. Wang, W. C. Hao, and L. He, "Electrolytic passivation of nitinol shape memory alloy in different electrolytes," *Chinese Journal of Aeronautics*, vol. 19, supplement 11, pp. S113–S118, 2006.
- [8] P. Dong, W. Hao, X. Wang, and T. Wang, "Fabrication and biocompatibility of polyethyleneimine/heparin self-assembly coating on NiTi alloy," *Thin Solid Films*, vol. 516, no. 16, pp. 5168–5171, 2008.
- [9] X. D. SU, W. Tianmin, H. Weichang et al., "Characterisation of oxide layer formed on NiTi alloy by anodic oxidation in a molybdate electrolyte," in *Proceedings of the 6th International Conference on Materials Processing for Properties and Performance*, Beijing, China, 2007.
- [10] P. Dong, L. Yuan, W. Hao, Y. Xia, G. Da, and T. Wang, "Biocompatibility of chitosan/heparin multilayer coating on NiTi alloy," *Materials Science Forum*, vol. 610-613, pp. 1179–1182, 2009.
- [11] X. M. Li, H. Liu, H. F. Liu et al., "Osteogenic differentiation of human adipose-derived stem cells induced by osteoinductive calcium phosphate ceramics," *Journal of Biomedical Materials Research*, vol. 97, no. 1, pp. 10–19, 2011.
- [12] X. Li, C. A. van Blitterswijk, Q. Feng, F. Cui, and F. Watari, "The effect of calcium phosphate microstructure on bone-related cells in vitro," *Biomaterials*, vol. 29, no. 23, pp. 3306–3316, 2008.
- [13] T. J. Webster and J. U. Ejiofor, "Increased osteoblast adhesion on nanophasic metals: Ti, Ti6Al4V, and CoCrMo," *Biomaterials*, vol. 25, no. 19, pp. 4731–4739, 2004.
- [14] Y. Huang, G. Zhou, L. Zheng, H. Liu, X. Niu, and Y. Fan, "Micro-/Nano-sized hydroxyapatite directs differentiation of rat bone marrow derived mesenchymal stem cells towards an osteoblast lineage," *Nanoscale*, vol. 4, no. 7, pp. 2484–2490, 2012.
- [15] X. Liu, X. Li, Y. Fan et al., "Repairing goat tibia segmental bone defect using scaffold cultured with mesenchymal stem cells," *Journal of Biomedical Materials Research*, vol. 94, no. 1, pp. 44–52, 2010.
- [16] X. M. Li, H. F. Liu, X. F. Niu et al., "The use of carbon nanotubes to induce osteogenic differentiation of human adipose-derived MSCs *in vitro* and ectopic bone formation *in vivo*," *Biomaterials*, vol. 33, no. 19, pp. 4818–4827, 2012.
- [17] V. Juniantito, T. Izawa, T. Yuasa et al., "Immunophenotypical analyses of myofibroblasts in rat excisional wound healing: possible transdifferentiation of blood vessel pericytes and perifollicular dermal sheath cells into myofibroblasts," *Histology and Histopathology*, vol. 27, no. 4, pp. 515–527, 2012.

- [18] L. Po, Q. Shaohai, S. Bin, X. Julin, X. Yingbin, and L. Xusheng, “Experimental study on dermal papillary cells improving vascularization of tissue engineered skin substitutes,” *Chinese Journal of Reparative and Reconstructive Surgery*, vol. 26, no. 2, pp. 135–140, 2012.
- [19] K. Kizjakina, J. M. Bryson, G. Grandinetti, and T. M. Reineke, “Cationic glycopolymers for the delivery of pDNA to human dermal fibroblasts and rat mesenchymal stem cells,” *Biomaterials*, vol. 33, no. 6, pp. 1851–1862, 2012.
- [20] H. Yamanishi, S. Fujiwara, and T. Soma, “Perivascular localization of dermal stem cells in human scalp,” *Experimental Dermatology*, vol. 21, no. 1, pp. 78–80, 2012.
- [21] J. G. Toma, M. Akhavan, K. J. L. Fernandes et al., “Isolation of multipotent adult stem cells from the dermis of mammalian skin,” *Nature Cell Biology*, vol. 3, no. 9, pp. 778–784, 2001.
- [22] K. J. L. Fernandes, I. A. McKenzie, P. Mill et al., “A dermal niche for multipotent adult skin-derived precursor cells,” *Nature Cell Biology*, vol. 6, no. 11, pp. 1082–1093, 2004.
- [23] X. D. Su, Y. l. Huang, W.C. Hao, T. M. Wang et al., “Surface characteristics of NiTi alloys modified by dealloying at low temperature,” *Rare Metal Materials and Engineering*, vol. 40, no. 8, pp. 1446–1449, 2011.

## Research Article

# Noninvasive Evaluation of Injectable Chitosan/Nano-Hydroxyapatite/Collagen Scaffold via Ultrasound

**Yan Chen,<sup>1</sup> Songjian Li,<sup>2</sup> Xiaoming Li,<sup>3</sup> Yichen Zhang,<sup>2</sup> Zhi Huang,<sup>4</sup> Qingling Feng,<sup>5</sup> Zhilai Zhou,<sup>2</sup> Bomiao Lin,<sup>6</sup> and Bo Yu<sup>2</sup>**

<sup>1</sup> Department of Ultrasonic Diagnosis, Zhujiang Hospital of Southern Medical University, Guangzhou 510282, China

<sup>2</sup> Department of Orthopedics, Zhujiang Hospital of Southern Medical University, Guangzhou 510282, China

<sup>3</sup> Key Laboratory for Biomechanics and Mechanobiology of Ministry of Education, School of Biological Science and Medical Engineering, Beihang University, Beijing 100191, China

<sup>4</sup> School of Geosciences and Info-Physics, Central South University, Changsha 410083, China

<sup>5</sup> State Key Laboratory of New Ceramic and Fine Processing, Tsinghua University, Beijing 100084, China

<sup>6</sup> Department of Radiology, Zhujiang Hospital of Southern Medical University, Guangzhou 510282, China

Correspondence should be addressed to Xiaoming Li, x.m.li@hotmail.com and Bo Yu, gzyubo@gmail.com

Received 1 March 2012; Accepted 3 April 2012

Academic Editor: Shuming Zhang

Copyright © 2012 Yan Chen et al. This is an open access article distributed under the Creative Commons Attribution License, which permits unrestricted use, distribution, and reproduction in any medium, provided the original work is properly cited.

To meet the challenges of designing an *in situ* forming scaffold and regenerating bone with complex three-dimensional (3D) structures, an *in situ* forming hydrogel scaffold based on nano-hydroxyapatite (nHA), collagen (Col), and chitosan (CS) was synthesized. Currently, only a limited number of techniques are available to mediate and visualize the injection process of the injectable biomaterials directly and noninvasively. In this study, the potential of ultrasound for the quantitative *in vivo* evaluation of tissue development in CS/nHAC scaffold was evaluated. The CS/nHAC scaffold was injected into rat subcutaneous tissue and evaluated for 28 days. Quantitative measurements of the gray-scale value, volume, and blood flow of the scaffold were evaluated using diagnostic technique. This study demonstrates that ultrasound can be used to noninvasively and nondestructively monitor and evaluate the *in vivo* characteristics of injectable bone scaffold. In comparison to the CS, the CS/nHAC scaffold showed a greater stiffness, less degradation rate, and better blood supply in the *in vivo* evaluation. In conclusion, the diagnostic ultrasound method is a good tool to evaluate the *in vivo* formation of injectable bone scaffolds and facilitates the broad use to monitor tissue development and remodeling in bone tissue engineering.

## 1. Introduction

Each year, more than a million people worldwide require bone grafts to create or repair bone. Currently, autografts are the gold-standard treatment to replace or augment bone. However, because autografts must be taken from a separate donor site on the patient's body and, therefore, require two surgical procedures, there is a limited supply of available bone as well as serious risk of donor-site pain, infection, and bleeding. To overcome these issues, there is a significant clinical need to develop alternatives to autografts and allografts for bone grafting procedures. From a clinical perspective, the use of injectable scaffolds is very attractive as it minimizes patient discomfort, risk of infection, scar formation, and the cost of treatment [1].

These scaffolds are liquid before and during the injection, but they undergo gelation *in situ*, during the procedure of surgery, allowing them to fill in a bone defect of any shape. Chitosan is currently seen as a promising biodegradable biomaterial, while  $\beta$ -glycerophosphate (GP) is a well-known biocompatible agent [2–4]. The chitosan solution with GP salts possesses a physiological pH and can be held liquid below room temperature for encapsulating living cells and therapeutic proteins [5–7]. Recent studies have demonstrated the application of the C/GP hydrogel as an injectable scaffold for tissue engineering [8–11].

Bone is mainly composed of nano-hydroxyapatite and collagen fibers, in which the *c*-axes of the HA are regularly aligned along the collagen fibers [12–14]. While considerable effort has gone into determining the relationship between

collagen structure and mineral orientation, synthetic recreation of this most fundamental level of bone structure has eluded the materials engineer seeking to fabricate bone-like composites. It would be desirable to mimic both the composition and structure of bone for synthetic bone graft substitutes [15–17]. Biomimetic bone materials can be used in conjunction with natural bone, to induce new bone tissue formation and promote bone remodeling. At present this is the most promising route for the repair of defects in natural bone [18–22]. The ideal bone scaffold should promote early mineralization and support new bone formation while at the same time allowing for replacement by new bone. A bone-like nano-hydroxyapatite/collagen (nHAC) composite by mineralizing type 1 collagen seems to be a very promising system for bone reconstructive or regenerative surgery. In our preliminary study, a new type of thermosensitive material based on CS, HA, and Col was fabricated with a biomimetic strategy. NHAC uniformly dispersed in the chitosan matrix and this CS/nHAC composite showed some features of natural bone. Thus, the CS/nHAC scaffolds have shown to possess promising physicochemical and biological properties for use in bone tissue engineering approaches [23–26].

In the field of tissue engineering, there is a growing need for quantitative methods to analyze *in situ* and in real time the tissue development in three-dimensional scaffolds. Ultrasound is a well-known noninvasive and nondestructive imaging method [27–30]. The goal of the current study was to demonstrate the utility of ultrasound as a noninvasive, nondestructive tool to evaluate the *in vivo* development of the CS/nHAC scaffold under subcutaneous implantation on the back of rats for the period of 4 weeks.

## 2. Materials and Methods

**2.1. Materials.** Medical grade type 1 collagen powder was purchased from YierKang Company (China), medical grade chitosan (Mw 250000 and a degree of deacetylation of 95.6%) was provided by Shandong AKBiotech Ltd (China), and  $\beta$ -glycerophosphate (GP,  $C_3H_7Na_2O_6P$ ) was from Sigma (USA). The water used in the experiments was triply distilled.

**2.2. Preparation of CS/nHAC and CS.** The CS/nHAC composite was prepared by the procedure reported previously. Firstly, nHAC powder was synthesized by self-assembly of nanofibrils of mineralized collagen and sterilized by  $\gamma$ -ray irradiation (1.5 Mrad). Secondly, chitosan (2 g) was dissolved in hydrochloric acid solution (98 mL, 0.1 M). Thirdly, the nHAC powder was added to the chitosan solution (0.02 g/mL) with the ratio of 1 : 1 in weight. Finally, the pH of the CS/nHAC solution was adjusted to 7.0 by adding droplets of  $\beta$ -glycerophosphate solution (30% (w/v)).

The CS was prepared similar to the procedure of CS/nHAC. Chitosan (2 g) was dissolved in hydrochloric acid solution (98 mL, 0.1 M), and then the pH of the CS solution was adjusted to 7.0 by adding droplets of  $\beta$ -glycerophosphate solution [30% (w/v)]. The samples for biological tests were

prepared in line with the aseptic technique in an aseptic manipulation cabinet.

**2.3. Implantation Experiments in Rats.** All the animals were operated according to the guidelines for animal experiments. In this study, ten female Wistar rats (average body weight 300 g) were carried out under general gas anesthesia strictly following a protocol approved by the Southern medical University Institutional Animal Care and Use Committee. Anesthesia consisted of 1% isoflurane delivered via facemask. The solutions were prepared by gently mixing 1 mL of CS and nHAC. A 1 mL syringe with a 26-gauge needle was used to inject the solution into the subcutaneous dorsum of a rat.

**2.4. Ultrasound Image.** The implants were imaged using an ALOKA prosound  $\alpha$ -10 premier diagnostic ultrasound system with a 12 MHz transducer using the following parameters: a dynamic range of 55, a mechanical index of 1.1, a gain of 80, and a depth of 3 cm. Images were taken at 1 h, 14 days, and 28 days after injection. Anesthetized rats were laid in the supine position, and an ultrasound transducer was positioned on the surface of the back. Images were taken always with the same settings (contrast: 50%, brightness 40%, and zoom: 100%) at different time point. At each time point, five images from the scaffolds in each group were stored. The images were transferred to an offline computer (Q-lab, Philips Medical Systems) to measure the gray-scale value (GV) intensity. A region of interest (ROI) was set to encompass the entire scaffold. Next, the ultrasound system was set to color Doppler to detect the blood flow surround the scaffold.

**2.5. Image Analysis.** Ultrasound images are the visualization of the backscattered signal that arises due to the difference in mechanical impedance between different materials and phases. The backscattered signal is displayed as a gray-scale array with values ranging from 0 to 256, with 0 indicating a negligible difference in impedance from the surrounding media; the development of an ultrasound signal over time was interpreted as an increase in stiffness that may due to the solidify development of the scaffold. The gray-scale value (GV) was analyzed by measuring the mean GV of the implants over time by the method of histogram echo intensity. The measurements from the five images were averaged together for each implant. Implant volume was determined *in vivo* from the images of the total area of the scaffold. Since the images were binary, the number of implant pixels could be determined by summation of the pixels. All image analysis was performed using MATLAB.

**2.6. Statistical Analysis.** Statistical significance of differences was determined using one-way analysis of variance ANOVA. If differences were detected, pairwise comparisons were made using Turkey's HSD test at a confidence interval of 95% ( $P < 0.05$ ).

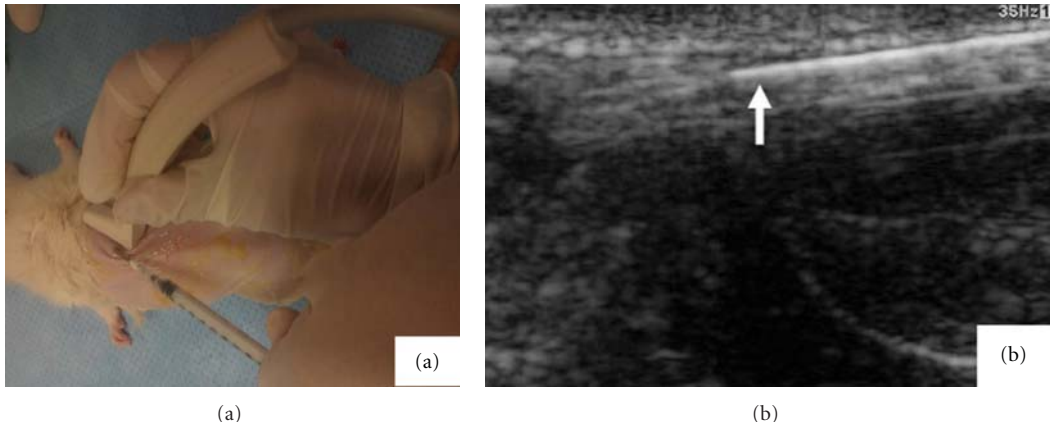


FIGURE 1: Ultrasound imaging of the injection process of the *in situ* formation of the CS and CS/nHAC gel: (a) subcutaneous injection of the CS/nHAC solution under the ultrasound transducer. (b) The injection process was monitored by ultrasound (arrow: the needle of the syringe).

### 3. Result and Discussion

Over the past decades, nano-biomaterials have played significant roles in the field of biomedical engineering and pharmaceuticals. For successful clinical applications, the investigations into biocompatibility and toxicity of nano-biomaterials are research interests of great significances. The use of diagnostic ultrasound to study the *in vivo* compatibility of injectable nano-biomaterials is a novel means in a noninvasive, nondestructive manner. The primary advantage of this technique is the real-time visualization of the implant formation process. Long-term information regarding formation and degeneration behavior for the same implant over time can be obtained. In the current study, the utility of monitoring implant formation using ultrasound was demonstrated by analyzing the formation and degeneration of injectable chitosan and chitosan/nano-hydroxyapatite/collagen scaffold. Figure 1 showed the feasibility of using the ultrasound to manipulate the CS/nHAC system injecting into the Wistar back as *in situ* forming scaffold. The CS/nHAC solution was injected into the subcutaneous dorsum of the Wistar rat with a 1 mL syringe under the ultrasound transducer (Figure 1(a)); the needle and the process of the injection could be easily visualized by the ultrasound (Figure 1(b)).

**3.1. Implant Formation.** Ultrasound has been used to evaluate tissue properties of articular cartilage with the aim of developing a noninvasive clinical method to assess articular cartilage degeneration and repair [27–29]. Recently, it was also used to evaluate the *in vivo* tissue engineering structures. Kreitz et al. [30] found that the gray-scale value of the ultrasound demonstrated a good correlation with the hydroxyapatite content as marker of collagen formation and with the histological findings. Oe et al. [31] used the ultrasound to evaluate the cell numbers in bone marrow stromal cell/β-tricalcium phosphate composites and found ultrasound effectively responded to the quantity of BMSC/β-TCP composites and was well correlated to the actual number of cells contained. Therefore, we chose to use a

TABLE 1: The grey-scale value of ultrasound image on experimental group and control group after 0, 14, and 28 days of incubation. The values are shown as mean  $\pm$  standard deviation.

Group	Time (day)	n	GV	P value
CS	0	5	52.7 $\pm$ 13.0	1.00
CS/nHAC	0	5	51.4 $\pm$ 11.5	
CS	14	5	68.6 $\pm$ 6.5	0.80
CS/nHAC	14	5	81.1 $\pm$ 4.6	
CS	28	5	74.9 $\pm$ 7.5	0.02
CS/nHAC	28	5	99.8 $\pm$ 33.2	

medical diagnostic ultrasound device with the advantage of ensuring the absence of damage to the surrounding tissues. Ultrasound images of the CS and CS/nHAC scaffold taken at different time points (days 0, 14, and 28) are shown in Figure 2. The average GV was intended to be used as an index to determine the degree of the hydroxyproline content as marker of collagen formation and implant stiffness, with lower mean GVs corresponding to a more fluid matrix and larger mean GVs correlating to solid implant. The ultrasound grey-scale signal increased with time, which may demonstrate production of extracellular matrix. The CS/nHAC had a mean GV of  $51.7 \pm 11$  after 1 h of injection; the mean GV increased to  $81.1 \pm 4.6$  after 14 days and attained the highest mean GV of  $107.8 \pm 22$  after 28 days. Significant differences were observed between the GVs on day 1, 14, and 28 in CS/nHAC group. In contrast, the CS scaffold had a mean GV of  $52.7 \pm 13$  after 1 h of injection; the mean GV increased to  $68.5 \pm 6.4$  after 14 days and had a maximum GV of  $74.8 \pm 7.4$  after 28 days. But no significant differences were observed between the GVs on day 1, 14, and 28 in CS group. On day 28, the mean GVs of the CS/nHAC group were significantly higher than the CS group ( $P < 0.05$ ) (Figure 3, Table 1). Using this measurement, it was observed that the CS/nHAC scaffold attained the highest gray-scale value at day 28, indicating the CS/nHAC scaffold had the highest implant stiffness, which maybe related to the early osteogenesis.

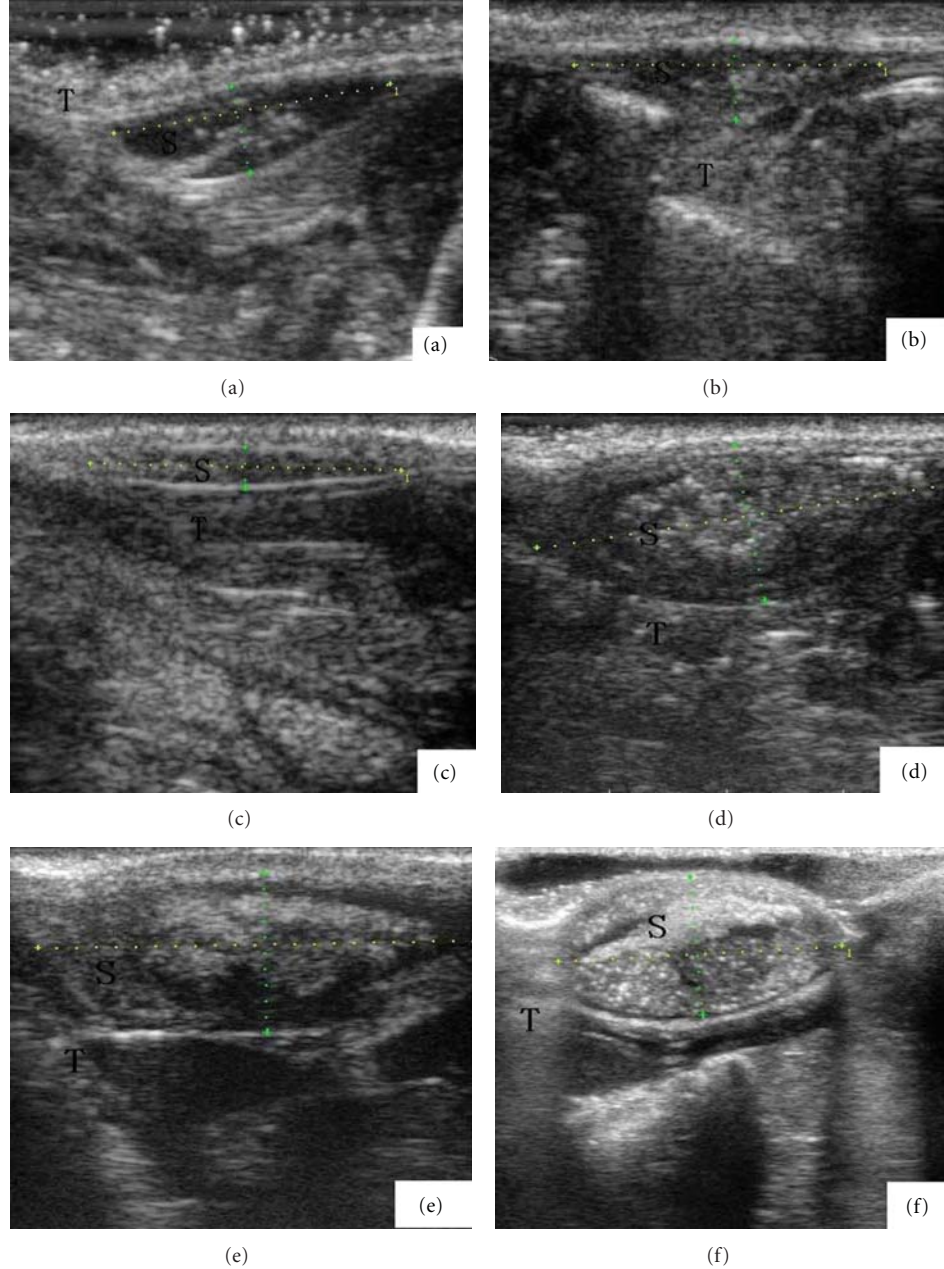


FIGURE 2: The ultrasound images of the scaffold taken on day 0 (a) and (d), day 14 (b) and (e), and day 28 (c) and (f). (CS scaffolds: (a), (b), (c); CS/nHAC scaffolds: (d), (e), (f); S: scaffold; T: surrounding tissues, cross-section area: the blue and yellow dot cross in the scaffold).

**3.2. Implant Volume.** The volumetric changes of the CS/nHAC and CS scaffold were assessed after 1 h, 14 days, and 28 days, respectively. The use of percutaneous ultrasound would allow volume monitoring over time after administration of CS and CS/nHAC gel. This procedure of calculation has been used in radiology ultrasound for more than 20 years to measure breast cysts, renal cysts, and more. Volume calculation is reported in the literature that the detection volume may have 10 percent differences in two-dimensional ultrasound, which is at least as good as that obtained by three-dimensional calculation [32–34]. Implant degeneration was measured as a change in cross-sectional area over time in both groups. The CS scaffold

exhibited decreasing in size more than 80% over the 28 days. However, the CS/nHAC scaffold showed a slight decrease and remained 62% for the duration of 28 days (Table 2, Figure 4). Significant bigger cross-section area was observed in the CS/nHAC scaffold on day 14 (Figures 2(b) and 2(e),  $P < 0.05$ ) and day 28 (Figures 2(c) and 2(f)  $P < 0.01$ ). The results demonstrated a stable material degeneration rate of the CS/nHAC scaffold, which is suitable to be used as a bone substitute. However, the CS scaffold seemed to degenerate too fast in the first 4 weeks to be a good bone substitute.

**3.3. Implant Blood Supply.** The successful clinical outcome of the implanted tissue-engineered bone is dependent on

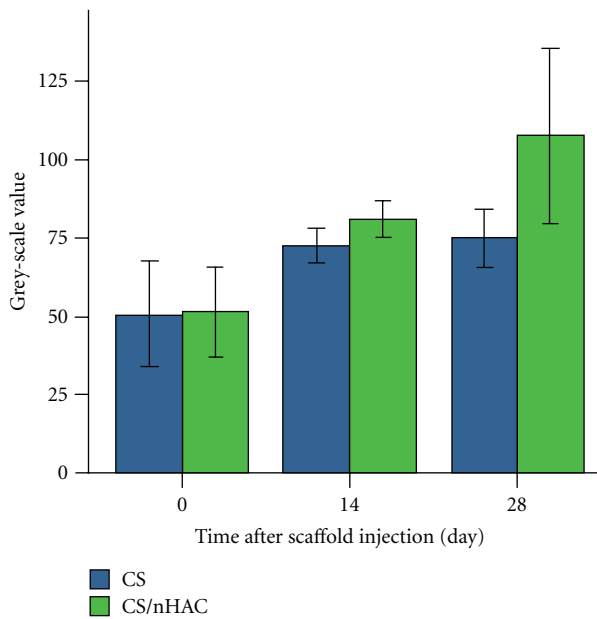


FIGURE 3: The grey-scale value of ultrasound image on experimental group and control group after 0, 14, and 28 days of incubation. The values are shown as mean  $\pm$  standard deviation ( $n = 5$ ,  $*P < 0.05$ ).

TABLE 2: The cross-section area of ultrasound image on experimental group and control group after 0, 14, and 28 days of incubation. The values are shown as mean  $\pm$  standard deviation.

Group	Time (day)	n	Pixel	P value
CS	0	5	$28982.8 \pm 6782.9$	0.16
CS/nHAC	0	5	$35662.0 \pm 3321.5$	
CS	14	5	$17084.8 \pm 256.3$	0.04
CS/nHAC	14	5	$35662.0 \pm 6341.7$	
CS	28	5	$5169.2 \pm 613.4$	0.00
CS/nHAC	28	5	$22050.2 \pm 3449.4$	

the establishment of a functional vascular network. So it is very important to evaluate the vascularization of the implant *in vivo*. The blood flow surrounding the implant was shown in Figure 5. In the CS scaffold group, no blood flow was detected by the color Doppler imaging during 28 days after implantation. However sporadic blood flow was found around the CS/nHAC scaffold on day 14 and 28 after implantation (Figure 5) which maybe related to the material vascularization. Although no blood flow was found inside the scaffold during the 28-day observation, the blood flow surrounding the materials indicates that there were new vessels surrounding the scaffold and new capillary may penetrate into the implant and form a network to promote osteogenesis. The use of ultrasound imaging is of growing interest as new technologies become available for *in vivo* analysis of blood flow. Despite some limitations including a lower degree of sensitivity to changes in tissue perfusion and the inability to assess rapid or transient changes in tissue perfusion, we found that the ultrasound method can be used successfully to examine regional blood perfusion of the biomaterials *in vivo* [35]. As this method does not involve a surgical procedure, ultrasound offers a rapid, noninvasive

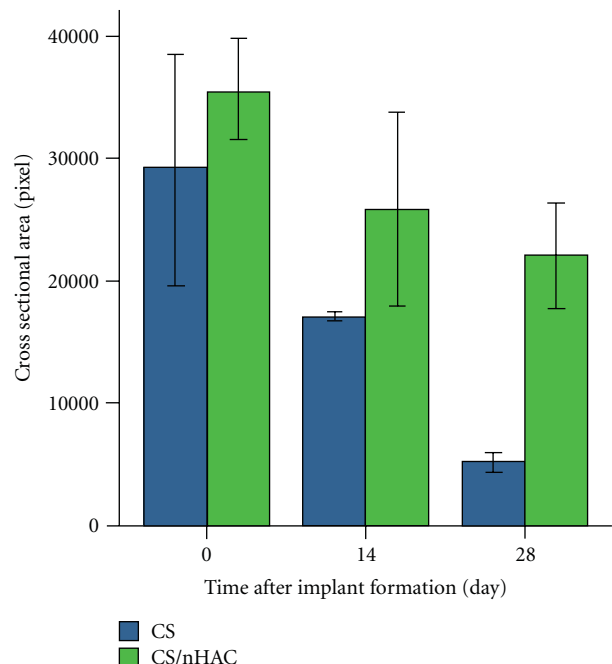


FIGURE 4: The cross-section area of ultrasound image on experimental group and control group after 0, 14, and 28 days of incubation. The values are shown as mean  $\pm$  standard deviation ( $n = 5$ ,  $^{**}P < 0.01$ ,  $*P < 0.05$ ).

way to obtain hemodynamic measurements with little risk to the experimental subject.

## 4. Conclusions

This study has demonstrated that it is possible to noninvasively and nondestructively evaluate the volume, stiffness, and blood supply of the injectable bone scaffold using a diagnostic ultrasound, providing a new means for the biocompatibility study of *in situ* forming implants in *in vivo* applications. The primary advantage of this technique is the real-time visualization of the implant formation process. Through the use of quantitative image analysis techniques, long-term information regarding formation and degeneration behavior for the same implant over time can be obtained. In comparison to the CS, the CS/nHAC scaffold showed a greater stiffness, less degeneration rate, and better blood supply in the *in vivo* biocompatibility evaluation. The results shown in this paper support the proof of principle of using ultrasound for the evaluation of tissue development in hydrogel-based tissue-engineered structures.

## Authors' Contribution

Y. Chen and S. Li contributed equally to this paper.

## Acknowledgments

The authors are grateful for the financial support from National Natural Science Foundation of China (no. 81101348 and no. 31000431), Natural Science Foundation

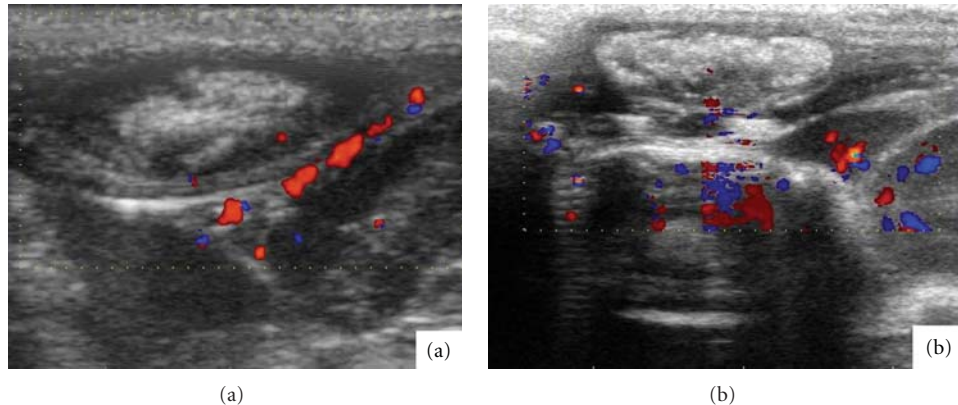


FIGURE 5: The blood supply to the CS/nHAC scaffold after 14 (a) and 28 days (b).

of Guangdong Province, China (10451051501004727), Guangdong Province Science and Technology project, China (ultrasound evaluation of injectable nanobiomaterials), Doctoral Fund of Ministry of Education, China (20114433120004), the Beijing Nova Program (no. 2010B011), and State Key Laboratory of New Ceramic and Fine Processing Tsinghua University, outstanding person fund of Zhujiang Hospital.

## References

- [1] Q. Hou, P. A. De Bank, and K. M. Shakesheff, "Injectable scaffolds for tissue regeneration," *Journal of Materials Chemistry*, vol. 14, no. 13, pp. 1915–1923, 2004.
- [2] A. Chenite, M. Buschmann, D. Wang, C. Chaput, and N. Kandani, "Rheological characterisation of thermogelling chitosan/glycerol-phosphate solutions," *Carbohydrate Polymers*, vol. 46, no. 1, pp. 39–47, 2001.
- [3] A. Chenite, C. Chaput, D. Wang et al., "Novel injectable neutral solutions of chitosan form biodegradable gels in situ," *Biomaterials*, vol. 21, no. 21, pp. 2155–2161, 2000.
- [4] A. Chenite, S. Gori, M. Shive, E. Desrosiers, and M. D. Buschmann, "Monolithic gelation of chitosan solutions via enzymatic hydrolysis of urea," *Carbohydrate Polymers*, vol. 64, no. 3, pp. 419–424, 2006.
- [5] E. Ruel-Gariépy, A. Chenite, C. Chaput, S. Guirguis, and J. C. Leroux, "Characterization of thermosensitive chitosan gels for the sustained delivery of drugs," *International Journal of Pharmaceutics*, vol. 203, no. 1-2, pp. 89–98, 2000.
- [6] E. Ruel-Gariépy, G. Leclair, P. Hildgen, A. Gupta, and J. C. Leroux, "Thermosensitive chitosan-based hydrogel containing liposomes for the delivery of hydrophilic molecules," *Journal of Controlled Release*, vol. 82, no. 2-3, pp. 373–383, 2002.
- [7] E. Ruel-Gariépy and J. C. Leroux, "Chitosan: a natural polycation with multiple applications," *ACS Symposium Series*, vol. 934, pp. 243–259, 2006.
- [8] S. M. Richardson, N. Hughes, J. A. Hunt, A. J. Freemont, and J. A. Hoyland, "Human mesenchymal stem cell differentiation to NP-like cells in chitosan-glycerophosphate hydrogels," *Biomaterials*, vol. 29, no. 1, pp. 85–93, 2008.
- [9] M. H. Cho, K. S. Kim, H. H. Ahn et al., "Chitosan gel as an *in situ*-forming scaffold for rat bone marrow mesenchymal stem cells *in vivo*," *Tissue Engineering, Part A*, vol. 14, no. 6, pp. 1099–1108, 2008.
- [10] C. D. Hoemann, A. Chenite, J. Sun et al., "Cytocompatible gel formation of chitosan-glycerol phosphate solutions supplemented with hydroxyl ethyl cellulose is due to the presence of glyoxal," *Journal of Biomedical Materials Research*, vol. 83, no. 2, pp. 521–529, 2007.
- [11] C. D. Hoemann, J. Sun, A. Légaré, M. D. McKee, and M. D. Buschmann, "Tissue engineering of cartilage using an injectable and adhesive chitosan-based cell-delivery vehicle," *Osteoarthritis and Cartilage*, vol. 13, no. 4, pp. 318–329, 2005.
- [12] X. Li, C. A. van Blitterswijk, Q. Feng, F. Cui, and F. Watari, "The effect of calcium phosphate microstructure on bone-related cells in vitro," *Biomaterials*, vol. 29, no. 23, pp. 3306–3316, 2008.
- [13] X. Li, H. Liu, X. Niu et al., "Osteogenic differentiation of human adipose-derived stem cells induced by osteoinductive calcium phosphate ceramics," *Journal of Biomedical Materials Research*, vol. 97, no. 1, pp. 10–19, 2011.
- [14] X. M. Li, X. H. Liu, M. Uo, Q. L. Feng, F. Z. Cui, and F. Watari, "Investigation on the mechanism of the osteoinduction for calcium phosphate," *Bone*, vol. 43, pp. 111–112, 2008.
- [15] X. Li, Q. Feng, X. Liu, W. Dong, and F. Cui, "Collagen-based implants reinforced by chitin fibres in a goat shank bone defect model," *Biomaterials*, vol. 27, no. 9, pp. 1917–1923, 2006.
- [16] X. Li, H. Gao, M. Uo et al., "Effect of carbon nanotubes on cellular functions in vitro," *Journal of Biomedical Materials Research*, vol. 91, no. 1, pp. 132–139, 2009.
- [17] X. Li, H. Gao, M. Uo et al., "Maturation of osteoblast-like *SaoS*<sub>2</sub> induced by carbon nanotubes," *Biomedical Materials*, vol. 4, no. 1, Article ID 015005, 2009.
- [18] X. Li, Y. Fan, and F. Watari, "Current investigations into carbon nanotubes for biomedical application," *Biomedical Materials*, vol. 5, no. 2, Article ID 022001, 2010.
- [19] X. Li, X. Liu, J. Huang, Y. Fan, and F. Z. Cui, "Biomedical investigation of CNT based coatings," *Surface and Coatings Technology*, vol. 206, no. 4, pp. 759–766, 2011.
- [20] X. Li, Q. Feng, and F. Cui, "In vitro degradation of porous nano-hydroxyapatite/collagen/PLLA scaffold reinforced by chitin fibres," *Materials Science and Engineering C*, vol. 26, no. 4, pp. 716–720, 2006.
- [21] X. M. Li, X. H. Liu, G. P. Zhang et al., "Repairing 25 mm bone defect using fibres reinforced scaffolds as well as autograft bone," *Bone*, vol. 43, pp. 94–94, 2008.
- [22] X. M. Li, H. F. Liu, X. F. Niu et al., "The use of carbon nanotubes to induce osteogenic differentiation of human

- adipose-derived MSCs in vitro and ectopic bone formation *in vivo*,” *Biomaterials*, vol. 33, no. 19, pp. 4818–4827, 2012.
- [23] Z. Huang, J. Tian, B. Yu, Y. Xu, and Q. Feng, “A bone-like nano-hydroxyapatite/collagen loaded injectable scaffold,” *Biomedical Materials*, vol. 4, no. 5, Article ID 055005, 2009.
- [24] Z. Huang, Q. Feng, B. Yu, and S. Li, “Biomimetic properties of an injectable chitosan/nano-hydroxyapatite/ collagen composite,” *Materials Science and Engineering C*, vol. 31, no. 3, pp. 683–687, 2011.
- [25] Z. Huang, B. Yu, Q. Feng, S. Li, Y. Chen, and L. Luo, “In situ-forming chitosan/nano-hydroxyapatite/collagen gel for the delivery of bone marrow mesenchymal stem cells,” *Carbohydrate Polymers*, vol. 85, no. 1, pp. 261–267, 2011.
- [26] Z. Huang, Y. Chen, Q. L. Feng et al., “In vivo bone regeneration with injectable chitosan/hydroxyapatite/collagen composites and mesenchymal stem cells,” *Frontiers of Materials Science*, vol. 5, no. 3, pp. 301–310, 2011.
- [27] D. H. Agemura, W. D. O’Brien, J. E. Olerud, L. E. Chun, and D. E. Eyre, “Ultrasonic propagation properties of articular cartilage at 100 MHz,” *Journal of the Acoustical Society of America*, vol. 87, no. 4, pp. 1786–1791, 1990.
- [28] D. A. Senzig, F. K. Forster, and J. E. Olerud, “Ultrasonic attenuation in articular cartilage,” *Journal of the Acoustical Society of America*, vol. 92, no. 2, pp. 676–681, 1992.
- [29] K. Hattori, Y. Takakura, Y. Morita, M. Takenaka, K. Uematsu, and K. Ikeuchi, “Can ultrasound predict histological findings in regenerated cartilage?” *Rheumatology*, vol. 43, no. 3, pp. 302–305, 2004.
- [30] S. Kreitz, G. Dohmen, S. Hasken, T. Schmitz-Rode, P. Mela, and S. Jockenhoevel, “Nondestructive method to evaluate the collagen content of fibrin-based tissue engineered structures via ultrasound,” *Tissue Engineering, Part C*, vol. 17, no. 10, pp. 1021–1026, 2011.
- [31] K. Oe, M. Miwa, K. Nagamune et al., “Nondestructive evaluation of cell numbers in bone marrow stromal cell/β-tricalcium phosphate composites using ultrasound,” *Tissue Engineering, Part C*, vol. 16, no. 3, pp. 347–353, 2010.
- [32] J. Wong, E. O. Gerscovich, M. S. Cronan, and J. A. Seibert, “Accuracy and precision of in vitro volumetric measurements by three-dimensional sonography,” *Investigative Radiology*, vol. 31, no. 1, pp. 26–29, 1996.
- [33] N. J. Raine-Fenning, J. S. Clewes, N. R. Kendall, A. K. Bunkheila, B. K. Campbell, and I. R. Johnson, “The interobserver reliability and validity of volume calculation from three-dimensional ultrasound datasets in the in vitro setting,” *Ultrasound in Obstetrics and Gynecology*, vol. 21, no. 3, pp. 283–291, 2003.
- [34] B. L. Partik, A. Stadler, S. Schamp et al., “3D versus 2D ultrasound: accuracy of volume measurement in human cadaver kidneys,” *Investigative Radiology*, vol. 37, no. 9, pp. 489–495, 2002.
- [35] S. M. Stieger, S. H. Bloch, O. Foreman, E. R. Wisner, K. W. Ferrara, and P. A. Dayton, “Ultrasound assessment of angiogenesis in a matrigel model in rats,” *Ultrasound in Medicine and Biology*, vol. 32, no. 5, pp. 673–681, 2006.

## Research Article

# Biocompatible Single-Crystal Selenium Nanobelt Based Nanodevice as a Temperature-Tunable Photosensor

**Yongshan Niu,<sup>1</sup> Aimiao Qin,<sup>2</sup> Wei Song,<sup>1</sup> Menghang Wang,<sup>1</sup>  
Xuenan Gu,<sup>1</sup> Yangfei Zhang,<sup>3</sup> Min Yu,<sup>3</sup> Xiaoguang Zhao,<sup>4</sup> Ming Dai,<sup>1</sup>  
Ling Yan,<sup>1</sup> Zhou Li,<sup>1</sup> and Yubo Fan<sup>1</sup>**

<sup>1</sup>Key Laboratory for Biomechanics and Mechanobiology of Ministry of Education, School of Biological Science and Medical Engineering, Beihang University, Beijing 100191, China

<sup>2</sup>Key Lab of New Processing Technology for Nonferrous Metals & Materials Ministry of Education, School of Materials Science & Engineering, Guilin University of Technology, Guilin 541004, China

<sup>3</sup>College of Engineering, Peking University, Beijing 100871, China

<sup>4</sup>Mechanical and Manufacturing Engineering, University of New South Wales, Sydney, NSW 2052, Australia

Correspondence should be addressed to Zhou Li, lizhou@buaa.edu.cn and Yubo Fan, yubofan@buaa.edu.cn

Received 1 March 2012; Accepted 19 March 2012

Academic Editor: Xiaoming Li

Copyright © 2012 Yongshan Niu et al. This is an open access article distributed under the Creative Commons Attribution License, which permits unrestricted use, distribution, and reproduction in any medium, provided the original work is properly cited.

Selenium materials are widely used in photoelectrical devices, owing to their unique semiconductive properties. Single-crystal selenium nanobelts with large specific surface area, fine photoconductivity, and biocompatibility provide potential applications in biomedical nanodevices, such as implantable artificial retina and rapid photon detector/stimulator for optogenetics. Here, we present a selenium nanobelt based nanodevice, which is fabricated with single Se nanobelt. This device shows a rapid photo response, different sensitivities to visible light of variable wave length, and temperature-tunable property. The biocompatibility of the Se nanobelts was proved by MTT test using two cell lines. Our investigation introduced a photosensor that will be important for multiple potential applications in human visual system, photocells in energy or MEMS, and temperature-tunable photoelectrical device for optogenetics research.

## 1. Introduction

One-dimensional (1D) nanostructures such as nanowires [1, 2], nanobelts [3], and nanotubes [4] showed their fascinating features and characteristic during the past few decades. Intensive researches focused on their applications in microcosmic physics and nanodevices [5–8]. Selenium material is a crucial semiconductor, widely used in solar cell, photoelectrical element, xerography, and pressure sensors, owing to its unique photoconductivity, thermoelectric, and piezoelectric properties [9–16]. Previously, most research about the selenium mainly focused on bulk or amorphous materials and hexagonal metallic selenium film.

Recently, the 1D selenium nanostructures, such as single-crystalline nanowires [16, 17] and nanobelts [18], become a new research focus. Numerous works are about synthesis of

1D selenium nanostructures. However, the study about their properties and applications in photoelectrical nanodevices is limited. Meanwhile, the biocompatibility and biosafety of nanostructure is also a serious public concern.

A new single-crystalline selenium nanobelt based photosensor is presented here. This single nanobelt device exhibits ultrafast photon response and temperature-tunable properties. We used a cushiony and large-scale synthesis method to prepare the single-crystalline nanobelts and investigated their cellular level biocompatibility to two different cell lines. This photosensor also presented a variable photoconductivity responding to visible light of different wavelengths. Those novel properties endue the nanodevice multiple potential applications, such as implantable visual nanodevice as artificial retina, rapid photon sensors, photocells, or temperature-tunable photoelectrical element.

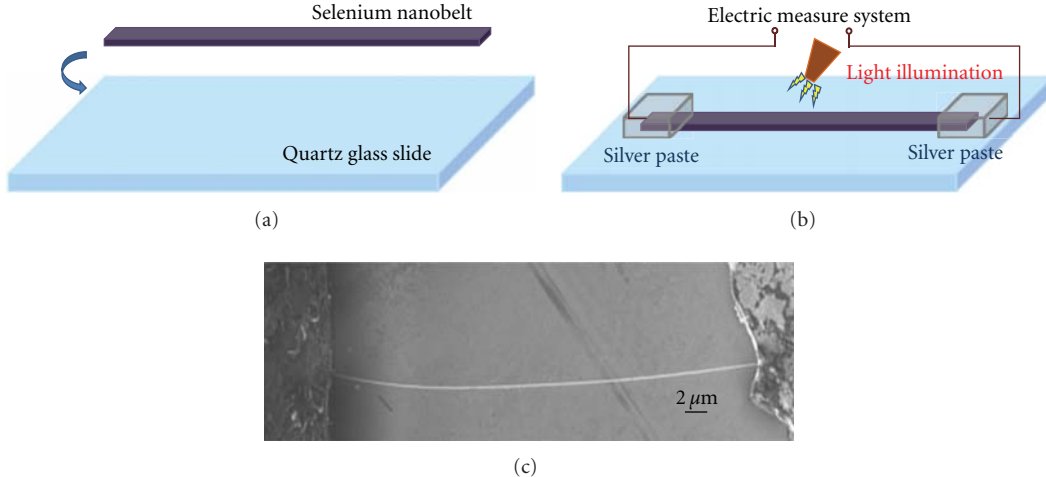


FIGURE 1: Fabrication of a single selenium nanobelt nanodevice. (a) Transfer a single selenium nanobelt to a cleaned quartz glass slide. (b) Fix both ends of nanobelt by silver paste through suitable masks and connect with electric measure system by enameled copper wire. (c) The SEM image of fabricated nanodevice. Two ends are silver pasted, and the bright line is a Se nanobelt.

## 2. Experiment

**2.1. Synthesis.** Single-crystalline t-selenium nanobelts were synthesized by solvothermal method. A typical experimental procedure is described as following: 1.3 mmol (0.1 g) Se powder and 17 mL ethanol were loaded into teflon-lined autoclave of 25 mL capacity. This autoclave was sealed and maintained at 200°C for 24 h. Then the autoclave was taken out and cooled in room temperature. Precipitates were filtered out, rinsed with absolute alcohol for several times, and dried naturally. All of chemicals used for the synthesis were of analytical grade and used as received without further purification.

**2.2. Characterization and Fabrication.** The synthesized selenium nanobelts were characterized and analyzed by X-ray diffraction (XRD, Alpha-1) using CuKa radiation, SEM (FE-SEM, Leon 1530 with EDS), and TEM (TEM, HF-2000).

A single selenium nanobelt was transferred to a cleaned quartz glass slide to fabricate a nanodevice. Both ends of the Se nanobelt were fixed by silver paste and connected with copper wire (Figure 1). The electronic transportation property was conducted on the single nanobelt device by an electric measure system. Besides, we used fluorescent lamp, ultraviolet lamp, and photoluminescence measure instrument to investigate the photoconductivity of the device. The electric property was measured in constant temperature environment. All measurement was carried out and recorded by same electric measure system.

**2.3. Biocompatibility Test.** For our study, two cell lines were utilized [19, 20]. One was HeLa cell (American Type Culture Collection, ATCC, CCL-2) and the other one was L-929 cell (ATCC, CCL-1). Two kind of cells were cultured in Dulbecco's modified Eagle's medium (DMEM, ATCC) supplemented with 10% fetal bovine serum (FBS, ATCC) and

1% penicillin/streptomycin (ATCC). Cell suspension was added to 25 cm<sup>2</sup> vials and put into an incubator (37°C, 5% CO<sub>2</sub>).

After being incubated for 24 h, cells were trypsinized with 0.05% trypsin solution and rushed down from the bottom of 25 cm<sup>2</sup> vials when they were in a semiconfluent state and still in log phase of growth. Ten microliter cell suspension was mixed with 10 μL trypan blue, and the total number of harvest cells was counted under an optical microscope. The density of the cell was calculated and cellular viability was greater than 90%. The cell suspension was added to 96-well plates with 5000 cells per well (90 μL). 96-well plates were incubated in 37°C, 5% CO<sub>2</sub> for 12 h.

Se nanobelts were suspended in PBS (10 μL) for four different concentrations. These suspensions were added into 96-well plates until the mass concentration of 0.1, 1, 10, and 100 μg/mL, respectively. Some wells were preserved without adding nanobelts for comparison purpose. After dispersing nanobelts by micropipettes, the 96-well plates were incubated in 37°C, 5% CO<sub>2</sub> for 12, 24, and 48 h, respectively.

The biocompatibility of the Se nanobelt was investigated through an in vitro cell viability test. We measured the activity of mitochondrial enzyme succinate dehydrogenase (SDH) [21] in two different cell lines, after adding Se nanobelts and incubating for 12, 24, and 48 h.

The Se nanobelts were not removed from each well and an MTT (3-[4,5-dimethyl-thiazol-2-yl]-2,5-diphenyl tetrazolium bromide)-succinate solution (20 μL, 0.5 mg/mL MTT) was added, and the plates were incubated again at 37°C for 4 h. Then all solution in the 96-well plates was removed. The MTT-formazan formed by the mitochondrial enzyme SDH was preserved at the bottom of the well and dissolved in added dimethyl sulfoxide (DMSO). The 96-well plates were shaken softly for 5 minutes to dissolve formazan absolutely. Then the plates were put in a microplate reader

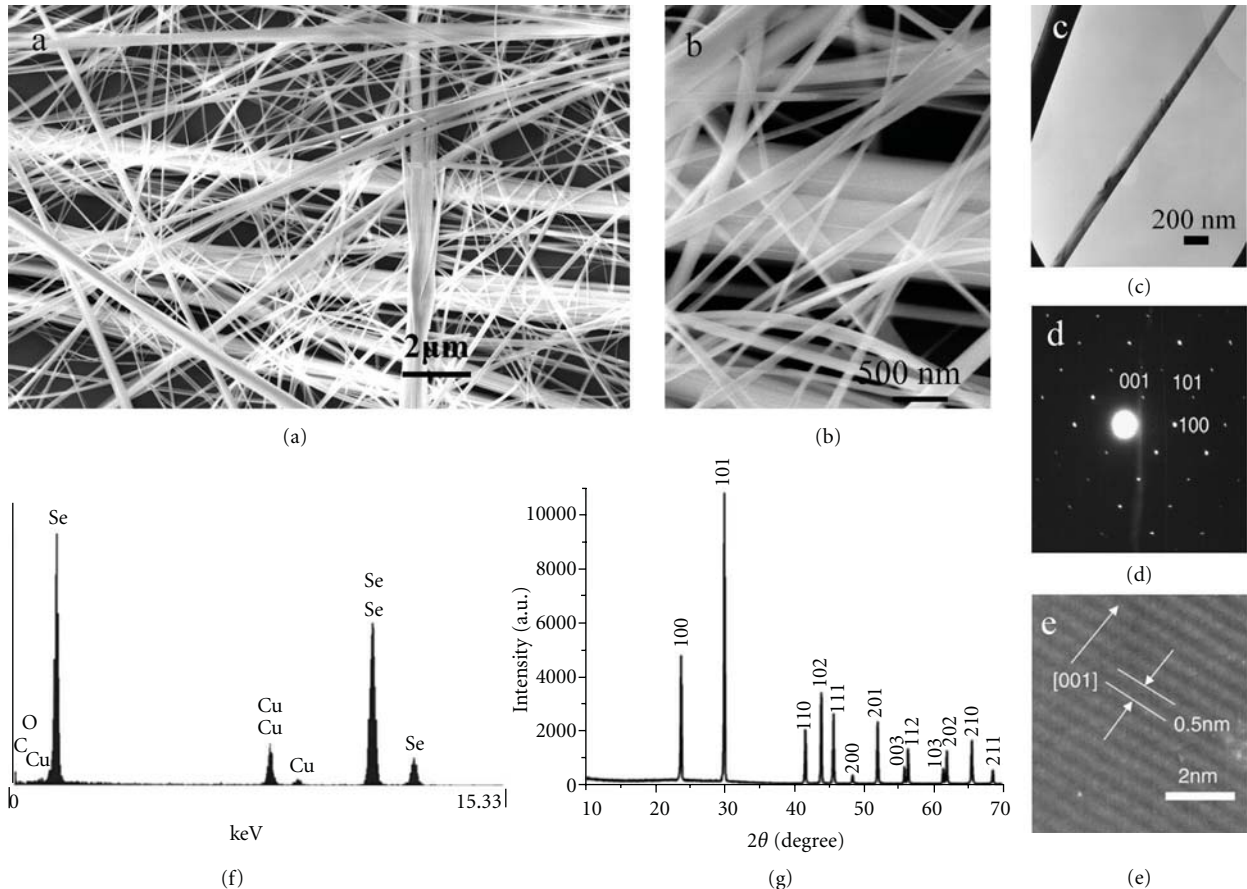


FIGURE 2: SEM, HRTEM, EDS, and XRD characterization of selenium nanobelts. ((a), (b)) SEM images of single-crystalline Se nanobelts in different magnifications. ((c)–(e)) HRTEM images taken from the middle of the Se nanobelt show that the corresponding electron diffraction pattern and its growth direction is [001]. (f) EDS indicates the Se nanobelts with pure composition. (g) XRD pattern confirms that the Se nanobelts are trigonal structure.

(EL808 IU-PC, BioTek Instruments, Inc.), recording the photon absorbance of each well at 630 nm wavelength for investigating the viability of cells.

### 3. Results and Discussion

As shown in the SEM images of different magnifications, the size range of the t-Se nanobelts was from 100 to 500 nm in width and tens to hundreds of micrometers in length. The ratio of length to diameter was  $10^2 \sim 10^4$  (Figures 2(a) and 2(b)). We did chemical element analysis using EDS to test the purity of Se nanobelt (Figure 2(f)). The XRD showed the structure of Se nanobelt is trigonal (Figure 2(g)). And HRTEM study further confirmed that the t-Se nanobelts had single-crystal structure with growth direction [001] (Figures 2(c), 2(d), and 2(e)).

In MTT test, we found that single-crystal Se nanobelts are biocompatible and biosafe to the two cell lines (Figure 3). Our investigation was designed by time sequence and concentration. The incubation time was 12, 24, and 48 h, and the concentration was  $10^{-3}$ ,  $10^{-2}$ , 0.1, and 1 mg/mL. The viability of HeLa and L929 cells showed no difference comparing

with control after incubating with nanobelts. More than 85% of the HeLa cells and >80% L929 cells were viable after incubation, and there was no significant statistic difference in viability among the plates of time sequence (tested by SPSS, paired-sample *t*-test). Meanwhile, different concentrations of Se nanobelts showed no significant effect to the viability of HeLa and L929 cells too (Figure 3).

A single-crystal selenium photosensor device was fabricated (Figure 1). Two ends of the Se nanobelt were fixed by silver paste. The electrical measurement system was connected with the device through enameled copper wires. The photoconductivity measurement was first performed in room temperature and room light (fluorescent lamp). The response time of the Se nanobelt to visible light is calculated. With the light turned on and off, the current changed immediately. From the *I-t* curve, it is observed that the current transported through a single nanobelt drastically increases by a factor of 10 when the light was turned on. As measured at half maximum from *I-t* curve, the increasing and the decay response time was about 30 and 50 ms, respectively. This nanobelt based nanodevice presented a high sensitivity and rapid response to light at room temperature.

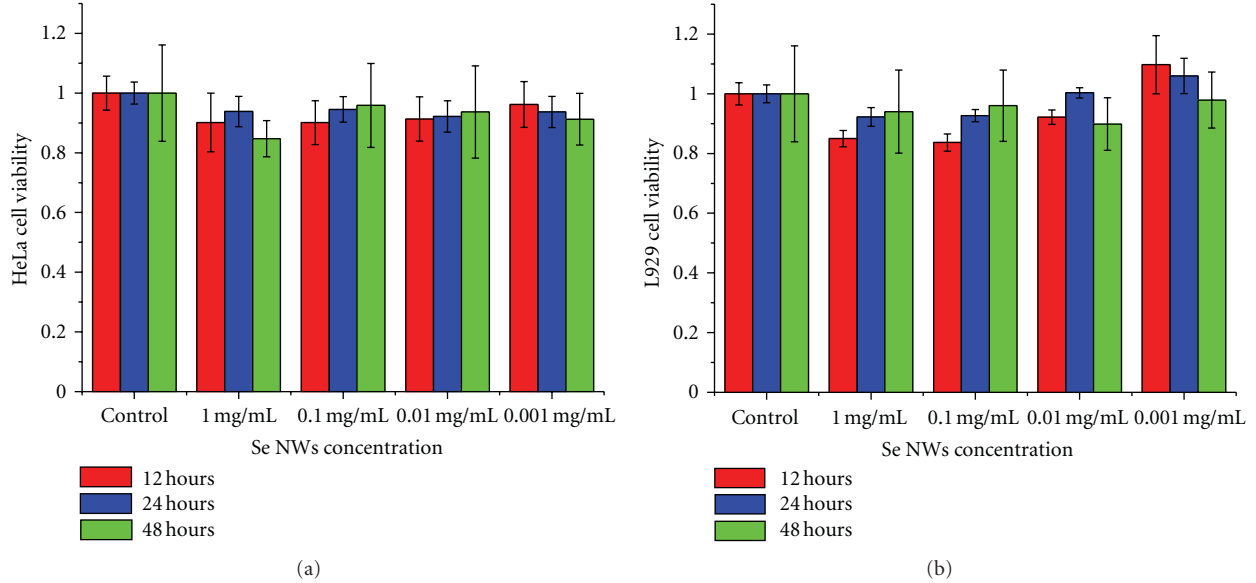


FIGURE 3: The cell viability tested by MTT method as a function of Se nanobelt concentration and time. (a) Cell viability of HeLa cells in MTT test, cultured with different concentrations of Se nanobelts for 12, 24, and 48 h. (b) Viability of L929 cells in MTT test, cultured with different concentrations of Se nanobelts for 12, 24, and 48 h.

This nanobelt based photosensor also exhibited a temperature-tunable property (Figure 4(a)). In this experiment, we changed environmental temperature from  $-80^{\circ}\text{C}$  to  $80^{\circ}\text{C}$ . The voltage was applied to 1 V. The current change in volume reduced with the temperature rise. In semiconductive material, the conductivity is mainly determined by the recombination and trapping of the electron-hole pairs. Generally, when temperature rises, the rate of recombination and trapping increases, displayed as the increasing of conductivity in semiconductor. This trigonal selenium was accepted as a p-type extrinsic semiconductor, and conduction occurred due to valence band hole transportation [22]. The increased thermal conductivity was likely due to the thermal excitation of the electron-hole pairs in the valence band as governed by  $\exp(-E_g/KT)$ , where  $E_g = 1.6\text{ eV}$  was the bandgap of selenium,  $K$  is Boltzmann constant, and  $T$  is temperature.

The rate of recombination and trapping in this selenium nanobelt was shown strongly depending on light and temperature [22, 23]. The photosensitivity, defined as  $S = (I - I_o)/I_o$  where  $I$  and  $I_o$  were the currents measured when the light was on and off, respectively, was strongly affected by temperature.  $S$  decreased as temperature increased. In our experiment, the best photosensitivity was received at temperatures lower than  $40^{\circ}\text{C}$ . The carriers in Se nanobelt were contributed by photon excitation and thermal excitation. With the temperature increasing, the thermal excitation was enhanced and the photosensitivity was relatively reduced. This property of the nanodevice was a temperature-tunable ability, which was likely to be important for the applications in human visual system, implantable light-adjusted medical devices, and the new scientific field of optogenetics [24–26].

In order to investigate the photon sensitivity of the Se nanobelt to the light of different wavelengths, the photocurrent was measured under a chopped light (75 Watt xenon

lamp) to give monochromatic light. The wave length was set from UV to infrared light (300 to 800 nm).  $I-t$  curve showed a significant result as the photosensor's response (Figure 4(b)). The higher response was observed in the visible wave length, which was in agreement with the previous report [12]. This was attributed to the particular photo character of Se nanobelts with some other semiconductors, such as ZnO nanobelts [27, 28]. The maximum photo response of our single-crystal t-Se nanobelt was at  $\sim 650\text{ nm}$  in room temperature, which was a little different with previous report: 650 nm at  $-190^{\circ}\text{C}$  and 750 nm at  $20^{\circ}\text{C}$  [28]. The sensitive response to visible light and temperature-tunable ability was superiority for this Se nanobelt based photosensor applied in implantable biomedical device, such as artificial retina and the optogenetics detector/stimulator.

#### 4. Conclusion

In summary, we synthesized and characterized the single-crystal selenium nanobelts. We also investigated their biocompatibility to different cells. The viability of cells incubated with Se nanobelts showed no difference with the control. More than 80% cells were viable indicating the Se nanobelts behaving a good biocompatibility and biosafety. A photoelectrical nanodevice was fabricated here, and it showed a significant result to visual light of different wavelengths. Moreover, this photosensor exhibited a temperature-tunable ability. As a conclusion, this biocompatible single-crystal Se nanobelt based temperature-tunable photosensor seems to be important for multiple potential applications, such as artificial retina for human visual system, photocells in energy or MEMS, and temperature-tunable photoelectrical device for optogenetics research.

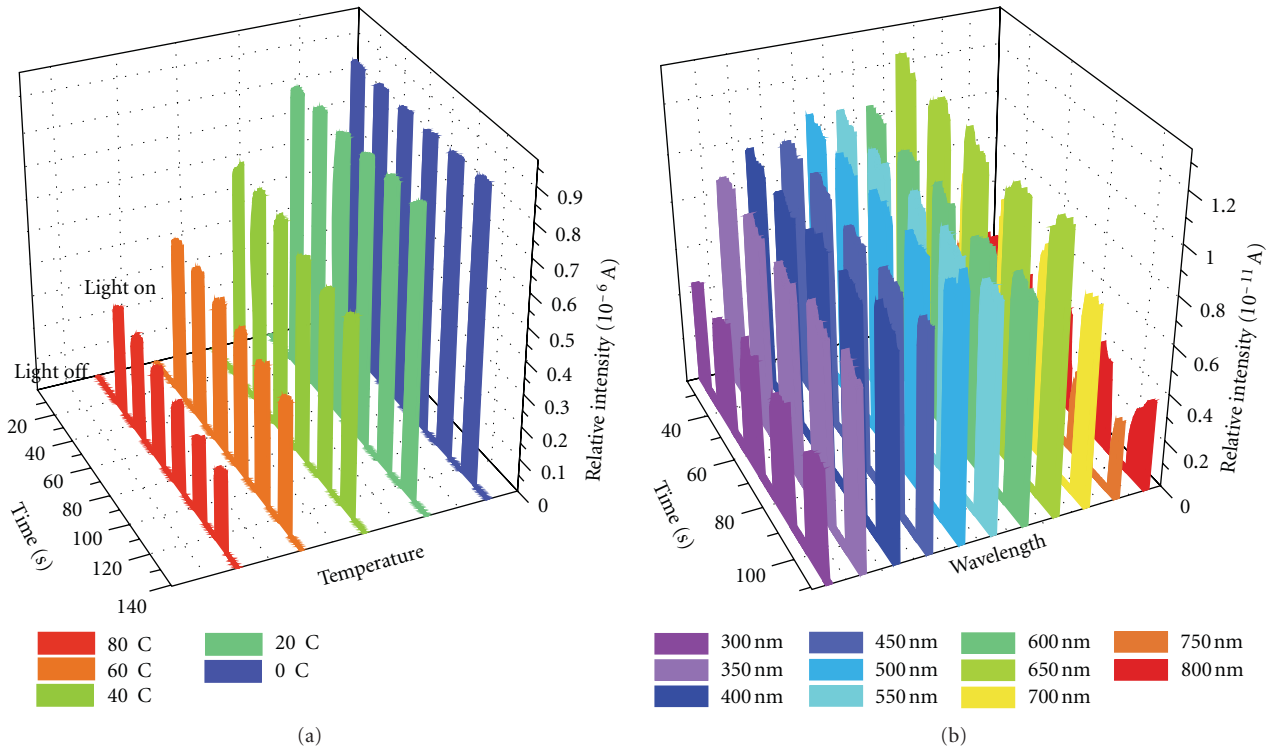


FIGURE 4: The  $I-t$  curve of Se nanobelt based photosensor. (a) The temperature-tunable property of our photosensor. Relative current intensity defines as  $(I - I_0)$ . Temperature changes from  $0^\circ\text{C}$  to  $80^\circ\text{C}$ . (b) Our photosensor presents sensitive response to the light of different wavelengths, from  $300\text{ nm}$  to  $800\text{ nm}$ .

## Acknowledgments

This work was supported under the Scientific Research Foundation for the Returned Overseas Chinese Scholars (20091341) and the Doctoral Fund of the Ministry of Education of China (20111102120038), the National Natural Science Foundation of China (no. 10925208) and NSF of Guangxi Province (2010GXNSFC013007), and National Basic Research Program of China (973 Program, 2011CB710901). Z. Li also thanks the support from the Excellent Scientist Program of the Beihang University. Yongshan Niu and Aimiao Qin are equally contributed to this paper.

## References

- [1] Y. Cui, L. J. Lauhon, M. S. Gudiksen, J. Wang, and C. M. Lieber, "Diameter-controlled synthesis of single-crystal silicon nanowires," *Applied Physics Letters*, vol. 78, no. 15, pp. 2214–2216, 2001.
- [2] Z. L. Wang and J. H. Song, "Piezoelectric nanogenerators based on zinc oxide nanowire arrays," *Science*, vol. 312, no. 5771, pp. 242–246, 2006.
- [3] Z. W. Pan, Z. R. Dai, and Z. L. Wang, "Nanobelts of semiconducting oxides," *Science*, vol. 291, no. 5510, pp. 1947–1949, 2001.
- [4] S. Iijima, "Helical microtubules of graphitic carbon," *Nature*, vol. 354, no. 6348, pp. 56–58, 1991.
- [5] Z. Li, G. Zhu, R. S. Yang, A. C. Wang, and Z. L. Wang, "Muscle-driven *in vivo* nanogenerator," *Advanced Materials*, vol. 22, no. 23, pp. 2534–2537, 2010.
- [6] P. H. Yeh, Z. Li, and Z. L. Wang, "Schottky-gated probe-free ZnO nanowire biosensor," *Advanced Materials*, vol. 21, no. 48, pp. 4975–4978, 2009.
- [7] X. Li, C. A. van Blitterswijk, Q. Feng, F. Cui, and F. Watari, "The effect of calcium phosphate microstructure on bone-related cells *in vitro*," *Biomaterials*, vol. 29, no. 23, pp. 3306–3316, 2008.
- [8] X. M. Li, H. F. Liu, X. F. Niu et al., "Osteogenic differentiation of human adipose-derived stem cells induced by osteoinductive calcium phosphate ceramics," *Journal of Biomedical Materials Research B*, vol. 97, no. 1, pp. 10–19, 2011.
- [9] X. M. Li, H. F. Liu, X. F. Niu et al., "Osteogenic differentiation of human adipose-derived stem cells induced by osteoinductive calcium phosphate ceramics," *Journal of Biomedical Materials Research B*, vol. 97, no. 1, pp. 10–19, 2011.
- [10] J. A. Johnson, M. L. Saboungi, P. Thiagarajan, R. Csencsits, and D. Meisel, "Selenium nanoparticles: a small-angle neutron scattering study," *Journal of Physical Chemistry B*, vol. 103, no. 1, pp. 59–63, 1999.
- [11] R. A. Zingaro and W. C. Cooper, Eds., *Selenium*, Van Nostrand Reinhold, New York, NY, USA, 1974.
- [12] L. I. Berger, *Semiconducting Materials*, CRC Press, Boca Raton, Fla, USA, 1997.
- [13] B. Gates, B. Mayers, A. Grossman, and Y. Xia, "A sonochemical approach to the synthesis of crystalline selenium nanowires in solutions and on solid supports," *Advanced Materials*, vol. 14, pp. 1749–1752, 2002.

- [14] U. K. Gautam, M. Nath, and C. N. R. Rao, "New strategies for the synthesis of t-selenium nanorods and nanowires," *Journal of Materials Chemistry*, vol. 13, no. 12, pp. 2845–2847, 2003.
- [15] H. T. Li and P. J. Regensburger, "Photoinduced discharge characteristics of amorphous selenium plates," *Journal of Applied Physics*, vol. 34, no. 6, pp. 1730–1735, 1963.
- [16] B. Gates, B. Mayers, B. Cattle, and Y. Xia, "Synthesis and characterization of uniform nanowires of trigonal selenium," *Advanced Functional Materials*, vol. 12, no. 3, pp. 219–227, 2002.
- [17] B. T. Mayers, K. Liu, D. Sunderland, and Y. Xia, "Sonochemical synthesis of trigonal selenium nanowires," *Chemistry of Materials*, vol. 15, no. 20, pp. 3852–3858, 2003.
- [18] Q. Wang, G. D. Li, Y. L. Liu, S. Xu, K. J. Wang, and J. S. Chen, "Fabrication and growth mechanism of selenium and tellurium nanobelts through a vacuum vapor deposition route," *Journal of Physical Chemistry C*, vol. 111, no. 35, pp. 12926–12932, 2007.
- [19] C. T. Hanks, J. C. Wataha, and Z. Sun, "In vitro models of biocompatibility: a review," *Dental Materials*, vol. 12, no. 3, pp. 186–193, 1996.
- [20] Z. Li, R. Yang, M. Yu, F. Bai, C. Li, and Z. L. Wang, "Cellular level biocompatibility and biosafety of ZnO nanowires," *Journal of Physical Chemistry C*, vol. 112, no. 51, pp. 20114–20117, 2008.
- [21] J. C. Wataha, R. G. Craig, and C. T. Hanks, "Precision of and new methods for testing in vitro alloy cytotoxicity," *Dental Materials*, vol. 8, no. 1, pp. 65–70, 1992.
- [22] W. E. Spear, "Carrier mobility and charge transport in monoclinic Se crystals," *Journal of Physics and Chemistry of Solids*, vol. 21, no. 1-2, pp. 110–IN1, 1961.
- [23] M. A. Gilleo, "Optical absorption and photoconductivity of amorphous and hexagonal selenium," *The Journal of Chemical Physics*, vol. 19, no. 10, pp. 1291–1297, 1951.
- [24] G. Miller, "Shining new light on neural circuits," *Science*, vol. 314, no. 5806, pp. 1674–1676, 2006.
- [25] D. L. McLean and J. R. Fetcho, "Movement, technology and discovery in the zebrafish," *Current Opinion in Neurobiology*, vol. 21, no. 1, pp. 110–115, 2011.
- [26] G. Miesenbock, "The optogenetic catechism," *Science*, vol. 326, no. 5951, pp. 395–399, 2009.
- [27] J. H. He, Y. H. Lin, M. E. McConney, V. V. Tsukruk, Z. L. Wang, and G. Bao, "Enhancing UV photoconductivity of ZnO nanobelt by polyacrylonitrile functionalization," *Journal of Applied Physics*, vol. 102, no. 8, Article ID 084303, 2007.
- [28] D. S. Elliott, "A comparative study of the light-sensitivity of selenium and stibnite at 20°C. and -190°C," *Physical Review*, vol. 5, no. 1, pp. 53–64, 1915.

## Research Article

# In Vitro Biocompatibility and Osteoblast Differentiation of an Injectable Chitosan/Nano-Hydroxyapatite/Collagen Scaffold

Yan Chen,<sup>1</sup> Zhi Huang,<sup>2</sup> Xiaoming Li,<sup>3</sup> Songjian Li,<sup>4</sup> Zhilai Zhou,<sup>4</sup> Yichen Zhang,<sup>4</sup> Qing ling Feng,<sup>5</sup> and Bo Yu<sup>4</sup>

<sup>1</sup> Department of Ultrasonic Diagnosis, Zhujiang Hospital of Southern Medical University, Guangzhou 510282, China

<sup>2</sup> School of Geosciences and Info-Physics, Central South University, Changsha 410083, China

<sup>3</sup> Key Laboratory for Biomechanics and Mechanobiology of Ministry of Education, School of Biological Science and Medical Engineering, Beihang University, Beijing 100191, China

<sup>4</sup> Department of Orthopedics, Zhujiang Hospital of Southern Medical University, Guangzhou 510282, China

<sup>5</sup> State Key Laboratory of New Ceramic and Fine Processing, Tsinghua University, Beijing 100084, China

Correspondence should be addressed to Xiaoming Li, x.m.li@hotmail.com and Bo Yu, gzyubo@gmail.com

Received 28 February 2012; Accepted 3 April 2012

Academic Editor: Shuming Zhang

Copyright © 2012 Yan Chen et al. This is an open access article distributed under the Creative Commons Attribution License, which permits unrestricted use, distribution, and reproduction in any medium, provided the original work is properly cited.

The purpose of this study was to evaluate the in vitro cell biocompatibility of an in situ forming composite consisting of chitosan (CS), nano-hydroxyapatite and collagen (nHAC), which has a complex hierarchical structure similar to natural bone. MC3T3-E1 mouse calvarial preosteoblasts were cultured on the surface of the injectable CS/nHAC and CS scaffold. The proliferations of seeded MC3T3-E1 were investigated for 10 days. Cytotoxicity, cell proliferation, and cell expression of osteogenic markers such as alkaline phosphatase (ALP), type 1 collagen (COL-1), RUNX-2, and osteocalcin (OCN) were examined by biochemical assay and reverse transcription polymerase chain reaction. Cell viability and total cellularity (measured by dsDNA) were similar between the two scaffold groups. However, ALP, COL-1, OCN, and RUNX-2 production were significantly greater when osteoblasts were cultured on CS/nHAC scaffolds. The increase in osteogenic markers production on CS/nHAC scaffolds indicated that these scaffolds were superior to chitosan-only scaffolds in facilitating osteoblast mineralization. These results demonstrate the potential of the CS/nHAC scaffolds to be used in bone tissue engineering.

## 1. Introduction

Annually, more than 2.2 million bone grafting procedures (autologous bone graft and banked bone) are performed worldwide to ensure adequate bone healing in many skeletal problems, such as nonunion fractures, cervical and lumbar spine fusion, joint arthrodesis, and revision arthroplasty [1]. Tissue engineering offers a strategy to circumvent those problems. The concept involves the use of a porous and biodegradable scaffold, allowing cells to adhere and proliferate, creating conditions for the formation of ECM-like structures [2–4]. Previous studies have shown that natural-based polymers such as chitosan [5–10] have great potential for bone tissue engineering applications. The main advantages of these materials include low immunogenic potential, bioactive behavior, good interaction with host

tissues, chemical versatility, and high availability in nature. Chitosan is a promising material for bone regeneration because it is biocompatible and biodegradable with a degradation rate that is dependent on factors such as degree of deacetylation (DDA) and crystallinity, and it can be easily formed into beads, fibers, or more complex structures [5, 11, 12].

Bone tissues are mainly constructed from nanosized hydroxyapatite (HA) minerals and type 1 collagen (Col-1) matrix with complex hierarchically assembled structures [13–16]. The ideal scaffolds for bone regeneration should promote early mineralization and support new bone formation [17–19]. Mineralized collagen fibrils (nHAC) composites seem to be very promising biomaterials for bone regeneration [20–23]. In the previous study, the feasibility of developing a thermosensitive and injectable chitosan

solution in the presence of nHAC was demonstrated [23–25]. Combining nHAC and chitosan has the potential to maximize the beneficial properties of each and creates an injectable scaffold with properties similar to physiological bone which would undoubtedly aid in the formation of new bone at the tissue/biomaterial interface [24–27].

In the present study, the cytocompatibility of the injectable CS/nHAC scaffolds to act as a bone substitute and its potential for bone tissue engineering were investigated *in vitro*. The ability of the injectable CS/nHAC scaffolds to maintain the viability and functionality of seeded MC3T3-E1 preosteoblasts was investigated in terms of their proliferation and osteoblastic differentiation over 10 days of culture.

## 2. Materials and Methods

**2.1. Scaffold Processing.** The CS/nHAC composite was prepared by the procedure reported previously [24–27]. nHAC powder was synthesized by self-assembly of nanofibrils of mineralized collagen and sterilized by  $\gamma$ -ray irradiation (1.5 Mrad). Chitosan (2 g) was dissolved in hydrochloric acid solution (98 mL, 0.1 M). The nHAC powder was added to the chitosan solution (0.02 g/mL). Finally, the pH of the CS/nHAC solution was adjusted to 7.0 by adding droplets of  $\beta$ -glycerophosphate solution (30% (w/v)). The samples for biological tests were prepared in line with the aseptic technique in an aseptic manipulation cabinet. Solutions were injected into a circular mold (12 mm diameter and 2 mm thickness) and solidified in an incubator at 37°C for 10 min to form a hydrogel scaffold.

The CS was prepared similar to the procedure of CS/nHAC. Chitosan (2 g) was dissolved in hydrochloric acid solution (98 mL, 0.1 M), and then the pH of the CS solution was adjusted to 7.0 by adding droplets of  $\beta$ -glycerophosphate solution (30% (w/v)). The samples for biological tests were prepared in line with the aseptic technique in an aseptic manipulation cabinet.

**2.2. Cell Culture Studies.** MC3T3-E1 murine calvarial osteoblasts (subclone 14) cells were purchased from the cell bank of the Chinese Academy of Sciences (Shanghai, China). The cells were grown in a culture medium consisting of  $\alpha$ -MEM (Sigma, St. Louis, MO), 10% fetal bovine serum (Biochrom AG, Germany), and 1% of antibiotic-antimycotic mixture (Sigma, St. Louis, MO) at 37.8°C in a humidified atmosphere of 5% CO<sub>2</sub>. When an adequate cell number was obtained, cells at passage 2 were detached with trypsin/EDTA. Cells were seeded at a density of  $2 \times 10^4$  cells/scaffold under static conditions, by means of a cell suspension. The culture medium was changed every 2–3 days until the end of the experiment.

**2.3. In Vitro Cytotoxicity Tests.** A Cell Count Kit-8 (Cell Count Kit-8, Beyotime, China) was employed in this experiment to quantitatively evaluate the cytotoxicity of the scaffold. Cell viability was assessed after MC3T3-E1 were

inoculated on the samples 24-well disks using the CCK-8 kit after 1, 3, 7 and 10 days. CCK-8 reagent (100  $\mu$ L) was added to MC3T3 in 1 mL medium per well. The plates were incubated at 37°C for 4 h and shaken for 1 min. After this, 200  $\mu$ L ( $n = 5$ ) were transferred to 96-well plates and the optical density (OD) was measured on a microplate reader (BioTek, USA) using an absorbance of 490 nm. All the procedures were replicated 3 times.

**2.4. Cell Proliferation by DNA Quantification.** MC3T3 proliferation on the CS/nHAC scaffolds was determined using a fluorimetric dsDNA quantification kit (PicoGreen, Molecular Probes, Invitrogen, USA). Samples collected at days 1, 3, 7, and 10 were washed twice with a sterile phosphate-buffered saline solution and transferred into 1.5 mL microtubes containing 1 mL of ultrapure water. Cell constructs were cryopreserved at -80°C for further analysis. Prior to DNA quantification, samples were thawed and sonicated for 15 min. Standards were prepared with concentrations ranging between 0 and 2 mg/mL. Per each well of an opaque 96-well plate were added 28.7  $\mu$ L of sample ( $n = 3$ ) or standard, 71.3  $\mu$ L of PicoGreen solution, and 100  $\mu$ L of Tris-EDTA buffer. The plate was incubated for 10 min in the dark and fluorescence was measured using an excitation wavelength of 260 nm and an emission wavelength of 280 nm. All the procedures were replicated 3 times.

**2.5. Alkaline Phosphatase Quantification.** After culturing for 1, 3, 7, and 10 days, the cells were washed and lysed in 0.1 vol% Triton X-100. The alkaline phosphatase (ALP) activity in the lysis was determined through a p-nitrophenyl phosphate (pNPP) liquid substrate system (Nanjing Jiancheng, China). Five milliliters of each cell lysate solution was added to 195  $\mu$ L of pNPP substrate and incubated in the dark at room temperature for 1 min. The absorbance was read using a plate reader (Molecular Devices, USA) at 405 nm. The intracellular total protein content was determined using a Micro BCA Protein Assay Kit (Nanjing Kaiji, China) and the ALP activity was normalized to it.

**2.6. Osteogenic Differentiation by Reverse Transcriptase PCR.** The expression levels of osteogenesis-related genes were measured using the quantitative reverse transcription-polymerase chain reaction (qRT-PCR). The cells were seeded at a density of  $2 \times 10^4$  cells/well, cultured for 1, 3, 7 and 10 days, and then harvested using TRIzol (Gibco) to extract RNA. An equivalent amount of RNA from each sample was reverse-transcribed into complementary DNA (cDNA) using the Superscript II first-strand cDNA synthesis kit (Invitrogen). The qRT-PCR analysis of genes including type 1 collagen (COL-1), osteocalcin (OCN), Runt-related transcription factor 2 (RUNX-2), and 18S ribosomal RNA (18 s rRNA) was performed on the Applied Biosystems 7500 using the Quantitect Sybr Green Kit (Qiagen). The primers for the target genes were listed in Table 1. The Ct values of target genes were normalized by the Ct values of the TaqMan

TABLE 1: Primer sequences and product size for real-time PCR reactions.

Target	Sense and anti-sense sequences	bp
OCN	5' AGGGCAATAAGGTAGTGAA 5' CGTAGATGCGTCTGTAGGC	159
RUNX-2	5' TGCCCAGTGAGAACAGAAAGAC 5' CTCCTCCCTCTAACCTCTAA	123
COLL	5' CTTCACCTACAGCACCCCTGT 5' AAGGGAGCCACATCGATGAT	120
18 s rRNA	5' CCTGGATACCGCAGCTAGGA 5' GCGGCGCAATACGAATGCC	112

human housekeeping gene 18 s rRNA to obtain the DCt values. These values were then subtracted by the Ct value of the cells cultured on the blank disks to obtain the DDCt values. The fold of change was obtained with  $n = 3$ .

**2.7. Statistical Analysis.** Statistical significance of differences was determined using one-way and two-way analysis of variance ANOVA. If differences were detected, pairwise comparisons were made using Tukey's HSD test at a confidence interval of 95% ( $P < 0.05$ ).

### 3. Result and Discussion

**3.1. In Vitro Cytotoxicity Tests.** The viable cell density increases over initial days up to a plateau based on the CCK-8 assay (Figure 1). The experimental group and control group share similar trend of viable cell density over 10 days. the CS/nHAC group reach a maximum value at day 10, and the CS group reach a maximum value at day 7; no significant growth difference was observed between the two groups after 10 days of incubation ( $n = 5$ ,  $P > 0.05$ ). The results of the CCK-8 assay reflect an overall activity which is affected by both cell proliferation and cell viability. The cell proliferation assay showed that cells grew normally with the scaffolds and these scaffolds were nontoxic for MC3T3-E1.

**3.2. Cell Proliferation by DNA Quantification.** Over the 10 days of the study, the number of cells, as measured by dsDNA, was essentially equivalent between both CS and CS/nHAC scaffold groups (Figure 2). Overall, there was not a significant amount of cell proliferation detected over the course of the study. In vitro cell testing of biomaterials is a well-established method to determine the cytocompatibility of the materials [27–29] by using either cell lines or primary cells. This study was designed primarily to analyze the ability of the composite scaffold to support osteoblast matrix production, and maintaining similar cell numbers in each group allowed differences in these parameters to be studied without the confounding effects of cell number differences. The DNA concentration result of the two groups showed a similar trend to the CCK-8 result. These results demonstrated that both the CS and CS/nHAC scaffold had good cytocompatibility and MC3T3-E1 viability, so it highlights the application of CS/nHAC to be a biomaterial for bone tissue engineering.

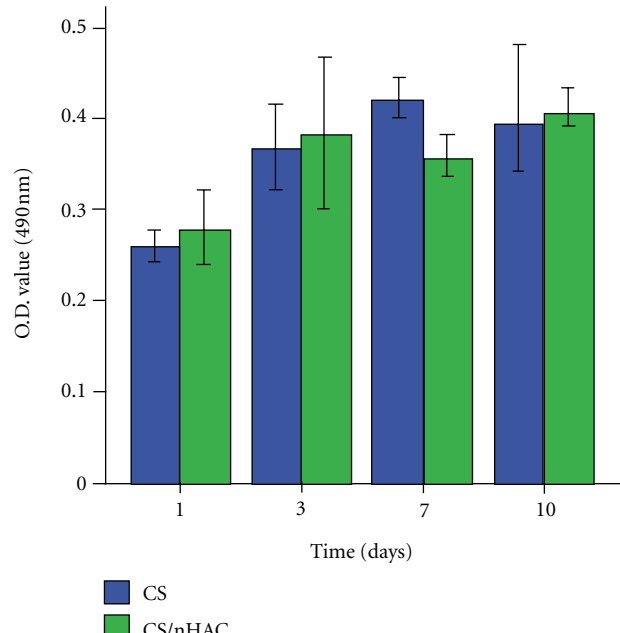


FIGURE 1: CCK-8 assays of MC3T3-E1 proliferation on experimental group and control group after 1, 3, 7, and 10 days of incubation. The values are shown as mean  $\pm$  standard deviation ( $n = 5$ ).

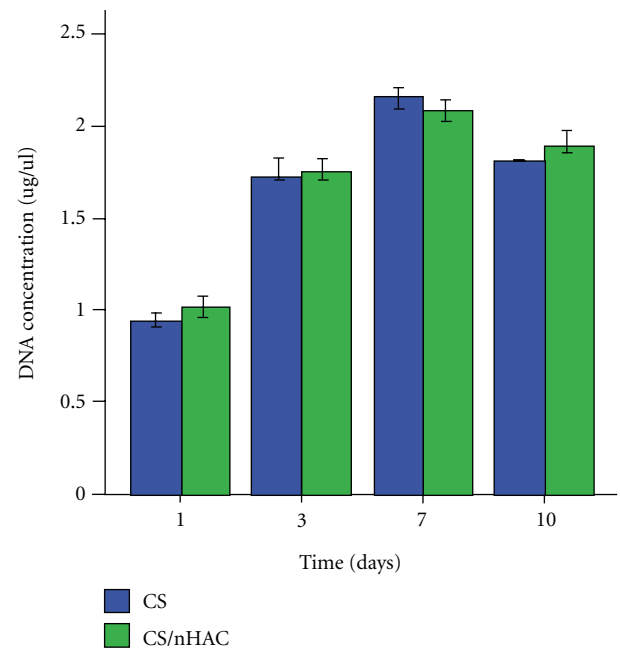


FIGURE 2: DNA concentration of MC3T3-E1 proliferation on experimental group and control group after 1, 3, 7, and 10 days of incubation. The values are shown as mean  $\pm$  standard deviation ( $n = 5$ ).

**3.3. Alkaline Phosphatase Quantification.** ALP activity and calcium mineralization are mostly used as markers for early and late differentiation of osteoblast cells, respectively [21, 22]. Osteoblastic cell differentiation was assessed by measuring ALP activity normalized to total protein content after 1, 3, 7, and 10 days of culture. Figure 3 shows the

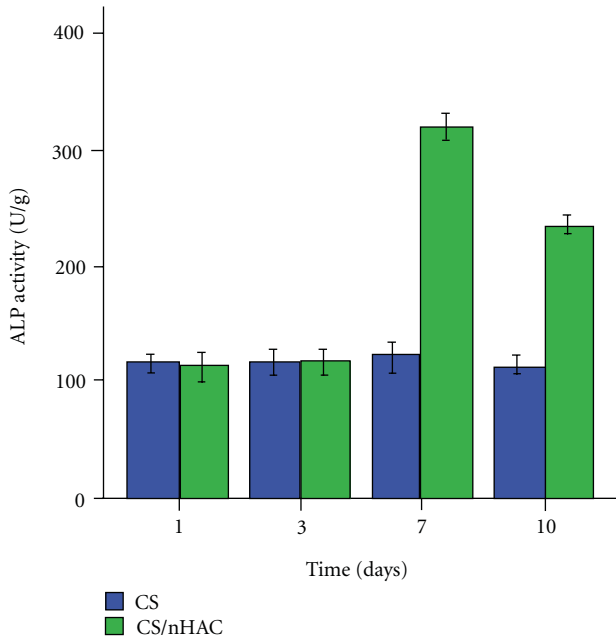


FIGURE 3: ALP assays of MC3T3-E1 proliferation on experimental group and control group after 1, 3, 7, and 10 days of incubation. The values are shown as mean  $\pm$  standard deviation ( $n = 3$ ). Bars with dissimilar letters indicate significantly different values (\*\* $P < 0.01$ ).

evolution of ALP activity for MC3T3-E1 cells cultured on the CS/nHAC surfaces in comparison with CS. The ALP activity of MC3T3-E1 cells grown on both groups was not significantly different for day 1 and 3. However, MC3T3-E1 cells cultured on CS/nHAC scaffold had significantly higher ALP activity than those cultured on CS group on day 7 and 10 ( $P < 0.001$ ). The ALP activity of CS/nHAC group reaching a top on day 7 was observed. The following decrease on day 10 is likely due to reaching an advanced cell culture stage. ALP activity is mostly used as markers for early and late differentiation of osteoblast cells, respectively [30, 31]. These results indicate that the CS/nHAC scaffold can stimulate matrix formation and enhance osteoblast cell differentiation.

**3.4. Osteogenic Differentiation by Reverse Transcriptase PCR.** A semiquantitative RT-PCR method was used to assess gene expression of osteoblasts after 1, 3, 7, and 10 days. In order to know whether primary osteoblast differentiation was affected by nano-hydroxyapatite/collagen, we selected COL-1, OCN, and RUNX-2 as markers for osteoblastic differentiation in this study. Among bone matrices, COL-1 is the most abundant protein synthesized by active osteoblasts and conductive to mineral deposition. Osteocalcin is secreted solely by osteoblasts and thought to play a role in the body's metabolic regulation and is proosteoblastic or bone-building [28]. It is also involved in bone mineralization and calcium ion homeostasis. RUNX-2 gene is a member of the RUNX family of transcription factors and encodes a nuclear protein with a Runt DNA-binding domain. The protein can bind DNA both as a monomer and, with more affinity, as a subunit

of a heterodimeric complex. This protein has been implicated as a key transcription factor associated with osteoblast differentiation [29]. The results of real-time PCR for mRNA expression of osteocalcin and RUNX-2, both of which are osteoblast markers, are represented as fold increases. As shown in Figures 4(a) and 4(b), there are significant differences in the osteocalcin expression between CS/nHAC and CS at day 1, 7, and 10 ( $P < 0.001$ ) (Figure 4(a)). The osteocalcin expression was 5.5-fold higher on day 7 and 2.7-fold higher on day 10 for the CS/nHAC as opposed to the CS. Also, the RUNX-2 expression was significantly higher by day 7 and 10 for the CS/nHAC as opposed to the CS group. The COL-1 expression was significantly lower by day 1 and 3 for the CS/nHAC as opposed to the CS group. However, significant higher COL-1 expression of CS/nHAC than CS was observed at day 7 and 10 ( $P < 0.01$ ).

Due to the current results *in vitro*, better osteoblasts viability, and differentiation marked by higher OCN, RUNX-2 and COL-1 expression were observed on CS/nHAC surfaces. The addition of nHAC to the chitosan did lead to significantly enhanced osteoblasts differentiation. There are several factors that could contribute to the enhanced mineralized matrix production seen when osteoblasts were cultured on CS/nHAC scaffolds. When calcium phosphate-containing materials are hydrated in cell culture media, a continuous process of calcium and phosphate ion dissolution and reprecipitation occurs. This creates a dense carbonated apatite layer on the surface of the scaffold that is similar to the structure of native bone and may therefore induce more rapid osteoblast differentiation and mineralization [30–32]. Taken together, these gene expression data associated with the osteoblast phenotype provides evidence that the scaffold constitutes a good substrate for MC3T3-E1 cell differentiation leading to ECM mineralization.

## 4. Conclusions

In this study, we conclude that the CS/nHAC scaffold has a suitable biocompatibility for its use as cell culture scaffold for hard tissue regeneration. *In vitro* experiments revealed more prominent activation of osteoblast differentiation in cells grown on CS/nHAC than in those grown on CS. Collectively, these data indicates the CS/nHAC may give greater results concerning cell proliferation and differentiation compared to chitosan in this *in vitro* study. We suggest an excellent applicability of the CS/nHAC as bone substitutes.

## Authors' Contribution

Y. Chen and Z. Huang contributed equally to this paper.

## Acknowledgments

The authors are grateful for the financial support from National Natural Science Foundation of China (no. 81101348 and no. 31000431), Natural Science Foundation

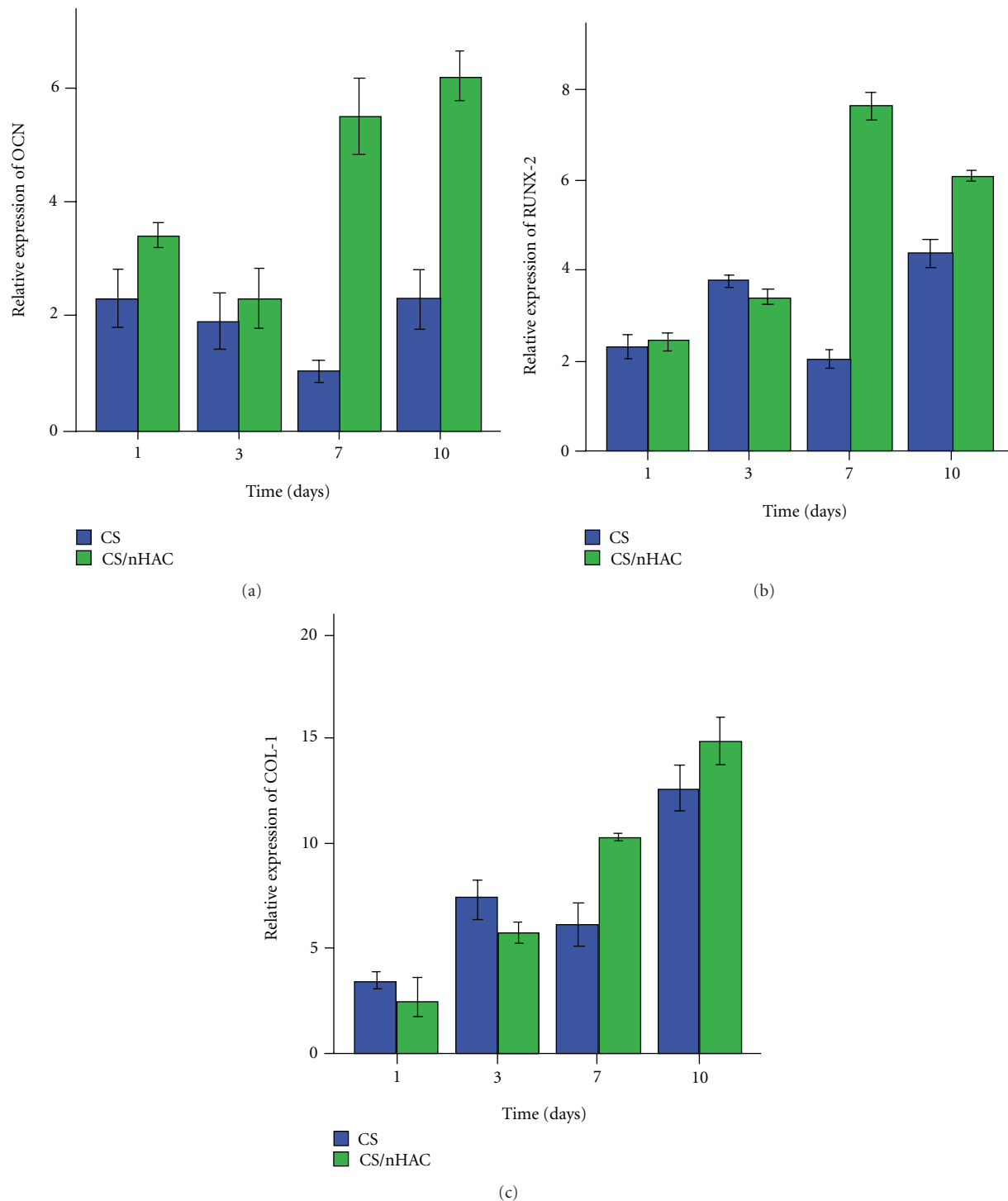


FIGURE 4: Real-time PCR analysis of osteoblast-specific gene expression. Values were normalized to 18 s rRNA expression and shown relative to gene expression on (b) for comparison. (a) OCN, (b) RUNX-2, (c) COL-1. The values are shown as mean  $\pm$  standard deviation ( $n = 3$ ). Bars with dissimilar letters indicate significantly different values (\* $P < 0.05$ , \*\* $P < 0.01$ ).

of Guangdong Province, China (10451051501004727), Guangdong Province Science and Technology project, China (ultrasound evaluation of injectable nanobiomaterials), Doctoral Fund of Ministry of Education,

China (20114433120004), the Beijing Nova Program (no. 2010B011), and State Key Laboratory of New Ceramic and Fine Processing, Tsinghua University, outstanding person fund of Zhujiang Hospital.

## References

- [1] P. V. Giannoudis, H. Dinopoulos, and E. Tsiridis, "Bone substitutes: an update," *Injury*, supplement 36, pp. S20–S27, 2005.
- [2] R. Langer and J. P. Vacanti, "Tissue engineering," *Science*, vol. 260, no. 5110, pp. 920–926, 1993.
- [3] R. Cancedda, B. Dozin, P. Giannoni, and R. Quarto, "Tissue engineering and cell therapy of cartilage and bone," *Matrix Biology*, vol. 22, no. 1, pp. 81–91, 2003.
- [4] D. W. Hutmacher, J. T. Schantz, C. X. Lam, K. C. Tan, and T. C. Lim, "State of the art and future directions of scaffold-based bone engineering from a biomaterials perspective," *Journal of Tissue Engineering and Regenerative Medicine*, vol. 1, no. 4, pp. 245–260, 2007.
- [5] A. Di Martino, M. Sittiger, and M. V. Risbud, "Chitosan: a versatile biopolymer for orthopaedic tissue-engineering," *Biomaterials*, vol. 26, no. 30, pp. 5983–5990, 2005.
- [6] S. H. Elder, D. L. Nettles, and J. D. Bumgardner, "Synthesis and characterization of chitosan scaffolds for cartilage-tissue engineering," *Methods in Molecular Biology*, vol. 238, pp. 41–48, 2004.
- [7] Z. Li, H. R. Ramay, K. D. Hauch, D. Xiao, and M. Zhang, "Chitosan-alginate hybrid scaffolds for bone tissue engineering," *Biomaterials*, vol. 26, no. 18, pp. 3919–3928, 2005.
- [8] D. P. Mukherjee, A. S. Tunkle, R. A. Roberts, A. Clavenna, S. Rogers, and D. Smith, "An animal evaluation of a paste of chitosan glutamate and hydroxyapatite as a synthetic bone graft material," *Journal of Biomedical Materials Research*, vol. 67, no. 1, pp. 603–609, 2003.
- [9] L. Kong, Y. Gao, W. Cao, Y. Gong, N. Zhao, and X. Zhang, "Preparation and characterization of nano-hydroxyapatite/chitosan composite scaffolds," *Journal of Biomedical Materials Research*, vol. 75, no. 2, pp. 275–282, 2005.
- [10] B. M. Chesnutt, A. M. Viano, Y. Yuan et al., "Design and characterization of a novel chitosan/nanocrystalline calcium phosphate composite scaffold for bone regeneration," *Journal of Biomedical Materials Research*, vol. 88, no. 2, pp. 491–502, 2009.
- [11] L. Qi, Z. Xu, X. Jiang, C. Hu, and X. Zou, "Preparation and antibacterial activity of chitosan nanoparticles," *Carbohydrate Research*, vol. 339, no. 16, pp. 2693–2700, 2004.
- [12] A. K. Azad, N. Sermsintham, S. Chandrkrachang, and W. F. Stevens, "Chitosan membrane as a wound-healing dressing: characterization and clinical application," *Journal of Biomedical Materials Research*, vol. 69, no. 2, pp. 216–222, 2004.
- [13] X. Li, C. A. van Blitterswijk, Q. Feng, F. Cui, and F. Watari, "The effect of calcium phosphate microstructure on bone-related cells in vitro," *Biomaterials*, vol. 29, no. 23, pp. 3306–3316, 2008.
- [14] X. Li, H. Liu, X. Niu et al., "Osteogenic differentiation of human adipose-derived stem cells induced by osteoinductive calcium phosphate ceramics," *Journal of Biomedical Materials Research*, vol. 97, no. 1, pp. 10–19, 2011.
- [15] X. M. Li, X. H. Liu, M. Uo, Q. L. Feng, F. Z. Cui, and F. Watari, "Investigation on the mechanism of the osteoinduction for calcium phosphate," *Bone*, vol. 43, pp. 111–112, 2008.
- [16] X. Li, Q. Feng, X. Liu, W. Dong, and F. Cui, "Collagen-based implants reinforced by chitin fibres in a goat shank bone defect model," *Biomaterials*, vol. 27, no. 9, pp. 1917–1923, 2006.
- [17] X. Li, H. Gao, M. Uo et al., "Effect of carbon nanotubes on cellular functions in vitro," *Journal of Biomedical Materials Research*, vol. 91, no. 1, pp. 132–139, 2009.
- [18] X. Li, H. Gao, M. Uo et al., "Maturation of osteoblast-like  $\text{SaoS}_2$  induced by carbon nanotubes," *Biomedical Materials*, vol. 4, no. 1, Article ID 015005, 2009.
- [19] X. Li, Y. Fan, and F. Watari, "Current investigations into carbon nanotubes for biomedical application," *Biomedical Materials*, vol. 5, no. 2, Article ID 022001, 2010.
- [20] X. Li, X. Liu, J. Huang, Y. Fan, and F. Z. Cui, "Biomedical investigation of CNT based coatings," *Surface and Coatings Technology*, vol. 206, no. 4, pp. 759–766, 2011.
- [21] X. Li, Q. Feng, and F. Cui, "In vitro degradation of porous nano-hydroxyapatite/collagen/PLLA scaffold reinforced by chitin fibres," *Materials Science and Engineering C*, vol. 26, no. 4, pp. 716–720, 2006.
- [22] X. M. Li, X. H. Liu, G. P. Zhang et al., "Repairing 25 mm bone defect using fibres reinforced scaffolds as well as autograft bone," *Bone*, vol. 43, p. 94, 2008.
- [23] X. M. Li, H. F. Liu, X. F. Niu et al., "The use of carbon nanotubes to induce osteogenic differentiation of human adipose-derived MSCs in vitro and ectopic bone formation *in vivo*," *Biomaterials*. In press.
- [24] Z. Huang, J. Tian, B. Yu, Y. Xu, and Q. Feng, "A bone-like nano-hydroxyapatite/collagen loaded injectable scaffold," *Biomedical Materials*, vol. 4, no. 5, Article ID 055005, 2009.
- [25] Z. Huang, Q. Feng, B. Yu, and S. Li, "Biomimetic properties of an injectable chitosan/nano-hydroxyapatite/collagen composite," *Materials Science and Engineering C*, vol. 31, no. 3, pp. 683–687, 2011.
- [26] Z. Huang, B. Yu, Q. Feng, S. Li, Y. Chen, and L. Luo, "In situ-forming chitosan/nano-hydroxyapatite/collagen gel for the delivery of bone marrow mesenchymal stem cells," *Carbohydrate Polymers*, vol. 85, no. 1, pp. 261–267, 2011.
- [27] Z. Huang, Y. Chen, Q. L. Feng et al., "In vivo bone regeneration with injectable chitosan/hydroxyapatite/collagen composites and mesenchymal stem cells," *Frontiers of Materials Science*, vol. 5, no. 3, pp. 301–310, 2011.
- [28] Y. Wang, S. Zhang, X. Zeng, L. M. Lwin, A. K. Khiam, and M. Qian, "Initial attachment of osteoblastic cells onto sol-gel derived fluoridated hydroxyapatite coatings," *Journal of Biomedical Materials Research*, vol. 84, no. 3, pp. 769–776, 2008.
- [29] S. Jalota, S. B. Bhaduri, and A. C. Tas, "In vitro testing of calcium phosphate (HA, TCP, and biphasic HA-TCP) whiskers," *Journal of Biomedical Materials Research*, vol. 78, no. 3, pp. 481–490, 2006.
- [30] S. A. Clarke, N. L. Hoskins, G. R. Jordan, S. A. Henderson, and D. R. Marsh, "In vitro testing of Advanced JAX Bone Void Filler System: species differences in the response of bone marrow stromal cells to  $\beta$  tri-calcium phosphate and carboxymethylcellulose gel," *Journal of Materials Science*, vol. 18, no. 12, pp. 2283–2290, 2007.
- [31] W. Att, N. Hori, M. Takeuchi et al., "Time-dependent degradation of titanium osteoconductivity: an implication of biological aging of implant materials," *Biomaterials*, vol. 30, no. 29, pp. 5352–5363, 2009.
- [32] W. Att, N. Hori, F. Iwasa, M. Yamada, T. Ueno, and T. Ogawa, "The effect of UV-photofunctionalization on the time-related bioactivity of titanium and chromium-cobalt alloys," *Biomaterials*, vol. 30, no. 26, pp. 4268–4276, 2009.

## Review Article

# Nanotechnology-Based Therapies for Skin Wound Regeneration

**Ilaria Tocco,<sup>1</sup> Barbara Zavan,<sup>2</sup> Franco Bassetto,<sup>1</sup> and Vincenzo Vindigni<sup>1</sup>**

<sup>1</sup> Institute of Plastic Surgery, University Hospital of Padova, 35128 Padova, Italy

<sup>2</sup> Department of Histology, Microbiology and Biomedical Technologies, University of Padova, 35128 Padova, Italy

Correspondence should be addressed to Ilaria Tocco, toccolalaria@gmail.com

Received 8 February 2012; Revised 19 February 2012; Accepted 24 February 2012

Academic Editor: Xiaoming Li

Copyright © 2012 Ilaria Tocco et al. This is an open access article distributed under the Creative Commons Attribution License, which permits unrestricted use, distribution, and reproduction in any medium, provided the original work is properly cited.

The cutting-edge combination of nanotechnology with medicine offers the unprecedented opportunity to create materials and devices at a nanoscale level, holding the potential to revolutionize currently available macroscale therapeutics. Nanotechnology already provides a plethora of advantages to medical care, and the success of nanoparticulate systems suggests that a progressive increase in the exploration of their potential will take place in the near future. An overview on the current applications of nanotechnology to wound healing and wound care is presented.

## 1. Introduction

Nobel Prize winner Richard Feynman was the first in 1959 to predict the future emergence of a new science which could be able to deal with structures on a scale 1–100 nm. Fifty years after, the unpredictable result is the ability to manipulate materials on the same unimaginably small scale which is used by nature [1]. The repercussions that nanotechnology is having in our lives nowadays are towering: the current applications to molecular biology are leading to the development of structures, devices, and systems bearing a capacity to revolutionize medical therapeutics and diagnostics, which has never been seen before.

Nanodevices are innovative and can provide a wide range of advantages: from the ability of nanoparticles to enter into the cytoplasmic space across cellular barriers, like Trojan horses, and activate specific transport mechanisms [2, 3]; to the modulation of drugs biocompatibility, bioavailability and safety profiles through nanodelivery systems [4]. Furthermore, therapeutic selection can increasingly be tailored to each patient's profile. Nanotherapies represent a great opportunity to enhance currently available medical treatments, improving standard care and prognosis for challenging healthcare issues, like impaired wound healing.

The public health impact of chronic wounds is staggering. An estimated 1.3 to 3 million US individuals are believed to have pressure ulcers and as many as 10% to 15% of the 20 million individuals with diabetes are at risk of

developing diabetic ulcers [5]. Nonhealing wounds are the results of a stop in the progression of the normal sequence of cellular and biochemical events towards the restoration of the skin's integrity. Factors delaying wound healing include either preexisting comorbidities (diabetes, chronic peripheral vasculopathy, and immunosuppression), leading to lack of appropriate metabolism and clearance from toxic substances of the wound, and/or sudden complications, such as infections, exalting the inflammatory state. Nanobiotechnology combined with the knowledge on cellular and subcellular dysfunctional events occurring in delayed wound healing offers great opportunities for improving wound care.

This paper will focus on the currently available nanotechnology-based therapies in the field of wound healing and skin regeneration. To appreciate the importance of the functions of the innovative nanosystems, an understanding of the wound healing process is essential.

**1.1. The Wound Healing Process.** The wound healing process is classically defined as a series of continuous, sometimes overlapping, events. These are haemostasis, inflammation, proliferation, epithelialisation, maturation, and remodelling of the scar tissue [6] (Figure 1).

Haemostatic events occur immediately after injury. The exposure of subendothelial collagen and the formation of thrombin lead to the activation of the platelets, located in

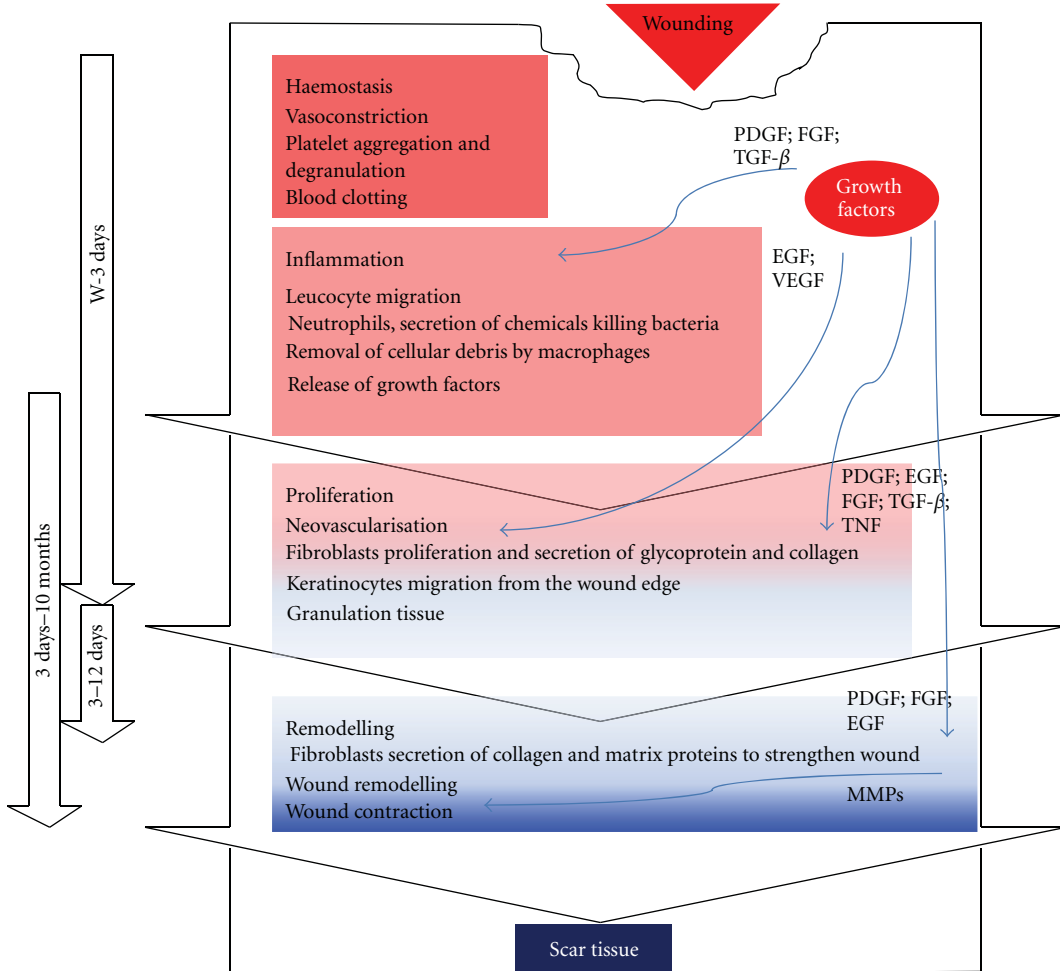


FIGURE 1: The main biological phases in wound healing. The events in wound healing and the soluble factors involved in each phase are well defined. Although presented as separated for absolute clarity, no phase is initiated exactly at the complexion of the previous one, and all phases overlap to a certain degree (see arrows on the left).

the intravascular space. Activated platelets play a trigger role in a number of events:

- activation of the coagulation cascade. This eventually leads to the formation of a fibrin clot that acts as scaffolding for other cells that later enter the wound;
- activation of the complement system;
- platelet degranulation: cells release an array of cytokines, growth factors, and vasoactive substances from the platelet  $\alpha$ -granules, such as platelet-derived growth factor (PDGF), transforming growth factor- $\beta$  (TGF- $\beta$ ), fibroblast growth factor (FGF), endothelial growth factor (EGF), platelet-derived angiogenesis factor, serotonin, bradykinin, platelet-activating factor, thromboxane A2, platelet factor IV, prostaglandins, and histamine. These platelet releases initiate the early events of wound healing [6, 7].

The inflammatory phase begins immediately after injury and may continue for up to 6 days [8]. Growth factors released from the platelets diffuse into tissues surrounding the wound and chemotactically draw inflammatory cells into the

injured area. Neutrophils are the first inflammatory cells to enter the wound, followed by monocytes. Once chemotaxis is completed, local mediators activate the inflammatory cells. Activated neutrophils release a number of lysosomal enzymes (such as elastase, neutral proteases, and collagenase) which proteolytically remove damaged components of extracellular matrix (ECM) [8]. Activated monocytes acquire the macrophage phenotype and aid in host defence [8].

The proliferation phase is characterised by the formation of the ECM and the beginning of angiogenesis. The primary cells involved in this phase are fibroblasts and endothelial cells. They proliferate in response to growth factors and cytokines that are released from macrophages, platelets and mesenchymal cells, or have been stored in the fibrin clot. In addition to chemotactically drawing fibroblasts into the wound, PDGF, FGF, and EGF induce fibroblast activation and proliferation [9]. During the first 2-3 days after-injury, fibroblasts activity predominantly involves migration and proliferation. After this time, fibroblasts release collagen and glycosaminoglycans (mainly hyaluronic acid, chondroitin-4-sulphate, dermatan sulphate, and heparin sulphate) in

response to macrophage-released growth factors, hypoxia and by-products of anaerobic metabolism. The combination of collagen and fibronectin forms the new ECM, which is essential for the development of granulation tissue that eventually fills the wound [6]. Angiogenesis accompanies fibroblast proliferation and allows nutrients and healing factors to enter the wound space. It is also essential for the growth of granulation tissue. The principle growth factors that regulate angiogenesis are FGF, released by damaged endothelial cells and macrophages, and vascular endothelial growth factor (VEGF) which is released by keratinocytes and macrophages [6].

The maturation phase usually begins 3 weeks after injury and can take up to 2 years to complete [10]. Unlike uninjured skin, the arrangement of newly formed collagen fibres in the wound is random and disorganised. The remodelling of collagen fibres into a more organised lattice structure gradually increases the tensile strength of the scar tissue, though this never exceeds 80 percent of the strength of intact skin. Remodelling of the ECM involves a balance between collagen synthesis and degradation, which is operated by several enzymes, like matrix metalloproteinases (MMPs), neutrophil-released elastase and gelatinase, collagenases and stromelysins [11].

Wounds that do not heal within three months are considered chronic. In acute wounds, there is a precise balance between production and degradation of molecules such as collagen; in chronic wounds this balance is lost and degradation plays too large a role. Chronic wound bed has been demonstrated to differ from acute wounds for a higher concentrations of proteases (such as MMPs) [12] and lower levels of growth factors and cytokines [13]. A high and prolonged proteolytic activity may lead to the degradation of growth factors, detaining the wound in the inflammatory stage for too long [14].

## 2. Nanotherapies for Wound Healing

An increasing number of products emerging from the application of nanotechnology to the science of wound healing is currently under clinical investigation. The current nanoscale strategies, both carrier, drug related and scaffold (Figure 2), that target the main phases of wound repair will be discussed, highlighting the cellular signals involved (Table 1).

**2.1. Nanoparticle-Bearing Endogenous Molecules.** As we pointed out previously, soluble active proteins (cytokines and growth factors) govern the progression of the healing phases through the modulation of the cellular and molecular components involved [43]. Because of the control they exert on wound repair, bioactive proteins have gained progressive interest for the treatment of chronic dehiscent wounds. Clinical trials involving the application of exogenous recombinant growth factors to chronic wounds have been conducted for the past 10 years in an attempt to find a way to accelerate healing [44]. Although the results of several pilot trials have been encouraging, the overall results have been somewhat discouraging. To date, only a single recombinant

growth factor—recombinant human PDGF-BB—has been approved by the United States Food and Drug Administration, and only for use in diabetic foot ulcers [45]. In fact, the major limitation to the topical use of growth substances is that in human plasma the half-life of proteins involved in signalling cascades is very short (few seconds) due to close control and inactivation by protease inhibitors [46]. Therefore, the clinical use of endogenous factors as pure compounds is limited by the breakdown by the proteolytic enzymes that enrich the wound site [47]. Several attempts have been already made to provide biological molecules long-term protection from enzymatic degradation (liquids, gels, collagen sponges, and gene transfer). Recently, the development of nanoscale systems for drug delivery has opened new possibilities to enhance the biological efficacy of molecules through a controlled release for extended periods of time [48]. Endogenous active molecules that have been engineered nowadays include thrombin, nitric oxide, growth factors, opioids, and protease inhibitors.

Thrombin (also termed activated factor II or factor IIa) is a protein involved in the final stage of the coagulation cascade activated by wounding. In addition to its well-documented role in the formation of fibrin clots and platelet activation, thrombin has direct effects on inflammatory cells, fibroblasts, and endothelial cells: it stimulates chemotaxis and aggregation of neutrophils, lymphocytes, and monocytes cells, and the proliferation of fibroblasts, epithelial and endothelial cells [49, 50]. Thus, thrombin may play an important role in initiating early cellular events in tissue repair [49]. Since 1988 researchers suggested that thrombin receptor-activating peptides could be useful *in vivo* to mimic the natural effects of thrombin interaction with receptors on various types of cells [51], a delivery systems that could provide thrombin a long-term protection from its natural inhibitors (antithrombin and activated protein C) has been pursued. In recent years, nanobiotechnology has provided the means to enhance the bioavailability of thrombin by conjugation with iron oxide nanoparticles ( $\gamma$ -Fe<sub>2</sub>O<sub>3</sub> conjugation) [15]. Animal models were tested for wound response to the treatment with conjugated thrombin: on a 28-day treated wound, results obtained analysing tensile strength indicated a significant acceleration of healing process when compared with free-thrombin-treated wounds and untreated wounds. Obtaining a greater tensile strength may potentially reduce surgical complications such as wound dehiscence.

Nitric oxide (NO) is a small radical, formed from the amino acid L-arginine by three distinct isoforms of nitric oxide synthase. The inducible isoform (iNOS) is synthesized in the early phase of wound healing by inflammatory cells, mainly macrophages. However, many cells participate in NO synthesis during the proliferative phase after wounding. NO regulates collagen formation, cell proliferation, and wound contraction in distinct ways in animal models of wound healing [52]. NO is also a well-known antimicrobial agent, interfering directly with DNA replication and cell respiration through the inactivation of zinc metalloproteins [53]. Treatment of acute and chronic wound failure with NO has been for years a major unresolved goal. Attempts at novel nitric

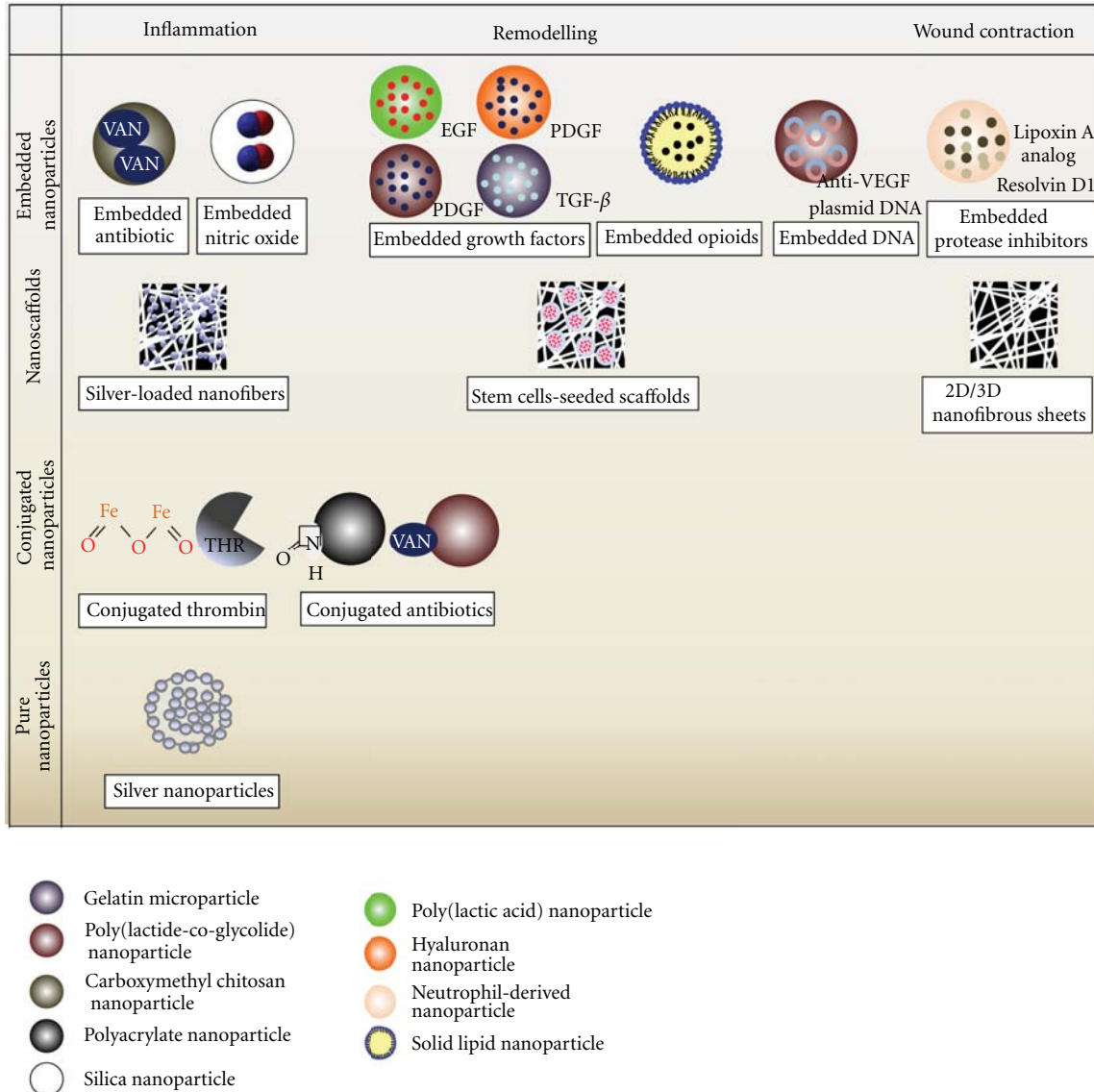


FIGURE 2: Nanostrategies currently in use for promoting skin wound healing. In the main panel, nanostrategies currently in use to improve healing are illustrated. The therapeutic potential of nanosphere-based strategies and nanoscaffolds is emphasized through correlation with the healing phase to which the biological action is targeted. In the right panel, materials explored for nanoparticulate-delivery systems are listed. Two- and three-dimensional nanofibrous sheets can be made of both degradable (collagen and chitosan) and nondegradable (PLA, PLACL, polyurethane, and PVA polymers) nanofibers.

oxide therapies, in the form of nitric oxide donors, have shown limited potential in treating cutaneous infection [54]. A novel approach is offered by recently engineered nanoporous materials, that make possible the storage and delivery of small gaseous short-lived NO, allowing the free radicals to exert their antibacterial activity. Using silane hydrogel-based nanotechnology [23], NO remains trapped and stable within a dry matrix until the matrix is exposed to moisture. The dry matrix allows for NO nanoparticles to be easily stored and applied. Once exposed to moisture, the drug is released from the nanoparticle over an extended period of time at a relatively fixed concentration. This sustained release distinguishes nanoparticles from other vehicles, such as injections, that release a large concentration of the drug with a rapid

return to baseline. The ease of storage, application, and the ability to alter release rate and concentration with minimal risk of toxicity make this powder formulation ideal for cutaneous delivery. Authors showed promising results from NO-releasing nanodelivery systems in preventing and treating skin infections caused by methicillin-resistant *Staphylococcus aureus* (MRSA), which is one of the major causes of hospital-acquired infections [55, 56]. Moreover, NO-releasing silica nanomolecules have been demonstrated to exert a bactericidal activity against *Pseudomonas aeruginosa* [57] and *Acinetobacter baumannii* [58]; both microbial agents have become an increasingly prevalent cause of hospital-acquired infections during the last 15 years, the majority of clinical *A. baumannii*

TABLE 1: Executive summary table.

*Inflammation*

- (i) thrombin is one of the first products of the coagulation cascade occurring during haemostasis, and is responsible for platelet activation and aggregation, leading to the formation of the “platelet plug” and allowing cells and fluid to enter the wound bed. In human plasma, thrombin is rapidly degraded (15 sec). In order to provide long-term protection, it has been conjugated with iron-oxide nanoparticles for treatment of incisional wounds in rats [15]
- (ii) bacterial infection and sepsis exacerbate the inflammatory state and cause tissue damage
  - (a) nanoparticles bearing vancomycin or N-methyliolated  $\beta$  lactams have been developed to act against wound contamination by MRSA [16–19]
  - (b) silver-based nanoparticles were developed to take advantage on the multilevel antibacterial action of silver and try to reduce the development of microbial resistance. Pure biostable nanoparticles were produced through photoassisted reduction and ion stabilization. Silver nanoparticles were also loaded into nanofibers [20]. A direct promotion of wound healing by silver nanoparticles through reduction of the cytokine-modulated inflammation and cell migration and proliferation was also demonstrated [21, 22]
  - (c) donor NO silica nanoparticles showed speed healing by killing both Gram-positive and Gram-negative bacteria and overcoming the NO deficiency [23]. No-releasing nanoparticles may also potentially accelerate healing by a promotion of angiogenesis and tissue remodelling [24]

*Proliferation*

- (i) the aim of growth factors is to promote cell migration into the wound site, stimulate the growth of epithelial cells and fibroblasts, start the formation of new blood vessels, and profoundly influence the remodelling of the scar. To enhance the *in vivo* efficacy of growth factors they have been incorporated into polymer nanocarriers to sustain release. PLA/PLGA/PEG/hyaluronan/gelatin nanoparticles embedded with different growth factors have been successfully applied on skin wounds [25–31]
- (ii) opioids have been recently indicated as factors promoting keratinocytes migration. Solid lipid nanoparticles were embedded with opioids, confirming the influence of these drugs on keratinocytes migration [32, 33]
- (iii) nanofibrous scaffolds: electrospun nanofibers networks support cell adhesion, proliferation, and differentiation mimicking the fibrous architecture of the extracellular matrix. Both degradable (collagen and chitosan) and nondegradable (PLA, PVA, PLACL, and polyurethane) fibers are used for 2D and 3D constructs [34–36]. Scaffolds were also engineered to contain growth factors-releasing nanoparticles enhancing wound repair [37]

*Remodelling*

- (i) matrix metalloproteinase collagenolytic activity appears to be upregulated in chronic wounds. Protease inhibitors were loaded into human derived nanoparticles, showing a proresolving action and accelerated healing [38]
- (ii) gene therapy: nonviral polymeric gene delivery systems offer increased protection from nuclease degradation, enhanced plasmid DNA uptake, and controlled dosing to sustain the duration of plasmid DNA administration. Gene delivery systems are formulated from PLGA polymers, polysaccharides, and chitosan [39–41]
- (iii) stem cells: cell-based therapies hold the potential to promote vascularization and tissue regeneration. The hVEGF gene was delivered through biodegradable polymeric nanoparticles: treated stem cells showed the engraftment of the tissue [42]

isolates displaying high-level resistance to common antibiotics [59]. Also, the beneficial effects of NO seem to overcome the antimicrobial activity and involve directly the healing process. Experiments demonstrated that pharmacological or genetic (NOS knockout) reduction of NO impairs the speed and effectiveness of wound healing, and that this process can be reversed by restoring NO production with increased NOS substrate (arginine), or by transfecting with the missing NOS gene [24]. Thus, application of NO-releasing nanoparticles may potentially accelerate healing not only by killing bacteria but also by a promotion of angiogenesis and tissue remodelling.

The clinical use of growth factors in wound healing has been of great interest recently. They have the potential to accelerate the healing process by attracting cells into the wound site ( $TGF-\beta$ ), promoting cell migration, stimulating the proliferation of epithelial cells and fibroblasts (FGF and PDGF), as well as initiating the formation of new blood vessels (FGF and VEGF), and finally participating in the remodelling of the scar [46]. A mean of enhancing the *in vivo* efficacy of growth factors, preventing degradation from proteolytic

enzymes, is to stabilize protein structure and biological activity, prolonging the length of time over which growth factors are released at the delivery site [60, 61]. The period of drug release from a polymer matrix can be regulated by drug loading, type of polymer used and the processing conditions. Delivery systems have been designed in a variety of configurations and have been fabricated from different types of natural and synthetic polymers, both degradable and non degradable. Poly(lactic acid) (PLA) and poly(lactic-co-glycolic acid) (PLGA) have been demonstrated to be biocompatible and biodegradable suitable materials. To achieve long-term *in vivo* circulation, the surface is generally modified with polyethylene glycol (PEG), reducing the clearance by the reticuloendothelial system [25]. In biodegradable carriers, growth factor release is controlled by the polymer matrix's rate of degradation, which causes changes in the morphological characteristics of the materials, such as porosity and permeability [26]. Particulate delivery systems explored involve  $TGF-\beta$ -embedded gelatine microparticles [27], EGF in PLA microspheres [28], FGF in gelatin microspheres [29], and PDGF-embedded PLGA nanospheres [30]. In general,

porous materials seem to retain a higher specific surface for the adsorption and release of active components and enhancement of drug release. Nevertheless, the particles show some limits which are associated with the use of organic solvents in the production process, leading to pollution and toxicity of the product [62]. Therefore, alternative techniques of fabrications have been proposed, such as spray drying, which is based on the use of supercritical fluids (especially CO<sub>2</sub>) and offers the advantages of being environmentally safe and inexpensive [63]. A notable recent application of this technology for the delivery of growth factors *in vivo* was offered by Zavan et al. [31]: hyaluronan-based (HYAFF11) porous nanoparticles were embedded with PDGF as a system designed for the *in vivo* treatment of skin ulcers. PDGF is known since 1986 to successfully promote chronic wounds healing through a stimulation of chemotaxis, proliferation and ECM deposition [64]. HYAFF11, the benzyl ester of hyaluronic acid, is a biopolymer that has found numerous applications for *in vitro* reconstruction of skin as well as for the *in vivo* regeneration of small arteries and veins [65]. HYAFF particles have the ability to absorb growth factors and to release them in a temporally and spatially specific event-driven manner. This timed and localized release of PDGF promoted optimal tissue repair and regeneration of full-thickness wounds.

Beside the dedicated growth factors, opioids have been recently indicated as factors promoting keratinocytes migration [66]. This finding is of great interest because of a possible enhancement of wound healing through topical applications of opioids at the wound site for pain reduction. Conventional formulations failed to consistently provide sufficient pain control in patients, possibly due to local drug degradation or insufficient concentrations at the target site [32]. Since long intervals for painful wound dressing changes are intended, the formulations should allow for prolonged opioid release. Bigliardi et al. [32] first developed nanoparticulate carriers to increase opioids skin penetration and slow the release of the loaded drug. Experiments on human keratinocyte-derived cell line HaCaT showed that opioids stimulated cell migration and closure of experimental wounds. Enhancement of migration was concentration-dependent and could be blocked by the opioid receptor antagonist naloxone, indicating a specific opioid-receptor interaction. Küchler followed [33] demonstrating that morphine-loaded solid lipid nanoparticles accelerated reepithelialisation on a human-based 3D-wound healing model. On standardised wounds, keratinocytes almost completely covered the dermis equivalent after 4 days, which was not the case when applying the unloaded particles. In conclusion, acceleration of wound closure, low cytotoxicity, and irritation as well as possible prolonged morphine release make solid lipid nanoparticles an interesting approach for innovative wound management.

Matrix metallo proteinases (MMPs) are zinc-dependent endopeptidases that cleave most macromolecules within the ECM during the maturation of the wound [67]. The process of remodelling constitutes a balance between collagen production, breakdown, and remodelling. The biological activity of MMPs is strictly balanced by the presence of specific tissue inhibitors (TIMPs). A tightly coordinated expression of specific combinations of MMPs and TIMPs appears to be

necessary for proper wound maturation. As previously stated, an uncontrolled proteolytic activity leads to delayed healing through degradation of growth factors. In light of these considerations, research approaches to improve the remodelling phase are directed to manage enzymatic activity of MMPs through the topical application of protease inhibitors. Norling et al. [38] recently took advantage of aspirin-triggered resolving D1 and lipoxin A4 analogs and developed a carrier providing stable biological activity to these natural compounds. Human-derived nanoparticles were enriched with the protease inhibitors, and wound healing reactions were tested in a murine model. Polymorphonuclear cell influx showed a dramatical reduction in treated wounds, with shortened resolution intervals, and a proresolving action that in the end accelerated healing.

**2.2. Nanoparticle-Bearing Antibiotics.** During the healing process, infection is an issue potentially compromising the final wound closure, exacerbating the tissue damage [68]. Nowadays, wound infection is no longer the ominous event as at the beginning of the 20th Century, when infection of wounds, especially burns, was the major cause of morbidity and mortality (over 50%) [69]. Nevertheless, an appropriate antimicrobial therapy of the wound controlling colonization and proliferation of microbial pathogens, including multi-drug-resistant organisms, is still required for an appropriate wound care. *Staphylococcus aureus* one of the most common pathogens involved in wound infections. The pharmaceutical treatment encounters today severe limitations due to the development of antibiotic resistant strains. For example, penicillinase (an enzyme that breaks down the β-lactam ring of the penicillin molecule) is responsible for the resistance to penicillin of *Staphylococcus aureus*: the failed treatment of staphylococcal local infections leads to the onset of serious late complications (bacteraemia, sepsis, toxic shock syndrome) [69].

The delivery of antibiotic therapy via nanoparticles offers great potential advantages. Particularly, a controlled release would decrease the number of doses required to achieve the desired clinical effect, potentially reducing the risk of development of antibiotic resistance. The physicochemical properties of nanoparticulate drug delivery systems (size, surface charge, and nature) are determinant *in vivo* for the factors delivery. In particular, it is known that 20–200 nm particulates are suitable for delivery of therapeutics; larger size particles suffer from quick uptake by the reticulo-endothelial system and rapid clearance from circulation, whereas the smaller size will tend to cross the fenestration in the hepatic sinusoidal endothelium, leading to hepatic accumulation [70].

In the treatment of staphylococcal infections, the latest generation antibiotic and assumed to be the most useful at the moment is vancomycin. Several vancomycin-modified nanoparticles have been developed to enhance the pharmacokinetics and pharmacodynamics of the antibiotic molecule. Hachicha et al. [16] recently proposed the use of vancomycin-conjugated nanoparticles for intraocular continuous release injection for endophthalmitis prophylaxis. The drug concentration was proved to be maintained above

the minimal inhibitory limit for 24 hours. Chakraborty et al. [17] developed carboxymethyl chitosan-based nanoparticles, which were loaded with vancomycin and proved effective against drug-resistant staphylococcal strains.

The effectiveness of nanobiotechnology in enhancing the therapeutic properties of antibiotic molecules is emphasized by the case of N-methylthiolated  $\beta$ -lactams: these compounds have been recently identified and proved effective against *Staphylococcus* bacteria, including MRSA. These lactams exert growth inhibitory effects on bacteria through a mode of action that is distinctively different from other  $\beta$ -lactam antibiotics, with peculiar structure-activity patterns. Nevertheless, their potential application is limited by the exceeding low water solubility [18]. Thus, a methodology was developed by Turos et al. [19] to obtain an emulsion of polyacrylate nanoparticles in which the drug monomer was incorporated into the polymeric matrix: *in vitro* screens confirmed the nanoparticles to be nontoxic to human dermal fibroblasts and stable in blood serum for 24 hours.

Within the bacterial species, resistance to all known antibiotic classes has occurred due to mutation and horizontal gene transfer. This has led to anxiety regarding the future availability of effective chemotherapeutic options. Due to the outbreak of infectious diseases caused by different pathogenic bacteria and the development of antibiotic resistance, the pharmaceutical companies and the researchers are now searching for new antibacterial agents.

**2.3. Silver-Based Nanoparticles.** The use of silver for the treatment of ulcers is reported since the 5th Century B.C. In the 17th and 18th centuries, silver nitrate was already used for ulcer treatment. The antimicrobial activity of silver was established in the 19th century. Nevertheless, after the introduction of antibiotics in 1940 the use of silver salts decreased. Subsequently, silver salts and silver compounds have been used in different biomedical fields, especially in burn treatment [71].

The antimicrobial activity of silver appears high: due to its multilevel (including multidrug resistance) antibacterial effects [72] and low systemic toxicity [73], it provides an antibacterial effect that considerably reduce the chances of developing resistance. Evidently, the greatest rate of silver ions release is wished in order to enhance the clinical effect and avoid the insurgence of silver-resistant mutant bacteria. Nanotechnology has provided the means of producing pure biostable silver nanoparticles, either through photoassisted reduction and ion stabilization or loading of the metallic particles into nanofibers [20]. In all cases, 7–20 nm silver nanoparticles exhibited antibacterial (especially anti-Gram negative) and antifungal activity, and they are also synergistic to common antibiotic therapy (streptomycin, kanamycin, and polymyxin B) [20]. Studies *in vivo* demonstrated also a direct promotion of wound healing by silver nanoparticles through reduction of the cytokine-modulated inflammation: silver-induced neutrophils apoptosis, decreased MMPs activity, and negative modulation on TGF- $\beta$  resulted in an overall acceleration of wound healing rate and reduction on hypertrophic scarring [21]. Also, wound healing rate was demonstrated to be increased by silver ions by a promotion of proliferation

and migration of keratinocytes along with a differentiation of fibroblasts into myofibroblasts, thereby promoting wound contraction [22].

Though the progressive expansion of the therapeutic application of silver nanoparticles, the use of a metallic compound carries possible side effects that must be taken into consideration. Studies have been investigating the biosafety of silver as a therapeutic agent, reporting an acceptable biocompatibility [74], though the occasional development of argyria (a cosmetic blue-grey coloration of the skin).

**2.4. Nanoparticles and Gene Therapy.** Polymeric gene delivery systems offer several advantages for plasmid DNA delivery, such as protection from degradation by the nuclelease and controlled prolonged release. The potential retained by the modulation of gene expression in the process of wound healing lead researchers to apply for an engineered system for DNA transfection. Actually, transfection capability has been tested *in vitro*: biocompatible and biodegradable PLGA polymers [39] were engineered to obtain high plasmid loading efficiency [75] and then loaded with antiangiogenic plasmid DNA (pFlt23k). The PLGA nanoparticles were prepared by a supercritical fluid extraction of emulsions based on CO<sub>2</sub>: this allowed high loading of pDNA (19.7%, w/w), high loading efficiency (>98%), and low residual solvents (<50 ppm). The VEGF secretion by epithelial cells was significantly reduced, showing a potential value in treating wound disorders in which VEGF is elevated.

In the course of studies on nonviral DNA carriers for gene delivery and therapy other materials have been applied, like polysaccharides and other cationic polymers. Chitosan also was found to be particularly suitable, since it can promote long-term release of incorporated drugs [76]. Masotti and Ortaggi recently described a nanofabrication method that may be useful for obtaining small DNA-containing chitosan nanospheres (38 ± 4 nm) for biomedical applications [40]. Their reported osmosis-based method has general applicability to various synthetic or natural biopolymers, resulting in nanostructured systems of different size and shape that may be used in several biotechnological applications. Chellat et al. also recently took advantage of the biochemical properties of chitosan to test DNA-loaded nanoparticles on a human macrophage cell line to study the potential modulation of the expression of proinflammatory cytokines, metalloproteinases and their specific inhibitors [41]. The secretion of MMP-9 in cell supernatants increased significantly after 24 and 48 h in comparison with nontreated cells. MMP-2 secretion was augmented only after 48 h with incubation of the highest concentrations of nanoparticles (10 and 20  $\mu$ g/mL DNA content). However, zymography studies showed that secreted MMPs were in their proactive form, while in the presence of 10 and 20  $\mu$ g/mL DNA-containing nanoparticles, the active form of MMP-9, but not MMP-2, was detected in cell lysates. The results obtained were significative only for increased secretion of metalloproteinases, possibly related to nanoparticles phagocytosis.

**2.5. Nanoparticles and Stem Cells.** Stem cells are lauded for their unique ability to develop into every kind of cell. Even if

*in vivo* studies and clinical trials have demonstrated limitations in reconstituting tissue due to the lack of microenvironment-control on proliferation and survival, the successful use of these cells for investigation towards disease therapy is still pursued. Last decade has witnessed a growth in the field of nanoparticles technology for stem cells isolation, maintenance, and regulation: nanoparticles and nano 3D architectures have been developed to control stem cells proliferation, differentiation, and maturation [77]. In terms of skin regeneration, VEGF high-expressing, transiently modified stem cells have been developed for the purpose of promoting angiogenesis [42]. In order to overcome the insufficient expression of angiogenic factors and low cell viability after transplantation, nanotechnology has provided nonviral, biodegradable polymeric nanoparticles to deliver hVEGF gene to human mesenchymal stem cells (hMSCs) and human embryonic stem cell-derived cells (hESCs). Treated stem cells demonstrated markedly enhanced hVEGF production, cell viability, and engraftment into target tissues. Implantation of scaffolds seeded with VEGF-expressing stem cells (hMSCs and hESCs) led from 2 to 4 fold higher vessel densities 2 weeks after implantation, compared with control cells or cells transfected with VEGF by using Lipofectamine 2000, a leading commercial reagent. Four weeks after intramuscular injection into mouse ischemic hindlimbs, genetically modified hMSCs substantially enhanced angiogenesis and limb salvage, while reducing muscle degeneration and tissue fibrosis [42]. These results indicate that stem cells engineered with biodegradable polymer nanoparticles may be therapeutic tools for vascularizing tissue constructs and treating ischemic disease.

**2.6. Nanofibrous Scaffolds.** The basic strategy of engineered tissue regeneration is the construction of a biocompatible scaffold that, in combination with living cells and/or bioactive molecules, replaces, regenerates, or repairs damaged tissues. The scaffold should possess suitable properties, like biocompatibility, controlled porosity and permeability, and, additionally, support for cell attachment and proliferation. This artificial “dermal layer” needs to adhere to and integrate with the wound, which is not always successful for the current artificial dermal analogues available. The high cost of these artificial dermal analogues also makes their application prohibitive both to surgeons and patients. Engineering dermal substitutes with electrospun nanofibres have lately been of prime importance for skin tissue regeneration. Simple electro spinning technology served to produce nanofibrous scaffolds morphologically and structurally similar to the extracellular matrix of native tissues. The engineered network has been shown to support cell adhesion, proliferation, and differentiation mimicking the fibrous architecture of the extracellular matrix [60]. The large surface area and porosity of electrospun nanofibers enables good permeability for oxygen and water and the adsorption of liquids, and concomitantly protects the wound from bacterial penetration and dehydration. This feature shows electrospun nanofibers to be a suitable material for wound dressing, especially for chronic wounds such as diabetic ulcers or burns.

The electro spinning technique can provide both degradable (collagen; chitosan) and nondegradable (PLA, polyvinyl alcohol (PVA) polymers) nanofibers for two-dimensional nanofibrous sheets. Both sorts of biomaterials have been tested *in vivo* showing an increased rate of wound epithelialisation and dermis organization [34], as well as good antibacterial activity against the Gram-positive and Gram-negative bacteria [35]. Nanofibrous scaffolds of poly(L-lactic acid)-co-poly( $\epsilon$ -caprolactone) (PLACL) and PLACL/gelatin complexes were fabricated by Chandrasekaran et al. [36]. These nanofibres were characterized by fiber morphology, membrane porosity, wettability, and chemical properties by FTIR analysis to culture human foreskin fibroblasts for skin tissue engineering. The results showed that fibroblasts proliferation, morphology, and secretion of collagen were significantly increased in plasma-treated PLACL/gelatin scaffolds compared to PLACL nanofibrous scaffolds. The obtained results proved that the plasma-treated PLACL/gelatin nanofibrous scaffold is a potential biocomposite material for skin tissue regeneration.

Moreover, nanofibrous constructs can be obtained with a 3D profile, even though they scarcely support cells seeding because of their high porosity. Several strategies have been developed to improve cell infiltration, showing promising results [79]. Chong et al. [80] proposed a cost-effective composite consisting of a nanofibrous scaffold directly electrospun onto a polyurethane dressing (Tegaderm, 3 M Medical)—Tegaderm-nanofiber (TG-NF) construct—for dermal wound healing. Cell culture was performed on both sides of the nanofibrous scaffold and tested for fibroblast adhesion and proliferation. Results obtained in this study suggested that both the TG-NF construct and dual-sided fibroblast-populated nanofiber construct achieved significant cell adhesion, growth, and proliferation. This was a successful first step for the nanofiber construct in establishing itself as a suitable three-dimensional scaffold for autogenous fibroblast populations and providing great potential in the treatment of dermal wounds through layered application.

Steps towards an enhanced regenerative effect will be to provide scaffolds a delivery system for drugs, growth factors or cytokines that may further promote cell function and tissue regeneration [81]. Jin et al. already worked towards this direction engineering PLGA microspheres in nanofibrous scaffolds to control the release of PDGF *in vivo* [37]. PDGF concentration was evaluated in a soft tissue wound repair model in the dorsa of rats. At 3, 7, 14, and 21 days after-implantation, the scaffold implants were harvested followed by assessments of cell penetration, vasculogenesis, and tissue neogenesis. Gene expression profiles using cDNA microarrays were performed on the PDGF-releasing NFS. The percentage of tissue invasion into microspheres-containing nanofibrous scaffolds at 7 days was higher in the PDGF groups when compared to controls. Blood vessel number in the groups containing either 2.5 or 25  $\mu$ g PDGF was increased above those of other groups at 7d ( $P < 0.01$ ). Results from cDNA array showed that PDGF strongly enhanced *in vivo* gene expression of the CXC chemokine family members such as CXCL1, CXCL2, and CXCL5. Thus, sustained release of rhPDGF-BB, controlled by slow-releasing microspheres

associated with the nanofibrous scaffold delivery system, enhanced cell migration and angiogenesis *in vivo*, and may be related to an induced expression of chemokine-related genes. This approach offers a technology to accurately control growth factor release to promote soft tissue engineering *in vivo*.

### 3. Conclusions

In recent years, nanomedicine has experienced a progressive expansion: its great potential has attracted considerable investments from governments and industry, which are predicted to increase in the near future, leading to further enhancement and development. Similarly, the knowledge of the cellular and molecular processes underlying wound healing has reached a level which let researchers apply for new therapeutic approaches that act directly on cellular and subcellular events during the healing process. Nanotechnology today offers the means to overcome the dimensional barrier of currently used therapies for wounds and ulcers, to reach a dysfunctional molecular target and exert the therapeutic action straight at the origin of the chronic condition. Nanocarriers possess an enormous potential, as nanoparticles-based delivery systems can be highly beneficial to augment the therapeutic power of biological and synthetic molecules. However the promising results brought by new technologies in therapeutics, the real biological effects of nanoparticles have to be carefully assessed before introducing their use in clinical practice. In particular, the release of active peptides may possibly cause interferences with some biological functions and cellular processes. With regard to this, the incorporation of a targeting ligand into nanoparticles has been proposed, in order to give them site-specificity; also, a wide variety of biomaterials has been prompted to meet the specific biological requirements [82]. This could be especially critical for tissue regeneration, where the biomaterial properties could augment the reparative process, or hinder it due to undesirable attributes of the material.

Despite its recognized importance, there have not been systemic studies that probe the targeting efficiency of nanoparticles nor international standards on their toxicology and biocompatibility. Our wish is that further research is to be extended to the applied science of nanotechnology. The revolutionary potential offered by nanoscale therapeutics applied to wound healing involves the need to develop international standards on their biocompatibility. A safe and targeted use is required to prove beneficial to such a world-wide issue, which is chronic wounds and ulcers care.

### References

- [1] R. N. Seetharam, "Nanomedicine—emerging area of nanobiotechnology research," *Current Science*, vol. 91, no. 3, p. 260, 2006.
- [2] S. Sandhiya, S. A. Dkhar, and A. Surendiran, "Emerging trends of nanomedicine—an overview," *Fundamental and Clinical Pharmacology*, vol. 23, no. 3, pp. 263–269, 2009.
- [3] S. S. Suri, H. Fenniri, and B. Singh, "Nanotechnology-based drug delivery systems," *Journal of Occupational Medicine and Toxicology*, vol. 2, no. 1, article no. 16, 2007.
- [4] I. L. Medintz, H. Mattoussi, and A. R. Clapp, "Potential clinical applications of quantum dots," *International Journal of Nanomedicine*, vol. 3, no. 2, pp. 151–167, 2008.
- [5] B. M. Kuehn, "Chronic wound care guidelines issued," *Journal of the American Medical Association*, vol. 297, no. 9, pp. 938–939, 2007.
- [6] W. K. Stadelmann, A. G. Digenis, and G. R. Tobin, "Physiology and healing dynamics of chronic cutaneous wounds," *The American Journal of Surgery*, vol. 176, no. 2, supplement 1, pp. 26S–38S, 1998.
- [7] D. L. Steed, "The role of growth factors in wound healing," *Surgical Clinics of North America*, vol. 77, no. 3, pp. 575–586, 1997.
- [8] D. M. Simpson and R. Ross, "The neutrophilic leukocyte in wound repair a study with antineutrophil serum," *Journal of Clinical Investigation*, vol. 51, no. 8, pp. 2009–2023, 1972.
- [9] M. B. Witte and A. Barbul, "General principles of wound healing," *Surgical Clinics of North America*, vol. 77, no. 3, pp. 509–528, 1997.
- [10] D. M. Cooper, "Optimizing wound healing. A practice within nursing's domain," *Nursing Clinics of North America*, vol. 25, no. 1, pp. 165–180, 1990.
- [11] J. W. Madden and E. E. Peacock, "Studies on the biology of collagen during wound healing. I. Rate of collagen synthesis and deposition in cutaneous wounds of the rat," *Surgery*, vol. 64, no. 1, pp. 288–294, 1968.
- [12] N. T. Bennett and G. S. Schultz, "Growth factors and wound healing: part II. Role in normal and chronic wound healing," *The American Journal of Surgery*, vol. 166, no. 1, pp. 74–81, 1993.
- [13] C. Chen, G. S. Schultz, M. Bloch, P. D. Edwards, S. Tebes, and B. A. Mast, "Molecular and mechanistic validation of delayed healing rat wounds as a model for human chronic wounds," *Wound Repair and Regeneration*, vol. 7, no. 6, pp. 486–494, 1999.
- [14] D. R. Yager, S. M. Chen, S. I. Ward, O. O. Olutoye, R. F. Diegelmann, and I. K. Cohen, "Ability of chronic wound fluids to degrade peptide growth factors is associated with increased levels of elastase activity and diminished levels of proteinase inhibitors," *Wound Repair and Regeneration*, vol. 5, no. 1, pp. 23–32, 1997.
- [15] O. Ziv-Polat, M. Topaz, T. Brosh, and S. Margel, "Enhancement of incisional wound healing by thrombin conjugated iron oxide nanoparticles," *Biomaterials*, vol. 31, no. 4, pp. 741–747, 2010.
- [16] W. Hachicha, L. Kodjikian, and H. Fessi, "Preparation of vancomycin microparticles: importance of preparation parameters," *International Journal of Pharmaceutics*, vol. 324, no. 2, pp. 176–184, 2006.
- [17] S. P. Chakraborty, S. K. Sahu, S. K. Mahapatra et al., "Nan conjugated vancomycin: new opportunities for the development of anti-VRSA agents," *Nanotechnology*, vol. 21, no. 10, Article ID 105103, 2010.
- [18] K. Greenhalgh and E. Turos, "In vivo studies of polyacrylate nanoparticle emulsions for topical and systemic applications," *Nanomedicine*, vol. 5, no. 1, pp. 46–54, 2009.
- [19] E. Turos, J. Y. Shim, Y. Wang et al., "Antibiotic-conjugated polyacrylate nanoparticles: new opportunities for development of anti-MRSA agents," *Bioorganic and Medicinal Chemistry Letters*, vol. 17, no. 1, pp. 53–56, 2007.

- [20] J. Jain, S. Arora, J. M. Rajwade, P. Omray, S. Khandelwal, and K. M. Paknikar, "Silver nanoparticles in therapeutics: development of an antimicrobial gel formulation for topical use," *Molecular Pharmaceutics*, vol. 6, no. 5, pp. 1388–1401, 2009.
- [21] A. D. Widgerow, "Nanocrystalline silver, gelatinases and the clinical implications," *Burns*, vol. 36, no. 7, pp. 965–974, 2010.
- [22] X. Liu, P. Y. Lee, C. M. Ho et al., "Silver nanoparticles mediate differential responses in keratinocytes and fibroblasts during skin wound healing," *ChemMedChem*, vol. 5, no. 3, pp. 468–475, 2010.
- [23] A. J. Friedman, G. Han, M. S. Navati et al., "Sustained release nitric oxide releasing nanoparticles: characterization of a novel delivery platform based on nitrite containing hydrogel/glass composites," *Nitric Oxide*, vol. 19, no. 1, pp. 12–20, 2008.
- [24] K. Yamasaki, H. D. J. Edington, C. McClosky et al., "Reversal of impaired wound repair in iNOS-deficient mice by topical adenoviral-mediated iNOS gene transfer," *Journal of Clinical Investigation*, vol. 101, no. 5, pp. 967–971, 1998.
- [25] G. Molineux, "Pegylation: engineering improved pharmaceuticals for enhanced therapy," *Cancer Treatment Reviews*, vol. 28, supplement 1, pp. 13–16, 2002.
- [26] O. I. Corrigan and X. Li, "Quantifying drug release from PLGA nanoparticulates," *European Journal of Pharmaceutical Sciences*, vol. 37, no. 3-4, pp. 477–485, 2009.
- [27] T. A. Holland, J. K. V. Tessmar, Y. Tabata, and A. G. Mikos, "Transforming growth factor- $\beta$ 1 release from oligo(ethylene glycol) fumarate hydrogels in conditions that model the cartilage wound healing environment," *Journal of Controlled Release*, vol. 94, no. 1, pp. 101–114, 2004.
- [28] K. Han, K. D. Lee, Z. G. Gao, and J. S. Park, "Preparation and evaluation of poly(L-lactic acid) microspheres containing rhEGF for chronic gastric ulcer healing," *Journal of Controlled Release*, vol. 75, no. 3, pp. 259–269, 2001.
- [29] K. Kawai, S. Suzuki, Y. Tabata, and Y. Nishimura, "Accelerated wound healing through the incorporation of basic fibroblast growth factor-impregnated gelatin microspheres into artificial dermis using a pressure-induced decubitus ulcer model in genetically diabetic mice," *British Journal of Plastic Surgery*, vol. 58, no. 8, pp. 1115–1123, 2005.
- [30] G. Wei, Q. Jin, W. V. Giannobile, and P. X. Ma, "Nano-fibrous scaffold for controlled delivery of recombinant human PDGF-BB," *Journal of Controlled Release*, vol. 112, no. 1, pp. 103–110, 2006.
- [31] B. Zavan, V. Vindigni, K. Vezzù et al., "Hyaluronan based porous nano-particles enriched with growth factors for the treatment of ulcers: a placebo-controlled study," *Journal of Materials Science: Materials in Medicine*, vol. 20, no. 1, pp. 235–247, 2009.
- [32] P. L. Bigliardi, D. J. Tobin, C. Gaveriaux-Ruff, and M. Bigliardini-Qi, "Opioids and the skin—where do we stand?" *Experimental Dermatology*, vol. 18, no. 5, pp. 424–430, 2009.
- [33] S. Küchler, N. B. Wolf, S. Heilmann et al., "3D-Wound healing model: influence of morphine and solid lipid nanoparticles," *Journal of Biotechnology*, vol. 148, no. 1, pp. 24–30, 2010.
- [34] M.-S. Khil, D.-I. Cha, H.-Y. Kim, I.-S. Kim, and N. Bhattacharai, "Electrospun nanofibrous polyurethane membrane as wound dressing," *Journal of Biomedical Materials Research B*, vol. 67, no. 2, pp. 675–679, 2003.
- [35] C. C. Wang, C. H. Su, and C. C. Chen, "Water absorbing and antibacterial properties of N-isopropyl acrylamide grafted and collagen/chitosan immobilized polypropylene nonwoven fabric and its application on wound healing enhancement," *Journal of Biomedical Materials Research A*, vol. 84, no. 4, pp. 1006–1017, 2008.
- [36] A. R. Chandrasekaran, J. Venugopal, S. Sundarrajan, and S. Ramakrishna, "Fabrication of a nanofibrous scaffold with improved bioactivity for culture of human dermal fibroblasts for skin regeneration," *Biomedical Materials*, vol. 6, no. 1, 2011.
- [37] Q. Jin, G. Wei, Z. Lin et al., "Nanofibrous scaffolds incorporating PDGF-BB microspheres induce chemokine expression and tissue neogenesis in vivo," *PLoS One*, vol. 3, no. 3, Article ID e1729, 2008.
- [38] L. V. Norling, M. Spite, R. Yang, R. J. Flower, M. Perretti, and C. N. Serhan, "Cutting edge: Humanized nano-proresolving medicines mimic inflammation-resolution and enhance wound healing," *Journal of Immunology*, vol. 186, no. 10, pp. 5543–5547, 2011.
- [39] I.-S. Kim, S.-K. Lee, Y.-M. Park et al., "Physicochemical characterization of poly(l-lactic acid) and poly(d,l-lactide-co-glycolide) nanoparticles with polyethylenimine as gene delivery carrier," *International Journal of Pharmaceutics*, vol. 298, no. 1, pp. 255–262, 2005.
- [40] A. Masotti and G. Ortaggi, "Chitosan micro- and nanospheres: fabrication and applications for drug and DNA delivery," *Mini-Reviews in Medicinal Chemistry*, vol. 9, no. 4, pp. 463–469, 2009.
- [41] F. Chellat, A. Grandjean-Laquerrière, R. Le Naour et al., "Metalloproteinase and cytokine production by THP-1 macrophages following exposure to chitosan-DNA nanoparticles," *Biomaterials*, vol. 26, no. 9, pp. 961–970, 2005.
- [42] F. Yang, S.-W. Cho, S. M. Son et al., "Genetic engineering of human stem cells for enhanced angiogenesis using biodegradable polymeric nanoparticles," *Proceedings of the National Academy of Sciences of the United States of America*, vol. 107, no. 8, pp. 3317–3322, 2010.
- [43] S. Werner and R. Grose, "Regulation of wound healing by growth factors and cytokines," *Physiological Reviews*, vol. 83, no. 3, pp. 835–870, 2003.
- [44] G. Lenz and P. Mansson, "Growth factors as pharmaceuticals," *Pharmaceutical technology*, vol. 15, no. 1, pp. 34–38, 1991.
- [45] P. Senet, E. Vicaut, N. Beneton, C. Debure, C. Lok, and O. Chosidow, "Topical treatment of hypertensive leg ulcers with platelet-derived growth factor-BB: a randomized controlled trial," *Archives of Dermatology*, vol. 147, no. 8, pp. 926–930, 2011.
- [46] A. J. Singer and R. A. F. Clark, "Cutaneous wound healing," *The New England Journal of Medicine*, vol. 341, no. 10, pp. 738–746, 1999.
- [47] G. Murphy and H. Nagase, "Progress in matrix metalloproteinase research," *Molecular Aspects of Medicine*, vol. 29, no. 5, pp. 290–308, 2009.
- [48] A. MaHam, Z. Tang, H. Wu, J. Wang, and Y. Lin, "Protein-based nanomedicine platforms for drug delivery," *Small*, vol. 5, no. 15, pp. 1706–1721, 2009.
- [49] D. H. Carney, R. Mann, W. R. Redin et al., "Enhancement of incisional wound healing and neovascularization in normal rats by thrombin and synthetic thrombin receptor-activating peptides," *Journal of Clinical Investigation*, vol. 89, no. 5, pp. 1469–1477, 1992.
- [50] U. Amara, D. Rittirsch, M. Flierl et al., "Interaction between the coagulation and complement system," *Advances in Experimental Medicine and Biology*, vol. 632, pp. 71–79, 2008.
- [51] K. C. Glenn, G. H. Frost, J. S. Bergmann, and D. H. Carney, "Synthetic peptides bind to high-affinity thrombin receptors and modulate thrombin mitogenesis," *Peptide Research*, vol. 1, no. 2, pp. 65–73, 1988.
- [52] M. R. Schäffer, P. A. Efron, F. J. Thornton, K. Klingel, S. S. Gross, and A. Barbul, "Nitric Oxide, and Autocrine Regulator

- of Wound Fibroblast Synthetic Function,” *The Journal of Immunology*, vol. 158, no. 5, pp. 2375–2381, 1997.
- [53] R. Weller, R. J. Price, A. D. Ormerod, N. Benjamin, and C. Leifert, “Antimicrobial effect of acidified nitrite on dermatophyte fungi, *Candida* and bacterial skin pathogens,” *Journal of Applied Microbiology*, vol. 90, no. 4, pp. 648–652, 2001.
- [54] L. Englande and A. Friedman, “Nitric oxide nanoparticle technology: a novel antimicrobial agent in the context of current treatment of skin and soft tissue infection,” *Journal of Clinical and Aesthetic Dermatology*, vol. 3, no. 6, pp. 45–50, 2010.
- [55] C. Miller, B. McMullin, A. Ghaffari et al., “Gaseous nitric oxide bactericidal activity retained during intermittent high-dose short duration exposure,” *Nitric Oxide*, vol. 20, no. 1, pp. 16–23, 2009.
- [56] L. R. Martinez, G. Han, M. Chacko et al., “Antimicrobial and healing efficacy of sustained release nitric oxide nanoparticles against *Staphylococcus aureus* skin infection,” *Journal of Investigative Dermatology*, vol. 129, no. 10, pp. 2463–2469, 2009.
- [57] N. Barraud, D. Schleheck, J. Klebensberger et al., “Nitric oxide signaling in *Pseudomonas aeruginosa* biofilms mediates phosphodiesterase activity, decreased cyclic di-GMP levels, and enhanced dispersal,” *Journal of Bacteriology*, vol. 191, no. 23, pp. 7333–7342, 2009.
- [58] M. R. Mihu, U. Sandkovsky, G. Han, J. M. Friedman, J. D. Nosanchuk, and L. R. Martinez, “Nitric oxide releasing nanoparticles are therapeutic for *Acinetobacter baumannii* wound infections,” *Virulence*, vol. 1, no. 2, pp. 62–67, 2010.
- [59] A. Y. Peleg, H. Seifert, and D. L. Paterson, “*Acinetobacter baumannii*: emergence of a successful pathogen,” *Clinical Microbiology Reviews*, vol. 21, no. 3, pp. 538–582, 2008.
- [60] P. A. Tran, L. Zhang, and T. J. Webster, “Carbon nanofibers and carbon nanotubes in regenerative medicine,” *Advanced Drug Delivery Reviews*, vol. 61, no. 12, pp. 1097–1114, 2009.
- [61] Z. Degim, “Use of microparticulate systems to accelerate skin wound healing,” *Journal of Drug Targeting*, vol. 16, no. 6, pp. 437–448, 2008.
- [62] F. Ungaro, G. De Rosa, A. Miro, F. Quaglia, and M. I. La Rotonda, “Cyclodextrins in the production of large porous particles: development of dry powders for the sustained release of insulin to the lungs,” *European Journal of Pharmaceutical Sciences*, vol. 28, no. 5, pp. 423–432, 2006.
- [63] K. A. Abbas, A. Mohamed, A. S. Abdulamir, and H. A. Abas, “A review on supercritical fluid extraction as new analytical method,” *American Journal of Biochemistry and Biotechnology*, vol. 4, no. 4, pp. 345–353, 2008.
- [64] D. R. Knighton, K. F. Ciresi, and V. D. Fiegel, “Classification and treatment of chronic nonhealing wounds: successful treatment with autologous platelet-derived wound healing factors (PDWHF),” *Annals of Surgery*, vol. 204, no. 3, pp. 322–330, 1986.
- [65] S. Lepidi, G. Abatangelo, V. Vindigni et al., “In vivo regeneration of small-diameter (2 mm) arteries using a polymer scaffold,” *The FASEB Journal*, vol. 20, no. 1, pp. 103–105, 2006.
- [66] N. B. Wolf, S. Küchler, M. R. Radowski et al., “Influences of opioids and nanoparticles on in vitro wound healing models,” *European Journal of Pharmaceutics and Biopharmaceutics*, vol. 73, no. 1, pp. 34–42, 2009.
- [67] C. L. Baum and C. J. Arpey, “Normal cutaneous wound healing: clinical correlation with cellular and molecular events,” *Dermatologic Surgery*, vol. 31, no. 6, pp. 674–686, 2005.
- [68] J. Hurlow and P. G. Bowler, “Clinical experience with wound biofilm and management: a case series,” *Ostomy Wound Management*, vol. 55, no. 4, pp. 38–49, 2009.
- [69] M. Qadan and W. G. Cheadle, “Common Microbial Pathogens in Surgical Practice,” *Surgical Clinics of North America*, vol. 89, no. 2, pp. 295–310, 2009.
- [70] S. M. Moghimi, A. C. Hunter, and J. C. Murray, “Long-circulating and target-specific nanoparticles: theory to practice,” *Pharmacological Reviews*, vol. 53, no. 2, pp. 283–318, 2001.
- [71] H. J. Klasen, “A historical review of the use of silver in the treatment of burns. II. Renewed interest for silver,” *Burns*, vol. 26, no. 2, pp. 131–138, 2000.
- [72] A. Melaiye and W. J. Youngs, “Silver and its application as an antimicrobial agent,” *Expert Opinion on Therapeutic Patents*, vol. 15, no. 2, pp. 125–130, 2005.
- [73] J. Fong and F. Wood, “Nanocrystalline silver dressings in wound management: a review,” *International Journal of Nanomedicine*, vol. 1, no. 4, pp. 441–449, 2006.
- [74] J. Ai, E. Biazar, M. Jafarpour et al., “Nanotoxicology and nanoparticle safety in biomedical designs,” *International Journal of Nanomedicine*, vol. 6, pp. 1117–1127, 2011.
- [75] A. S. Mayo, B. K. Ambati, and U. B. Kompella, “Gene delivery nanoparticles fabricated by supercritical fluid extraction of emulsions,” *International Journal of Pharmaceutics*, vol. 387, no. 1-2, pp. 278–285, 2010.
- [76] A. Masotti, F. Bordi, G. Ortaggi, F. Marino, and C. Palocci, “A novel method to obtain chitosan/DNA nanospheres and a study of their release properties,” *Nanotechnology*, vol. 19, no. 5, Article ID 055302, 2008.
- [77] X. Yang, J. D. Shah, and H. Wang, “Nanofiber enabled layer-by-layer approach toward three-dimensional tissue formation,” *Tissue Engineering A*, vol. 15, no. 4, pp. 945–956, 2009.
- [78] P. A. Tran, L. Zhang, and T. J. Webster, “Carbon nanofibers and carbon nanotubes in regenerativemedicine,” *Advanced Drug Delivery Reviews*, vol. 61, no. 12, pp. 1097–1114, 2009.
- [79] C. P. Barnes, S. A. Sell, E. D. Boland, D. G. Simpson, and G. L. Bowlin, “Nanofiber technology: designing the next generation of tissue engineering scaffolds,” *Advanced Drug Delivery Reviews*, vol. 59, no. 14, pp. 1413–1433, 2007.
- [80] E. J. Chong, T. T. Phan, I. J. Lim et al., “Evaluation of electro-spun PCL/gelatin nanofibrous scaffold for wound healing and layered dermal reconstitution,” *Acta Biomaterialia*, vol. 3, no. 3, pp. 321–330, 2007.
- [81] H. S. Yoo, T. G. Kim, and T. G. Park, “Surface-functionalized electrospun nanofibers for tissue engineering and drug delivery,” *Advanced Drug Delivery Reviews*, vol. 61, no. 12, pp. 1033–1042, 2009.
- [82] G. Wang and H. Uludag, “Recent developments in nanoparticle-based drug delivery and targeting systems with emphasis on protein-based nanoparticles,” *Expert Opinion on Drug Delivery*, vol. 5, no. 5, pp. 499–515, 2008.

## Research Article

# Evaluation on Cartilage Morphology after Intra-Articular Injection of Titanium Dioxide Nanoparticles in Rats

Jiangxue Wang,<sup>1</sup> Yu Gao,<sup>1</sup> Ying Hou,<sup>1</sup> Feng Zhao,<sup>1</sup> Fang Pu,<sup>1</sup> Xiaoyu Liu,<sup>1</sup> Zhihong Wu,<sup>2</sup> and Yubo Fan<sup>1</sup>

<sup>1</sup> Key Laboratory for Biomechanics and Mechanobiology of the Ministry of Education, School of Biological Science and Medical Engineering, Beihang University, Beijing 100191, China

<sup>2</sup> Department of Orthopedics, Peking Union Medical College Hospital, Beijing 100730, China

Correspondence should be addressed to Yubo Fan, yubofan@buaa.edu.cn

Received 16 November 2011; Accepted 5 January 2012

Academic Editor: Xiaoming Li

Copyright © 2012 Jiangxue Wang et al. This is an open access article distributed under the Creative Commons Attribution License, which permits unrestricted use, distribution, and reproduction in any medium, provided the original work is properly cited.

Nanoscale wear particles would generate from orthopedic implants with nanoscale surface topography because of residual stress. In this study, the effect of TiO<sub>2</sub> nanoparticles on articular cartilage was investigated by intra-articular injection in rats. Using contrast-enhanced high-resolution microcomputed tomography (micro-CT) technology, the decreased thickness of articular cartilage in distal femur was determined at 1, 7, 14, and 30 days after nanoparticle exposure. A strong linear correlation ( $r = 0.928$ ,  $P < 0.0001$ ) was observed with the results obtained by needle probe testing. After exposure to TiO<sub>2</sub> nanoparticles, cartilage thickness showed time-dependent decrease, and cartilage volume was decreased too. Further, the histopathological examination showed the edema chondrocyte and shranked nucleus in the radial and calcified zone of cartilage. The ultrastructure of articular cartilage implied that the chondrocyte was degenerated, expressing as the condensed chromatin, the dilated endoplasmic reticulum, and the rich mitochondria. Even, the fragments of ruptured endoplasmic reticulum were observed in the cytoplasm of chondrocytes at postexposure day 30. Results indicate that potential damage of articular cartilage was induced by particles existed in knee joint and imply that the biomonitoring should be strengthened in patients with prostheses replacement.

## 1. Introduction

The nanoscale (less than 100 nm) surface topography endows nanomaterials as high biological active matrix for protein adsorption and focal attachment [1, 2], which provides a forthcoming prospect in tissue regeneration and orthopedic prostheses [3–5]. Titanium is widely used in hip and joint implants and is biocompatible because it spontaneously forms a protective oxide thin film (TiO<sub>2</sub> coating, typically 4–6 nm thin) at its surface. It is reported that nanoscale coating creates a conditioned interface for osteoblast and chondrocyte adhesion [6–10] and promotes the osteointegration and bone mineralization *in vivo* [11]. However, because of corrosion, fretting, friction, and mechanical loss, many wear particles would generate at the bone-implant interface or in the joint space [12, 13]. Kuster et al. [14] reported that wear particles with lamellar, chunky, osseous, elongated, and rod shapes were observed in healthy and osteoarthritic

human knee joints. Except the different shapes, the nanoscale polyethylene wear particles below 0.05 μm and metal wear particles with sizes from 40 to 120 nm containing Co, Cr, and Ti are detected *in vivo* with high-resolution microscopy technology [15, 16]. Many researchers reported that nanoscale particles have a potential impact on living organism [17, 18]. *In vivo*, TiO<sub>2</sub> nanoparticles would be phagocytosed by the epithelial and endothelial cells or macrophages, be translocated into the heart, lung and liver tissues with the blood circulation and cause the oxidative stress and inflammatory response [19, 20]. For the interaction with cells, TiO<sub>2</sub> nanoparticles are generally studied *in vitro* that the DNA damage and cell membrane decomposition are induced by the photocatalysis of TiO<sub>2</sub> [21–23]. In our pilot study, the intra-articular-injected TiO<sub>2</sub> nanoparticles have a potential toxicological effect on the knee joint and could be disseminated to the major organs of rats from joint cavity [24]. The aggregated TiO<sub>2</sub> nanoparticles deposited in the

knee joint induce the synovium hypertrophy, lymphocytes and plasma cells infiltration, fibroblast proliferation, and oxidative damage. However, some studies reported that the inflammatory response occurred in synovium involved in regulating the remodeling of articular cartilage, leading to a loss of cartilage [25, 26].

Articular cartilage is very important in the joint movement for providing a resilient and low-friction bearing surface. The thickness of articular cartilage is related either to the age, to the osteoarthritis, or to the mass of donors. Shepherd and Seedhom [27] reported that thick cartilage existed in the incongruent knee joint where most body weight loaded on. Generally, the cartilage thickness is measured by needle probe, ultrasonic technique, optical stereomicroscope, and magnetic resonance imaging (MRI) technique [28]. MRI technique is successfully used for measuring the articular cartilage thickness of humans [29], but the resolution of current clinical MRI systems ( $200\text{ }\mu\text{m}$ ) is not enough to analyze the small animal models and limits its application. With the needle probe method, the intact, *in situ* cartilage can be tested.

X-ray microcomputed tomography ( $\mu$ -CT) is an X-ray-based nondestructive 3D imaging modality with micrometer-level voxel resolutions and quantitative morphological analysis of electron-dense tissues such as tooth and bone of rat, mouse, and rabbit. It is widely used for diagnosing disease in medicine and scientific research in material science, pharmacy, and biology, and so forth. Golding et al. [30] proved that  $\mu$ -CT is a faster and more accurate spatially 3D technique than histological sections for reconstruction of molluscan anatomy. For soft tissues, the contrast-enhanced technique with iodine-contained solution agent is developed to compensate poor radiopacity and to improve the X-ray images. The successful measurement of kidney volume, length, and thickness in mice was performed *in vivo* and *ex vivo* by Almajdub et al. [31] using the contrast-enhanced high-resolution  $\mu$ -CT technology as well as the liver and spleen tumor assessment in living mice [32]. Recently, the equilibrium partitioning of an ionic contrast agent via  $\mu$ -CT (EPIC- $\mu$ CT) is presented as a noninvasive imaging technique and used to assess the articular cartilage morphology in rabbit [33] and rat model [34].

In this study, the potential influence of intra-articular injected  $\text{TiO}_2$  nanoparticles on the articular cartilage in distal femur of rats are investigated at postexposure days 1, 7, 14, and 30. The general approach is to expose rats to the well-characterized nanoparticles by intra-articular injection, to estimate the cartilage thickness and volume with time course using 3D cartilage model which was reconstructed by contrast-enhanced high-resolution  $\mu$ -CT technology and to assess the potential cartilage injury by morphology analysis.

## 2. Material and Methods

**2.1. Materials.**  $\text{TiO}_2$  nanomaterials (Hangzhou Wan Jing New Material Co., Ltd.) without any coating were used in this study. Its purity was higher than 99.8%. The properties such as size, crystal profile, and structure state of  $\text{TiO}_2$  were well characterized previously [24]. Briefly,  $\text{TiO}_2$  nanoparticles

were red blood cells-like wafers with the average diameter of  $45.87 \pm 7.75\text{ nm}$ , the thickness of  $10 \sim 15\text{ nm}$ , and the average pore size of  $7.50 \pm 2.58\text{ nm}$ . The crystal profile was pure anatase. The surface area was  $105.03\text{ m}^2/\text{g}$  with the cumulative pore volume of  $0.42\text{ cm}^3/\text{g}$ , which was determined under Quadrasorb SI analyzer (Quantachrome Instruments, USA) by  $\text{N}_2$  absorption at  $77.3\text{ K}$ . In sterile physiological solution,  $\text{TiO}_2$  tended to aggregate and clustered from  $183.7$  to  $282.0\text{ nm}$  and from  $575.6$  to  $1018.9\text{ nm}$ .

The contrast agent used in this study was Compound Meglumine Diatrizoate Injection (CMDI, ionic monomer iodine contrast agent, iodine concentration =  $370\text{ mg/mL}$ ; Shanghai Xudong Haipu Pharmaceutical Co., Ltd, Shanghai) consisting of  $32\text{ mg/mL}$  sodium diatrizoate and  $268\text{ mg/mL}$  meglumine diatrizoate. The ultrapure water was prepared with a resistivity of  $18.2\text{ M}\Omega\text{-cm}$  (PureLab Plus, Pall, USA). Phenylmethanesulfonyl fluoride (PMSF) was provided by Roche. All other reagents used in this study were at least of analytical grade.

**2.2. Animals.** Male Sprague Dawley rats with  $180 \sim 200\text{ g}$  body weight (about 7-8 weeks old, Experimental animal center of Peking University) were housed in polycarbonate cages placed in a ventilated, temperature-controlled room. The standard conditions were supplied and maintained at  $20 \pm 2^\circ\text{C}$  room temperature,  $60 \pm 10\%$  relative humidity, and  $12\text{ h}$  light/dark cycle. The commercial pellet diet and distilled water for rats were available *ad libitum*. All procedures used in these animal studies were compliant with the local approved protocols of the Administration Office Committee of Laboratory Animal. Animals were acclimated to this environment for five days prior to treatment.

**2.3. Experimental Protocol.** We prepared  $\text{TiO}_2$  suspension using physiological saline solution at  $2\text{ mg/mL}$ . Briefly, the powdered  $\text{TiO}_2$  nanoparticles were dispersed in the fresh sterilized physiological saline solution, and the suspension was ultrasonicated for  $10\text{ min}$  in  $4^\circ\text{C}$  at  $200\text{ W}$  to disperse completely as much as possible.

The animals' experiments were set at four time intervals (postexposure days 1, 7, 14, and 30) to evaluate the change of articular cartilage thickness and morphology. Based on our previous study [24], both control and nanoparticles-exposed rats were included (10 rats per group) in each time interval because the intra-articular nanoparticles would be disseminated to other tissues. The dosage of  $2\text{ mg/kg}$  was selected, which is lower than the detected Ti particles in patients [35]. Before treatment, animals were anesthetized by  $30\text{ mg/kg}$  bw i.p. sodium pentobarbital (Germany). The furs on bilateral hind knees were shaved softly after soaking with soaps liquid, and the povidone iodine was applied to prevent infection. The two hind knee joints were intra-articular injected with  $100\text{ }\mu\text{L}$  of  $2\text{ mg/mL}$   $\text{TiO}_2$  suspensions every other day for 4 times, respectively.  $\text{TiO}_2$  suspension was vortexed for  $3\text{ min}$  before injections. The equal volume physiological saline solution was given to the control rats. Following the exposure, all rats were held for drink and food *ad libitum*. The daily activity and body weight of all rats were recorded carefully. At postexposure days 1, 7, 14,

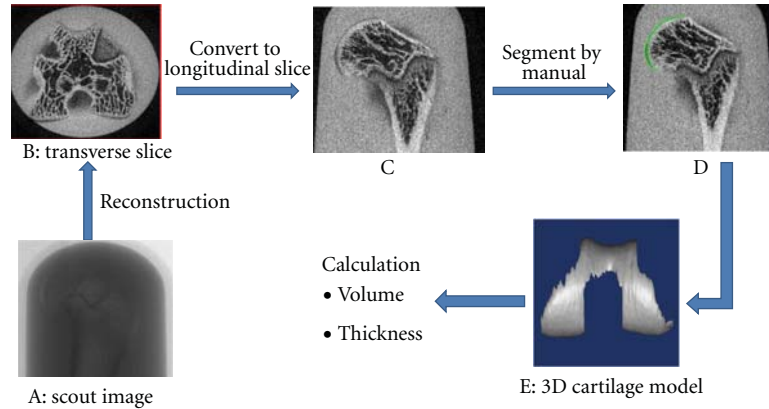


FIGURE 1: Scanning, segmenting, and remodeling of articular cartilage in distal femur. (A): scout image of distal femur obtained by  $\mu$ -CT; (B): transverse slice of distal femur; (C): sagittal slice of distal femur; (D): the green part is cartilage; E: 3D cartilage model.

and 30, the hind knee joints were collected both in the control and exposed group. To cut off the peripheral muscle and ligament carefully, six distal femurs from three rats per group were fixed in 10% formalin solution for histopathological analysis. Three fresh cartilages from three rats per group were immediately immersed in 2.5% glutaraldehyde at  $4^{\circ}\text{C}$  for transmission electron microscopy observation. The remainder distal femurs were cut transversely at the midpoint of the femoral neck, wrapped in sterilized gauze which was soaked with phosphate buffered saline (PBS), and then stored in  $-20^{\circ}\text{C}$ . To protect the cartilage from degeneration, 0.1 mmol/L PMSF was used in PBS.

**2.4. Determination of Contrast Agent Concentration.** The concentration of contrast agent is very important for distinguishing the cartilage and calcified bone tissue, segmenting the cartilage contour accurately, and remodeling the cartilage. To determine the optimal contrast agent concentration, the contrast agent CMDI was diluted in different concentration by PBS solution. The four distal femurs from 10-week-old rats additionally was incubated in 5 mL tube containing 20%, 30%, and 40% CMDI dilution of PBS for 10 min at  $37^{\circ}\text{C}$ , then immediately transferred to a  $\mu$ -CT system for scanning, respectively. All scanning were carried out at 70 kV, 142  $\mu\text{A}$ , and with 18  $\mu\text{m}$  isotropic pixel size.

**2.5. Cartilage Scanning and Remodeling.** Based on the above determined contrast agent concentration, the incubation in 30% CMDI for 10 min at  $37^{\circ}\text{C}$  was selected as the best protocol. The freezed distal femurs were thawed at  $37^{\circ}\text{C}$ , incubated in 30% CMDI for 10 min, and then scanned with 18  $\mu\text{m}$  isotropic pixel size using SkyScan 1076 microtomograph (Aartselaar, Belgium) at 70 kV, 142  $\mu\text{A}$ . The whole procedure of scanning, segmenting, and remodeling of articular cartilage was shown in Figure 1. The specimen tube was fixed on object bed at horizontal level. After preview, the  $35 \times 200$  mm area was scanned with the source-detector pair rotating with  $0.02^{\circ}/\text{min}/\text{step}$ . To enhance tissue features in image, aluminum 1.0 mm physical filter was

selected to absorb the low-energy X-ray. The transverse slices of distal femur were reconstructed using cone-beam reconstruction program and transformed to sagittal slices using DataViewer software package (Aartselaar, Belgium). In order to accurately partition the contrast agent, articular cartilage, and calcified bone, the cartilage contour was segmented by manual according to the CT value. Finally, the 3D cartilage model was reconstructed (Figure 1(e)). The 3D cartilage model was imported into the 3D software Geomagic Studio (Raindrop Geomagic Inc., USA) and to calculate the volume of articular cartilage. Because the change of articular cartilage thickness occurred at the femoral weight bearing sites [33], the cartilage thickness was determined at six points on the superior load-bearing aspect of the medial condyle and lateral condyle of femur by virtually sectioning 3D cartilage model at the desired sagittal plane. All scans and analyses were performed by a single-experienced operator.

**2.6. Needle Probe Testing.** The distal femurs used in  $\mu$ -CT scanning were potted in dental resin using a cylindrical pot and then used to measure cartilage thickness by needle probe testing. The potted specimen was mounted on a specially designed apparatus that could adjust the articular cartilage surface precisely in five degree-of-freedom directions ( $x$ ,  $y$ ,  $\theta_x$ ,  $\theta_y$ , and  $\theta_z$ ) to perpendicular to the needle probe (Figure 2(a)). The apparatus was positioned on the base groove of an Autograph AG-IS material testing machine (Shimadzu, Japan). Once positioned, the assembly was locked strictly to provide enough rigidity through the tests.

Articular cartilage thickness was measured by slow (0.03 mm/min) insertion of a blunt needle probe (0.5 mm in diameter) attached to a 50 N load sensor (sensitivity: 0.25 N). All tests were conducted at room temperature. In whole test procedure, the cartilage surface was kept hydrated with PBS-containing PMSF. The load and displacement outputs were recorded at 0.05 sec interval as the probe penetrated into the cartilage tissue. A change of the slope of the load-displacement curve indicated the probe penetrated from the cartilage to the calcified bone. Cartilage thickness was measured using the probe to sense the moments when the

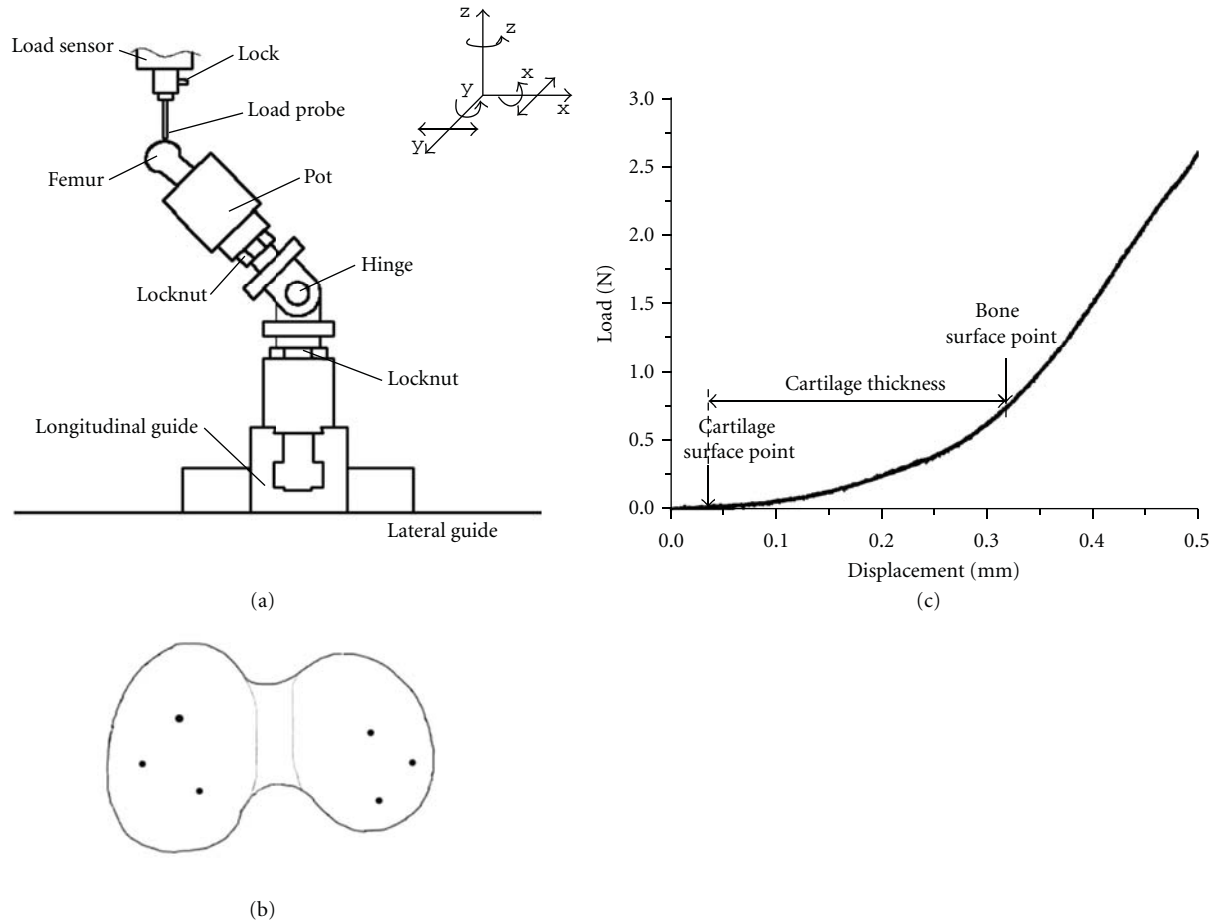


FIGURE 2: (a) the sketch of specially designed apparatus with five degree-of-freedom direction, ( $x$ ,  $y$ ,  $\theta x$ ,  $\theta y$ , and  $\theta z$ ) adjustment of articular cartilage surface perpendicular to the load probe (b) the six points on the superior load bearing aspect of the medial condyle and lateral condyle of distal femur, which is subjected to needle probe tests (c) the representative load-displacement curve.

probe pressed the articular surface and when it contacted the calcified bone (Figure 2(c)). Needle probe testing was performed at six points on the medial condyle and lateral condyle of femur (Figure 2(b)) in corresponding to the sites on 3D cartilage model.

**2.7. Histopathology Examination of Articular Cartilage.** The distal femurs were fixed in 10% formalin solution, decalcified with 10% nitric acid for 24 h, and rinsed by tap water for 4 h. And then, the histopathological tests were performed using standard laboratory procedures. Briefly, the tissues were dehydrated in graded series of 80%, 90%, 95%, and 100% ethanol, followed by clearing in toluene, infiltrated in hot liquid paraffin, finally embedded in paraffin blocks to allow for  $5\text{ }\mu\text{m}$  sections, and mounted onto the glass slides. They were stained with hematoxylin-eosin (H&E) for microscopic analysis. All sections were observed, and the photos were taken using optical microscope (Olympus BX51, USA). The identity and analysis of pathology sections were blind to the pathologist.

**2.8. Ultrastructure of Cartilage by Transmission Electron Microscopy.** The fresh cartilage was carefully cut off by scalpel

and immediately immersed in 2.5% glutaraldehyde at  $4^\circ\text{C}$ . After washing with PBS sufficiently, the cartilage was fixed with 1% osmium tetroxide, dehydrated in a graded series of ethanol, embedded in araldite, and polymerized for 24 h at  $37^\circ\text{C}$ . Ultrathin sections (50 nm) were cut with ultramicrotome (LKB-V, Sweden), contrasted with uranyl acetate and lead citrate, and observed with TEM (H-600, Hitachi).

**2.9. Statistical Analysis.** For statistical analysis, all data are expressed as mean  $\pm$  standard deviation (SD). The one-way analysis of variance (ANOVA) was performed to analyze the significance using the statistical software SPSS 13.0 for windows. A LSD post hoc multiple comparison test was used for different groups.  $P < 0.05$  was considered as the statistical significance.

### 3. Results

**3.1. Concentration of Contrast Agent.** According to the different X-ray attenuation (CT value) of contrast agent, cartilage and calcified bone, the optimal contrast agent concentration was determined. Figure 3 showed the representative saggittal

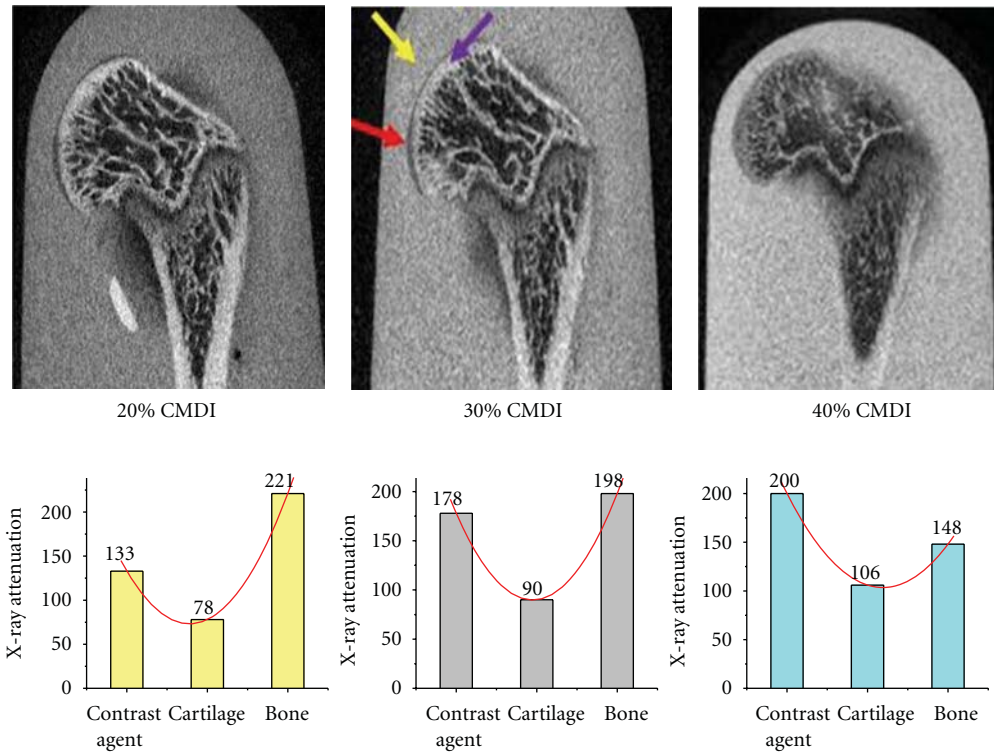


FIGURE 3: The representative sagittal slice of distal femur in 20%, 30%, and 40% CMDI for  $\mu$ -CT in the rat model, the average X-ray attenuation of contrast agent, articular cartilage, and calcified bone in the corresponding CMDI. Yellow, red, and purple arrows refer to the contrast agent, articular cartilage, and calcified bone, respectively.

slice of distal femur in 20%, 30%, and 40% CMDI for  $\mu$ -CT in the rat model and the average X-ray attenuation of contrast agent, articular cartilage, and calcified bone in the corresponding CMDI. In 20% CMDI, the average X-ray attenuation of femoral articular cartilage and calcified bone was 78 and 221, respectively. This contrast difference was enough to segment the cartilage from calcified bone, but not enough to differentiate the cartilage from contrast agent accurately. In 40% CMDI, the average X-ray attenuation of cartilage was 106, which was close to that of calcified bone (148). Therefore, it was difficult to distinguish between the cartilage and calcified bone in segmenting by manual. However, when the distal femur was incubated in 30% CMDI, the average X-ray attenuation of contrast agent, cartilage, and calcified bone was 178, 90, and 198, respectively, which provided the appropriate contrast difference for accurately segmenting the cartilage from the contrast agent

and calcified bone. In the following scanning, therefore, all the distal femurs were incubated in 30% CMDI to remodel the cartilage.

**3.2. Thickness and Volume of Articular Cartilage Determined by  $\mu$ -CT.** According to the above-determined concentration of contrast agent, the incubation in 30% CMDI for 10 min at  $37^{\circ}\text{C}$  was selected as the best protocol. Three distal femurs per group were scanned to obtain the 3D cartilage model. The thickness of articular cartilage exposed to  $\text{TiO}_2$  nanoparticles were calculated and shown in Figure 4. At day 1 after exposure to  $\text{TiO}_2$  nanoparticles, the thickness of articular cartilage was  $0.2754 \pm 0.0207$  mm, which was smaller than that of the corresponding control ( $0.2942 \pm 0.0150$  mm). The changes in cartilage thickness were calculated comparing with that in the corresponding control at each particular time point. The % reduction was calculated as follows.

$$\% \text{ reduction} = \frac{(\text{thickness in the corresponding control} - \text{thickness in } \text{TiO}_2 \text{ exposed rats})}{\text{thickness in the corresponding control}} * 100 \quad (1)$$

At postexposure days 1, 7, 14, and 30, the thickness of articular cartilage was reduced with the rate of 6.41%, 4.52%, 8.64%, and 11.03%, respectively. Comparing with the corresponding control, the significant difference was

detected in rats at days 7, 14, and 30 after exposure to  $\text{TiO}_2$  nanoparticles ( $P < 0.05$ ) (Figure 4).

Using the 3D cartilage model, the volume of articular cartilage covered on the distal femur was measured and

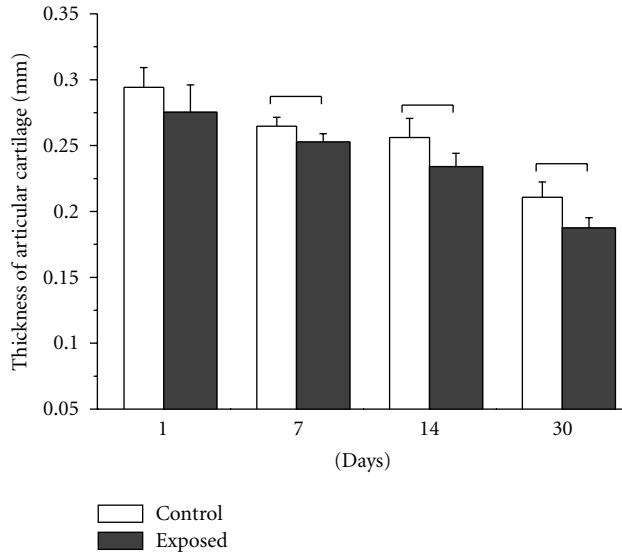


FIGURE 4: Thickness of articular cartilage in the distal femur by 3D cartilage model. \* $P < 0.05$  compared with the corresponding control.

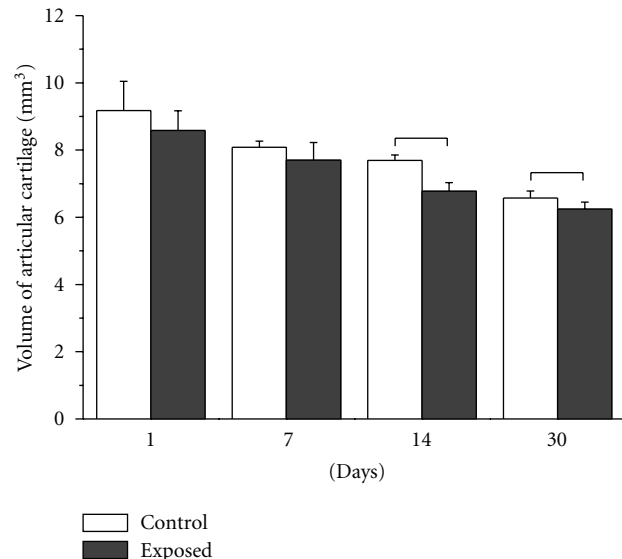


FIGURE 5: Volume of articular cartilage in the distal femur by 3D cartilage model. \* $P < 0.05$  compared with the corresponding control.

illustrated in Figure 5. At postexposure days 1 and 7, the volume of cartilage showed a little decrease compared to the corresponding control ( $P > 0.05$ ); whereas, at days 14 and 30, the significant reduced cartilage volume was detected ( $P < 0.05$ ). It indicated that the growth of articular cartilage might be disturbed by TiO<sub>2</sub> nanoparticles existed in the joint cavity.

For the control rats at different time points, we determined that the thickness and volume of articular cartilage decreased with the rat age. This was important in cartilage development and consistent with the reported results

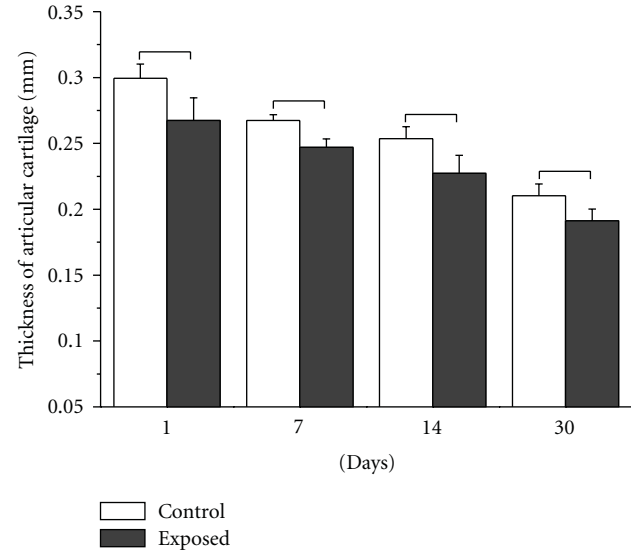


FIGURE 6: Thickness of articular cartilage in the distal femur by needle probe testing. \* $P < 0.05$  compared with the corresponding control.

[34, 35], which could be due to the endochondral bone development and fibrillation under function adaptation or physiological adaptation in rats during normal growth.

**3.3. Thickness of Articular Cartilage Detected by Needle Probe Testing.** In testing, the load-displacement curves were recorded as the load probe penetrated to the cartilage with 0.03 mm/min. According to the slope change of the load-displacement curve, the thickness of articular cartilage in distal femur of rats in each group was determined and illustrated in Figure 6. For the control rats, the thickness of articular cartilage became reduced with the rat age increase, which was consistent with the results obtained by the 3D cartilage model. For the rats exposed to TiO<sub>2</sub> nanoparticles, the cartilage thickness showed the significant decrease compared to the corresponding control ( $P < 0.05$ ) at postexposure days 1, 7, 14, and 30, respectively.

These results showed a strong linear correlation ( $r = 0.928$ ,  $P < 0.0001$ ,  $n = 48$ ) with that determined by the 3D cartilage model (Figure 7), which suggested that the determination of cartilage thickness obtained both by 3D cartilage model and by needle probe testing was accurate and creditable.

**3.4. Morphology Change of Articular Cartilage.** In whole exposure and postexposure period, animals were given food and water *ad libitum*, no abnormal daily activity was observed. After sacrificing the rats, the smooth and moist knee cavity including synovial capsule were observed in the control rats; whereas, the white particles-xanthoproteic complexes were observed in the synovial joint capsule of exposed rats, which indicated the deposition of intra-articular TiO<sub>2</sub> particles. With the time prolong from the postexposure days 1 to 30, the deposited particles-xanthoproteic complexes were reduced, as shown in Figure 8.

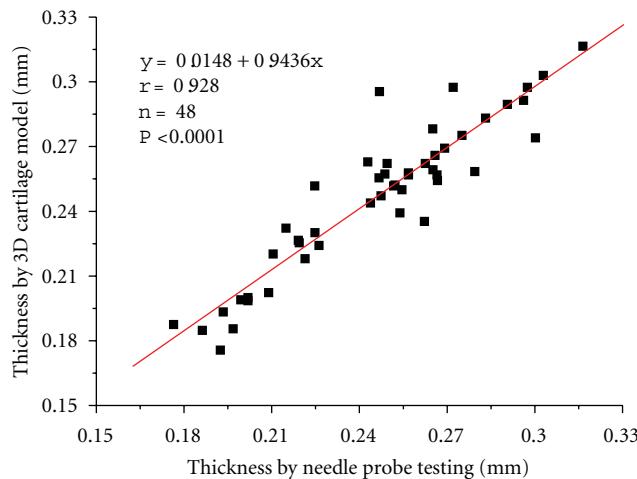


FIGURE 7: The linear correlation between the values of cartilage thickness obtained by 3D cartilage model and needle probe testing. The correlation function  $y = 0.0148 + 0.9436x$ , and  $P < 0.0001$  showed a strong linear correlation ( $r = 0.928$ ).

The histopathology of articular cartilage by H&E staining was shown in Figure 9. Both in the control and exposed rats, the articular cartilage had the intact perichondrium and homogenous cartilage matrix. Depending on the arrangement of chondrocytes and collagen fibres, articular cartilage is divided into several zones including the tangential layer, the transitional zone, the radial zone, and the calcified cartilage layer. In the control, the matrix of the calcified cartilage layer stained slightly darker than the matrix of the other cartilage zones. However, at postexposure day 30, the calcified cartilage layer was eosin-stained, which stained lighter than that of the other groups. In the radial and calcified zone of the cartilage, the chondrocyte was edema, and the cell nucleus was shrunk. These implied that the cartilage injury was induced by the intervention of deposited  $\text{TiO}_2$  nanoparticles at day 30.

Figure 10 showed the ultrastructure of articular cartilage in the distal femur observed by TEM. After exposure to  $\text{TiO}_2$  nanoparticles, the chromatin was condensed and distributed over the fringe of nucleus, the nuclear membrane was invaginated, endoplasmic reticulum was dilated, and ribosomes were decreased in chondrocyte at day 1. The rough endoplasmic reticulum had a lamellar arrangement in the cytoplasm at days 7. The intense axons on the cell surface were developed, and the mitochondria were rich and became swollen in chondrocyte at day 14. At postexposure day 30, to our surprise, the endoplasmic reticulum ruptured, and the fragments were distributed in the cytoplasm.

#### 4. Discussion

Herein, the impact of  $\text{TiO}_2$  nanoparticles on the articular cartilage in the knee joint was reported. By intra-articular injecting the nanoscale  $\text{TiO}_2$  suspension, we observed that there was some particles deposition in the knee joint of

rats. Using contrast-enhanced high-resolution  $\mu$ -CT technology, we determined that the cartilage thickness decreased significantly at postexposure days 7, 14, and 30, which has a strong linear correlation ( $r = 0.928$ ,  $P < 0.0001$ ) with the results obtained by needle probe testing. It is reported that the cartilage change would occur on the medial condyle and lateral condyle of femur because of the compression from weight [36]. Articular cartilage is the smooth, glistening white tissue that covers the surface of all the diarthrodial joints. The main structure of cartilage is the “Benninghoff” collagenous fibre (mainly type II collagen) and the hydrated proteoglycan embedded in it to provide the proper biomechanical function. In our previous study [24], the intra-articular  $\text{TiO}_2$  nanoparticles resulted in the synovium hypotrophy, oxidative damage, and inflammation, such as lymphocytes and plasma cells infiltration and fibroblast proliferation. Some studies reported that the inflammatory response occurred in synovium was involved in regulating the remodeling of articular cartilage and affecting the chondrocyte function, leading to a loss of cartilage and erosion and weakness of the bones [25, 26]. It is to say that the activated synovial fibroblasts attached to the pannus-cartilage interface and released matrix-degrading enzymes, such as matrix metalloproteinases and the proinflammatory cytokines (TNF- $\alpha$  and IL-1) [26, 37]. The matrix-degrading enzymes would inhibit the synthesis of type II collagen through regulating the chondrocyte and the aggregation of proteoglycans [38]. The reduced extracellular matrix would lead to the thinner articular cartilage. Therefore, in this study, the significant decreased articular cartilage thickness was detected in the distal femur of rats exposed to intra-articular  $\text{TiO}_2$  nanoparticles. As determined by the 3D cartilage model, the cartilage thickness reduced about 4.52%, 8.64%, and 11.03% at postexposure days 7, 14, and 30, respectively.

It needs to be pointed out that the thickness and volume of articular cartilage in the control rats also showed a reduction with age. In the weight-bearing joint, studies reported that the cartilage thickness reduced with age both in human [36, 39] and in horse [40]. This is important in cartilage development and ascribed to the endochondral bone development and fibrillation under functional or physiological adaptation. The fetal cartilage is homogenous, showing no site-dependent differences. As the animal gets older and cartilage matures, cartilage becomes gradually heterogeneous under the influence of joint loading, showing topographical variations in both thickness and compressive stiffness. It is worth to emphasize that Xie et al. [34] also showed that the thickness and volume of cartilage in distal femur decreased in rat during normal growth from 4 to 8 weeks, and even to 16 weeks.

As the only living element of the articular cartilage, the chondrocyte holds a key position in the development of cartilage. It produces the components of the matrix, that is, collagens and proteoglycans. Therefore, besides the above determination of the articular cartilage thickness, the histopathology and ultrastructure of articular cartilage were analyzed in this study to observe the change of chondrocytes after exposure to  $\text{TiO}_2$  nanoparticles. Results showed that the chondrocytes were edema and degenerated

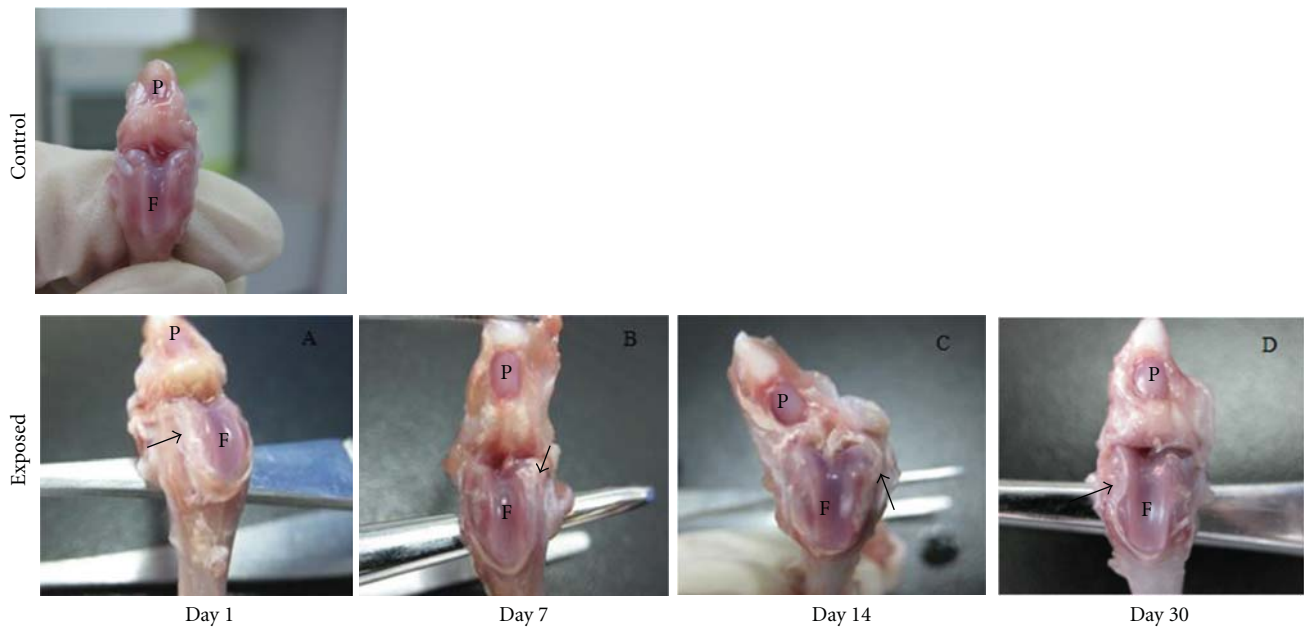


FIGURE 8: Photograph of knee joint cavity in rats after intra-articular injection of  $\text{TiO}_2$  nanoparticles. Control: the smooth and moist knee cavity; exposed: the white particles-xanthoproteic complexes (arrows) in the synovial joint capsule of exposed rats, which indicate the deposition of  $\text{TiO}_2$  particles. With the time prolong from the postexposure days 1 to 30, the deposited particles-xanthoproteic complexes were reduced. P: patellar; F: femur.

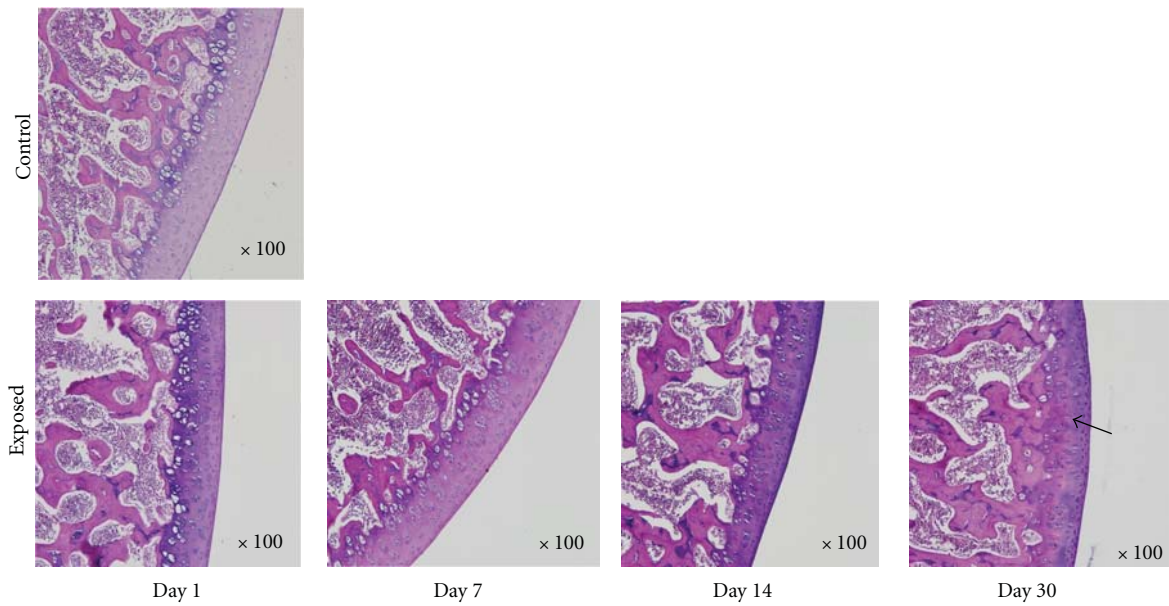


FIGURE 9: Microphotograph of articular cartilage in the distal femur exposed to  $\text{TiO}_2$  nanoparticles by H&E staining. Arrow indicates the edema and degenerated chondrocytes in the radial and calcified zone at postexposure day 30.

in the radial and calcified zone at postexposure day 30. The ultrastructural study of cartilage suggested the degeneration of chondrocyte. More importantly, the mitochondria were rich and became swollen in chondrocyte at postexposure day 14; the endoplasmic reticulum were ruptured in the chondrocyte at postexposure day 30. It is well known that the endoplasmic reticulum plays an important role in the hydroxylation and glycosylation of procollagen, and the

mitochondrion takes part in oxidative phosphorylation and functions as the energy factory of cell. The ruptured endoplasmic reticulum would inhibit the synthesis of collagen and glycosaminoglycans [41]. The reduction in matrix synthesis may provide a potential explanation for the thinning of articular cartilage observed in our study. Further, it is reported that chondrocyte promotes the articular cartilage loss because the surface receptors for cytokines respond to

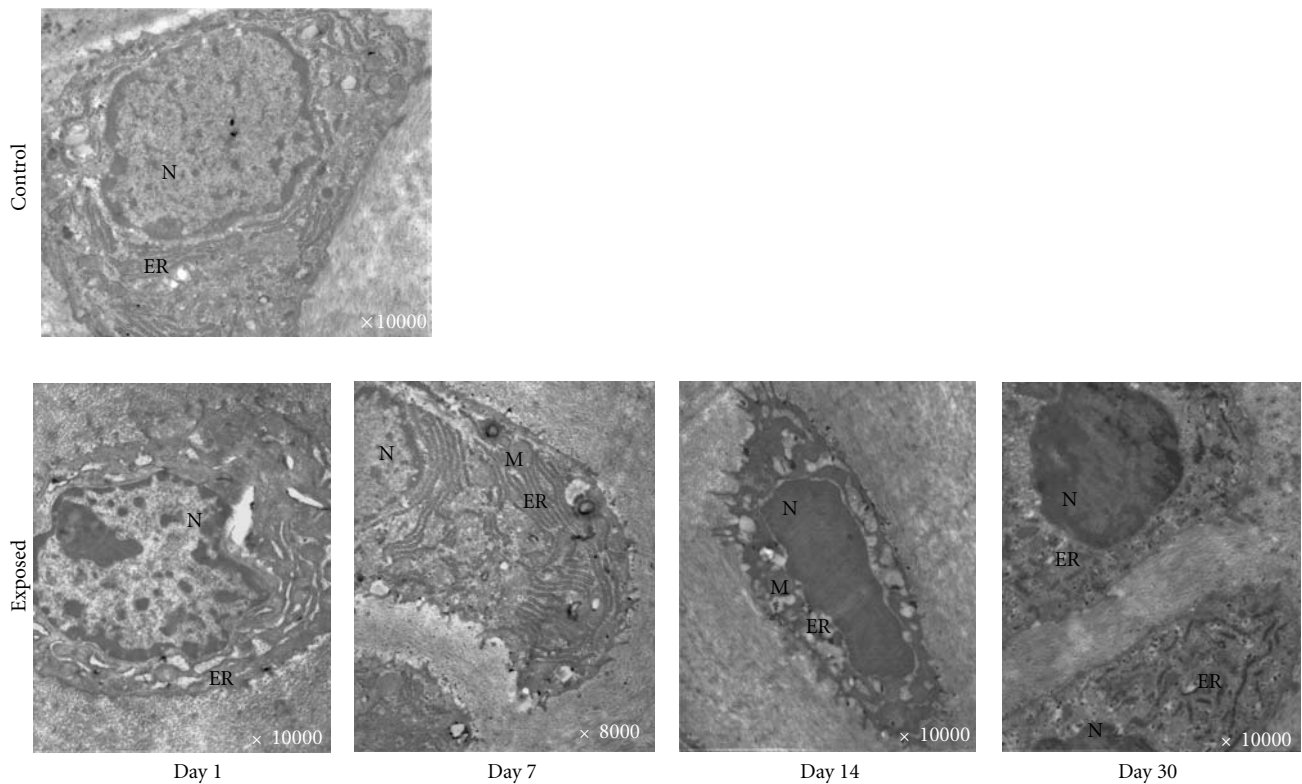


FIGURE 10: The ultrastructure of articular cartilage in the distal femur exposed to  $\text{TiO}_2$  nanoparticles. N: nucleus; ER: endoplasmic reticulum; M: mitochondria. After  $\text{TiO}_2$  nanoparticles exposure, the chromatin was condensed and distributed over the fringe of nucleus, the nuclear membrane was invaginated, the endoplasmic reticulum was dilated, and the ribosomes were decreased in chondrocyte at postexposure day 1. At day 7, a lamellar arrangement for rough endoplasmic reticulum was observed in cytoplasm. At day 14, the intense axons on the cell surface were developed and the mitochondria were rich and became swollen in chondrocyte. At day 30, the endoplasmic reticulum ruptured, and the fragments were distributed in cytoplasm.

the ligands with the production of prostaglandin E<sub>2</sub> and metalloproteinases in synovitis [42]. Of course, to unveil the detailed mechanism of cartilage loss, it is necessary to further research the influence of nanoparticles on the synthesis of extracellular matrix in cartilage, including the collagen and proteoglycan.

## 5. Conclusion

In conclusion, after intra-articular injection of  $\text{TiO}_2$  nanoparticles, we determined that the thickness of articular cartilage was decreased using contrast-enhanced high-resolution  $\mu\text{-CT}$  technology, which had a strong linear correlation ( $r = 0.928$ ,  $P < 0.0001$ ) with the results obtained by needle probe testing. The cartilage thickness was significant decreased with the rat age, and the same trend was observed in cartilage volume. The analysis of morphology and ultrastructure of articular cartilage indicated the chondrocyte was degenerated. Results suggested that the articular cartilage is a potential target for wear particles in knee joint.

## Acknowledgments

This paper is financially supported by the National Natural Science Foundation of China (Grant nos. 30800217,

10925208, and 11032012) and the Postdoctoral Science Foundation of China (20080430304).

## References

- [1] J. Park, S. Bauer, K. von der Mark, and P. Schmuki, "Nanosize and vitality:  $\text{TiO}_2$  nanotube diameter directs cell fate," *Nano Letters*, vol. 7, no. 6, pp. 1686–1691, 2007.
- [2] X. Li, C. A. van Blitterswijk, Q. Feng, F. Cui, and F. Watari, "The effect of calcium phosphate microstructure on bone-related cells in vitro," *Biomaterials*, vol. 29, no. 23, pp. 3306–3316, 2008.
- [3] R. N. Shah, N. A. Shah, M. M. D. R. Lim, C. Hsieh, G. Nuber, and S. I. Stupp, "Supramolecular design of self-assembling nanofibers for cartilage regeneration," *Proceedings of the National Academy of Sciences of the United States of America*, vol. 107, no. 8, pp. 3293–3298, 2010.
- [4] E. Engel, A. Michiardi, M. Navarro, D. Lacroix, and J. A. Planell, "Nanotechnology in regenerative medicine: the materials side," *Trends in Biotechnology*, vol. 26, no. 1, pp. 39–47, 2008.
- [5] X. Li, Q. Feng, X. Liu, W. Dong, and F. Cui, "Collagen-based implants reinforced by chitin fibres in a goat shank bone defect model," *Biomaterials*, vol. 27, no. 9, pp. 1917–1923, 2006.

- [6] B. D. Boyan, T. W. Hummert, D. D. Dean, and Z. Schwartz, "Role of material surfaces in regulating bone and cartilage cell response," *Biomaterials*, vol. 17, no. 2, pp. 137–146, 1996.
- [7] K. Burns, C. Yao, and T. J. Webster, "Increased chondrocyte adhesion on nanotubular anodized titanium," *Journal of Biomedical Materials Research—Part A*, vol. 88, no. 3, pp. 561–568, 2009.
- [8] X. Li, Y. Fan, and F. Watari, "Current investigations into carbon nanotubes for biomedical application," *Biomedical Materials*, vol. 5, no. 2, Article ID 022001, 2010.
- [9] X. Li, H. Gao, M. Uo et al., "Effect of carbon nanotubes on cellular functions in vitro," *Journal of Biomedical Materials Research—Part A*, vol. 91, no. 1, pp. 132–139, 2009.
- [10] X. Li, H. Gao, M. Uo et al., "Maturation of osteoblast-like SaOS2 induced by carbon nanotubes," *Biomedical Materials*, vol. 4, no. 1, Article ID 015005, 2009.
- [11] G. Giavaresi, L. Ambrosio, G. A. Battiston et al., "Histo-morphometric, ultrastructural and microhardness evaluation of the osseointegration of a nanostructured titanium oxide coating by metal-organic chemical vapour deposition: an in vivo study," *Biomaterials*, vol. 25, no. 25, pp. 5583–5591, 2004.
- [12] A. Hatton, J. E. Nevelos, J. B. Matthews, J. Fisher, and E. Ingham, "Effects of clinically relevant alumina ceramic wear particles on TNF- $\alpha$  production by human peripheral blood mononuclear phagocytes," *Biomaterials*, vol. 24, no. 7, pp. 1193–1204, 2003.
- [13] R. Niimi, M. Hasegawa, A. Sudo, and A. Uchida, "A large metallic cyst caused by wear particles after total knee arthroplasty," *Archives of Orthopaedic and Trauma Surgery*, vol. 127, no. 1, pp. 51–54, 2007.
- [14] M. S. Kuster, P. Podsiadlo, and G. W. Stachowiak, "Shape of wear particles found in human knee joints and their relationship to osteoarthritis," *British Journal of Rheumatology*, vol. 37, no. 9, pp. 978–984, 1998.
- [15] M. Lapcikova, M. Slouf, J. Dybal et al., "Nanometer size wear debris generated from ultra high molecular weight polyethylene in vivo," *Wear*, vol. 266, no. 1-2, pp. 349–355, 2009.
- [16] I. Milošev and M. Remškar, "In vivo production of nanosized metal wear debris formed by tribochemical reaction as confirmed by high-resolution TEM and XPS analyses," *Journal of Biomedical Materials Research—Part A*, vol. 91, no. 4, pp. 1100–1110, 2009.
- [17] A. Nel, T. Xia, L. Mädler, and N. Li, "Toxic potential of materials at the nanolevel," *Science*, vol. 311, no. 5761, pp. 622–627, 2006.
- [18] D. B. Warheit, R. A. Hoke, C. Finlay, E. M. Donner, K. L. Reed, and C. M. Sayes, "Development of a base set of toxicity tests using ultrafine TiO<sub>2</sub> particles as a component of nanoparticle risk management," *Toxicology Letters*, vol. 171, no. 3, pp. 99–110, 2007.
- [19] V. Stone and K. Donaldson, "Nanotoxicology: signs of stress," *Nature Nanotechnology*, vol. 1, no. 1, pp. 23–24, 2006.
- [20] J. Wang, Y. Liu, F. Jiao et al., "Time-dependent translocation and potential impairment on central nervous system by intranasally instilled TiO<sub>2</sub> nanoparticles," *Toxicology*, vol. 254, no. 1-2, pp. 82–90, 2008.
- [21] Z. X. Lu, L. Zhou, Z. L. Zhang et al., "Cell damage induced by photocatalysis of TiO<sub>2</sub> thin films," *Langmuir*, vol. 19, no. 21, pp. 8765–8768, 2003.
- [22] W. G. Wamer, J. J. Yin, and R. R. Wei, "Oxidative damage to nucleic acids photosensitized by titanium dioxide," *Free Radical Biology and Medicine*, vol. 23, no. 6, pp. 851–858, 1997.
- [23] S. Hussain, S. Boland, A. Baeza-Squiban et al., "Oxidative stress and proinflammatory effects of carbon black and titanium dioxide nanoparticles: role of particle surface area and internalized amount," *Toxicology*, vol. 260, no. 1–3, pp. 142–149, 2009.
- [24] J. X. Wang, Y. B. Fan, Y. Gao, Q. H. Hu, and T. C. Wang, "TiO<sub>2</sub> nanoparticles translocation and potential toxicological effect in rats after intraarticular injection," *Biomaterials*, vol. 30, no. 27, pp. 4590–4600, 2009.
- [25] S. R. Goldring, "Pathogenesis of bone and cartilage destruction in rheumatoid arthritis," *Rheumatology*, vol. 42, no. 2, pp. ii11–ii16, 2003.
- [26] F. Rannou, M. François, M. T. Corvol, and F. Berenbaum, "Cartilage breakdown in rheumatoid arthritis," *Joint Bone Spine*, vol. 73, no. 1, pp. 29–36, 2006.
- [27] D. E. T. Shepherd and B. B. Seedhom, "Thickness of human articular cartilage in joints of the lower limb," *Annals of the Rheumatic Diseases*, vol. 58, no. 1, pp. 27–34, 1999.
- [28] J. S. Jurvelin, T. Räsänen, P. Kolmonens, and T. Lyyra, "Comparison of optical, needle probe and ultrasonic techniques for the measurement of articular cartilage thickness," *Journal of Biomechanics*, vol. 28, no. 2, pp. 231–235, 1995.
- [29] F. Eckstein, H. Sittek, S. Milz et al., "The potential of magnetic resonance imaging (MRI) for quantifying articular cartilage thickness—a methodological study," *Clinical Biomechanics*, vol. 10, no. 8, pp. 434–440, 1995.
- [30] R. E. Golding, W. F. Ponder, and M. Byrne, "Three-dimensional reconstruction of the odontophoral cartilages of caenogastropoda (mollusca: gastropoda) using micro-ct: morphology and phylogenetic significance," *Journal of Morphology*, vol. 270, no. 5, pp. 558–587, 2009.
- [31] M. Almajdub, L. Magnier, L. Juillard, and M. Janier, "Kidney volume quantification using contrast-enhanced in vivo X-ray micro-CT in mice," *Contrast Media and Molecular Imaging*, vol. 3, no. 3, pp. 120–126, 2008.
- [32] M. Almajdub, M. Nejari, G. Poncet et al., "In-vivo high-resolution X-ray microtomography for liver and spleen tumor assessment in mice," *Contrast Media and Molecular Imaging*, vol. 2, no. 2, pp. 88–93, 2007.
- [33] A. W. Palmer, R. E. Guldberg, and M. E. Levenston, "Analysis of cartilage matrix fixed charge density and three-dimensional morphology via contrast-enhanced microcomputed tomography," *Proceedings of the National Academy of Sciences of the United States of America*, vol. 103, no. 51, pp. 19255–19260, 2006.
- [34] L. Xie, A. S. P. Lin, M. E. Levenston, and R. E. Guldberg, "Quantitative assessment of articular cartilage morphology via EPIC- $\mu$ CT," *Osteoarthritis and Cartilage*, vol. 17, no. 3, pp. 313–320, 2009.
- [35] H. J. Agins, N. W. Alcock, M. Bansal et al., "Metallic wear in failed titanium-alloy total hip replacements. A histological and quantitative analysis," *Journal of Bone and Joint Surgery—Series A*, vol. 70, no. 3, pp. 347–356, 1988.
- [36] R. L. Karvonen, W. G. Negendank, R. A. Teitge, A. H. Reed, P. R. Miller, and F. Fernandez- Madrid, "Factors affecting articular cartilage thickness in osteoarthritis and aging," *Journal of Rheumatology*, vol. 21, no. 7, pp. 1310–1318, 1994.
- [37] W. H. van der Laan, P. H. A. Quax, C. A. Seemayer et al., "Cartilage degradation and invasion by rheumatoid synovial fibroblasts is inhibited by gene transfer of TIMP-1 and TIMP-3," *Gene Therapy*, vol. 10, no. 3, pp. 234–242, 2003.
- [38] P. Seckinger, I. Yaron, F. A. Meyer, M. Yaron, and J. M. Dayer, "Modulation of the effects of interleukin-1 on glycosaminoglycan synthesis by the urine-derived interleukin-1 inhibitor,"

- but not by interleukin-6,” *Arthritis and Rheumatism*, vol. 33, no. 12, pp. 1807–1814, 1990.
- [39] G. Meachim, G. Bentley, and R. Baker, “Effect of age on thickness of adult patellar articular cartilage,” *Annals of the Rheumatic Diseases*, vol. 36, no. 6, pp. 563–568, 1977.
- [40] H. Brommer, P. A. J. Brama, M. S. Laasanen, H. J. Helminen, P. R. Van Weeren, and J. S. Jurvelin, “Functional adaptation of articular cartilage from birth to maturity under the influence of loading: a biomechanical analysis,” *Equine Veterinary Journal*, vol. 37, no. 2, pp. 148–154, 2005.
- [41] N. Mitchell and N. Shepard, “The ultrastructure of articular cartilage in rheumatoid arthritis. A preliminary report,” *Journal of Bone and Joint Surgery—Series A*, vol. 52, no. 7, pp. 1405–1423, 1970.
- [42] H. A. Kim and Y. W. Song, “Apoptotic chondrocyte death in rheumatoid arthritis,” *Arthritis and Rheumatism*, vol. 42, no. 7, pp. 1528–1537, 1999.